DFT-based microscopic magnetic modeling for low-dimensional spin systems

DISSERTATION

zur Erlangung des akademischen Grades

Doctor rerum naturalium
(Dr. rer. nat.)

vorgelegt

der Fakultät Mathematik und Naturwissenschaften
der Technischen Universität Dresden

von

M. Sc. Oleg Janson

geboren am 03.07.1984 in St. Petersburg (Russland)

Eingereicht am 09.01.2012

Die Dissertation wurde in der Zeit von 07/2007 bis 12/2011
im Max-Planck-Institut für Chemische Physik fester Stoffe angefertigt.

Contents

List of Figures 6

List of Tables 9

List of Abbreviations 10

1 Introduction 12

2 Magnetism of cuprates 16
- 2.1 Electronic structure of cuprates 16
  - 2.1.1 Crystal field splitting 16
  - 2.1.2 Covalency 18
  - 2.1.3 Correlations 19
- 2.2 Magnetic properties of cuprates 19
  - 2.2.1 Superexchange 20
  - 2.2.2 Ferromagnetic exchange 20
  - 2.2.3 Frustration 21
  - 2.2.4 DZYALOSHINSKII-MORIYA couplings 22
- 2.3 Magnetic ground states 23
  - 2.3.1 Magnetically ordered ground states 23
  - 2.3.2 Ground states lacking long-range magnetic order 25
  - 2.3.3 Coupling to orbital and lattice degrees of freedom 27

3 Experimental methods 28
- 3.1 Diffraction methods 29
  - 3.1.1 X-ray diffraction 29
  - 3.1.2 Neutron diffraction 32
- 3.2 Thermodynamical measurements 34
  - 3.2.1 Magnetic susceptibility 34
  - 3.2.2 Specific heat 39
- 3.3 Magnetization 41
- 3.4 Resonance spectroscopy 42

4 DFT-based microscopic modeling **44**
4.1 Band structure calculations 44
4.1.1 Density functional theory 44
4.1.2 Approximations to the exchange and correlation potential 46
4.1.3 Correlated systems. DFT+U 47
4.1.4 FPLO 49
4.1.5 Relevant information 50
4.2 Model approach 51
4.2.1 Tight-binding model 53
4.2.2 Tight-binding fit 54
4.2.3 WANNIER functions 57
4.2.4 HUBBARD model 58
4.2.5 Effective low-energy model 59
4.2.6 HEISENBERG model 61
4.2.7 Ferromagnetic coupling 62

5 Simulations of a magnetic model **65**
5.1 High-temperature series expansion 65
5.2 Exact diagonalization 67
5.3 Quantum Monte Carlo 72
5.4 Density-matrix renormalization group 72
5.5 Bridge to experiments 73
5.5.1 Magnetic susceptibility 74
5.5.2 Magnetization 75
5.5.3 LRMO temperature and order parameter 76

6 Model spin systems **77**
6.1 Uniform chains 77
6.1.1 $CuSe_2O_5$ 80
6.1.2 $[NO]Cu(NO_3)_3$ 87
6.1.3 $CaCu_2(SeO_3)_2Cl_2$ 91
6.1.4 Magnetic frustration as a key to the LRMO temperature 99
6.2 2D models with dimer-like couplings 103
6.2.1 $Cu_2A_2O_7$ (A = P, As, V) 105
6.2.2 $CdCu_2(BO_3)_2$ 113
6.3 3D model with 1D features in dioptase $Cu_6Si_6O_{18}\cdot 6H_2O$ 121
6.3.1 Crystal structure 122
6.3.2 DFT calculations 123
6.3.3 Simulations 124
6.3.4 Discussion 126

6.4 Summary 127

7 Kagome lattice compounds 128

7.1 Introduction 128

7.2 Herbertsmithite $Cu_3Zn(OH)_6Cl_2$ 131

7.2.1 Crystal structure 132

7.2.2 DFT calculations 133

7.2.3 Simulations 140

7.2.4 Discussion 142

7.3 Kapellasite $Cu_3Zn(OH)_6Cl_2$ and haydeeite $Cu_3Mg(OH)_6Cl_2$ 143

7.3.1 Crystal structure 143

7.3.2 DFT calculations 145

7.3.3 Spin model and simulations 148

7.3.4 Discussion 150

7.4 Volborthite $Cu_3[V_2O_7](OH)_2 \cdot 2H_2O$ 152

7.4.1 Crystal structure 154

7.4.2 DFT calculations 155

7.4.3 Ground state and thermodynamics of the J_1–J_2–J_{ic} model 161

8 Summary and outlook 165

Appendix 171

A1 Exact diagonalization 171

A2 Details of the experimental studies (Chapter 6) 173

A3 Details of the DFT band structure calculations (Chapters 6 and 7) 176

A4 Details of the simulations (Chapters 6 and 7) 182

Bibliography 185

List of publications 217

Acknowledgments 220

List of Figures

2.1 The CuO_4 plaquette . . . 17
2.2 Electronic structure of cuprates . . . 18
2.3 Competition between superexchange and HUND's rule coupling . . . 21
2.4 Two kinds of magnetic frustration . . . 22
2.5 Basic characteristics of a magnetically ordered GS . . . 23
2.6 Basic characteristics of a singlet GS . . . 26

3.1 The EWALD construction . . . 29
3.2 Strongly anisotropic displacement and split position . . . 32
3.3 Three regimes of $\chi(T)$ . . . 35
3.4 The choice of T_{min} for the CURIE-WEISS fit . . . 37

4.1 Convergence of the total energy with respect to the $\vec{k}$-mesh . . . 51

5.1 Difference between an infinite lattice, a cluster and a finite lattice . . . 68
5.2 Maximal spin-spin separation for open and periodic boundary conditions . . . 69
5.3 Correlation length for finite lattices . . . 70

6.1 Crystal structure of $CuSe_2O_5$ . . . 80
6.2 Magnetic susceptibility of $CuSe_2O_5$ . . . 81
6.3 DOS and band structure of $CuSe_2O_5$ . . . 83
6.4 LDA TB fit for $CuSe_2O_5$ . . . 84
6.5 Wannier functions for $3d_{x^2-y^2}$ states in $CuSe_2O_5$ . . . 84
6.6 LSDA+U calculations for $CuSe_2O_5$ . . . 85
6.7 QMC simulations of $\chi(T)$ for $CuSe_2O_5$ . . . 86
6.8 Crystal structure of $[NO]Cu(NO_3)_3$ . . . 88
6.9 LDA DOS and band structure of $[NO]Cu(NO_3)_3$ . . . 89
6.10 WF for Cu $3d_{x^2-y^2}$ in $[NO]Cu(NO_3)_3$ . . . 89
6.11 Microscopic magnetic model for $[NO]Cu(NO_3)_3$ . . . 90
6.12 Crystal structure of $CaCu_2(SeO_3)_2Cl_2$ . . . 92
6.13 $\chi(T)$ and $M(H)$ for $CaCu_2(SeO_3)_2Cl_2$ . . . 94
6.14 LDA DOS and band structure for $CaCu_2(SeO_3)_2Cl_2$ . . . 94

6.15 Microscopic magnetic model for $CaCu_2(SeO_3)_2Cl_2$ 97
6.16 Coordination number and interchain coupling topologies in quasi-1D systems 100
6.17 Crystal structure and leading exchange couplings in $Cu_2A_2O_7$ (A = P, As, V) . 106
6.18 LDA DOS for $Cu_2A_2O_7$ (A = P, As, V) 107
6.19 WF fits and LDA band structure for $Cu_2A_2O_7$ (A = P, As, V) 108
6.20 Cu $3d_{x^2-y^2}$ WFs for $Cu_2A_2O_7$ (A = P, As, V) 109
6.21 Finite size scaling of m for the anisotropic honeycomb lattice 110
6.22 Diagonal spin correlations for the anisotropic honeycomb lattice 111
6.23 QMC fits to $\chi(T)$ and $M(H)$ of α-$Cu_2P_2O_7$ 112
6.24 LRMO in the magnetic model of α-$Cu_2As_2O_7$ 112
6.25 The original SHASTRY–SUTHERLAND model and the microscopic magnetic model of $CdCu_2(BO_3)_2$ 114
6.26 Crystal structure of $CdCu_2(BO_3)_2$ 115
6.27 LDA DOS and band structure of $CdCu_2(BO_3)_2$ 116
6.28 Cu $3d_{x^2-y^2}$ WF for $CdCu_2(BO_3)_2$ 117
6.29 Microscopic magnetic model for $CdCu_2(BO_3)_2$ 118
6.30 Spin correlations in the GS of $CdCu_2(BO_3)_2$ 119
6.31 ED fit to $\chi(T)$ of $CdCu_2(BO_3)_2$ 120
6.32 Experimental and ED-simulated $M(H)$ of $CdCu_2(BO_3)_2$ 120
6.33 Crystal structure of dioptase $Cu_6Si_6O_{18}{\cdot}6H_2O$ 122
6.34 LDA DOS and band structure of dioptase 123
6.35 LSDA+U results for dioptase 124
6.36 Microscopic magnetic model for dioptase 125
6.37 QMC simulations for dioptase 125

7.1 Crystal structure of herbertsmithite $Cu_3Zn(OH)_6Cl_2$ 133
7.2 LDA DOS and band structure of herbertsmithite $Cu_3Zn(OH)_6Cl_2$ 134
7.3 LDA band structures of herbertsmithite: experimental versus optimized structure134
7.4 Idealized microscopic magnetic model of herbertsmithite $Cu_3Zn(OH)_6Cl_2$ . . 135
7.5 Nonequivalent magnetic couplings resulting from a structural distortion in the hypothetical Zn-free herbertsmithite $Cu_3Cu(OH)_6Cl_2$. 138
7.6 NN spin correlations in the GS of Zn-free herbertsmithite 141
7.7 Crystal structure of kapellasite $Cu_3Zn(OH)_6Cl_2$ and haydeeite $Cu_3Mg(OH)_6Cl_2$ 144
7.8 Interlayer separation in herbertsmithite and kapellasite 144
7.9 DOS and band structure of kapellasite and haydeeite 145
7.10 Orbital-projected DOS for kapellasite 146
7.11 Band structure and TB fit for kapellasite and haydeeite 147
7.12 J_1–J_d model on a kagome lattice 148
7.13 The classical 12-sublattice state realized in the J_1–J_d model on the kagome lattice 149

7.14 Magnetic model and spin correlations for kapellasite and haydeeite 150
7.15 Spin correlations in the J_1–J_d model 152
7.16 Crystal structure of volborthite $Cu_3[V_2O_7](OH)_2{\cdot}2H_2O$ 154
7.17 DOS and band structure of volborthite 156
7.18 Orbital-resolved DOS for volborthite 157
7.19 Orbital ground state for volborthite 157
7.20 Microscopic magnetic model for volborthite 159
7.21 Phase diagram of the J_1–J_2–J_{ic} model 160
7.22 Ground state spin correlations in volborthite 163
7.23 Simulated $M(H)$ and $\chi(T)$ for volborthite 164

A1 Specific heat of $CuSe_2O_5$ 174
A2 Magnetic field dependence of $\chi(T)$ for $CaCu_2(SeO_3)_2Cl_2$ 175
A3 LSDA+U supercells for $CuSe_2O_5$ 176
A4 Cu $3d_{x^2-y^2}$ WFs for $CaCu_2(SeO_3)_2Cl_2$ 178
A5 LSDA+U results for herbertsmithite $Cu_3(Zn_{0.85}Cu_{0.15})(OH)_6Cl_2$ 180
A6 Total energy as a function of O–H distance in kapellasite and haydeeite . . . 181
A7 Finite lattices used for the ED studies of volborthite $Cu_3[V_2O_7](OH)_2{\cdot}2H_2O$. 184

List of Tables

4.1 HILBERT space of a two-site HUBBARD model 60

6.1 Leading transfer and exchange integrals in $CuSe_2O_5$ 84
6.2 Cu–Cu distances, transfer and exchange integrals in $CaCu_2(SeO_3)_2Cl_2$ 95
6.3 T_N in quasi-1D systems 101
6.4 Transfer and exchange integrals for α-$Cu_2P_2O_7$, α-$Cu_2As_2O_7$ and β-$Cu_2V_2O_7$ 108
6.5 Cu–O–Cu angles in $CdCu_2(BO_3)_2$ 116
6.6 LSDA+U results for $CdCu_2(BO_3)_2$ 117

7.1 Distortion of Zn-free herbertsmithite $Cu_3Cu(OH)_6Cl_2$ as a function of spin and orbital degrees of freedom 139
7.2 Leading exchange integrals in the Zn-free herbertsmithite $Cu_3Cu(OH)_6Cl_2$ . . 140
7.3 Leading couplings in kapellasite $Cu_3Zn(OH)_6Cl_2$ and haydeeite $Cu_3Mg(OH)_6Cl_2$ 147
7.4 Structural parameters of volborthite $Cu_3[V_2O_7](OH)_2{\cdot}2H_2O$ 155
7.5 Leading couplings in volborthite 159

A1 Crystallographic data for $CuSe_2O_5$ 173
A2 Selected interatomic distances d (bond lengths) in the $CaCu_2(SeO_3)_2Cl_2$ structure. 175
A3 Experimental crystal structure of $[NO]Cu(NO_3)_3$ 177
A4 Transfer and exchange integrals for the leading couplings in $CdCu_2(BO_3)_2$ . . 179
A5 Experimental and optimized crystal structures of herbertsmithite 180
A6 Optimized H positions for kapellasite and haydeeite 181
A7 Optimized crystal structure of volborthite 182

List of Abbreviations

μSR	muon spin resonance
ADP	atomic displacement parameter
AFM	antiferromagnetic
AMF	around-the-mean-field
bdc	benzenedicarboxylate
BEC	Bose–Einstein condensation
CF	crystal field
DCC	double-counting correction
DFT	density functional theory
DM	Dzyaloshinskii–Moriya
DMFT	dynamical mean-field theory
DMRG	density-matrix renormalization group
DOS	density of states
ED	exact diagonalization
EDXS	energy-dispersive X-ray spectroscopy
EMU	electromagnetic units
ESR	electron spin resonance
EXAFS	extended X-ray absorption fine structure
FLL	fully localized limit
FM	ferromagnetic
GGA	generalized gradient approximation
HTSE	high-temperature series expansion
HZDR HLD	Helmholtz-Zentrum Dresden-Rossendorf, Hochfeld-Magnetlabor Dresden
LDA	local density approximation
LFT	local force theorem
LR(M)O	long-range (magnetic) ordering
MERA	multiscale entanglement renormalization ansatz
mol	mole
MPI CPfS	Max-Planck-Institut für Chemische Physik fester Stoffe
MPMS	magnetic property measurement system

N(P)D	neutron (powder) diffraction
NMR	nuclear magnetic resonance
NN	nearest-neighbor
QMC	quantum Monte Carlo
RG	renormalization group
SQUID	superconducting quantum interference device
VBC	valence bond crystal
WF	WANNIER function
XR(P)D	X-ray (powder) diffraction

Constants

Å	ÅNGSTRÖM, 1×10^{-10} m
eV	electron volt, $1.60217649(4) \times 10^{-19}$ J
μ_B	BOHR magneton, $9.2740091(2) \times 10^{-24}$ J/T
k_B	BOLTZMANN constant, $1.380650(2) \times 10^{-23}$ J/K
N_A	AVOGADRO constant, $6.0221418(3) \times 10^{23}$ mol^{-1}
R	molar gas constant, $8.314462(8)$ J mol^{-1} K^{-1}

Electromagnetic units

1 erg	10^{-7} J
1 G	gauss, 10^{-4} T
1 erg/G	EMU magnetization (“emu”), 10^{-3} J/T

Chapter 1

Introduction

Since 1986, the scientific community is puzzled with the microscopic mechanism giving rise to high-temperature superconductivity in doped cuprates [1]. Despite the burst of excitement right after this seminal discovery, the discussion is still far from being settled [2]. The activity in the field of doped cuprates drew attention to their parent compounds—stoichiometric low-dimensional cuprates that are magnetic insulators with localized spin $S = 1/2$ [3]. Subsequent studies revealed a fascinating variety of magnetic ground states (GSs) realized in these seemingly simple systems, leaving no doubt that undoped cuprates are interesting *per se*. In particular, their insulating orbitally-ordered GS together with the unique diversity of structural motives, and consequently, magnetic lattice topologies, makes cuprates an excellent playground to investigate real material implementations for spin-only quantum models, such as a spin chain or a square lattice, which for years existed as a *Ding an sich*, out of the reach for experimental methods.

The macroscopic magnetism originates from short-range (typically well below 1 nm) exchange couplings that constitute the microscopic magnetic model. The topology of any microscopic magnetic model is apparently related to the geometrical features of the underlying crystal structure—the mutual arrangement of atoms in solids. Already at the early stages of real material studies, it became gradually evident that the assignment of a microscopic magnetic model (spin model) to a particular system is a highly nontrivial task. Several instructive examples illustrate this complexity. The first system is the $S = 1/2$ vanadate compound $(VO)_2P_2O_7$.[1] The magnetic susceptibility of $(VO)_2P_2O_7$ can be well described by an alternating chain model, although the crystal structure bears a ladder-like arrangement of magnetic V^{4+} atoms [4]. At the same time, a certain parameterization of the ladder model also conforms to the experimental data [5]. Later on, the analysis of INS data in Ref. 6 disclosed the irrelevance of the ladder model for $(VO)_2P_2O_7$. Besides, the experimental spectra exhibited a pronounced high-energy mode, which was interpreted as a signature of a two-magnon bound state [6]. Subsequent studies based on alternative techniques refuted this conjecture and revealed that the high-energy mode and the accompanying double-gap feature arise from two nonequivalent alternating chains present in this system [7]. Another example, the frustrated HEISENBERG chain $LiCu_2O_2$, had been proposed to imply two relevant AFM exchange integrals J_1 and J_2, based on thermodynamical measurements and neutron diffraction data [8–10], while a combined NMR and DFT study [11] as well as the INS investigation [12] revealed the FM nature of J_1. The nature of relevant couplings—whether they are AFM or FM—was controversially debated for many other systems, e.g. azurite $Cu_3(CO_3)_2(OH)_2$ [13–15], dioptase $Cu_6Si_6O_{18}\cdot 6H_2O$ [16, 17], $LiVCuO_4$ [18, 19] etc.

---

[1] Vanadates have a $3d^1$ electronic configuration of V^{4+}. The $S = 1/2$ nature of magnetic atoms as well as the absence of charge and orbital degrees of freedom, make them close relatives to cuprates, at least for the magnetic properties.

The source of these mistaken and controversial magnetic models is concealed deep in the methodological issues. There is no doubt that experiments typically provide robust and unbiased results for the basic characteristics of the magnetic GS and the excitation spectrum, such as for instance, the presence or the absence of the singlet-triplet gap (spin gap). However, a quantitative description of the magnetic properties requires the knowledge of the underlying magnetic model, i.e. the microscopic Hamiltonian, which key parameters are the magnetic exchange couplings. Although experimental information can be indeed used to challenge and refine such models, it is generally very tricky to *derive* the magnetic model itself (some instructive examples were discussed above). Therefore, a magnetic model should be chosen *prior* to the analysis of experimental data. To a large extent, the assignment of a particular model is done based on structural considerations by applying simplified empirical rules, such as the GOODENOUGH–KANAMORI rules [20, 21], trying essentially to *guess* the magnetic model. However, recent theoretical, numerical as well as experimental studies on a number of materials evidence that such approach is at best not universally applicable, and can be quite misleading.

In the present study, an alternative, multi-step microscopic approach is developed. This approach is capable of evaluating reliable quantitative magnetic models for rather complex systems, in particular, a family of cuprates with a kagome-lattice-like arrangement of magnetic atoms. The starting point of this procedure is a consideration of the experimental structural data, used as an input for DFT calculations. Unfortunately, this step is sometimes carelessly skipped in DFT studies. Several instructive examples, demonstrating the crucial importance of the structural input, will be discussed. Next, a minimal DFT-based microscopic magnetic model is evaluated. This part of the study comprises band structure calculations, the analysis of the relevant bands, supercell calculations, and finally, the evaluation of a microscopic magnetic model. It will be shown that a combination of full-potential calculation with a rigorous analysis of the relevant orbitals and couplings, together with an accurate treatment of correlations within parameter-dependent procedures, yield reliable quantitative magnetic models.

The GS and the magnetic excitation spectrum of the evaluated model are analyzed by using various simulation techniques, such as quantum Monte Carlo, exact diagonalization and density-matrix renormalization groups, while the choice of a particular technique is governed by the dimensionality of the model, and the presence or absence of magnetic frustration. Unfortunately, extensive literature on the methodology of the simulation techniques contrasts with a lack of information concerning the comparison of the simulated results with the experimental data. One of the aims of the present study is to fill this gap.

The approach used and developed in the present study is universal, and can be applied even in the absence of any experimental information beyond the crystal structure. In this case, the guiding goal of a study is a search for unusual spin models, based on the analysis of the crystal structure or by considering the available experimental data for related systems. In particular, such studies can be motivated by peculiar structural features of a certain compound that govern its magnetic coupling regime, and thus tailor the respective spin lattice. Moreover, it is possible to predict the magnetic properties of the compound and estimate its potential to exhibit interesting physics.

Furthermore, this approach is useful for studying the subtle interplay between the crystal structure and the magnetic properties. For instance, a substitution of a group of atoms in a particular compound is an appealing way to tune the magnetism. Based on empirical considerations or chemical intuition, it is in general tricky to predict how the magnetic properties change upon a structural substitution, i.e. to perform a *directed* substitution. In this case, DFT calculations combined with simulations of the microscopic magnetic model are capable to guide such studies and largely reduce the efforts needed to synthesize new materials and investigate their magnetic properties experimentally.

The thesis is organized as follows. Chapter 2 contains essential information on the magnetism of cuprates: typical structural features, the basics of their electronic structure, the relevant coupling mechanisms and the magnetic GSs. It can be regarded as an extended introduction, focused on the problems characteristic to cuprates as magnetic materials.

The next three chapters generally follow the main lines of the developed procedure, which may be subdivided into four steps. The first step is a careful examination and evaluation of the available experimental data, particularly the structural input. This apparently requires profound knowledge of the relevant experimental techniques. Thus, Chapter 3 of this thesis comprises a description of the most popular techniques for determination and refinement of a crystal structure and measurement of magnetic properties, focusing on particular capabilities and limitations of a certain method, while all methodological and technical details are intentionally omitted.

Band structure calculations are the second step of the procedure. Their major role in the developed approach requires an extensive discussion. A brief summary on the basics of DFT is followed by a more extended discussion on the most popular approximations used for the exchange-and-correlation potential, as well as the most common schemes to account for strong correlations. Then, the software used for band structure calculations, is described. Finally, the step-by-step evaluation of a magnetic model is presented.

The third part of the approach—model simulations, enable direct comparisons between the resulting magnetic model and the experimental data. In the beginning of Chapter 5, the criteria for the choice of a certain simulation technique are discussed. Besides, the essentials of the most popular techniques—QMC, exact diagonalization and DMRG, widely used in the present study, are described. A detailed discussion is devoted to the methodological aspects of bridging together the experimental data and the simulated quantities.

The final step, comparison or prediction for the experimental data, largely depends on the properties of the system under investigation. Considering the complexity of the described approach, it is reasonable (if not necessary) to test it for various crystal structure geometries and motives that give rise to rather simple or well-understood magnetic models. Such test-cases are discussed in Chapter 6, making it a sort of a "cookbook" for DFT-based studies of low-dimensional cuprates. The results presented in Chapter 6 justify the calculational approach and can be used as a benchmark for more complex situations.

In Chapter 7, the developed approach is applied to materials claimed to imply the physics of the $S = 1/2$ HEISENBERG kagome model, and thus candidates for a spin liquid magnetic GS. Based on the DFT calculations, microscopic magnetic models are evaluated. As will be shown, several features relevant for the magnetic properties have been disclosed this way.

Finally, the Chapter 8 summarizes the results of the present study. Besides, the performance as well as limitations of the developed approach are discussed, and its possible extensions and modifications are outlined.

Chapter 2

Magnetism of cuprates

The title of this Chapter requires an immediate addition concerning the word “cuprates”: throughout the thesis, this term is used for stoichiometric crystalline compounds that contain both divalent copper Cu^{2+} and oxygen. In the scientific literature, these compounds are sometimes referred as “undoped cuprates”, to sharpen the contrast with their doped counterparts. Since the complex physics of doped cuprates is not discussed in this thesis, in the following, the word “undoped” is omitted but implied throughout this work.

Another remark concerns the obligatory presence of oxygen in cuprates. As revealed by numerous studies, the magnetism of cuprates bears strong similarities to other stoichiometric Cu^{2+} systems, such as chlorides, bromides, nitrides. Therefore, these systems will be used for comparisons, although they are not subject of the present study.

Sec. 2.1 is devoted to general aspects of the electronic structure of cuprates. In particular, it is explained how the localized magnetism of cuprates emerges from the joint effect of crystal field (CF), covalency and correlations. In Sec. 2.2, the types of magnetic interactions relevant for cuprates, are discussed. These are, in the first place, superexchange and HUND’s rule exchange. The variety of magnetic GSs found in cuprates, is reviewed in a systematic way in Sec. 2.3.

2.1 Electronic structure of cuprates

2.1.1 Crystal field splitting

The local environment of copper determines the CF splitting and therefore plays a key role for the magnetic properties. In cuprates, the idealized coordination of Cu^{2+} is a regular octahedron CuO_6. This geometrical configuration splits the five $3d$ orbitals into two manifolds: the twofold-degenerate e_g and the threefold-degenerate t_{2g}. Repulsion between the $3d$ electrons of Cu and the electrons of ligands gives rise to the difference in energy between the two manifolds: the e_g orbitals “point” to the ligand O atoms, leading to sizable repulsion between the electrons, while the t_{2g} orbitals are located between the ligands, which is energetically favorable.

In the regular octahedral coordination, both e_g orbitals ($3d_{x^2-y^2}$ and $3d_{3z^2-r^2}$) are degenerate. Since the electronic configuration of a Cu^{2+} atom is $3d^9$, i.e. there is only one hole in the $3d$ level, the degenerate configuration is electronically unstable. This instability typically leads to a sizable distortion of the CuO_6 octahedra, lifting the degeneracy. This distortion is generally acknowledged as a JAHN–TELLER distortion, although there is at best no evidence that the mechanism put forward by JAHN and TELLER [22] plays the leading role in cuprates [3]: this mechanism accounts for instability and the resulting distortion, but does not account for a particular way the degeneracy is lifted. Although many hypothetical distortions can be conceived, the overwhelming majority of cuprates exhibits a particular type of distortion, which involves shortening of the four intraplane Cu–O bonds and a concomitant elongation of the two apical bonds. This leads to formation of a CuO_4 plaquette —a square of four O atoms bonded to the central Cu atom(Fig. 2.1), with the typical Cu–O bond length 1.90–2.05 Å. In many low-symmetry compounds, the plaquette can be distorted, which leads to nonequivalent bond lengths and a nonzero volume of the CuO_4 polyhedron.

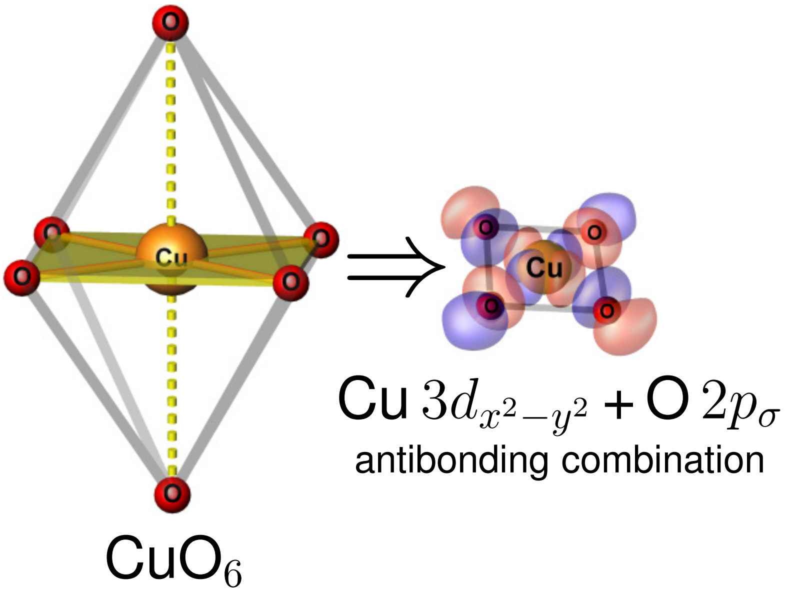

Figure 2.1: Left panel: formation of a CuO_4 plaquette. Right: A WANNIER function (FOURIER-transform of the respective BLOCH state, see Sec. 4.2.3 for details) for the Cu $3d_{x^2-y^2}$ state. Distortion of the initially octahedral coordination leads to sizable hybridization of Cu $3d_{x^2-y^2}$ and O $2p_\sigma$ orbitals, as indicated by the large weights of the Wannier function on the ligand atoms.

The formation of plaquettes is usually referred as the "4+2" distortion (four short and two long Cu–O bonds). The opposite type of distortion, "2+4", also misleadingly called "anti-JAHN–TELLER", describes the situation where the two apical bonds shorten, while the four intraplane bonds elongate. Such distortion is uncommon for cuprates, with notable exceptions of $CuSb_2O_6$, volborthite $Cu_3[V_2O_7](OH)_2 \cdot 2H_2O$, and presumably, vesigneite $BaCu_3V_2O_8(OH)_2$.

Cu^{2+} can bear a local coordination which essentially differs from the octahedral. In the simplest case, apical O atoms are absent, and the elementary units are CuO_4 plaquettes, as in Bi_2CuO_4. Another type of the local coordination is the triangular bipyramid CuO_5 ("2+3"), which occurs in the systems with sufficiently high symmetry, e.g. in Cu_2OSeO_3.

The local environment of Cu can contain, in addition to O atoms, also halogen atoms like Cl or Br. In this case, for the correct understanding of CF effects, the difference in radii of ligand atoms should be taken into account. As a result, mixed oxygen-halogen plaquettes, e.g. CuO_3Cl or CuO_2Cl_2, can appear. The instructive example of $CaCu_2(SeO_3)_2Cl_2$ is discussed in Sec. 6.1.3.

2.1.2 Covalency

Distortion of the local coordination is an ubiquitous phenomenon in metallate systems. The special feature of cuprates is the strong hybridization of a particular Cu 3d orbital and the respective O $2p_\sigma$ orbitals (Fig. 2.1). This effect is known as covalency, and it gives rise to the splitting between the bonding and the antibonding $(dp)_\sigma$ bands. This splitting is typically much stronger than the CF splitting and amounts to 5–8 eV (Fig. 2.2).

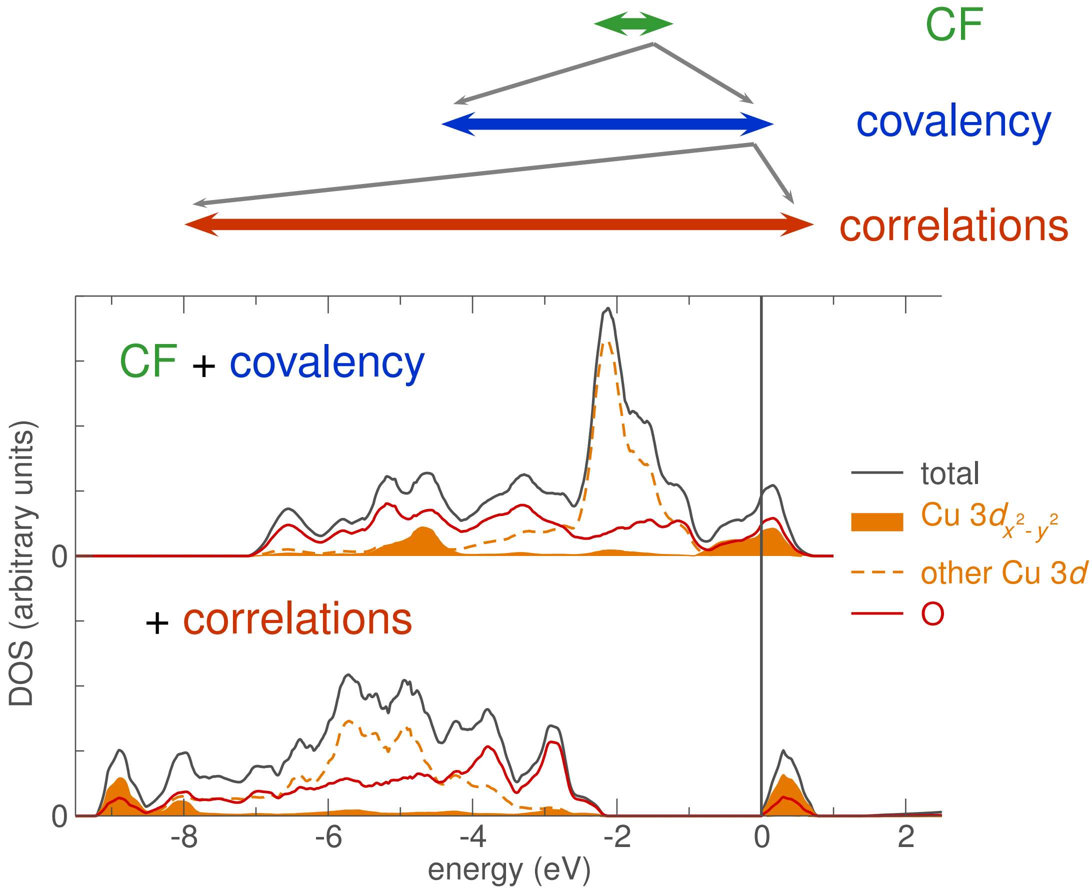

Figure 2.2: The principal effects (top) giving rise to the electronic structure of cuprates and a typical electronic structure of a cuprate compound (melanothallite Cu_2OCl_2), as yielded by a full-potential DFT code (bottom). Bottom panel, upper part: a weakly correlated functional (LDA, GGA) leads to correct treatment of crystal field (CF) and covalency effects, but underestimates correlations, which results in a metallic solution (states at ε_F). Bottom panel, lower part: static mean-field treatment of correlations (DFT+U) leads to the correct insulating GS, but worsen the description of covalency effects (note the different ratio of Cu $3d_{x^2-y^2}$ and O states in the vicinity of ε_F).

The orbital character of the relevant 3d orbital is defined by short Cu–O bonds and thus is ruled by the local coordination. For the most common case of the “4+2” distortion, the covalency affects the $3d_{x^2-y^2}$ orbital. The less common "2+4" and "2+3" environments are characterized by short distances between the central Cu and apical O atoms, thus the $3d_{3z^2-r^2}$ orbital is active.

The effect of covalency drastically alters the electronic structure: the bonding $(dp)_\sigma$ states of Cu and O become the lowest-lying states of the valence band. The non-bonding Cu and O states lie higher in energy and form the bulk of the valence band. All these states are fully filled. The half-filled antibonding $(dp)_\sigma$ bands are located at the FERMI energy ε_F.

2.1.3 Correlations

The discussion of the CF and covalency effects so far was based on a molecule-like model for a single CuO_6 octahedron. However, cuprates are crystalline materials, and the molecular description is not fully appropriate. In particular, discrete energy levels transform into bands. Therefore, band structure calculations are a natural way to resort to the bulk picture. The resulting effect of CF and covalency splitting can be visualized by considering the electronic DOS (Fig. 2.2, upper part of the bottom panel) of a typical cuprate material, as yielded by standard approximations for the exchange and correlation potential, such LDA or GGA. Although the CF effects are substantially smeared, the covalency splitting of Cu $3d_{x^2-y^2}$ states is clearly visible.

Unfortunately, this simplified picture is wrong even qualitatively: it predicts a metallic GS in contrast to the insulating GS, experimentally well-justified for undoped cuprates [3]. The reason for this discrepancy is the small extension of Cu $3d_{x^2-y^2}$ orbitals which gives rise to large COULOMB repulsion (correlation) of two electrons occupying this orbital. As a result, the antibonding $(dp)_\sigma$ states bifurcate, and the material becomes insulating (Fig. 2.2, lower part of the bottom panel).

Depending on the character of the lowest-lying unoccupied states, two types of correlated insulators are distinguished. In MOTT insulators, the lowest lying excited states are empty d-states of transition metal. Typical examples are vanadates (V^{4+}) or titanates (Ti^{5+}). In contrast, cuprates have a $3d^9$ electronic configuration, with no empty d states. Thus, the process of electron transfer between Cu d states and O p states has the lowest energy. Such materials are classified as charge-transfer insulators.

To summarize, the qualitative understanding of the electronic structure of cuprates requires a proper accounting for three major effects: CF splitting, covalency and correlations.

2.2 Magnetic properties of cuprates

The magnetism of cuprates originates from interaction between unpaired electrons, localized at the Cu sites. This interaction has a purely quantum nature and will be discussed below.

An important remark concerning the exchange integrals J_i: throughout the thesis, positive and negative values denote AFM and FM exchange, respectively. The units are K (this simplifies comparison to experiments). Strictly speaking, these quantities should be denoted as J_i/k_B. For ease of notation, the BOLTZMANN constant k_B is generally omitted throughout the thesis (except for the numerated equations).

2.2.1 Superexchange

The concept of superexchange was introduced by P. W. ANDERSON [23, 24] to describe the AFM coupling between two magnetic atoms, which involves at least one intermediate non-magnetic atom. The simplest physical interpretation of this phenomenon is the reduction of energy by delocalization. Overlaps between the d orbitals and the ligand orbitals are gateways that allow for such a delocalization, provided that the electron spins are antiparallel. This gives rise to an AFM interaction. For cuprates, the theory of superexchange can be regarded as the microscopic theory for the WEISS molecular field concept [25].

The antibonding σ-combination of Cu $3d_{x^2-y^2}$ and O $2p$ orbitals, realized in the majority of cuprates gives rise to a strong superexchange, making it the leading AFM coupling mechanism. However, superexchange can be realized not only via Cu–O–Cu connections, but also more complex paths such as Cu–O–O–Cu (the surplus term “super-superexchange” is sometimes used for such paths) or Cu–O–M–O–Cu, where M is a non-magnetic atom.

The energy scale of superexchange in cuprates strongly depends on the respective superexchange path. Thus, the strength of the resulting exchange coupling can vary in a broad range from zero to about 2000 K in Sr_2CuO_3 [26]. However, such high values are rare. The leading exchange typically does not exceed several hundreds of K, whereas in many cases it is even below 100 K.

The strength of the coupling generally decreases upon increase of the distance between the respective Cu atoms. However, this rule is not universal, since the strength also depends on the mutual orientation of the magnetic orbitals as well as the ligand orbitals. In many cases, e.g. $CaCu_2(SeO_3)_2Cl_2$ (Sec. 6.1.3) and $Cu_2A_2O_7$ (Sec. 6.2.1), long-range superexchange can give rise to a sizable coupling, which strongly exceeds the NN exchange.

2.2.2 Ferromagnetic exchange

Recent extensive studies on cuprates with structural chains of edge-sharing CuO_4 plaquettes leave no doubt that in nearly all these systems the NN coupling is FM. Therefore, the relevant FM coupling mechanism in these systems dominates over the superexchange. In principle, the direct coupling between the d electrons of the neighboring Cu atoms could give rise to an FM coupling. However, typical Cu–Cu distances exceed 2.8 Å, which is far too large for any appreciable direct coupling. Instead, the leading mechanism of FM coupling in cuprates is the HUND’s rule coupling J_H.

The mechanism of the Hund's rule coupling can be illustrated by considering a dimer of two CuO_4 plaquettes, and varying the Cu–O–Cu angle.[1] The staring point is the corner-sharing geometry with the Cu–O–Cu angle equal to 180° (Fig. 2.3, left). This configuration is optimal for superexchange, which is realized through the O $2p$ orbital which "connects" the Cu atoms, and the respective AFM coupling is large. The decrease of the Cu–O–Cu angle leads to a gradual diminishing of the σ-overlap of Cu $3d$ and O $2p$ orbitals and consequently, reduces the AFM coupling. At the same time, another O $2p$ orbital becomes involved in the superexchange process. As a result, electrons occupying the two different O $2p$ orbitals can reduce their energy by parallel alignment of their spins (Hund's rule), giving rise to an FM contribution.

At some critical value of the Cu–O–Cu angle close to 97°, the AFM and FM contributions balance each other and cancel the effective magnetic coupling. For smaller values of the Cu–O–Cu angle that are be realized in cuprates ($\leq\sim$85°), the FM coupling becomes dominant.

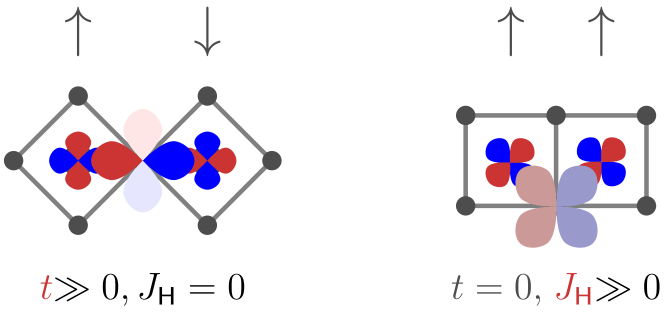
$t \gg 0,\ J_{\mathrm{H}} = 0$
$t = 0,\ J_{\mathrm{H}} \gg 0$

Figure 2.3: Competition between superexchange and Hund's rule coupling is a dimer of CuO_4 plaquettes. Left: superexchange is maximal, Hund's rule coupling is absent. Right: Hund's rule coupling is maximal, superexchange is absent.

The mechanism discussed can give rise to a sizable FM exchange of about -225 ± 25 K (e.g., Ref. 28). Although it is one order of magnitude smaller than the maximal values of superexchange, FM contributions can play a substantial role especially for short-range couplings.

2.2.3 Frustration

The set of all relevant exchange couplings forms a microscopic magnetic model, or a spin lattice of magnetic atoms (nodes) connected by AFM or FM couplings (bonds). The whole variety of possible lattice topologies can be subdivided into two major classes, non-frustrated and frustrated topologies.

On a microscopic level, magnetic frustration implies the absence of a magnetic structure that would match all microscopic exchange couplings. Here, the word "match" definitely needs an additional explanation. It can be given in terms of a classical Heisenberg model, in which spins are described by classical vectors $\vec{S}_i$ and $\vec{S}_j$ of length $1/2$, coupled by positive (AFM) or negative (FM) exchange interactions J_{ij}. Frustration can be illustrated by considering the products $-4[\vec{S}_i \cdot \vec{S}_j](J_{ij}/|J_{ij}|)$. For each pair of spins (i, j), this product is a real number from the interval $[-1,1]$. If this product is equal to unity, the spin arrangement matches the respective coupling (parallel arrangement for an FM coupling, antiparallel arrangement for an AFM coupling), i.e. the coupling is satisfied. If $-4[\vec{S}_i \cdot \vec{S}_j](J_{ij}/|J_{ij}|) < 1$, the coupling is not satisfied. If this is the case for at least one pair of spins, the respective magnetic model is frustrated.

---

[1] The magnetic behavior of this model is discussed in Ref. 27.

For a quantum model, the microscopic magnetic model should be investigated for the presence of competing interactions. Depending on the type of couplings that compete with each other, magnetic frustration can be of two kinds. If the competing couplings are symmetrically related, i.e. they have the same sign and exactly the same magnitude, the corresponding situation is called *geometrical frustration*. The opposite case, referred as *frustration due to competing interactions*, implies that the respective exchange couplings can differ in sign and magnitude.

The classical example of geometrical frustration is a triangle of antiferromagnetically coupled spins (Fig. 2.4, left). The prerequisite for a realization of this configuration is the presence of the threefold symmetry, i.e. the space group should be either trigonal or cubic. Most studied examples of geometrically frustrated spin lattices are the triangular and the kagome lattice (2D), as well as the pyrochlore lattice (3D).

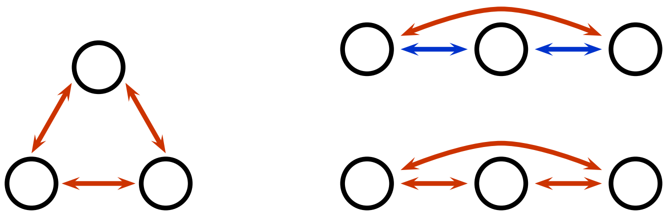
geometrical frustration

frustration due to competing interactions

Figure 2.4: Two kinds of magnetic frustration. Spins are depicted by open circles. Red and blue arrows denote AFM and FM exchange couplings, respectively.

Frustration due to competing interactions is a more frequent phenomenon than the geometrical frustration. First, even an infinitesimal deviation from the threefold symmetry destroys geometrical frustration. Second, any anisotropic version of a geometrically frustrated situation (e.g. anisotropic triangular lattice), falls into this class. Here, in contrast with the geometrical frustration, a competition between AFM and FM couplings is possible.

2.2.4 Dzyaloshinskii-Moriya couplings

At present, there is no doubt that the magnetic properties of cuprates are generally well accounted for by isotropic exchange couplings. However, isotropic couplings can not explain weak ferromagnetism, observed for several systems. This problem was brought to light by experiments on α-Fe_2O_3 [29]. Dzyaloshinskii argued [30] that the observed effect is related to the spin-orbit coupling. Following his phenomenological explanation of this phenomenon, Moriya derived the corresponding expression for the coupling by including the spin-orbit coupling into the theory of superexchange [31]. The energy correction appeared to proportional to the dot product of a certain vector $\vec{D}_{ij}$ and the cross product of the respective spin operators $\mathbf{S}_i \times \mathbf{S}_j$. In addition, MORIYA formulated several rules that relate the components of $\vec{D}_{ij}$ with local symmetry [31].

2.3 Magnetic ground states

The variety of magnetic GSs found in cuprates is probably the main reason why they are in the focus of solid state physics during the last 25 years. The vast number of studies on the subject allows for only a brief summary to be given here. Besides, the results presented in Chapters 6 and 7 should be also regarded as a contribution to this field.

2.3.1 Magnetically ordered ground states

Continuous symmetries, such as SU(2) symmetry of the HEISENBERG model, can not be spontaneously broken at finite temperature neither in 1D nor in 2D [32]. Thus, a 3D coupling regime is a prerequisite for a long-range magnetically ordered GS.

The two basic characteristics of an ordered GS are the propagation vector $\vec{q}$ and the ordered moment. The latter is traditionally decomposed into a vector norm m (also referred as order parameter) and direction of the moment. The components of the propagation vector describe the mutual arrangement of spins connected by the respective lattice translation vector (Fig. 2.5). There are two standard notations of the individual components. According to the first scheme, the components are given in the units the angle between the spins: 0 for a parallel arrangement, π for an antiparallel arrangement. This notation is typically used in theoretical works. In the other notation, the components are normalized to 2π, leading to $1/2$ for an antiparallel arrangement. This notation prevails in experimental works.

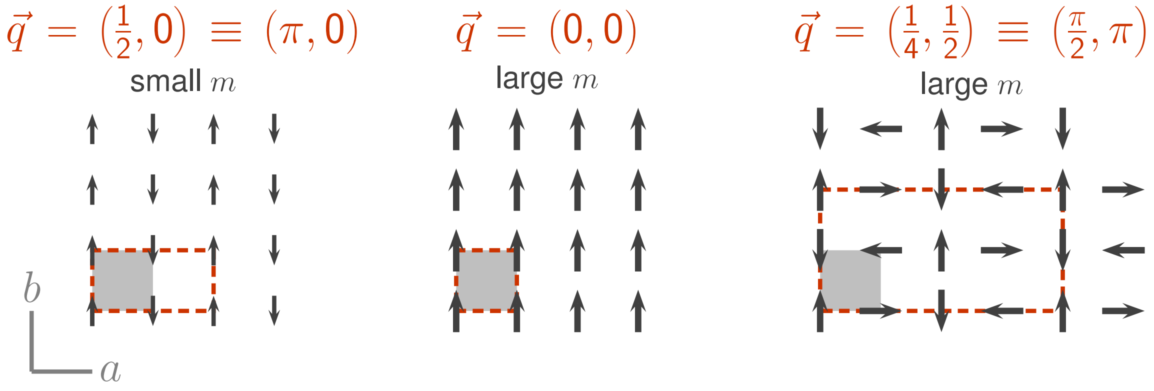
$\vec{q} = \left(\frac{1}{2}, 0\right) \equiv (\pi, 0)$
small m
$\vec{q} = (0, 0)$
large m
$\vec{q} = \left(\frac{1}{4}, \frac{1}{2}\right) \equiv \left(\frac{\pi}{2}, \pi\right)$
large m
b
a

Figure 2.5: Basic characteristics of a magnetically ordered GS: the propagation vector $\vec{q}$ and the ordered magnetic moment m. Two different notations for the $\vec{q}$ vectors are presented. Gray filled squares and red dashed lines denote the crystallographic and the magnetic unit cells, respectively.

The value of the magnetic moment is usually defined in μ_B. The $S = 1/2$ Cu^{2+} atom has a magnetic moment very close to 1 μ_B. However, quantum fluctuations can substantially reduce the ordered moment at $T \rightarrow 0$. Therefore, the value of the ordered moment is a direct measure of quantum effects.

Antiferromagnetic GS

The most common magnetic GS in cuprates is antiferromagnetic (AFM). This is not surprising, provided that the leading magnetic coupling mechanism in cuprates is the superexchange. Examples are ubiquitous, e.g. the archetype systems La_2CuO_4 (square lattice) and Sr_2CuO_3 (NN chains). The propagation vectors can be very different even in closely related or isostructural compounds (e.g. Sec. 6.2.1). Applying an external magnetic field, AFM ordered systems may exhibit highly nontrivial behavior, including magnetization jumps or plateaus, e.g. in $CdCu_2(BO_3)_2$ (Sec. 6.2.2) or azurite $Cu_3(CO_3)_2(OH)_2$.

The observed values of the ordered magnetic moment in AFM cuprates span a broad range from 0.06 μ_B in Sr_2CuO_3 [33] to 0.96 μ_B in Li_2CuO_2 [34], evidencing the variety of different microscopic mechanisms responsible for the formation of antiferromagnetically ordered states.

Quite often, the anisotropic DZYALOSHINSKII-MORIYA couplings give rise to a small macroscopic moment along a particular direction, e.g. in La_2CuO_4 [35]. This effect, typically referred as "weak ferromagnetism", should not be confused with the FM GS state. The alternative term "canted antiferromagnetism" is more appropriate from this point of view.

Ferromagnetic GS

For the FM GS, the FM couplings should dominate over the AFM ones along all three dimensions. Since the leading magnetic coupling mechanism in cuprates is superexchange, ferromagnetism is a very rare phenomenon. Still, the examples of $La_4Ba_2Cu_2O_{10}$ [36, 37], as well as $CaCu_3Ge_4O_{12}$ and $CaCu_3Sn_4O_{12}$ [38], evidence that for a particular orthogonal arrangement of CuO_4 plaquettes, which practically prohibits any appreciable superexchange, the FM GS can be stabilized. The microscopic mechanism responsible for the presence of long-range FM couplings is investigated in Ref. 39. As a consequence of the low energy scale, the ordering temperature T_C in these systems is usually below 10 K.

Ferrimagnetic GS

A ferrimagnetic GS is also uncommon for cuprates. It can be stable for systems that bear different multiplicities of structurally independent Cu atoms. For instance, Cu_2OSeO_3 has two nonequivalent Cu sites, Cu(1) and Cu(2) [40]. Within the unit cell, four Cu(1) and twelve Cu(2) are located. The Cu(1) atoms are coupled FM to each other, forming a sublattice of parallel spins. The Cu(2) are also coupled FM, forming another sublattice. The two sublattices are coupled to each other by a sizable AFM exchange, which gives rise to their mutually antiparallel arrangement. Thus, in the GS, four down spins of Cu(1) and twelve up spins Cu(2) result in a nonzero magnetization, which amounts to the half of the saturation magnetization.

Spiral GS

In spiral GSs, the neighboring spins are aligned neither parallel, nor antiparallel. As a result, spiral-like magnetic structures are formed. If all three components of the propagation vector are commensurate with the reciprocal lattice constants, the GS is called commensurate. In the opposite case, the magnetic structure is said to be incommensurate in 1D, 2D or 3D.

Typical examples are frustrated chain systems, where the competition of the NN FM coupling J_1 with the second-neighbor AFM coupling J_2 gives rise to a spiral GS for $J_2/|J_1| > 0.25$: $LiCu_2O_2$ [41], $LiCuVO_4$ [18], and linarite $PbCu(SO)_4(OH)_2$ [42].

2.3.2 Ground states lacking long-range magnetic order

Singlet GS

The spin singlet GS, characterized by a nonzero gap in the magnetic excitation spectrum, is a widespread magnetic GS in cuprates. It is typically realized if the leading exchange couples the spins pairwise, forming a dimer, while the interdimer couplings are substantially smaller. Interestingly, the magnetic dimers do not necessarily coincide with the structural ones, as revealed by the instructive examples of $CuTe_2O_5$ [43] and $Cu_2(PO_3)_2CH_2$ [44].

Two main characteristics of the singlet GS are the value of spin gap and its $\vec{q}$-position (Fig. 2.6). The value of the spin gap is the energy difference between the singlet and the lowest-lying triplet ($S^z = 1$) excitation. In general, the triplets are mobile, and their energy is a function of their wave vector $\vec{q}$ (for an exception, see the central panel of Fig. 2.6). The value of $\vec{q}$ at which the singlet-triplet gap is minimal, is referred as the $\vec{q}$ position of the gap. If several low-lying triplet branches exist, the system can exhibit multiple spin gaps, e.g. a double spin gap in the right panel of Fig. 2.6.

The phase diagrams of several archetypical models contain the regions of gapless (AFM ordered) and gapped phases. At zero temperature, the two regimes collide at a quantum critical point. A straightforward way to reach this critical point is to apply a magnetic field H_{c1}, which closes the spin gap and gives rise to long-range magnetic ordering. In this ordered phase, the system may exhibit the BOSE–EINSTEIN condensation of magnons, as was initially shown for $TlCuCl_3$ [45]. This discovery has spurred intense research on the gapped systems from both experimental and theoretical side. The essentials of this phenomenon are discussed in Sec. 6.2.1.

The case of $SrCu_2(BO_3)_2$ [46] deserves a separate discussion. The microscopic magnetic model for this system is the 2D SHASTRY–SUTHERLAND lattice, composed of dimer and interdimer couplings J and J', respectively. The J'/J ratio in $SrCu_2(BO_3)_2$ stabilizes the

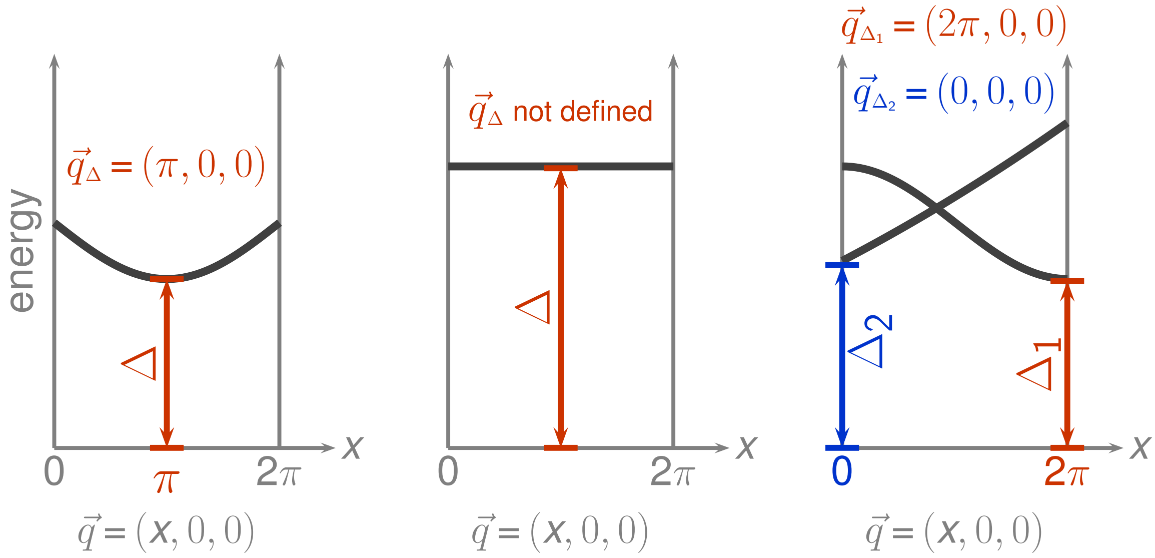

Figure 2.6: Basic characteristics of a singlet GS: the spin gap Δ and its $\vec{q}_\Delta$ position. The singlet states are at zero energy, the lowest-lying triplet excitations are shown with a bold black line. Left panel: $\vec{q}_\Delta$ at commensurate position. Central panel: localized excitation, $\vec{q}_\Delta$ can not be defined. Right panel: the case of "two spin gaps" (Δ_1 and Δ_2).

dimerized phase, close to the quantum critical point [47, 48]. Magnetization studies revealed a fascinating variety of field-induced phases, which were extensively studied in the last decade [49].

Alternatively, the spin gap can be closed upon directed chemical substitution or by applying external pressure, as evidenced by the examples of $BiCu_{2-x}Zn_xPO_6$ [50, 51] and $TlCuCl_3$ [52], respectively.

Spin liquid GS

At present, the research on the low-dimensional cuprates is largely focused on the search for materials that imply a spin-liquid GS. The prerequisites for this state are the absence of LRMO and sizable spin correlations beyond NNs (thus, dimerized systems are not spin liquids). The research on this GS is impeded, from both the theoretical as well as experimental side, by the complexity of the magnetic properties and the scarceness of real material realizations, respectively. In addition, obtaining the experimental evidence for the spin liquid GS is very challenging, since no clear experimental fingerprints ("smoking gun") for this type of GS have been proposed so far [53]. More information on spin liquids is given in the introduction of Chapter 7.

A recent discovery of herbertsmithite $Cu_3Zn(OH)_6Cl_2$ [54] gave hope that this compound as well as related kagome-lattice systems, such as kapellasite $Cu_3Zn(OH)_6Cl_2$, or haydeeite $Cu_3Mg(OH)_6Cl_2$, could exhibit the spin liquid physics. The magnetism of these systems is discussed in Chapter 7.

2.3.3 Coupling to orbital and lattice degrees of freedom

In general, cuprates are good spin-only model materials. However, in several cases, the coupling between the magnetic and other degrees of freedom becomes substantial. A classical example is the orbital ordering, also referred as a cooperative JAHN–TELLER distortion, in $KCuF_3$ [55], which gives rise to a pronounced 1D magnetic behavior of this material. Initially, the orbital ordering was believed to be of purely electronic origin [55–57]. Later, DFT+DMFT studies revealed that the electronic mechanism alone is not strong enough to provide the experimentally observed energy scale, and therefore an additional coupling to the lattice degrees of freedom should be taken into account [58, 59].

Spin-phonon interaction manifests itself in another archetype system $CuGeO_3$, leading to the spin-PEIERLS GS [60]. This exotic GS is a result of a structural transition which opens a finite spin gap in the system. The necessary condition for the spin-PEIERLS state is its magnetic origin, i.e. the spin-lattice coupling is the driving force of the transition. Further realizations of the spin-PEIERLS transition are actively sought.

Chapter 3

Experimental methods: crystal structure and magnetic properties

At present, numerous experimental methods and techniques are used to deliver information about the magnetic properties of solids. Even a birds-eye view on this vast topic would require the volume of a textbook, and thus this Chapter is by no means a review in its traditional sense. Therefore, the selection of methods discussed in this Chapter was done looking from a practical angle, by considering primarily the experimental techniques relevant for the discussions in Chapters 6 and 7. Such restriction as well as the limited volume of this Chapter leave no space to discuss several relevant techniques (such as RAMAN spectroscopy, heat transport measurements, and especially, INS). Instead, a particular emphasis is made on understanding *how to interpret* different kinds of experiments.

The numerical approach developed in this study is intimately related to the experimental information. First, many of the DFT-based studies are motivated by experimental findings. Second, DFT calculations require a structural input, which is typically known from experiments. Third, DFT calculations can be used to check the consistency of the experimental input, while the precision of theoretical results can even overcome the experimental error bars. In such cases, the information on the relative accuracy of the experimental technique and the theoretical approach is crucial. Finally, a deep knowledge of the performance and limitations of different experimental techniques is important to suggest key experiments that can challenge or refine the existing model, both theoretical and experimental. Therefore, an appropriate understanding of experimental results is an absolute prerequisite for a sound study of any real material.

3.1 Diffraction methods

3.1.1 X-ray diffraction

At present, despite dozens of alternative and supplementary methods have been or are being developed, the majority of structural studies is based on X-ray diffraction. The availability of the relevant equipment and a comprehensive strategy analyzing diffraction patterns, make this method a standard probe for a crystal structure.

Crystalline substances are formed by a regular arrangement of constituent atoms, with typical interatomic distances of several Å. The diffraction condition for the 1D case[1] is given by the Bragg's equation

$$d(\sin\theta_s - \sin\theta_i) = m\lambda, \tag{3.1}$$

where d is the distance between the grating elements, m is an integer, λ is the wavelength and θ_i and θ_s is the incident beam angle and the angle at which diffraction is observed. As follows from Eq. 3.1, for d amounting to several Å, λ should be of the same order as d. Hence, in the case of electromagnetic radiation (photons), diffraction on crystals can be observed only for X-rays. Most important, since the grating elements in crystals are atomic planes,[2] the resulting diffraction pattern reflects the arrangement of atoms in the crystal, thus giving a key to explore the inner structure of a crystal.

The diffraction condition can be illustrated by plotting the wave vectors of the incident and the scattered wave on top of a reciprocal lattice. The resulting plot (called Ewald construction) is shown in Fig. 3.1. Diffraction occurs only if the difference $\Delta\vec{k}$ between wave vectors of the incident wave and the scattered waves is commensurate with the basis vectors of the reciprocal lattice $\vec{a}^*$, $\vec{b}^*$ and $\vec{c}^*$:

$$\Delta\vec{k} = \vec{Q}\left\{\vec{Q},\vec{k} \in \mathbb{R}^3;\ h,k,l \in \mathbb{Z};\ \vec{Q} = h\vec{a}^* + k\vec{b}^* + l\vec{c}^*\right\} \tag{3.2}$$

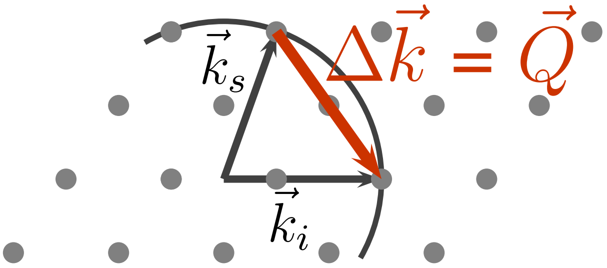

Figure 3.1: The Ewald construction. Gray dots represent the reciprocal lattice, $\vec{k}_i$ and $\vec{k}_s$ are the wave vectors of the incident and scattered waves, respectively. Diffraction occurs if $\vec{k}_i - \vec{k}_s$ is commensurate with the translation vectors of the reciprocal lattice.

Therefore, the observed diffracted pattern contains the information on the vectors of the reciprocal lattice. In the kinematic theory of scattering, the intensity of the scattered wave is proportional to the square of the structure factor F, which is defined by

---

[1] This principle holds for a 3D grating as well.

[2] This model is at best oversimplified, yet it is the simplest and probably the most instructive way to discuss diffraction in crystals.

$$F(\vec{Q}) = \int_{\vec{a}\cdot(\vec{b}\times\vec{c})} \rho(\vec{r}) \exp\left(2\pi i \left[\vec{Q}\cdot\vec{r}\right]\right) d\vec{r}. \tag{3.3}$$

The main objective of the structural analysis is the crystal structure, which is a discrete set of vectors $\vec{R}_i$ describing the equilibrium positions of constituent atoms. Therefore, it is reasonable to replace the integral in Eq. 3.3 with the following sum:

$$F(\vec{Q}) = \sum_{i=1}^{N} f_i(\vec{Q}) \exp\left(2\pi i \left[\vec{Q}\cdot\vec{R}_i\right]\right), \tag{3.4}$$

where $f_i(\vec{Q})$ is the atomic form factor, describing the scattering power of an isolated atom. The X-rays are scattered primarily by electrons, hence $f_i(\vec{Q})$ is roughly proportional to the atomic number Z. In addition, $f_i(\vec{Q})$ diminishes with increasing $|\vec{Q}|$, thus peaks with small $|\vec{Q}|$ have larger intensity.

The single-crystal structural analysis comprises two parts: (i) space group determination and indexing of the observed intensities and (ii) determination of internal atomic coordinates and displacement parameters. In most cases, the first part is straightforward and can be carried out in an automatic mode by diffractometer software. The second part of the analysis is less trivial. The main problem of the structural analysis is the gauge freedom (the phase problem) which impedes evaluation of the unique set of $\vec{R}_i$ based on the experimentally measured set of intensities $I(\vec{Q})$. Two standard procedures to solve this problem in a single crystal study are the PATTERSON function [61] or the direct methods [62, 63]. The powder diffraction allows to refine the structural model using the RIETVELD method [64] or even to define the crystal structure, essentially by guessing its principal features.

The $\vec{R}_i$ coordinate contains no information on the amplitude of oscillating motion for a particular atom i. To remedy this drawback, displacement parameters are introduced. In the simplest picture, atomic displacements are considered isotropic and thus described by only one parameter U_{iso}.[3] As a rule of thumb, U_{iso} for heavy atoms should be smaller than for light atoms. The violation of this rule is a likely evidence for insufficient accuracy of the structural model.[4] The isotropic approximation is typically too crude to account for atomic displacements. Much more appropriate is the harmonic oscillation model, in which U_{iso} is replaced by a second rank tensor U_{ij}, which components are typically referred as anisotropic displacement parameters (ADPs). A good test for the refined components of U_{ij} is to check whether they form an ellipsoid or another second quadratic surface. The latter case corresponds to an unphysical situation, thus an additional analysis is necessary.

---

[3] U_{iso} enters the summands in Eq. 3.4 as an additional factor: $\exp -(1/3[\vec{Q}\cdot\vec{Q}]U^2_{\text{iso}})$.

[4] A remarkable example of such mistaken structural model is (CuCl)LaNb$_2$O$_7$. The usually high isotropic displacement parameter $U_{\text{iso}} = 0.13$ Å^2 of the Cl atom reported in the original paper (Ref. 65) motivated the authors of Ref. 66 to challenge the structural input by DFT calculations. Based on the theoretical calculations, they suggested a structural distortion, which was later verified by high-precision X-ray and electron diffraction experiments [67].

Absorption edge In an in-house X-ray diffraction experiment, the wavelength of the incident beam is equal to the characteristic wavelength of a $3d$ element, typically Cu or Mo. If the material under investigation contains $3d$ elements, the K-absorption edges of these elements should be examined. In particular, the radiation energy should not exceed the absorption edge energy. For instance, the K-edges of Fe and Co have slightly lower energies than the characteristic Cu Kα wavelength, and thus a considerable fraction of X-rays is absorbed. Therefore, for Fe- or Co-containing materials, Cu Kα is not an appropriate choice. This shortcoming can be lifted by using hard X-rays available at synchrotron facilities.

Light atoms Since X-rays are scattered by electrons, the scattering intensity is a function of the electronic density. Therefore, heavy atoms with a large number of localized electrons have a substantially higher atomic form factor than light atoms. Since the intensity scales with the square of the atomic form factor, the difference in the observed intensity is even more pronounced. As a result, atomic coordinates of heavy atoms are defined with higher precision than those of light atoms. This difference is essential for structural optimizations: in many cases, the relaxation of light atoms yields reasonable results. However, if all internal atomic coordinates are relaxed, the discrepancy between the experimental and the optimized internal atomic coordinates for the heavy atoms should be considerably smaller than for the light atoms.

Hydrogen atoms Hydrogen is the extreme case of a light atom having only one electron (in the fully ionic picture, the number of core electrons is zero, leading to zero scattering). In many oxide compounds, it is bonded to an oxygen atom and forms an OH^- group. Since electronegativity of O is substantially larger than that of H, the electronic density is shifted toward the O atom. Although this density is very small, modern equipment and software are capable to identify it. Unfortunately, many X-ray structural studies are based on the wrong assumption that this small electronic density is centered around the H atom, resulting in far too short O–H bonds of about 0.7–0.8 Å. For comparison, neutron diffraction studies yield typical O–H bond lengths of 0.95–1.05 Å. Therefore, the atomic positions of hydrogen atoms evaluated from X-ray diffraction data should be carefully checked. In general, X-ray structural studies of H-containing compounds should be accompanied by alternative techniques, such as neutron diffraction, or supplied with a accurate DFT-based analysis.

Amorphous and non-detectable crystalline impurities A relevant outcome of X-ray powder analysis is the content of impurities. Amorphous impurities typically exhibit a wide halo for $|\vec{q}| = 2\text{–}3$ Å which corresponds to a typical interatomic distance in solids. If the amorphous phase has the same chemical composition as the crystalline substance, the integrated intensity of the halo can be compared to the integrated intensity of the crystalline phases, in order to estimate the fraction of the amorphous phase (e.g., Ref. 68).

Correlation between ADPs and site occupations An integral part of a structural determination is “placing” the atoms in accord with the evaluated electronic density. For the uniform-shaped density peaks, this procedure is straightforward. However, a peculiar non-uniform shape (e.g. cigar-like) can be accounted for by at least two models. First, such a shape can result from a strongly anisotropic displacement of the respective atom (Fig. 3.2, top). An alternative scenario, referred as the split position, comprises two (or more) randomly occupied atomic positions, with their total occupation equal to one (Fig. 3.2, bottom). Based exclusively on X-ray diffraction data, the choice between the two scenarios is rather subjective. Crystal structures with split positions or highly anisotropic ADPs should be carefully analyzed. Structural studies at different temperatures typically allow to distinguish between almost temperature-independent ADPs, characteristic for split positions, and considerable variations of ADPs that point to single position occupied by an atom exhibiting sizable displacement (Ref. 69 contains an instructive example).

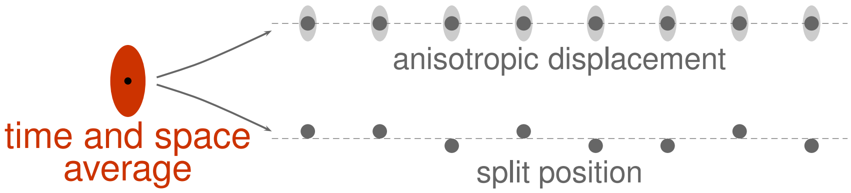

Figure 3.2: Two possible models describing sizable anisotropy of the electronic density: strongly anisotropic displacement (top) and split position (bottom).

3.1.2 Neutron diffraction

Neutron diffraction is widely used as a method for structure determination, alternative to X-ray diffraction. Besides, it is a standard technique for investigation of magnetically ordered structures.

Neutrons are charge-neutral $S = 1/2$ particles with the rest mass ∼1840 times larger than of that of an electron. Consequently, the magnetic moment of a neutron amounts to $\sim -10^{-3}\,\mu_B$ (aligns antiparallel to the direction of magnetic field). Unlike X-rays, the interactions of neutrons with matter are of two kinds: (i) strong force interaction with nuclei and (ii) magnetic interaction with the magnetic moments of unpaired electrons. The relatively large amount of sample needed for sufficient statistics (as a rule, several grams) is caused by low fluxes of neutron sources and the small probability of a diffraction event, characteristic of the both types of interactions.

Unlike X-rays, scattered by electrons, neutrons are scattered primarily by magnetic moments and by nuclei. Thus, neutron cross-sections do not scale with the atomic number, and the neighboring elements in the periodic table may show substantially different cross-sections. This phenomenon is widely used in structural studies to distinguish between the atoms having similar atomic numbers, such as, e.g. Cu and Zn. Besides the nontrivial dependence on the atomic number, neutron cross-section are isotope-specific: they can differ by several orders of magnitude for different isotopes of the same element. Additionally, the scattering power strongly depends on the spin state of a nucleus, which can be different for the same isotope.

Nuclear scattering is a sum of two contributions: coherent and incoherent. Incoherent scattering originates from random distribution of different isotopes or from different orientations of nuclear spins. A quantitative theory of neutron scattering lengths is still lacking, thus the values of coherent and incoherent scattering cross sections are determined experimentally. A special property of the cross sections for nuclear scattering is their $\vec{Q}$-independence. The nuclear structure factor is expressed as:

$$F(\vec{Q}) = \sum_{i=1}^{N} b_i^{\mathrm{coh}} \exp\left(i\,[\vec{Q}\cdot\vec{R_i}]\right). \tag{3.5}$$

In addition to the nuclear scattering, magnetization density gives rise to magnetic scattering. The amplitude of magnetic scattering is proportional to the product of the magnetic form factor $f(\vec{Q})$ and the transverse component of the magnetic moment [70]: $\vec{\mu}_\perp = \vec{Q} \times \vec{\mu} \times \vec{Q}$. Since the magnetization is associated with electrons, $f(\vec{Q})$ decay upon increase in $\vec{Q}$, and hence magnetic peaks are typically observed only in the low-$\vec{Q}$ range.

Weak and strong scatterers The nuclear cross-sections for different elements or different isotopes of the same element can differ by several orders of magnitude. In particular, the strongest neutron absorbers are ^{10}B (20 % of natural abundance), ^{113}Cd (12.22 %), ^{149}Sm (13.9 %), and ^{155,157}Gd (30.5 %). An appreciable amount of these isotopes present in a sample precludes a diffraction experiment. Besides, several isotopes have negligible coherent scattering cross sections: ^{6,7}Li (100 % of natural abundance), ^{51}V (99.75 %), thus the internal coordinates of the respective atoms can be neither defined nor refined.

H atoms Almost "invisible" with X-rays, hydrogen atoms exhibit appreciable neutron cross sections. However, the H nucleus, a proton, is extremely light compared to other nuclei, and its magnetic moment is consequently large, which gives rise to sizable incoherent scattering. In this case, the analysis of experimental data is at best challenging. A standard way to remedy the problem is deuterization of a sample, i.e. partial replacement of ^{1}H with ^{2}H (D).

Ambiguity of the fitting The number of magnetic peaks is typically of the same order as the number of the refined parameters (components of $\vec{\mu}$). The insufficient statistics leads to a considerable ambiguity of the resulting experimental magnetic model. In particular, a good fit to the experimental diffraction pattern does not exclude a possibility to obtain an equally good fit using another magnetic model. Thus, decisive experiments should be carried out using alternative methods.

Insensitivity to small moments Since the intensity of the magnetic scattering is proportional to $\vec{\mu}_\perp$, neutron diffraction is not sensitive to small ordered moments. Therefore, the absence of observed magnetic reflections should not be considered as an evidence for the lack of magnetic order: especially for low-dimensional systems, the value of the ordered moment can be considerably reduced. For instance, the first neutron diffraction study on the HEISENBERG chain system Sr_2CuO_3 yielded no evidence for LRMO [71]. However, the authors of Ref. 71 judiciously stated that LRMO with a small value of the ordered moments ($<0.1\,\mu_B$/Cu) can not be excluded. Two years later, the subsequent μSR and ND study [33] reported $T_N = 5$ K and estimated the magnitude of the ordered magnetic moments as $0.06\,\mu_B$/Cu.

3.2 Thermodynamical measurements

The term "thermodynamical measurement" implies the measurement which results in a set of observables $\{\langle A \rangle\} : \langle A \rangle(T) = Z^{-1} \sum_i A_i \exp(-E_i\, k_B^{-1}\, T^{-1})$ for a physical quantity A at various temperatures T. Here, Z is the partition function, A_i and E_i denote the values of A and energy for the i-th state, respectively, and the summation is done over all states i. This way, a thermodynamical measurement provides an indirect measure of the excitation spectrum, its thermal average. In addition, thermodynamical measurements yield spatially-averaged information, i.e. they are bulk measurements. As a result, the experimentally measured signal always contains in addition to the intrinsic signal, also extrinsic contributions (noise, impurities, defects), that are sometimes difficult to disentangle. Commonly arising problems concerning interpretation of experimental results, and their possible solutions will be in the focus of this section.

Thermodynamic measurements are an integral part of experimental characterization of magnetic properties for any real material. Typical probes are measurements of magnetic susceptibility χ (the actually measured quantity is magnetization M) and specific heat C_p (heat capacity at constant pressure is measured). Both measurements require small amounts of material (up to ~20 mg), and pose almost no limitations to the form of the material. In particular, for crystalline materials, both single-crystalline or powder samples can be measured.

3.2.1 Magnetic susceptibility

Temperature dependence of magnetic susceptibility χ is the most common magnetic measurement. Due to its relative simplicity and accessibility, and versatile information on the magnetism of a particular system, $\chi(T)$ data are commonly the first probe for magnetic properties.

For the overwhelming majority of magnetic insulators with localized spins, the temperature dependence of magnetic susceptibility splits into three distinct regimes (Fig. 3.3): the high-temperature part with only short-range correlations between the spins (the Curie-Weiss regime), intermediate temperatures where long-range spin correlations become increasingly important, and the low-temperature region with various anomalies and typically large extrinsic contributions.

Figure 3.3: Three regimes of $\chi(T)$: the high-temperature part (pink) well-described by the Curie-Weiss law (red line), intermediate temperatures (orange) with sizable long-range spin correlations, the low-temperature region (blue) where the magnetically ordered state is stable. T_N marks the magnetic ordering transition. For the experimental data, $\chi(T)$ for dioptase $Cu_6Si_6O_{18}\cdot 6H_2O$ is shown (Sec. 6.3).

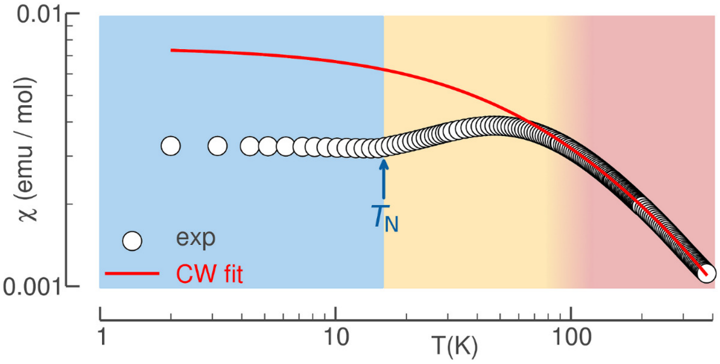

High-temperature magnetic susceptibility: the Curie-Weiss fit

For magnetic insulators with localized moments, the high-temperature behavior of magnetic susceptibility obeys the modified Curie-Weiss law:

$$\chi(T) = \frac{C}{T+\theta} + \frac{C_{\text{imp}}}{T} + \chi_0, \tag{3.6}$$

where C is the Curie constant of an ideal material (intrinsic), C_{imp} is the average Curie constant of impurities and/or defects, θ is the Weiss temperature, and χ_0 is the temperature-independent term. The latter is a sum of two contributions. First, closed atomic shells give rise to a diamagnetic (negative) susceptibility, which can be estimated in good approximation using the available reference data [72]. However, this approach does not account for diamagnetic impurities in the sample. Second, paramagnetic (positive) contribution originates from a small admixture of states with nonzero angular momentum in accord with the mechanism put forward by van Vleck [73]. Since there is no simple rule to estimate this paramagnetic contribution, neither the concentration of diamagnetic impurities is known, the term χ_0 is typically evaluated as a free parameter.

The nature of the C_{imp}/T term is rather complex and comprises at least two physical effects. First, any paramagnetic impurity in the sample gives rise to a nonzero C_{imp}. Second, defects of the underlying spin lattice often create isolated spins which behavior follows the same $1/T$ law. C_{imp}/T is typically small in the range of validity of the Curie-Weiss law, i.e. at high temperatures; and is in general visible only at rather low temperatures by a characteristic bending or upturn of the $\chi(T)$ dependence. The other way round, the absence of such a bending or an upturn can point to the small C_{imp}. In this case, the fitting should be possible without accounting for impurity and/or defect contribution, hence the term C_{imp}/T in Eq. 3.6 should be omitted.

The term $C/(T+\theta)$ is the intrinsic CURIE-WEISS contribution. Both C and θ are refined parameters. The value of C yields the effective magnetic moment

$$\mu_{\mathrm{eff}} = \sqrt{3\,C\,k_{\mathrm{B}}\,\mu_{\mathrm{B}}^{-2}\,N_{\mathrm{A}}^{-1}} \tag{3.7}$$

and, consequently, the g-factor

$$g = \mu_{\mathrm{eff}}\,[S(S+1)]^{-1/2}. \tag{3.8}$$

Together with θ, these quantities characterize the magnetism of a particular system. For $S = 1/2$ systems, the value of μ_{eff} should be compared to the spin-only contribution of $\sim 1.73\,\mu_{\mathrm{B}}$. The deviation $|\mu_{\mathrm{eff}} - 1.73|/1.73$ is an important measure for the strength of the spin-orbit coupling. The g value can be compared to independent experimental estimates, for instance, ESR results. On the other hand, the sign of θ provides important information for the magnetic coupling regime: $\theta > 0$ evidences that AFM couplings are predominant, while $\theta < 0$ points to the preponderance of FM couplings. More specifically, the sum of the magnetic couplings can be estimated using Eq. 5.3.

It is important to note that initially the CURIE-WEISS law was written in a different way: with a $(T-\theta)$ term in the denominator. This leads to a positive θ for the dominant FM couplings. However, the vibrant research on localized magnets (which followed the discovery of high-temperature superconductivity) gave evidence that AFM couplings in real materials largely outnumber the FM ones. Thus, the community gradually went over to the CURIE-WEISS law with $(T+\theta)$ in the denominator, aiming at a positive θ for the dominant AFM couplings. At present, the both versions of the CURIE-WEISS law are still used in the literature. This unfortunate duality may lead to confusion, especially if the value of θ is provided without specifying the sign convention.

A CURIE-WEISS fit is a procedure to evaluate the optimal values of C, θ, C_{imp} and χ_0 by fitting Eq. 3.6 to the experimental $\chi(T)$ data. The nontrivial part of the fitting procedure is the choice of the minimal fitting temperature T_{min}. A natural strategy is to take rather low T_{min} and then subsequently increase its value, until the resulting values of the refined parameters get stabilized, i.e. become independent of T_{min}. However, this approach suffers from several shortcomings.

First, for systems with large magnetic couplings, the experimentally accessible temperature range can be poorly described by the CURIE-WEISS law. A remarkable example, the $S = 1/2$ HEISENBERG chain system CuNCN, shows almost temperature-independent $\chi(T)$ in the temperature range 200–320 K [74], seemingly pointing to a very small C. However, DFT calculations disclosed that the leading magnetic coupling in CuNCN amounts $\sim$2000 K [75], thus the measured temperature range is extremely far from the CURIE-WEISS regime, which for this particular system largely exceeds the decomposition temperature and thus is not reachable due to decomposition of the compound.

The second remark concerns the dependence of T_{min} on the topology of the underlying magnetic model. To illustrate this effect, the $\chi(T)$ behavior is simulated for several archetypical $S = 1/2$ HEISENBERG models in the temperature range $1 \leq T\,k_{\mathrm{B}}\,J^{-1} \leq 10$ using exact diagonalization of the respective Hamiltonian, and subsequently a series of CURIE-WEISS fits is performed, adopting T_{min} from the range $1 \leq T_{\mathrm{min}}\,k_{\mathrm{B}}\,J^{-1} \leq 5$. Then, the fitted values θ_{fit} are compared with the estimates θ_{est} from Eq. 5.3 in Sec. 5.1.[5] The results are shown in Fig. 3.4. Quite remarkably, even the largest values of $T_{\mathrm{min}}\,k_{\mathrm{B}}\,J^{-1}$ yield $\theta_{\mathrm{fit}}/\theta_{\mathrm{est}}$ significantly deviating from unity. Keeping in mind the low expansion order used to obtain Eq. 5.3, this discrepancy is not surprising. More important are sizable deviations of the four curves in the range $1 \leq T_{\mathrm{min}}\,k_{\mathrm{B}}\,J^{-1} \leq 2$. Since for systems with large couplings (hundreds of K) this fitting is often possible only within this range, the respective estimates of θ, and especially, the subsequent conjectures on the strength of exchange couplings, should be carefully checked for consistency by independent methods.

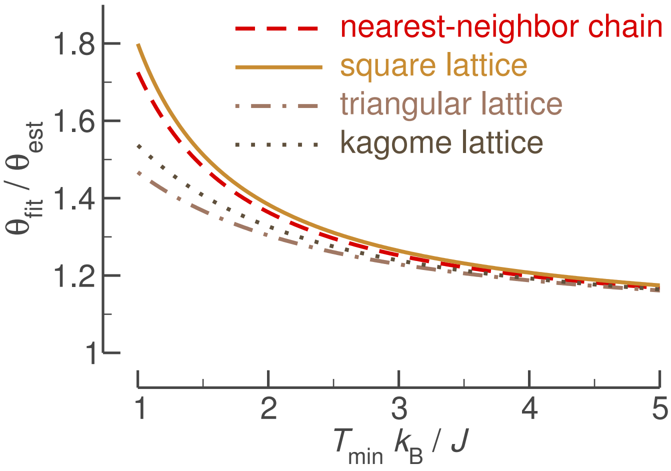

Figure 3.4: The choice of T_{min} for the CURIE-WEISS fit: $S = 1/2$ HEISENBERG model on various lattice topologies. $T_{\mathrm{min}}\,k_{\mathrm{B}}\,J^{-1}$ is the minimal fitting temperature in the units of the exchange coupling J. θ_{fit} is the fitted value of the WEISS temperature for the given T_{min}. θ_{est} is the value estimated using Eq. 5.3. See text for details.

Intermediate temperatures

As can be seen in Fig. 3.4, the CURIE-WEISS law definitely breaks down in the temperature range $1 \leq T_{\mathrm{min}}\,k_{\mathrm{B}}\,J^{-1} \leq 2$. At lower temperatures, the $\chi(T)$ behavior is governed by long-range spin correlations that are model-specific, i.e. depend on the underlying microscopic magnetic model. Low-dimensional systems are characterized by a distinct difference in the strength of exchange couplings along different directions of the magnetic lattice. Thus, for temperatures of the order of the leading coupling J_i, correlations between the spins can be strong along a certain direction, but substantially smaller in the perpendicular direction. In a response to enhanced correlations, $\chi(T)$ starts to decrease, but the 3D magnetic ordering is inhibited by the weakness of $J_\perp$. As a result, $\chi(T)$ exhibits a broad maximum around T_{max}, which is a typical indicator of low-dimensional magnetic behavior.

---

[5] For the nearest-neighbor chain, the square lattice, the triangular lattice and the kagome lattice models, θ_{est} amount to 1/2, 1, 3/2 and 1, respectively, in the units of J/k_{B}.

Provided the microscopic magnetic model is qualitatively known, the leading couplings can be estimated directly from T_{max}. For instance, the $S = 1/2$ HEISENBERG NN chain and square lattice models exhibit broad maxima in $\chi(T)$ at $0.64\,J/k_{\text{B}}$ [76] and $0.935\,J/k_{\text{B}}$ [77], respectively.

Although such broad maxima are ubiquitous for low-dimensional systems, in certain cases they might be absent. In particular, the maximum can be concealed by a large impurity and/or defect contribution. This situation is very typical for powder samples of HEISENBERG NN chain systems, as can be seen, e.g. for KCuF_3 [78], $\text{K}_2\text{CuP}_2\text{O}_7$ [79] and $(\text{NO})\text{Cu}(\text{NO}_3)_3$ (Sec. 6.1.2). In addition, for several highly frustrated magnetic models, T_{max} can be substantially low, as in the frustrated HEISENBERG chain system $\text{Li}_2\text{ZrCuO}_4$ [80], additionally impeding its experimental identification. In exotic cases, additional maxima appear, as in the distorted diamond chain system azurite $\text{Cu}_3(\text{CO}_3)_2(\text{OH})_2$ [13].

There are two strategies to evaluate $\chi(T)$ data in the intermediate temperature range. First, for certain models, HTSE can be used (Sec. 5.1). Alternatively, for rather complicated models, the $\chi^*(t^*)$ behavior can be simulated by different techniques, such as ED (Sec. 5.2) or QMC (Sec. 5.3), and fitted to the experimental $\chi(T)$ curve. This way, the numerical values of exchange couplings can be evaluated, using the procedure described in Sec. 5.5.

Low temperatures: anomalies and upturns

Many low-dimensional systems exhibit a gradual transition from the intermediate to the low-temperature regime. In certain cases, such as a clear fingerprint of a magnetic transition, a distinct low-temperature range can be singled out. Very often, the behavior of $\chi(T)$ at low temperatures is affected by various impurities, imperfections and anisotropies that are typically neglected in the microscopic magnetic model. Still, they can play a crucial role for the magnetic GS of the system. Therefore, the low-temperature part of the curve should be carefully examined.

Fingerprints of magnetic ordering are often (but not always) visible in a $\chi(T)$ curve: the transition between the paramagnetic and magnetically ordered regime is typically accompanied by a kink in the $\chi(T)$ dependence. If the magnetic GS has a nonzero magnetization (e.g. ferro- or ferrimagnetic state), the ordering temperature is accompanied by a drastic increase of $\chi(T)$. It is important to note that for single crystal measurements, $\chi(T)$ along a certain direction can exhibit an abrupt increase seemingly indicative of the onset of ferromagnetism. However, the true magnetic GS in this case can be canted AFM, e.g. in La_2CuO_4 [35]. Such situations can be distinguished from the ferro- and ferrimagnetic ordering by a very small value of the resulting magnetization ($\sim 10^{-3}$ of the saturation magnetization).

The magnetic GS for most of low-dimensional insulators lacks macroscopic magnetization. In this case, fingerprints for a transition to the magnetically ordered state are kinks that are often visible to the naked eye, at least in single crystal measurements. In contrast, powder materials yield weak or even imperceptible kinks. Moreover, kinks can be concealed by C_{imp}/T contribution, which often dominates at low temperatures. To visualize the ordering transitions, $\partial\chi/\partial T$ plots are a reasonable solution. Still, the presence of a magnetic ordering transition can be proven and its type reliably established only by using alternative experimental techniques, such as ND, μSR, or magnetostriction measurements.

Measurement of $\chi(T)$ in different magnetic fields provides additional information for the magnetically ordered phase. For easy-axis AFM materials, magnetic anisotropy gives rise to a spin-flop transition [81] which occurs at the critical magnetic field H_c. This transition results in a different slope of $\chi(T)$ of the magnetically ordered phase for the data measured at $H < H_c$ and $H > H_c$. In many low dimensional magnets, H_c is of the order of several tesla, and thus is reachable using standard lab equipment. The field dependence of $\chi(T)$ can hint at the amount of paramagnetic impurities, as they get suppressed by applied field.

Especially interesting are materials lacking long-range magnetic ordering, such as spin dimer systems and frustrated magnets. For the former, the gapped magnetic excitation spectrum gives rise to the exponential behavior of $\chi(T)$ at low temperatures. Therefore, for impurity- and defect-free samples, the exponential decay of $\chi(T)$ gives evidence for a gapped spectrum. On the contrary, the extrapolated finite value of $\chi(T)$ at zero temperature is a fingerprint of gapless magnetic excitations.

3.2.2 Specific heat

Measurements of the temperature dependence of specific heat are technically more demanding than $\chi(T)$, primarily due to the particular sample preparation procedure. The main advantage of this method is its sensitivity to magnetic and structural phase transitions, that are typically accompanied by sharp anomalies in specific heat. Its main drawback is the dual nature[6] of the measured quantity: it is the sum of the magnetic specific heat C_{magn} and the phonon contribution C_{phon}. The disentanglement of the two contributions is hampered by a strong dominance of C_{phon} for temperatures higher than $\sim$10 K.

The subtraction of the phonon contribution is a nontrivial task. The optimal solution to distinguish between C_{magn} and C_{phon} is to measure a nonmagnetic isostructural reference system, which phonon spectrum is similar to that of the magnetic system. This way, the magnetic specific heat can be evaluated as the difference between the measured C_p for a magnetic and the respective nonmagnetic system. Unfortunately, in most cases it is challenging to find a suitable nonmagnetic reference system. Alternatively, for the systems with small magnetic couplings, the phonon contribution C_{phon} is estimated from simplified models. Thus, at low temperatures, the phonon contribution can be approximated by $C_{\text{phon}}(T) = \quad {}_n A_n T^{-(2n+1)}$, where n are several first natural numbers. Alternatively, an estimate for $C_{\mathrm{phon}}(T)$ can be evaluated in a more sophisticated way using the DEBYE model (see Ref. 82 for an instructive example).

---

[6] This statement is restricted to magnetic insulators. Specific heat of conducting materials contains also an electronic contribution.

Despite the absence of a universal method to extract C_{magn} from the measured specific heat, the quality of this procedure can be checked by a universal measure—the magnetic entropy. Quantum mechanics permits $2S+1$ orientations for the spin value S. In the absence of magnetic field, all orientations have the same energy. Therefore, the magnetic entropy of N spins is expressed as

$$S_{\mathrm{magn}} = N\,k_{\mathrm{B}} \ln(2S+1). \tag{3.9}$$

Thus, for one mole of $S = 1/2$ spins, $S_{\mathrm{magn}} = R\ln 2 \simeq 5.76\,\mathrm{J/K}$. On the other hand, S_{magn} can be estimated from C_{magn}:

$$S_{\mathrm{magn}} = \int_{0}^{+\infty} \frac{C_{\mathrm{magn}}}{T} dT \tag{3.10}$$

The deviation between the value of S_{magn} evaluated using Eq. 3.10 and the ideal value given by Eq. 3.9 is a measure for quality of the decomposition for the measured C_p.

The magnetic specific heat C_{magn} provides valuable information on the magnetic excitation spectrum. The basic difference between gapped and gapless excitation spectra, discussed in Sec. 3.2.1, indeed holds for the $C_p(T)$ data. The peculiarity of magnetic specific heat is its sensitivity to singlet excitations. Therefore, specific heat studies are especially reasonable for systems with large density of low-lying singlet excitations, such as $S = 1/2$ HEISENBERG kagome lattice systems [83].

Sharp anomalies in C_{magn} are fingerprints of magnetic ordering transitions. However, their sharpness is not a prerequisite, since at low temperatures the residual entropy is typically small (most of excitations are frozen out), and the resulting anomalies can be less pronounced, and in extreme cases even wiped out completely [84].

For the magnetically ordered state, $C_p(T)$ the behavior characterizes the type of magnetic ordering: for instance, antiferromagnets exhibit the T^3-behavior, while for FM materials the $T^{3/2}$ dependence is characteristic [85].

An additional problem for interpretation of the experimental data arises from a small splitting of energy levels, yielding asymmetric peaks in specific heat. This effect, especially pronounced at low temperatures, was first discussed by SCHOTTKY [86] and later named after him. Distinguishing between the SCHOTTKY-type peaks and anomalies arising from magnetic ordering is a tricky problem, which in general requires independent experimental information.

In principle, the HTSE method, which allows to estimate the exchange couplings from $\chi(T)$, can be applied to magnetic specific heat data as well. It is especially valuable for systems featuring both AFM and FM couplings, since the high-temperature part of $C_{\mathrm{magn}}(T)$ behaves like A/T^2, where A is proportional to the sum of squares of magnetic exchange couplings: $A \propto \quad {}_i J_i^2$ [87]. Therefore, combining the values of θ and A from $\chi(T)$ and $C_p(T)$ measurements, respectively, relevant J_i's can be estimated.

For certain magnetic models, higher-order HTSE of $C_{\mathrm{magn}}(T)$ are available (Sec. 5.1). Unfortunately, high uncertainties for the values of $C_{\mathrm{magn}}(T)$ at high temperatures, i.e. in the temperature range where the phonon contribution is dominant, impede the applicability of this method, and make it feasible only for systems with weak magnetic couplings $|J_i| < 10\,\mathrm{K}$. In rare cases, for particularly simple models, low-temperature specific heat data can provide independent estimates for exchange integrals (see Ref. 88 for an instructive example).

3.3 Magnetization

Complementary to a $\chi(T)$ measurement, magnetization can be measured at constant, typically low temperature, as a function of magnetic field, yielding the $M(H)$ dependence. The behavior of magnetic spin-only insulators in magnetic field is described by the respective zero-field microscopic Hamiltonian with an additional field-dependent ZEEMAN term:

$$\hat{H} = \hat{H}_0 - g\mu_{\mathrm{B}} h \sum_i e_z \cdot \hat{\mathbf{S}}_i, \tag{3.11}$$

$\hat{H}_0$ is a zero-field Hamiltonian, and e_z is the direction of the magnetic field h. Therefore, at $T = 0$, the GS magnetization is measured. In magnetic fields exceeding the saturation field H_{sat}, required to align all the spins parallel, the GS is FM.

A severe limitation of the method is a rather narrow range of experimentally available magnetic fields: at present, up to 20 T in laboratories, and up to 45 T (steady field) and 100 T (pulsed fields) at high-field facilities. In exceptional cases, sample- and cryostat-destructive measurements can give access to the fields amounting to hundreds of tesla [89].

To compare the energy scale of J with the range of experimentally accessible magnetic fields, the two-site $S = 1/2$ HEISENBERG model, i.e. a dimer of two antiferromagnetically coupled spins, is considered. The solution of the Hamiltonian 3.11 yields the value of $H_{\mathrm{sat}} = J\, k_{\mathrm{B}}\, g^{-1}\, \mu_{\mathrm{B}}^{-1}$. Thus, for $J/k_{\mathrm{B}} = 1\,\mathrm{K}$, $H_{\mathrm{sat}} \quad 0.74\,\mathrm{T}$. For more complicated lattice topologies, the ratio $H_{\mathrm{sat}}/\max\{J_i/k_{\mathrm{B}}\}$ is typically between 1 and 3 T/K.

In low-dimensional magnetic $\mathrm{S} = 1/2$ insulators, the energy scale of exchange couplings can range from several K to several thousands K (Chapter 2). Therefore, the full magnetization curve (up to saturation) can be measured only for systems with particularly small couplings, such as frustrated square lattice systems $AA'(\mathrm{VO})_2(\mathrm{PO}_4)_2$ [82, 90, 91] or if AFM and FM couplings are balanced, like in frustrated HEISENBERG chain compounds $\mathrm{Li_2ZrCuO_4}$ [80], $\mathrm{LiCuVO_4}$ [92], $\mathrm{LiCu_2O_2}$ [8] etc. However, for majority of cuprates, even highest accessible magnetic fields do not provide access to the full magnetization curve.

There are two general methods to measure magnetization: in constant field or in pulsed fields. *Ceteris paribus*, the former is preferable, since it measures in equilibrium and yields the absolute value of the magnetic moment. The main limitation of a constant-field measurement is a rather low value of accessible magnetic fields (up to 45 T). The pulsed-field technique provides access to substantially higher magnetic fields (up to 100 T). The duration of a pulse typically amounts to 10^2-10^4 milliseconds, thus the resulting curves are affected by magnetocaloric effects.[7] Moreover, the particular amount of the exposed sample can not be reliably estimated. To estimate the absolute values of the magnetic moment, the pulsed-field measurements can be combined with a reference (constant field data). In addition, for systems that saturate below the highest accessible field, the scaling can be done using the saturation magnetization as a reference.

The low-field part of the curve provides substantial information on the GS and the lowest-lying excitations of the zero-field Hamiltonian. For instance, $\partial M/\partial H = 0$ at $T = 0$ evidence the gapped magnetic excitation spectrum. In this case, the maximum of the second derivative $\partial^2 M/\partial H^2$ provides a more precise estimate for the value of the spin gap than $\chi(T)$ data. However, a nonzero $\partial M/\partial H$ at $T = 0$ does not necessarily evidence the gapless excitation spectrum. In particular, anisotropic DZYALOSHINSKII-MORIYA couplings (Sec. 2.2.4), can give rise to a small admixture of triplets in the singlet GS [93]. This effect leads to a linear increase of $M(H)$ even in the gapped state.

Most of low-dimensional magnets exhibit no features between the H_c, at which the spin gap closes (for gapped systems), or from $H = 0$ (for gapless ones), up to the saturation field H_{sat}. However, frustrated magnets may exhibit magnetization plateaus or kinks, leading to a discontinuity in $\partial M/\partial H$.

Magnetization plateaus are characterized by $\partial M/\partial H = 0$ in the field range between the two critical fields H_{c1} and H_{c2} [94]. This emergent phase can be considered as a WIGNER crystal of magnons. Although $M(H)$ measurements provide the value of the critical fields and the fraction of polarized spins in the plateau phase, a detailed structure of this phase has to be accounted for by alternative techniques, such as NMR.

Magnetization plateaus can be accompanied by magnetization jumps at H_{c2} [94]. They originate from specific excitation bands that are almost $\vec{k}$-independent (dispersionless). Since these excitations are well-localized, they are susceptible to visualization in real space.

3.4 Resonance spectroscopy

Similar to magnetic susceptibility measurements, resonance spectroscopy recently became a standard probe for magnetism. Unlike bulk measurements, resonance spectroscopy probes local magnetic fields, thus the intrinsic properties can be measured. Additional advantage of resonance spectroscopy is its extreme sensitivity to magnetic order. In this Chapter, only the basics of these techniques (focusing on the information which an experiment of a particular type can yield) will be summarized.

---

[7] Insulating materials are more robust to this effect due to the absence of eddy currents.

All the resonance methods are generally based on the ZEEMAN splitting of levels in magnetic field, which yields the resonance condition:

$$\hbar\omega = g\,\beta\,B_{\text{eff}}. \tag{3.12}$$

Here, β is the magnetic dipole moment of the respective particle (ESR, μSR) or nucleus (NMR), and B_{eff} is the effective magnetic field, which is a difference of the external field B_0 and the local magnetic field σB_0. As follows from Eq. 3.12, change in B_{eff} gives rise to the respective change in ω, and consequently, to a shift of the resonance line. Provided the external magnetic field is constant, this shift is proportional to the magnetic susceptibility. Measurement of this shift as a function of temperature yields the intrinsic contribution to magnetic susceptibility (such shift observed in an NMR experiment is called the KNIGHT shift) and therefore is an excellent complement to bulk $\chi(T)$ measurements.

Abstracting from apparent differences in the measurement techniques, the principal difference between NMR, ESR, and μSR is the value of magnetic field, and consequently, the time scale of the excitations probed.

ESR This is the method of choice to measure the g-factor. In addition, ESR is a sensitive probe for the spin-orbit coupling. The frequency of a standard X-band experiment amount to $\sim 10^9$ Hz (microwaves), which corresponds to magnetic field of ~ 0.3 T (Eq. 3.12).

NMR The frequency range of NMR is 10^{-2} to 10^5 Hz, which is much slower than lattice vibrations. Therefore, NMR measures average magnetic field at the nuclear site. An important advantage of NMR is the possibility to probe internal magnetic fields at various sites, because the resonance lines of different nuclei typically do not overlap. A natural drawback of this method is its restriction to particular nuclei (the nuclei with zero spin are not sensitive to NMR). For excitations that are faster than the resonance field frequency, a single resonance line is observed. Comparable time scales give rise to line broadening. Finally, if excitations become slower than the resonance field frequency, the peaks split. The sequence “single line—broadening—multiple lines” is a typical indication of magnetic ordering.

μSR In contrast to the two previous methods, μSR spectroscopy is not a lab method, since it requires a muon source.[8] This method is very sensitive to low moments and reliably yields the fraction of the ordered phase. The drawback of this method is uncertainty of the μ^+ location in the sample. In particular, several independent O sites may give rise to a complex picture, which is difficult to interpret even qualitatively.

---

[8] At present, only four μSR facilities with user programs are available around the world.

Chapter 4

Density-functional-theory-based microscopic modeling

4.1 Band structure calculations

At present, band structure calculations are an integral part of solid state physics. Although the postulates of the density functional theory were formulated more than half a century ago, practical application of such techniques for a wide range of materials became feasible only after the rapid development of computational facilities since the late 1980's. Just two decades later, the variety of band structure codes available and a huge mass of DFT studies published every year, leave no doubt for the relevance of this computational method.

In the following, special emphasis will be made on the computational procedure used for the studies presented in Chapters 6 and 7. Therefore, the basics of DFT will be discussed as a minimal, albeit necessary basis for understanding this procedure. All theoretical schemes are evaluated within the Born–Oppenheimer approximation [95]. For the sake of simplicity, atomic units are used in this Chapter.

4.1.1 Density functional theory

The GS electron density $n(\vec{r})$ for a system of N electrons is defined as the expectation value of the density operator $\hat{n}(\vec{r})$:

$$n(\vec{r}) \equiv \langle\Psi|\,\hat{n}(\vec{r})\,|\Psi\rangle, \qquad \vec{r} \in {}^{3}, \qquad \hat{n}(\vec{r}) \equiv \sum_{i=1}^{N} \delta(|\vec{r}-\vec{r}_i|). \tag{4.1}$$

DFT postulates that the GS energy E of a system of interacting electrons in some external potential is a functional of the electron density $n(\vec{r})$ (the Hohenberg–Kohn theorem [96]):

$$E = E\,[n(\vec{r})]\,, \qquad E \equiv \langle\Psi|\,\hat{H}\,|\Psi\rangle. \tag{4.2}$$

Thus, the variational principle of Hohenberg and Kohn can be written as:

$$E = T[n] + W[n] + V[n] = \min_{n} \left\{ T[n] + W[n] + \quad n(\vec{r})v^{\text{ext}}(\vec{r})\, d^3\vec{r} \;\middle|\; \quad n(\vec{r})\, d^3\vec{r} = N \right\}, \tag{4.3}$$

where $T[n]$ and $W[n]$ are expectation values of the kinetic energy operator and the potential (electron-electron interaction) energy operator, respectively, v_{ext} is the external potential of the nuclei, and N is the number of particles (constant). Although formulation of the postulate and its proof is a salient achievement, a key to practical applications of DFT was given by development of the KOHN–SHAM equations [97]. The underlying idea is to use a non-interacting electron gas as a reference system. This way, $E[n]$ can be decomposed into a sum of (i) the kinetic energy of non-interacting electron gas $T_0[n]$, (ii) the classical electrostatic interaction energy $E_{\text{H}}[n]$ (HARTREE term) for the density $n(\vec{r})$, and (iii) the exchange and correlation energy E_{xc}:

$$E[n] = T_0[n] + E_{\text{H}}[n] + E_{\text{xc}}[n],$$

where all the information about kinematic (exchange) and dynamic (correlation) electron-electron interactions is contained in E_{xc}. The wave functions of a non-interacting electron gas are SLATER determinants, based on one-electron wave functions ϕ_i. KOHN and SHAM showed [97] that the density of interacting electrons moving in external potential v_{ext} can be calculated as a density of a non-interacting electron gas moving in the effective potential v_{eff}, which is defined as

$$v_{\text{eff}}(\vec{r}) = \quad \frac{n(\vec{r}')}{|\vec{r} - \vec{r}'|} d^3\vec{r}' + v_{\text{xc}}(\vec{r}) + v_{\text{ext}}(\vec{r}). \tag{4.4}$$

The first term in Eq. 4.4 is the HARTREE term, while v_{xc} is defined as the first variation of the exchange and correlation energy $E_{\text{xc}}[n(\vec{r})]$:

$$v_{\text{xc}}(\vec{r}) \equiv \frac{\delta}{\delta n(\vec{r})} E_{\text{xc}}[n(\vec{r})]. \tag{4.5}$$

Then, the problem is reduced to the following equations (KOHN–SHAM equations):

$$\left\langle \phi_i \middle| v_{\text{eff}}(\vec{r}) - \frac{\nabla^2_{\vec{r}}}{2} \middle| \phi_i \right\rangle = \epsilon_i, \tag{4.6}$$

$$\langle \phi_i | \phi_j \rangle = \delta_{ij}, \tag{4.7}$$

$$n(\vec{r}) = \sum_{i=1}^{N} \langle \phi_i | \phi_i \rangle. \tag{4.8}$$

These nonlinear equations can be solved self-consistently. DFT codes typically deal with a Fourier transform of this problem, i.e. Kohn–Sham equations are solved on a finite mesh of $\vec{k}$. The only remaining problem is E_{xc}, which is not known exactly, and calls for additional approximations.

4.1.2 Approximations to the exchange and correlation potential

The exchange and correlation energy can be formally decomposed into exchange and correlation contributions, E_{x} and E_{c}, respectively. The exchange term subtracts the unphysical interaction of an electron with itself, which is included in E_{H}. This term can be expressed in a two-center integral form [98]:

$$E_{\mathrm{x}} = -\frac{1}{2}\sum_{ij} \quad \frac{\phi_j^*(\vec{r})\,\phi_i^*(\vec{r}\,')\,\phi_j(\vec{r}\,')\,\phi_i(\vec{r})}{|r-r'|}\,d^3\vec{r}\,'\,d^3\vec{r}. \tag{4.9}$$

In contrast, the correlation term E_{c} can not be expressed analytically in terms of ϕ_i. Instead, different approximations for this term are used. The most popular is the local density approximation (LDA), which is based on the homogeneous interacting electron gas model. Within this model, the exchange energy is defined as

$$E_{\mathrm{x}}^{\mathrm{LDA}}[n(\vec{r})] = -\frac{3}{4}\left(\frac{3}{\pi}\right)^{1/3} \quad n(\vec{r})^{4/3}\,d^3\vec{r}. \tag{4.10}$$

The correlation energy $E_x[n(\vec{r})]$ is typically defined as a parameterized solution, attained by using quantum Monte Carlo (QMC) algorithms. At present, the parameterization of Perdew and Wang [99] is typically used for practical calculations.

As follows from the mapping onto the homogeneous electron gas problem, LDA is a good approximation for slowly varying densities. In the case of sizable density variations, it is reasonable to introduce a gradient correction, leading to the generalized gradient approximation (GGA):

$$E_{\mathrm{xc}}^{\mathrm{GGA}}[n(\vec{r})] = \quad f \quad n(\vec{r}), \vec{\nabla} n(\vec{r}) \quad d^3\vec{r}, \tag{4.11}$$

where the function f can be defined in different ways. The most widely used is the definition of Perdew, Burke and Ernzerhof [100]. Extensive comparisons showed that GGA yields an improvement for light atoms, while heavy atoms are better described in LDA. In general, LDA overestimates bonding, thus underestimating the interatomic distances [101, 102]. Comparative studies for cuprate materials, including the results of this work, do not reveal any systematic improvement in the description of the electronic structure by GGA in comparison to LDA.

To distinguish between non-magnetic and spin-polarized states, the theory was generalized already at early stages by von Barth and Hedin [103]. In particular, they replaced the density $n(\vec{r})$ by the spin density matrix $n_{\sigma\sigma'}(\vec{r})$, leading to independent spin up and spin down densities. The resulting (spin) magnetic moment μ will be

$$\vec{\mu} = -\mu_{\mathrm{B}} \quad \mathrm{Tr}\left\{\mathbf{S} \cdot n_{\sigma\sigma'}(\vec{r})\right\} d^3\vec{r}, \tag{4.12}$$

where $\mathbf{S}$ is the total spin operator. This spin-dependent theory is called local spin density approximation (LSDA).

4.1.3 Correlated systems. DFT+U

For a wide class of materials, such as Mott and charge transfer insulators, local functionals like LDA or GGA yield qualitatively wrong solutions, predicting these systems to be metallic. Although spin-polarized calculations typically yield a nonzero band gap, its value is substantially (e.g. one order of magnitude) smaller, than the experimentally measured. The underlying reason for this discrepancy is the insufficient treatment of electron-electron repulsion (correlation), which can be especially large if two electrons occupy a compact orbital having a rather small spread. For the $3d$ systems, such as cuprates, this effect is especially pronounced.

Adequate treatment of strongly correlated systems within DFT is a challenging task, and no universal solution to this problem has been proposed so far. The essential problem is to incorporate many-body effects such as correlations into the one-electron approach. The simplest and at present one of the most popular schemes is LDA+U, proposed by Anisimov, Zaanen and Andersen [104]. The general idea of LDA+U is to account for the missing part of Coulomb interaction by introducing a certain energy penalty for two electrons occupying the same orbital (Hubbard model). It is important to note that the reasoning of Ref. 104 is based on the neglect of fluctuations for average orbital occupancies (mean-field approach). This way, the additional energy term can be expressed in terms of Coulomb matrix elements $W_{mm'}^{\sigma\sigma'}$, comprising spin-independent $U_{mm'}$ and spin-dependent (exchange) $J_{mm'}\delta_{\sigma\sigma'}$ contributions [105].

In DFT codes, the parameters $U_d = U_{mm'}$ and $J_d = J_{mm'}$[1] are typically expressed in terms of Slater integrals F^{2n}. The most relevant parameter is $U_d = F^0$, which in the case of Cu^{2+} typically falls into the range 5–9 eV, while its particular value is often adjusted to provide the best agreement to the available experiments. In addition, non-universality of U_d should be emphasized: the difference in basis set definitions gives rise to difference in the values of U_d that yield the same value for a reference quantity (e.g. exchange coupling J). Therefore, the optimal[2] values of U_d for one DFT code are in general not directly transferable to the other code. Moreover, the optimal value of U_d depends also on the type of the reference quantity. As was shown in Ref. 106, the optimal U_d values that reproduce the experimentally measured components of the electric field gradient tensor are ~2 eV smaller than those yielding the best agreement for the J_i values derived from fits to magnetic susceptibility. Although Ref. 106 suggests that the difference is likely influenced by different time scales that specific are to a particular experiment, this issue definitely deserves a deeper investigation.

---

[1] Since the object of this study are $3d$ systems (cuprates), the notation U_d and J_d is used in the following.

[2] The value providing the best agreement with the respective experiment.

In contrast, extensive spectroscopic studies evidence that J_d is very close to 1 eV for all 3d elements. Therefore, in DFT+U calculations, this parameter is typically kept constant. The relevant terms F^2 and F^4 can be evaluated by combining the expression $J_d = (F^2 + F^4)/14$ [107] with the empirical value for F^4/F^2 which amounts to 0.62–0.63 for all 3d elements [108]. This way, for $J_d = 1$ eV, $F^2 = 8.6$ eV and $F^4 = 5.4$ eV. For the d orbitals, further F^{2n} terms ($n > 2$) are zero.

The original functional of Ref. 104 refers to the spin-independent average occupations, yielded by LDA. An alternative way to introduce the additional term is to use the spin-dependent occupations, yielded by LSDA [109]. Therefore, LDA+U and LSDA+U are different calculational schemes, although they are often confused in the literature, as discussed in [105]. In addition, the occupations can be taken from the GGA, leading to the GGA+U functional. A common abbreviation for the whole family of these "+U" functionals is DFT+U.

Besides obvious shortcomings, such as the absence of dynamical effects, the main problem of the DFT+U approach is the double counting of correlation energy already present in L(S)DA or GGA. To remedy this effect, the double-counting correction (DCC) is introduced. There is no unique way to introduce the DCC. Instead, two limiting cases were proposed. The first possibility is to subtract the averaged energy corresponding to the uniform occupancy of the orbitals. This scheme is typically referred as around-the-mean-field (AMF) [109]. Another option is to use the fully localized limit (FLL), with integer (0 or 1) orbital occupations as a reference. Although a combination of the two schemes can be used as well [110], pure AMF or FLL schemes are typically used for calculations.

The choice of the DCC scheme affects the resulting energies. Despite thorough theoretical works [105, 110] and comparative AMF/FLL studies (e.g., Refs. 111 and 112), the influence of the DCC is studied insufficiently. Many DFT+U-based studies of microscopic magnetic models ignore this problem, while the choice between the two DCC scheme is often done implicitly.

Recently, vibrant development of alternative methods for an appropriate description of strongly correlated systems lead to considerable progress in this field. Although these methods are not used in the present study, the vast improvement of computational facilities make these alternative techniques more and more appealing, and they are worth mentioning.

Since all feasible DFT-based computational schemes an approximation for the exchange and correlation potential, a natural alternative is to apply quantum chemical methods in order to provide a more realistic description of correlations. The variety of techniques exploiting this idea is referred as post-HARTREE–FOCK methods.[3] Although the applicability of these methods is presently restricted to rather small clusters, there is an empirical evidence that such small clusters can provide a reasonable description of bulk properties [113]. The most difficult part is to find an appropriate cluster and to introduce a reasonable embedding potential. Despite these difficulties, recent post-HARTREE–FOCK studies on quasi-1D [114, 115] and quasi-2D [116, 117] cuprates evidence good potential of such an approach.

---

[3] The starting point of such calculational schemes is a HARTREE–FOCK calculation, where the correlations

Another way of improving the DFT description is to combine it with the exact HARTREE–FOCK exchange [118]. Here, the tricky part is to choose the correct mixing ratio. Recent hybrid functional studies on several quasi-2D cuprates report considerable improved description of the electronic structure (e.g. the correct electronic ground state and the value of the band gap) compared to LDA and GGA [119].

A rational albeit computationally demanding idea is to improve the HARTREE–FOCK method by resorting to the screened COULOMB interaction W. The respective calculational method is known as the GW approximation [120–122], where G stands for a single-particle GREEN's function. A very promising development is the family of DFT+DMFT methods (LDA+DMFT [123], GGA+DMFT [124], GW+DMFT [125]), which can be regarded as a dynamical version of LDA+U. Here, a certain site or a small cluster are treated as impurities. The electron-electron interactions at the impurity sites is taken into account explicitly, while the interactions with the surrounding is treated as a dynamical mean-field. The development of more and more efficient impurity solvers contributes to popularity of this method.

4.1.4 FPLO

The DFT code `FPLO` ("full-potential local orbital") is an all-electron numerically efficient code which yields accurate GS density and energy, as well as the energies of the lowest-lying excitations [126]. The DFT calculations described in the present work were done using `FPLO` versions 6 to 9, where a constant basis set is used, in contrast to the older versions. The scope of the available options comprises different parameterizations of the exchange and correlation potential (different versions of LDA [99, 127] as well as GGA [100]), DFT+U, full-relativistic calculations, calculation of forces, structure optimizations, WANNIER functions [128], electric field gradients [106], and electron localization functions. Both crystalline systems and molecules can be treated.

FPLO uses the basis of atomic-like wave functions, subdivided into the core states (fully occupied, no overlap of wave functions of different sites), semi-core states (small, but non-negligible overlap), valence states (partially occupied) and extended states (lowest-lying unoccupied states). The spin-independent basis states, composed of analytical angular (spherical harmonics) and numerical radial parts (solutions to the DIRAC equation with an additional confining potential [126]). The basis set is extended, i.e. it contains a stock of polarization states, which ensures an appropriate description for the lowest-lying excited

---

effects arising from COULOMB repulsion of electrons are neglected completely. In the next step, these effects are taken into account (hence the name "post-HARTREE–FOCK").

states. Implementation of the extended basis set in `FPLO` contrasts with a more popular idea to describe valence and conduction electrons by plane waves, as implemented, e.g. in `vasp` [129], `WIEN2K` [130] or `fleur` [131].

4.1.5 Relevant information

This short section summarizes the information, which should necessarily accompany any DFT-based study, in order to make the results reproducible.

DFT code Apparently, different DFT codes use different calculational schemes and can substantially differ in their performance, and more important, in accuracy. The same applies to different versions of the same code. Therefore, the name and the version of the code used should be specified.

Basis set Most DFT codes feature a flexible basis set, which can be varied to reach the optimal balance between accuracy and performance. For the plane wave codes, this flexibility is ruled by the plane wave cutoff parameter, which should be specified in a publication. In local orbital codes, different sets of local orbitals (or their combinations) can be used as a basis. Consequently, this basis set should be explicitly specified.

Parameterization of E_{xc} Different parameterizations of E_{xc} yield in general different total energies, thus the parameterization used, should be specified.

Relativistic treatment DFT calculations can be performed by neglecting the relativistic effects completely (non-relativistic), or partly, by neglecting only the spin-orbital coupling (scalar relativistic [132]). However, systems with sizable spin-orbit coupling require computationally demanding full relativistic treatment.

Crystal structure Crystal structure (lattice constants and atomic coordinates) is a substantial part of the input for a DFT calculation. If an experimentally defined crystal structure is used, the reference to the structural information should be mentioned explicitly. For an optimized structure, the optimized structural parameters should be provided.

Unit cell and supercells In principle, the translational symmetry of crystalline materials can be characterized by an infinite number of vector sets $\vec{T}_1, \vec{T}_2, \vec{T}_3$. The majority of DFT studies use a primitive cell, i.e. the set of the basis vectors which yields the minimal volume $V = (\vec{T}_1 \times \vec{T}_2) \cdot \vec{T}_3$. In the case another cell is used (e.g. for LSDA+U supercells calculations), the basis vectors should be specified.

$\vec{k}$-meshes Since the KOHN–SHAM equations are solved on a discrete finite mesh of $\vec{k}$ vectors, convergence with respect to the $\vec{k}$-mesh should be addressed. Metals are notorious for strong $\vec{k}$-dependence of the calculated energies, while insulators yield converged results even for very small meshes (Fig. 4.1). Thus, especially for metallic systems, the k-meshes used for the calculation, should be specified.

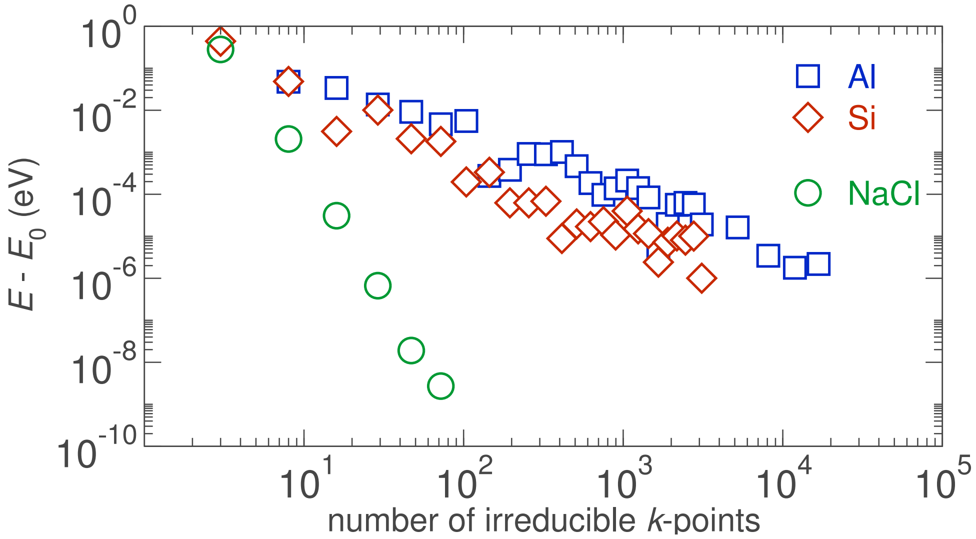

Figure 4.1: Convergence of the total energy with respect to the $\vec{k}$-mesh for several systems. The insulator NaCl exhibits good convergence even for small meshes. In contrast, the total energies of conducting systems (Al and Si) are strongly dependent on the $\vec{k}$-mesh (slow convergence). Note the logarithmic scales in both axes. The details of the calculations are given in App. A3.

DFT+U parameters In addition to the parameters U_d and J_d, the DCC scheme should be specified.

4.2 Model approach

Among all kinds of excitations in solid state, the magnetic excitations have the lowest energy. As a consequence, the states relevant for magnetism are typically bound to a close vicinity of the FERMI level. For these energies, modern DFT codes yield in general accurate dispersion relations. The atomic as well as the orbital character of the states relevant for magnetism can be identified by projecting the constituent bands onto a basis set of atomic-like orbitals.

As discussed in Sec. 4.1, DFT fails[4] to reproduce the correct GS for correlated insulators. Therefore, for the case of strong correlations (sizable COULOMB repulsion U), further analysis of the relevant bands largely depends on their dispersion. In the case of strongly dispersive bands ($\Delta\epsilon \gg U$), electron transfer processes dominate over correlations and magnetism has an itinerant nature. In contrast, small band dispersions ($\Delta\epsilon \ll U$) point to localized magnetism, which originates from polarization of spins bound to inner shells of an atom.

---

[4] Standard parameterizations of E_{xc}, such as LDA and GGA.

Since all undoped cuprates belong to the latter class, only localized magnetism is considered in the following discussion.

In general, a system of N interacting electrons can be described in a non-relativistic approach by the following Hamiltonian:

$$H = \sum_{i=1}^{N} \left[-\frac{\hbar^2}{2m_e} \nabla^2_{\vec{r}_i} + U(\vec{r}_i) + \frac{1}{2} \sum_{j \neq i} V(\vec{r}_i - \vec{r}_j) \right]. \tag{4.13}$$

The first and the second terms are the kinetic and the potential energy operators for a one-electron problem, and the last term describes the interaction between the electrons. To underscore the essential difference between the last term and the first two terms, the Hamiltonian 4.13 can be rewritten in terms of second quantization:

$$\hat{H} = -\sum_{ij} t_{ij}\, \hat{c}_i^{\dagger} \hat{c}_j + \frac{1}{2} \sum_{ijkl} V_{ijkl}\, \hat{c}_i^{\dagger} \hat{c}_k^{\dagger} \hat{c}_j \hat{c}_l, \tag{4.14}$$

$$\text{where } t_{ij} = \quad \phi_i^*(\vec{r}) \left[-\frac{\hbar^2}{2m_e} \nabla^2_{\vec{r}} + U(\vec{r}) \right] \phi_j(\vec{r})\, d^3\vec{r} \tag{4.15}$$

$$\text{and } V_{ijkl} = \quad \phi_i^*(\vec{r}_1)\phi_j(\vec{r}_1)\, V(\vec{r}_1 - \vec{r}_2)\, \phi_k^*(\vec{r}_2)\phi_l(\vec{r}_2)\, d^3\vec{r}_2\, d^3\vec{r}_1. \tag{4.16}$$

The first term in Eq. 4.14 describes the electron transfer (hopping) process, while the second term is related to the electron-electron interaction. The parameters of this Hamiltonian are the transfer integrals t_{ij} and the two-center integrals V_{ijkl}. A full set of t_{ij} and V_{ijkl} apparently provides a complete non-relativistic description of an N-electron system. However, restriction to several relevant terms is often a very good approximation. Since standard approximations to the exchange and correlation potential drastically underestimate the effect of strong correlations, it is convenient to start with the picture of non-interacting electrons (the interactions between the electrons are neglected by setting $V_{ijkl} = 0$ in Eq. 4.14).

The resulting simplified Hamiltonian is known as a tight-binding (TB) model (Sec. 4.2.1). Next, by varying the model parameters t_{ij}, the optimal description of the DFT band structure is obtained. To restore the insulating GS, the Hamiltonian 4.14 is supplemented by the interaction term with a realistic value for the onsite COULOMB repulsion $V_{ijkl} = U$, which leads to a HUBBARD model. As it will be shown (Sec. 4.2.5), low-energy (magnetic) excitations of this model are described by a HEISENBERG model (Sec. 4.2.6).

This effective one-orbital procedure provides a reliable estimate only for the AFM part of exchange. However in real systems, there are several sources for the FM exchange, apparently not accounted for in this approach. Relevant approaches to the evaluation of the FM part of exchange couplings will be described in Sec. 4.2.7.

4.2.1 Tight-binding model

As discussed in Sec. 4.1.3, standard parameterizations of the exchange and correlation potential, such as LDA or GGA, strongly underestimate the effect of COULOMB repulsion between the electrons of inner atomic shells. It is therefore reasonable, in first approximation, to neglect completely this small part of the COULOMB energy, contained in LDA or GGA. Such assumption leads to the TB approximation, in which electron-electron interactions are neglected ($V_{ijkl} = 0$ in Eq. 4.14). The resulting TB Hamiltonian is expressed as

$$\hat{H}_{\mathrm{TB}} = -\sum_{i>j,\sigma} t_{ij}(\hat{c}^{\dagger}_{i\sigma}\hat{c}_{j\sigma} + \hat{c}^{\dagger}_{j\sigma}\hat{c}_{i\sigma}) - \sum_{i,\sigma} \epsilon_i \hat{c}^{\dagger}_{i\sigma}\hat{c}_{i\sigma} \tag{4.17}$$

where t_{ij} are transfer integrals, and ϵ_i are constant energy shifts with respect to the FERMI level. The creation and annihilation operators can be FOURIER-transformed into

$$\begin{aligned} \hat{c}^{\dagger}_{i\sigma} &= K^{-1/2}\sum_{\vec{k}} \hat{c}^{\dagger}_{\vec{k}\sigma} \exp(-i[\vec{k}\cdot\vec{R}_i]), \\ \hat{c}_{i\sigma} &= K^{-1/2}\sum_{\vec{k}} \hat{c}_{\vec{k}\sigma} \exp(i[\vec{k}\cdot\vec{R}_i]), \end{aligned} \tag{4.18}$$

where K is the number of discrete reciprocal-space vectors $\vec{k}$ in the first BRILLOUIN zone, and $\vec{R}_i$ is the real-space position vector of the i-th site. Combining Eq. 4.18 with Eq. 4.17,

$$\begin{aligned} \hat{H}_{\mathrm{TB}} = -K^{-1}\sum_{\vec{k},\sigma}\sum_{i>j} t_{ij} \left[\hat{c}^{\dagger}_{\vec{k}\sigma}\hat{c}_{\vec{k}\sigma} \exp(i[\vec{k}\cdot\{\vec{R}_j - \vec{R}_i\}])\hat{c}^{\dagger}_{\vec{k}\sigma}\hat{c}_{\vec{k}\sigma} + \exp(-i[\vec{k}\cdot\{\vec{R}_j - \vec{R}_i\}])\right] + \\ - K^{-1}\sum_{\vec{k},\sigma}\sum_{i} \epsilon_i \hat{c}^{\dagger}_{\vec{k}\sigma}\hat{c}_{\vec{k}\sigma} = -K^{-1}\sum_{\vec{k},\sigma}\quad\sum_{i\geq j} \delta_{ij}\epsilon_i + (1-\delta_{ij})2t_{ij}\cos(\vec{k}\cdot[\vec{R}_j - \vec{R}_i]) \quad \hat{c}^{\dagger}_{\vec{k}\sigma}\hat{c}_{\vec{k}\sigma}. \end{aligned} \tag{4.19}$$

For periodic 3D systems, only a finite number N of vectors $\vec{R}_i$ within a unit cell are independent. All other radius-vectors are related by $\vec{R}'_i = \vec{R}_i + \vec{T} = \vec{R}_i + c_x\vec{t}_x + c_y\vec{t}_y + c_z\vec{t}_z$, where $\vec{t}_x$, $\vec{t}_x$ and $\vec{t}_x$ are translations along the edges of the unit cell, and c_x, c_y and c_z are arbitrary integers. Therefore, the Hamiltonian (Eq. 4.19) can be rewritten:

$$\hat{H}_{\mathrm{TB}} = -K^{-1}\sum_{\vec{k},\sigma}\left\{\sum_{i\geq j,\vec{T}} \delta_{ij}\delta_{\|\vec{T}\|0}\epsilon_i + (1-\delta_{ij}\delta_{\|\vec{T}\|0})2t_{i,j+\vec{T}}\cos(\vec{k}\cdot[\vec{R}_j + \vec{T} - \vec{R}_i])\right\}\hat{c}^{\dagger}_{\vec{k}\sigma}\hat{c}_{\vec{k}\sigma}, \tag{4.20}$$

where $1 \leq j \leq i \leq N$, and R_i and R_j belong to the same unit cell. Similar to Eq. 4.17, this sum contains an infinite number of terms. However, in practice, the increase of the intersite distance $\vec{R}_j + \vec{T} - \vec{R}_i$ leads to a rapid decay of the respective transfer integrals $t_{i,j+\vec{T}}$. Therefore, the sum in Eq. 4.20 can be reduced only to relevant terms (with small $\vec{T}$) in good approximation.

For practical computations, operators should be presented in the matrix form. Thus, the Hamiltonian (Eq. 4.20) can be written as a $\vec{k}$-dependent $N \times N$ matrix with the following matrix elements:

$$H_{\mathrm{TB}}(\vec{k}) = \langle \phi_j | \, \hat{H}_{\mathrm{TB}} \, | \phi_i \rangle = -\delta_{ij}\epsilon_i - \sum_{\vec{T}} t_{i,j+\vec{T}} \exp \;\; i \;\; \vec{k} \cdot (\vec{R}_j + \vec{T} - \vec{R}_i) \quad , \tag{4.21}$$

As soon as the values of all relevant $t_{i,j+\vec{T}}$ are known, the TB Hamiltonian matrix can be readily constructed. Its eigendecomposition yields the dispersions (the eigenvalues are $\vec{k}$-dependent). For particularly simple cases, the solution of this model is straightforward. An archetypical example is the chain of equidistant (separated by $\vec{T}$) sites with a NN hopping t_1. Here, the unit cell contains just one atom, and the Hamiltonian matrix is reduced to a scalar, which amounts to $-\epsilon_0 - t_1 \exp^{i(\vec{k}\cdot\vec{T})} - t_1 \exp^{i[\vec{k}\cdot(-\vec{T})]} = -\epsilon_0 - 2t\cos(\vec{k}\cdot\vec{T})$ (Eq. 4.21), leading to a simple analytical expression for the energy $E(\vec{k}) = -\epsilon_0 - 2t_1\cos(\vec{k}\cdot\vec{T})$.

Although there are many spin chain materials known (see, e.g. Sec. 6.1), the majority of quantum magnets feature a more complicated topology of magnetic couplings. In 1D, the simplest extension of the NN chain model is taking the NNN coupling t_2 into account (Fig. 4.2, bottom). In this case, the resulting dispersion, given by $E(\vec{k}) = -\epsilon_0 - 2t_1\cos(\vec{k}\cdot\vec{T}) - 2t_2\cos(\vec{k}\cdot 2\vec{T})$, strongly depends on the ratio of the leading couplings t_1 and t_2. Thus, a small t_2 has only a minor impact on the cosine-like shape of the dispersion (Fig. 4.2, left). For $t_1 = 2t_2$ and $t_1 = 2t_2$ (Fig. 4.2, middle and right, respectively), the resulting dispersion clearly contrasts with the NN chain ($t_2 = 0$) case. Thus, a careful inspection of dispersion along a certain direction of the $\vec{k}$-space provides valuable information on the coupling regime, in particular, whether restriction to the NN coupling is appropriate.

In this way, the dispersions $E(\vec{k})$ can be calculated for any set of transfer integrals. The nontrivial part of the problem is to obtain estimates for $t_{i,j+\vec{T}}$. At present, two approaches, both based on the evaluation of a DFT band structure, are used for this purpose. The TB fit is a clear and typically stable procedure yielding numerically precise results, although in many cases it suffers from ambiguous solutions. The other approach, based on WANNIER functions, is computationally more demanding, but provides a physically sound picture.

4.2.2 Tight-binding fit

The TB fit is an iterative procedure, in which the initially given set of transfer integrals $\{t^0_{i,j+\vec{T}}\}$ is varied in order to get the best fit to the set of bands adopted from the DFT band

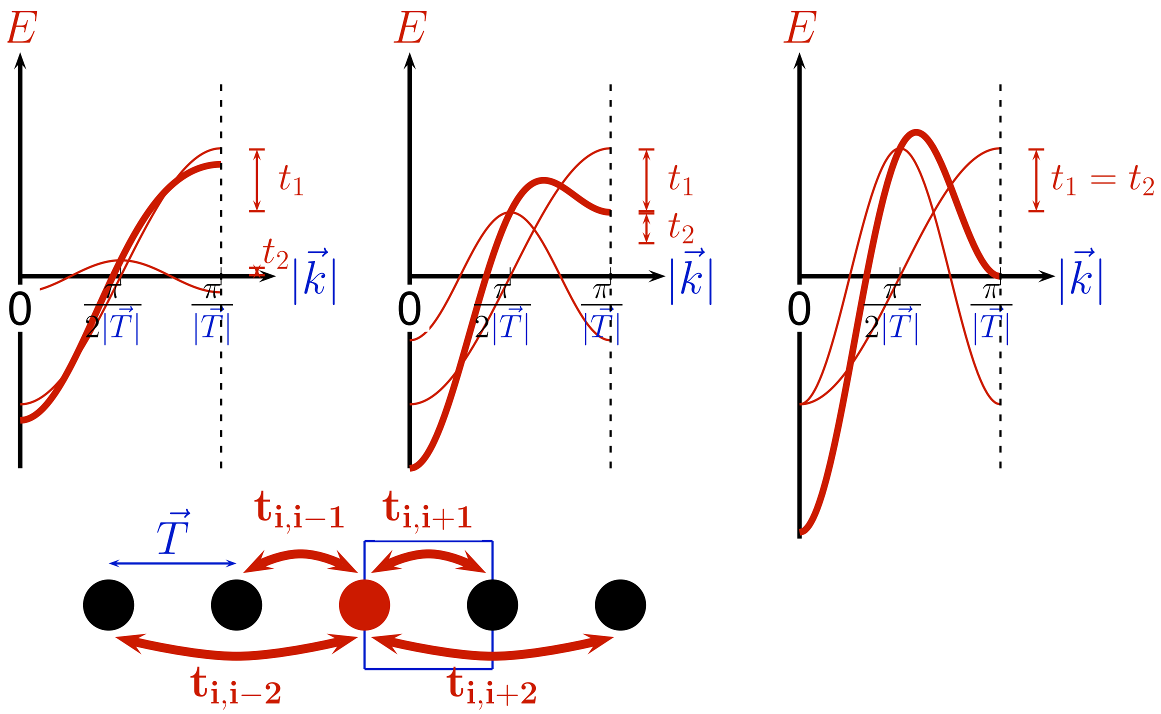

Figure 4.2: Band dispersions (bold red lines) of the TB model for a chain with NN t_1 and NNN t_2 couplings (bottom). Individual contributions of the t_1 and t_2 terms are shown by thin red lines. Left panel: t_1 t_2. The cosine-like shape of the resulting dispersion is preserved. Central panel: $t_1 = 2t_2$. Right panel: $t_1 = t_2$.

structure. For N magnetic orbitals (or magnetic sites in a one-orbital model) in the unit cell, the corresponding N-band complex having a sizable weight of the particular orbital character, should be selected. The choice of these bands can be carried out by analyzing the orbital-projected density of states or by plotting the band weights, both visualizing the orbital character. A typical feature of the electronic structure of many cuprate materials is a clearly separated band complex at the FERMI level, with the strongly dominant Cu $3d_{x^2-y^2}$ and O $2p_\sigma$ orbital character. In this case, selecting the relevant part of the band structure is straightforward. However, for several systems, the lower edge of the $(dp)_\sigma$ band complex is mixed or hybridized with other $3d$ bands, making the choice of N relevant bands ambiguous. As a rule of thumb, bands with a larger weight of the $3d_{x^2-y^2}$ states should be chosen.

Typical for a local optimization technique, the initial values of the leading terms $t_{i,j+\vec{T}}$ play a crucial role in the TB fitting. Choosing a reasonable set of starting $\{t^0_{i,j+\vec{T}}\}$ is a nontrivial task. There are several ways to guess the leading terms. In particular, the crystal structure can be analyzed by applying empirical rules for the strongest couplings, such as GOODENOUGH–KANAMORI rules [21, 23]. An additional, alternative insight can be gained from the available experimental data. This way, the energy scale of the leading couplings can be roughly determined. In the case such data are not available, the results for isostructural or closely related systems can be used. It should be explicitly noted that such techniques are not universal and unless their outcome is carefully analyzed, may yield an inappropriate guess for $\{t^0_{i,j+\vec{T}}\}$.

The TB procedure comprises (i) the construction of the TB Hamiltonian, (ii) its diagonalization and (iii) minimization of the difference between the resulting energy spectrum and the spectrum obtained from DFT. The TB fit algorithm implemented in `flyswatter` [133], comprises the following steps:

1. Define the starting values $\{t^0_{i,j+\vec{T}}\}$ and the criterion for convergence ϵ.
2. Read $\{\vec{R}_i\}$ (total number of $\vec{R}_i$ per cell is N), $\vec{T}$, the $\vec{k}$-mesh K, and the band structure $E_i^{\mathrm{DFT}}(\vec{k})$ from the DFT output.
3. Set $n = 0$ (initial cycle).
4. Construct and diagonalize the TB matrix $H^n_{\mathrm{TB}}(\vec{k})$.
5. Construct F^n : $F^n(\{t^n_{i,j+\vec{T}}\}) = \sum_{\vec{k}} \sum_{i=1}^{N} \left| \langle \phi_i | H^n_{\mathrm{TB}}(\vec{k}) | \phi_i \rangle - E_i^{\mathrm{DFT}}(\vec{k}) \right|^2$, where $|\phi_i\rangle$ is the i-th eigenvector of H^n_{TB}.
6. Perform a steepest descent step to minimize F^n. Keep the resulting set of new $\{t^{SD}_{i,j+\vec{T}}\}$.
7. If $F^n \leq \epsilon$, then stop, otherwise increase n by one, set $\{t^n_{i,j+\vec{T}}\} = \{t^{SD}_{i,j+\vec{T}}\}$ and go to step 4.

An important advantage of the TB fit technique is its flexibility. In particular, better agreement with the DFT bands can be achieved by extending the set of transfer integrals $\{t^0_{i,j+\vec{T}}\}$. To check the stability of the leading terms, the fitting can be repeated for a reduced set of the leading transfer integrals, only.

The TB fit usually works well for the systems with one or few leading couplings. If there is no clear separation between the leading and minor couplings, the procedure becomes less stable, and can converge to a local minimum.[5] For certain systems with low symmetry, there are several symmetrically-nonequivalent couplings corresponding to the same interatomic separation $|\vec{R}_j + \vec{T} - \vec{R}_i|$. Such situations may cause troubles for the TB fit method. Therefore, in these cases, an additional careful analysis (based on essentially empirical considerations) of the respective coupling paths is necessary.

Even more tricky is the problem of hybridization between different orbitals: it impedes the choice of the E_i^{DFT} values and prejudices the effective one-orbital approach. In this case, a reasonable solution would be to switch to a multi-orbital model. However, this would lead to a sizable increase in the number of relevant $\{t^0_{i,j+\vec{T}}\}$ terms, since there will be at least two sets of intra-orbital hoppings as well as inter-orbital ones. In practice, evaluation of multi-orbital models is carried out using the WANNIER functions technique, described in the next section.

---

[5] Unfortunately, this problem is inherent in the local optimization techniques.

4.2.3 WANNIER functions

Two essential drawbacks of the TB fit method are (i) its dependence on the initial guess of t_{ij} and (ii) its purely mathematical way of fitting to the DFT bands. It is intuitively clear that the information yielded by solving KOHN-SHAM equations can be used more efficiently than in the TB fitting procedure. In particular, any DFT code deals with the following problem:

$$\hat{H}_{\text{DFT}} = \sum_{n,n',\vec{k}} |\psi_{n,\vec{k}}\rangle H_{n,n'}(\vec{k}) \langle \psi_{n',\vec{k}}|, \tag{4.22}$$

where $|\psi_{n,\vec{k}}\rangle$ are eigenfunctions (BLOCH states) of the respective HILBERT space. Among the huge number of these eigenfunctions, the relevant subset can be selected (the set of states forming the bands at the FERMI level). The FOURIER transformation of this basis leads to the Hamiltonian

$$\hat{H}_{\text{WF}} = \sum_{n,n',\vec{T}} |w_n^0\rangle H_{n,n'} \langle w_{n'}^{\vec{T}}|. \tag{4.23}$$

In the old basis, the BLOCH states were real space functions that depend on $\vec{k}$ and the band index n. WANNIER functions that form the new basis, are not dependent on $\vec{k}$, but centered, or localized, at a certain position $\vec{R}_i$ in the real space. WANNIER functions can be expressed as

$$|w_n^{\vec{R}_i}\rangle = K^{-1/2} \sum_{\vec{k}} \exp(-i[\vec{k}\cdot\vec{R}_i])|\psi_{n,\vec{k}}\rangle, \tag{4.24}$$

where K is the number of $\vec{k}$-points.

Although the expression in Eq. 4.24 is seemingly simple, the evaluation of WANNIER functions is a tricky task due to the intrinsic arbitrariness in their definition: in the case of a single band, the BLOCH function $|\psi_{\vec{k}}\rangle$ can be multiplied by a phase factor $\exp(i\phi[\vec{k}])$, where ϕ is a real function of $\vec{k}$. The FOURIER transformation of the new BLOCH state leads to a new WANNIER function. Generalizing for a multiband model, this gauge freedom can be expressed by a unitary matrix $U_{mn}^{\vec{k}}$, which mixes different BLOCH states at a given $\vec{k}$:

$$|\psi_{n,\vec{k}}\rangle = \sum_m U_{m,n}^{\vec{k}} |\psi_{m,\vec{k}}\rangle. \tag{4.25}$$

Thus, Eq. 4.24 can be rewritten as

$$|w_n^{\vec{R}_i}\rangle = K^{-1/2} \sum_{\vec{k}} \sum_m U_{m,n}^{\vec{k}} \exp(-i[\vec{k}\cdot\vec{R}_i])|\psi_{m,\vec{k}}\rangle. \tag{4.26}$$

Depending on $U_{m,n}^{\vec{k}}$, the resulting WANNIER functions can have different degree of localization. Following the analysis performed in Ref. 134, by varying $U_{m,n}^{\vec{k}}$, a unique set of maximally localized WANNIER functions can be evaluated.

The calculation of maximally localized WANNIER functions is a computationally challenging task. Therefore, there are alternative procedures to evaluate well-localized WANNIER functions at smaller computational cost. Here, the basic ideas of the procedure [128] implemented in FPLO, which is extensively used in the present study, are discussed.

Since FPLO uses a chemically-optimized local orbital basis [126], it is appealing to use local orbitals (with their symmetry restrictions) as a starting point to define the WANNIER functions. Thus, the initial guess for the unitary transformations can be evaluated by projecting the BLOCH states $|\psi_{n,\vec{k}}\rangle$ onto local orbital functions $|S_i\rangle$. This way, only the states with a large weight of given local orbitals have a significant contribution to the expression in Eq. 4.26. An additional confinement to a certain energy range is done via energy windows functions, making a separate treatment of bonding and antibonding bands possible. Finally, the orthogonalization of the resulting BLOCH sums is performed. This way, the resulting WANNIER functions largely inherit the shape of the respective atomic-like orbitals $|S_i\rangle$. There is an empirical evidence that such approach provides a rather high degree of localization [39, 128].

Well-localized WANNIER functions provide a direct access to the transfer integrals $t_{i,j\vec{T}}$ that are evaluated as non-diagonal hopping matrix elements:

$$t_{i,j+\vec{T}} = \langle w_n^{\vec{R}_j+\vec{T}} | \hat{H} | w_n^{\vec{R}_i} \rangle. \tag{4.27}$$

In comparison to the TB fit, the WF approach is computationally more tricky and can be applied, provided that BLOCH sums can be exported from a DFT code.[6] However, the great advantage of this method is that the resulting model is physically sound. In other words, the ambiguity (multiple solutions) inherent to the TB fit procedure, is lifted. Next, the method can be efficiently applied to multiband models. Finally, WANNIER functions provide a visual insight into the relevant orbitals and superexchange paths, as will be shown for several compounds within this study (Chapters 6 and 7).

4.2.4 HUBBARD model

The relevant $t_{i,j\vec{T}}$ terms, known from either a TB fit (Sec. 4.2.2) or WANNIER functions (Sec. 4.2.3), parameterize the respective TB model. Although this model correctly accounts for the kinetic (electron transfer) terms, it is apparently inappropriate for strongly correlated materials, since the essence of correlations—interaction between the electrons—is completely neglected. To account for the correlation effects, the second term in Eq. 4.14 should be defined. A bare look at Eqs. 4.14 and 4.16 suffices to understand the substantial increase of the complexity. Therefore, the interaction term should be as simple as possible, in order to keep the problem solvable. HUBBARD suggested that among the huge number of V_{ijkl} terms, most relevant is the on-site COULOMB repulsion term, corresponding to the interactions of two electrons occupying the same orbital [135]:

---

[6] Typically, it is the other way round: the procedure calculating WFs is implemented directly into a DFT code.

$$\hat{H}_{\text{HUBBARD}} = \hat{H}_{\text{TB}} + U \sum_i \hat{c}^\dagger_{i\uparrow} \hat{c}_{i\uparrow} \hat{c}^\dagger_{i\downarrow} \hat{c}_{i\downarrow}, \tag{4.28}$$

The model in Eq. 4.28 is known as a HUBBARD model. Here, the sum $_i \hat{c}^\dagger_{i\uparrow} \hat{c}_{i\uparrow} \hat{c}^\dagger_{i\downarrow} \hat{c}_{i\downarrow}$ stands for the number of doubly-occupied orbitals, and the COULOMB repulsion U between the electrons occupying the same orbital given by

$$U = \quad |\phi(\vec{r}_1)|^2 \frac{e^2}{|\vec{r}_1 - \vec{r}_2|} |\phi(\vec{r}_2)|^2 \, d^3\vec{r}_2 \, d^3\vec{r}_1. \tag{4.29}$$

Although this model is apparently the simplest correlated model, it can be solved exactly only for particularly simple cases, e.g. a chain of spins with the NN coupling [136]. However, for realistic models, more involved geometry is typical, and consequently, the number of different terms t_{ij} can be larger, practically excluding any possibility to solve such models exactly. Therefore, the only computationally feasible way to account for the magnetic properties of a HUBBARD model is the so-called low-energy modeling [24], described in the next section.

4.2.5 Effective low-energy model

Although an exact solution of a HUBBARD model is generally not possible to attain, the magnetism of certain classes of real materials, in particular cuprates, can be accounted for by a simplified model. First, for the free $3d$ transition metal ions, the value of U typically amounts to 15−20 eV. In particular, $U = 16.3$ eV was reported for Cu^{2+} ions [137]. In a crystalline system, the screening effects reduce its value, and lead to the effective repulsion U_{eff} which is several times smaller than the value for a free ion [138]. Although the experimental estimates of U_{eff} are rather scarce, it is presently accepted that $U_{\text{eff}} = 4{-}5$ eV are the optimal values for cuprates.

In cuprates, the COULOMB repulsion energy largely exceeds the kinetic terms t_{ij} that are typically smaller than 0.5 eV. This substantial difference between the energy scales of U and t_{ij} gives rise to the insulating GS, common for undoped cuprates. Such situations, characterized by a clear dominance of the repulsion effects over the electron hopping are called the strongly correlated limit ($U \quad t_{ij}$). Second, for undoped cuprates, each Cu^{2+} atom has exactly one hole in the $3d$ shell, hence the respective HUBBARD model has one orbital per site and is necessarily half-filled.

To gain more insight into the physics of a HUBBARD model at half-filling, the simplest two-site problem ($N = 2$) is very instructive. For this case, the HUBBARD model can be solved exactly (see, e.g. Sec. IV/A/3 in Ref. 139). First, the HILBERT space of the model should be determined. Since the HUBBARD model contains no spin-flip terms, the total spin S is a conserved quantity and thus commutes with the Hamiltonian. Construction of the basis states for each spin sector is straightforward (Table 4.1). Next, the orthogonality of the basis is addressed by checking $\langle \phi_i \mid H_{\text{HUBBARD}} \mid \phi_j \rangle = \delta_{ij}$. This analysis readily yields that $\langle 4 \mid H_{\text{HUBBARD}} \mid 5 \rangle = \langle 5 \mid H_{\text{HUBBARD}} \mid 4 \rangle = -2t$, where 4 and 5 are indices from the first column of Table 4.1. These two states form a reduced Hamiltonian matrix with the eigenvalues $\frac{1}{2}(U \pm \sqrt{U^2 + 16t^2})$. The eigenvalue $\frac{1}{2}(U - \sqrt{U^2 + 16t^2})$ is negative for any infinitesimal t, and thus it is the GS energy.

index	state	S	E
1	$\lvert\uparrow\ \uparrow\rangle$	1	0
2	$\lvert\downarrow\ \downarrow\rangle$	1	0
3	$\frac{1}{\sqrt{2}}(\,\lvert\uparrow\ \downarrow\rangle + \lvert\downarrow\ \uparrow\rangle\,)$	1	0
4	$\frac{1}{\sqrt{2}}(\,\lvert\uparrow\ \downarrow\rangle - \lvert\downarrow\ \uparrow\rangle\,)$	0	0
5	$\frac{1}{\sqrt{2}}(\,\lvert\circ\ \uparrow\downarrow\rangle + \lvert\uparrow\downarrow\ \circ\rangle\,)$	0	U
6	$\frac{1}{\sqrt{2}}(\,\lvert\circ\ \uparrow\downarrow\rangle - \lvert\uparrow\downarrow\ \circ\rangle\,)$	0	U

Table 4.1: Total spin (S) and energy (E) for the states of a two-site HUBBARD model at half-filling. Open circles represent empty sites. The states 4 and 5 are not orthogonal and thus do not represent eigenstates of the HUBBARD Hamiltonian.

For the strongly correlated limit $U \gg t$, a more elegant expression for the GS energy can be obtained. Thus, t/U is treated as a parameter for a perturbation theory. In this way, the HUBBARD model can be rewritten as follows:

$$\hat{H}_{\text{HUBBARD}} = U(\hat{H}_0 + \frac{t}{U}\hat{H}_1), \text{ where } \hat{H}_0 = \sum_i \hat{c}^{\dagger}_{i\uparrow}\hat{c}_{i\uparrow}\hat{c}^{\dagger}_{i\downarrow}\hat{c}_{i\downarrow}, \text{ and } \hat{H}_1 = \sum_{\langle ij\rangle\sigma} \hat{c}^{\dagger}_{i\sigma}\hat{c}_{j\sigma}. \tag{4.30}$$

For $t/U = 0$, the GS has energy 0 and is four-fold degenerate (states 1, 2, 3 and 4 from Table 4.1). First order of a degenerate perturbation theory yields no correction to the GS energy, while second order delivers [24]:

$$\Delta E^{(2)} = -\frac{4t^2}{U}. \tag{4.31}$$

The physical picture is rather simple: the starting point is the singlet state where each site is singly occupied. The first hopping process creates an intermediate state with a doubly occupied site and an empty site. The energy of this state is higher than that of the GS, and this difference amounts to U. In the second hopping process, one of the electrons of the doubly occupied site can hop to the empty site. As a result, the gain in the kinetic energy associated with the hopping process lowers the GS energy by $4t^2/U$. However, if the triplet state is assumed to be the initial state, the PAULI exclusion principle impedes the electron hopping, thus the triplet state energy is unaffected in second order.

Since $U \gg t$, the eigenvalues of the HUBBARD Hamiltonian split into two sectors: the low-energy sector comprises the GS and a triplet, while the two charge-transfer states for a high-energy sector. The two sectors are separated in energy which amounts to $\sim U$.

Therefore, for the low-energy ($E \ll U$) excitations, the contribution of the high-energy sector is negligible, and the essential physics is accounted for by the low-energy part. As a consequence, the magnetic properties are well described by a reduced, low-energy model.

The low-energy model has a $S = 0$ GS and a three-fold degenerate $S = 1$ states, with the singlet-triplet separation equal to $4t^2/U$. ANDERSON noticed that this spectrum has exactly the same structure as the spectrum of a two-site HEISENBERG model for $J = 4t^2/U$ [24]. Therefore, the low-energy excitations of a half-filled HUBBARD model in the strongly-correlated limit at half-filling can be described by a HEISENBERG model. The result is not specific to the two-site model, and can be transferred to essentially any lattice geometry [140].

4.2.6 HEISENBERG model

HEISENBERG model is one of the basic models describing the behavior of insulating magnets, in which only spin degrees of freedom are preserved. The model parameters are exchange integrals J_{ij},[7] which correspond to the energy difference between antiparallel and parallel arrangements of spins at the sites i and j.

Unfortunately, neither an unified sign convention nor a unique definition for a HEISENBERG Hamiltonian exist. Therefore, prior to the discussion of the model itself, such definitions should be given. In this thesis, the following sign convention is adapted: if the antiparallel arrangement has lower energy, the exchange coupling is positive ($J_{ij} > 0$); in the opposite case, the exchange coupling is negative ($J_{ij} < 0$). The summation is done over pairs of spins, i.e. each pair of spins is counted once. In the following, only the $S = 1/2$ case, relevant for the present study, is discussed.

A generalized HEISENBERG model is given by the following Hamiltonian:

$$\hat{H}_{\text{HEISENBERG}} = \sum_{\langle ij \rangle} J_{ij}(\mathbf{S}_i \cdot \mathbf{S}_j), \text{ where } \mathbf{S}_i = 1/2\,\hat{\vec{\sigma}}_i = 1/2(\hat{\sigma}_x, \hat{\sigma}_y, \hat{\sigma}_z). \tag{4.32}$$

Although the HILBERT space of a HEISENBERG model is strongly reduced compared to a HUBBARD model, exactly solvable HEISENBERG models are also extremely scarce. In most cases, only approximate solutions, or solutions for largely simplified models, are computationally feasible. The particular method to solve a certain HEISENBERG model depends in the first place on the dimensionality of the model and the presence or absence of magnetic frustration. An overview of widely used present-day techniques is given in Chapter 5.

To complete this part, the widely used classical version of a HEISENBERG model should be mentioned. This approach utilizes the intimate relation between the SU(2) groups that describe spin operators, and the SO(3) groups describing rotations in 3D. In the latter case, the spin operators are replaced by real-space vectors $\vec{S} : \{\vec{S} \in \mathbb{R}^3, |\vec{S}| = 1\}$. This way, the energy of any spin configuration can be expressed in terms of angles between the respective spins:

---

[7] The notation "J_{ij}" is used to denote the exchange between the sites i and j. In the cases the sites are of no interest, a more general sign "J_i" is used.

$$\hat{E}^{\text{class.}}_{\text{Heisenberg}} = {}^1\!/_2 \sum_{i>j} J_{ij}(\vec{S}_i \cdot \vec{S}_j) = {}^1\!/_2 \sum_{i>j} J_{ij} \cos(\widehat{\vec{S}_i, \vec{S}_j}). \tag{4.33}$$

Apparently, for the $S = {}^1\!/_2$ case, strong quantum fluctuations are intrinsic. Thus, the classical approach provides too crude approximation for the quantum model. Still, numerous studies on the subject evidence that in many cases (for instance, in high magnetic fields), a classical model captures the essential physics correctly. Therefore, for any new Heisenberg model, a classical solution should be the first step to explore its phase space.

4.2.7 Ferromagnetic coupling

So far, the effective one-orbital approach (model approach) was discussed. By construction, this technique accounts only for the AFM exchange, since two electrons with the same spin can not occupy the same orbital, according to the Pauli principle. At present, there is an empirical evidence that the effective one-orbital approach correctly captures the leading mechanism of the AFM exchange coupling. However, in real magnetic insulators, the hopping process is more complicated and typically involves several ligand orbitals. In certain cases, different mechanisms give rise to sizable FM coupling, which can compensate or even overcome the AFM contribution (for the case of cuprates, this mechanism has been discussed in Sec. 2.2.2).

Extensive investigations of a huge family of magnetic insulators delivered a number of real materials with an FM leading exchange coupling. Moreover, even if all leading couplings are AFM, their values can be substantially smaller than estimates from the effective one-orbital approach, hinting at sizable FM contribution J_i^{FM} to the total exchange J_i.[8]

At present, there is no universal way to evaluate the FM contribution J_i^{FM}. However, microscopic magnetic modeling for strongly correlated insulators is typically done using spin-polarized DFT+U calculations. In the present work, only these methods are used. For the sake of completeness, alternative procedures are mentioned in Sec. 4.2.7.

DFT+U The underlying idea of the DFT+U methods is to calculate total energies for a series of magnetic supercells. These cells have the same symmetry, the same arrangement of atoms, and differ only by alignment of moments localized on magnetic atoms. Additional restriction arises from the limited performance of computational facilities, making calculations for large meshes not feasible. The empirical fact that for magnetic insulators even rather sparse $\vec{k}$-meshes still yield reasonable estimates for the leading couplings, largely remedies the situation.[9] The only prerequisite is that calculations should be performed for the same $\vec{k}$-mesh. Then, the difference in total energy originates solely from magnetic degrees of freedom, in particular, different collinear spin arrangements: the FM structure as well as ferrimagnetic and AFM ones. The resulting values of total energy can be mapped onto a classical HEISENBERG model. This way, J_i are evaluated as parameters of this classical model, and J_i^{FM} can be estimated by subtracting J_i^{AFM}, evaluated in the model approach, from J_i. For dozens of materials, independent experimental studies confirm the reliability of this approach, and the discrepancy for the values of J_i is typically lower than 10−15 % for leading couplings.

---

[8] J_i is the sum of the AFM and FM contributions $J_i = J_i^{\text{AFM}} + J_i^{\text{FM}}$.

[9] In contrast to metals, there is no $\vec{k}$-mesh-dependent change in occupation numbers.

The fundamental drawback of this method is its restriction to a given set of exchange couplings J_i. Moreover, this set is typically rather small: for N supercells, at best $N-1$ couplings can be evaluated. Therefore, it is crucial to know in advance which exchange couplings are relevant. A natural way is to use results of the model approach. In addition, short-range (<3 Å) couplings should be still taken into account in the DFT+U approach, even if the respective $t_{i,j}$ terms are small, since the resulting J_i^{FM} can be substantial. This way, a suitable set of supercells can be constructed.

If the original crystal structure does not provide a possibility to calculate all relevant terms, standard solutions are symmetry reduction and doubling of the unit cell. To check the results for consistency, it is reasonable to perform independent sets of calculations for supercells having different metrics and/or symmetry, and subsequently compare the resulting values of J_i.

It is important to discuss further limitations and drawbacks of the DFT+U method. As pointed out in Sec. 4.1.3, the exact value of U_d is not known. Therefore, the results of DFT+U calculations should be checked for consistency with respect to the U_d value. Second, in many cases the results of DFT+U calculations are strongly dependent on the DCC scheme. For complicated systems with multiple leading couplings, especially when both AFM and FM couplings are present, it is crucial to check the consistency of the results by applying different DCC schemes. Basically, the choice of a more appropriate DCC scheme and the value of U_d for any particular system should be carefully adjusted, since the optimal values depend not only on the nature of magnetic ions and ligands, but also geometry and topology the magnetic blocks. In Chapter 6, such adjustments are done for a series of cuprates with rather simple underlying magnetic models. Additional justification of the choice could be gained by comparing with available experimental data for the material under investigation, or structurally related materials.

DFT+U calculations for certain classes of real materials can be a more arduous task. Thus, if the magnetically active orbital has a character different from $3d_{x^2-y^2}$, or in the case of several different magnetically active orbitals (orbital order), the orbital occupations numbers yielded by DFT+U calculations, should be carefully inspected. Another recent example, a DFT+U study of non-collinear magnets revealed strongly nontrivial dependence of the canting angles on both U_d and J_d [141].

Alternative approaches As an alternative to the DFT+U methods, exchange integrals can be estimated as energy variation with respect to small rotations of magnetic moments from initially collinear configuration. The procedure is based on the ANDERSEN's local force theorem (LFT), stating that the total energy variation coincides with the sum of one-particle energy changes for the occupied states at the fixed GS potential [142]. This theorem can be extended for the spin-polarized case [143]. Then, considering a small rotation of spins i and j from their initially parallel mutual orientation, the GREEN function technique delivers an analytical expression for J_{ij} (Eq. 19 in Ref. 143):

$$J_{ij} = \frac{1}{4\pi} \int_{-\infty}^{\epsilon_{\mathrm{F}}} \mathrm{Im}(\Delta_i G_{i,j}^{\downarrow} \Delta_j G_{j,i}^{\uparrow})\, d\epsilon, \tag{4.34}$$

where

$$\Delta_i = H_i^{\uparrow} - H_i^{\downarrow} \qquad \text{and} \qquad G_{i,j}^{\sigma}(\epsilon) = \int_{\vec{k}} \frac{c_{i,\sigma} c_{j,\sigma}}{\epsilon - E_{\sigma}}\, d\vec{k}. \tag{4.35}$$

Despite its obvious success in understanding the magnetic properties of La_2CuO_4 [144], $LiCu_2O_2$ [145] and $SrCu_2(BO_3)_2$ [146], this calculational scheme is rarely used for magnetic insulators with localized magnets. Two apparent reasons are applicability of the well-justified DFT+U scheme and scarce implementations of the procedure from Ref. 143. In addition, comparisons for cuprate materials reveal only minor discrepancy between the results of the LFT-based procedure and DFT+U [147].

One of the major drawbacks of the DFT+U methods is the inappropriate description of covalency in transition metal compounds: the HUBBARD-terms are applied only to metal d-electrons, although the latter strongly hybridizes with ligand orbitals.[10] Therefore, a natural modification of the method is to reformulate the HUBBARD model in terms of WANNIER functions. This approach was developed in Ref. [145] and extended for the case of anisotropic exchange in Ref. [146]. The starting point of this approach is a planar configuration (all atoms lie in one plane) of magnetic plaquettes. In this case, the WANNIER functions can be constructed as a linear combination of the magnetic d orbital and the σ-bonded p-orbitals of the ligands. β, the contribution of the ligand orbital in the respective WANNIER function, plays a decisive role for the HUND's rule coupling. This parameter is directly related to magnetization on the ligand atoms. The intra-atomic exchange interaction of the ligand atom J_p^{Hund} can be estimated using DFT+U calculations. Then, the resulting $J_i^{\mathrm{FM}} \sim \beta^4 J_p^{\mathrm{Hund}}$. This method has been successfully applied to the archetype cuprates $LiCu_2O_2$ [145] and $SrCu_2(BO_3)_2$ [146]. Its main drawback, strongly limiting the range of its application, is the restriction to planar structural configurations.

---

[10] In the limit $U_d \to \infty$, the hybridization is reduced to zero.

Chapter 5

Simulations of a magnetic model

5.1 High-temperature series expansion

Temperature dependencies of magnetization (i.e. magnetic susceptibility χ) and heat capacity (i.e. specific heat C_p) are typically first experimental probes for the magnetic properties of a new magnetic compound. The correct interpretation of their results largely defines the strategy of further experimental investigation. It is therefore crucial to gain the maximal insight into the magnetism of a particular system by analyzing these thermodynamical dependencies.

As discussed in Sec. 3.2, $\chi(T)$ and $C_p(T)$ effectively probe the sample quality, disclose phase transitions and help to distinguish between gapped and gapless excitation spectra. In addition, for magnetic insulators with localized spins, the high-temperature region of the magnetic susceptibility obeys the CURIE-WEISS law, and the respective fitting of experimental data yields the overall energy scale of magnetic interactions and even indicates which couplings—AFM or FM—are dominant. However, resorting from such an averaged coupling to the values of individual exchange couplings is not straightforward. In contrast, the HTSE method gives access to accurate numerical estimates for the leading exchange couplings, provided that the relevant microscopic magnetic model is known. In this case, experimental thermodynamical measurements can be used to challenge and consequently refine the magnetic model.

In the following, HTSE for magnetic susceptibility are discussed. Although specific heat data can be in principle analyzed using exactly the same approach, reliable evaluation of magnetic contribution from experimental specific heat data is feasible only for systems with small (below 5–10 K) exchange couplings. None of the systems discussed in this work satisfy this criterion.

In the following, the $S = 1/2$ HEISENBERG model on an arbitrary lattice is considered. Assuming that all spins have equivalent environment, i.e. the set of relevant couplings J_{ij} is exactly the same for every spin in the lattice (this criterion is fulfilled for most of archetypical topologies), the reduced magnetic susceptibility $\chi^* \equiv \max\{|J_{ij}|\}\, N^{-1} g^{-2} \mu_{\mathrm{B}}^{-2}\, \chi$ can be expressed in powers of the reciprocal reduced temperature $\beta \equiv 1/t^{*} = \max\{|J_{ij}|\}\, k_{\mathrm{B}}^{-1}\, T^{-1}$ [87]:

$$\frac{1}{4\chi^{*}} = \sum_{n=0}^{N} d_n \beta^{n-1}, \tag{5.1}$$

where N is the order of the expansion. For a finite N, HTSE accounts for the experimental $\chi(T)$ data above T_{min}, which meaning is discussed below. The first two d_n terms are universal [87]:

$$d_0 = 1 \qquad d_1 = \frac{1}{4\max\{|J_{ij}|\}} \sum_{i>j} J_{ij}. \tag{5.2}$$

It can be shown [87] that the Curie-Weiss temperature θ is given by the universal expression

$$\theta = \frac{1}{4} \sum_{i>j} J_{ij}/k_{\mathrm{B}}. \tag{5.3}$$

Therefore, the Curie-Weiss fit is nothing but an HTSE in first order. Low-order expansions, such as the Curie-Weiss fit, diverge at rather high temperatures $T > \max\{|J_{ij}|\}/k_{\mathrm{B}}$. Switching to higher-order expansion improves the convergence, and for particular models yields an excellent description of $\chi(T)$ down to surprisingly low temperatures T $\max\{|J_{ij}|\}/k_{\mathrm{B}}$ [148].

Expansions in higher order are specific for a given model,[1] thus the particular spin lattice topology should be considered. At present, this work has been accomplished for archetype $S = 1/2$ Heisenberg lattices. In particular, the following 1D lattices were considered: a Heisenberg chain with alternating NN couplings (AFM and FM [149] as well as both AFM [87]), J_1–J_2 (zigzag) chain with AFM couplings [148], a distorted diamond chain [150], as well as two- and three-leg spin ladders [151]. Within the class of 2D spin lattices, series expansions are available for the frustrated square lattice [152], the kagome lattice [153], and the Shastry-Sutherland lattice [154]. For most of these topologies, HTSE for specific heat have been computed as well [87, 148, 151, 152, 155].

The only nontrivial part of the fitting procedure is the estimation of T_{min}, which sets the lower boundary of the high-temperature window ($T \geq T_{\mathrm{min}}$) used for the fit. The general strategy reads: T_{min} should be as low as possible provided that the HTSE is still converged. In most cases, estimates for the optimal T_{min} are given together with the respective HTSE coefficients. If such estimates are not available, the convergence can be checked by examination of the relative weight of the highest-order contribution to the HTSE at T_{min}.

HTSEs are especially powerful if the applicability of alternative techniques is strongly limited, i.e. for 2D or 3D frustrated models. For instance, HTSE results were an integral part of recent advances in understanding the magnetism of the $S = 1/2$ frustrated square lattice systems $AA'VO(PO_4)_2$ [91].

---

[1] In addition to the terms given by Eq. 5.2, $d_3 = \frac{1}{24\max\{|J_{ij}|\}^3} \quad {}_{j} J_{ij}^3$ for the class of non-frustrated models [87].

Besides its apparent limitation to a particular magnetic model, the HTSE method has several peculiarities which may impede an accurate estimation of exchange couplings or even lead to incorrect results. First, as already mentioned, the minimal fitting temperature should be carefully estimated with respect to convergence of the series. Second, HTSE is insecure against multiple solutions of a given model. Such ambiguity follows from the internal symmetry of the model itself. For instance, HTSE for the frustrated square lattice model always yields two solutions that belong to different regions of the phase diagram (see Ref. 156 for an instructive example). Another example, the frustrated spin chain model, yields very similar $\chi(T)$ for essentially different values of J_2/J_1. To distinguish between these solutions, HTSE should be combined with alternative numerical or experimental methods.

5.2 Exact diagonalization

Due to the rapid development of efficient computational facilities, exact diagonalization of a Hamiltonian matrix is a popular technique to solve spin Hamiltonians since about two decades. Its main features are universality and accuracy: this method yields exact results and at the same time imposes no limitations on the dimensionality (D) of a model. Quite remarkably, exact diagonalization is one of the few methods that can treat frustrated magnetic models. The unbeatable accuracy of the results yielded by exact diagonalization make them an excellent benchmark for other simulation techniques.

The only fundamental limitation of the method is its restriction to finite models with N constituent spins. However, limited performance of computational resources sets additional restrictions. Practically, only systems with low N and S, and consequently, only $D \leq 2$ cases are numerically feasible. Problems arising from extrapolation to the thermodynamic limit $N \longrightarrow \infty$, the underlying reason for high computational costs of the method together with typical present-day bounds for N will be discussed below.

For many problems related to the GS of a model and its lowest lying excitations, calculation of the full spectrum is not necessary. Instead, it is enough to restrict a calculation to a particular sector of the Hamiltonian and evaluate only its extreme eigenvalues using efficient diagonalization algorithms. For spin models, the LANCZOS algorithm, described in Sec. 5.2, is a standard solution. This way, models with larger N can be considered, which is particularly important for the $D = 2$ case.

Sizable finite-size effects are a major problem of exact diagonalization as a method to solve spin models. They are an inevitable consequence of sizable computational costs of the diagonalization procedure, leading to a rather low number of spins in computationally feasible models. Despite the ongoing development of faster computing facilities, the exponential growth of the matrix size (in response to a linear increase in N) will likely inhibit calculations for larger systems, at least in the near future. A real breakthrough toward much larger N could be expected only after bringing quantum computers into service.

Exact diagonalization represents the most straightforward and fully unbiased way to solve a Heisenberg model: namely, to construct a Hamiltonian matrix and evaluate all its eigenvectors and eigenvalues exactly (eigendecomposition). This approach apparently works only if the respective matrix is finite, hence the number of spins (N) in the model should be also finite ($D=0$). However, the magnetism of bulk materials is generally accounted for by models having larger dimensionality ($D > 0$), and consequently, an infinite number of spins $N = \infty$ (Fig. 5.1, left).

The mapping between infinite (Fig. 5.1, left) and finite systems is realized via boundary conditions. Open boundary conditions imply that a cluster of N coupled spins is simply a cut-out part of the respective infinite lattice, and only the couplings between the N spins are preserved (Fig. 5.1, middle). The main drawback of this approach is the resulting difference in the coordination numbers, i.e. the number of exchange couplings per site, for the boundary and inner spins. To remedy this effect, periodic boundary conditions are applied. More specifically, the boundary spins are coupled to each other in order to keep their coordination number and topology same as in the infinite model. This way, a cluster is transformed into a finite lattice (Fig. 5.1, right), which is generally a more appropriate model of an infinite lattice. It is worth to note that if the type of boundary conditions is not explicitly specified, periodic boundary conditions are presumed for $D > 0$ spin models.

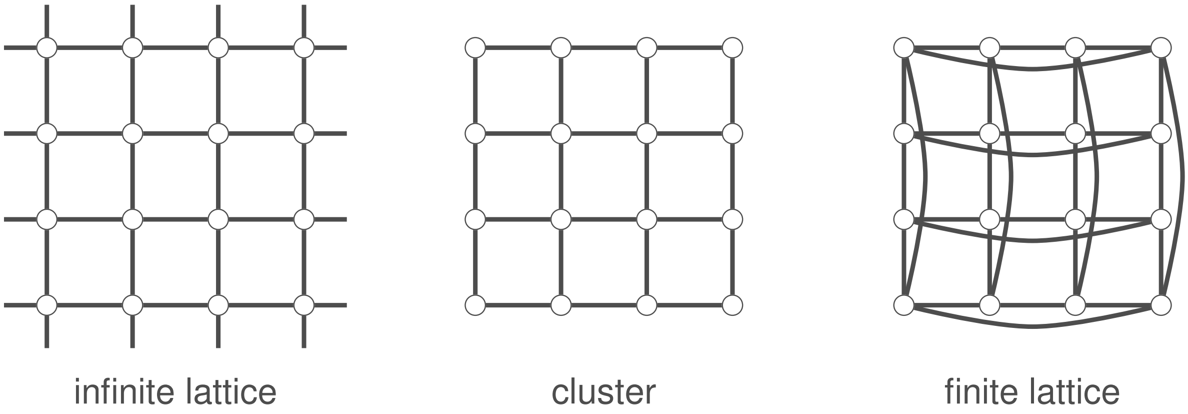

Figure 5.1: Square lattice: difference between an infinite lattice, an $N = 16$ cluster (open boundary conditions) and an $N = 16$ finite lattice (periodic boundary conditions). Spins and exchange couplings are denoted by circles and lines, respectively.

The price to pay for retaining the correct coordination number is the reduction of the effective cluster size. In particular, the maximal separation between two spins on a finite lattice is strongly reduced compared to the cluster comprising the same number of spins N. This can be illustrated by the example of a Heisenberg chain (Fig. 5.2): for open boundary conditions, the maximal separation corresponds to the distance between the two boundary spins and amounts to $N-1$. In the case of periodic boundary conditions, the former boundary spins become coupled, and the maximal separation is thus reduced down to $N/2$ and $(N-1)/2$ for even and odd N, respectively.

Figure 5.2: Difference in the maximal separation between the spins of a HEISENBERG chain for the cases of open (top) and periodic (bottom) boundary conditions. Spins and exchange couplings are denoted by circles and lines, respectively.

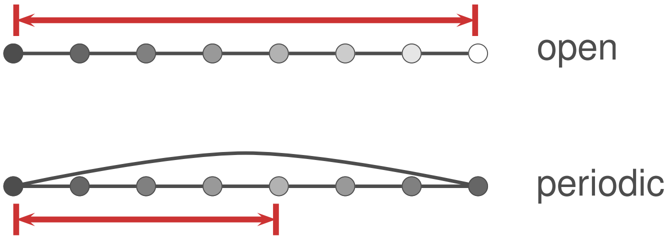

For certain problems, the discrete k-grid provided by the periodic boundary conditions is inappropriate. In particular, the large gap between $|\vec{k}| = 0$ and the lowest nonzero $|\vec{k}|$ may conceal important physical information. To vary the shift of the $\vec{k}$-grid with respect to $|\vec{k}| = 0$, twisted boundary conditions can be applied. In this approach, the boundary spins are rotated with respect to the quantization axis. In the resulting Hamiltonian, the SU(2) invariance is lost for all nonzero momenta, but the commutation with total S^z is preserved.

So far, the mapping between an infinite model and its finite counterparts, clusters and finite lattices, is clarified. The next question is whether a particular finite lattice provides an adequate description for the physics of an infinite model. It is intuitively clear that if the correlations between the constituent spins are short-range, the results for a finite lattice are closer to the infinite model. And vice versa: long-range spin correlations give rise to discrepancies of the finite lattice results. To put these considerations on a quantitative footing, the correlation length ξ of the infinite model and the transversal size of the finite lattice d, can be introduced. If the spin correlation length ξ for any direction of the finite lattice is smaller than the half-length $d/2$ of the finite lattice (Fig. 5.3, right), exact diagonalization provides an excellent description for the thermodynamic limit $N \to \infty$. On the contrary, $\xi > d/2$ gives rise to discrepancies between the exact diagonalization for a finite lattice (cluster) and an infinite system (Fig. 5.3, right).

A direct connection between the correlation length ξ and the discrepancy between the finite lattice and the respective infinite model, allows to infer two important remarks. First, exact diagonalization is expected to work well for models with a short correlation length, e.g. particular geometrically frustrated systems. Second, since spin correlations decay at elevated temperatures, exact diagonalization provides particularly accurate results in the high-temperature limit.

Extending the exact diagonalization results to the thermodynamic limit is at best tricky. The issue of a finite spin gap in the $S = 1/2$ HEISENBERG kagome model—whether it survives in the thermodynamic limit $N \to \infty$—is a remarkable example evidencing the complexity of such extrapolations. Still, in many cases the extrapolation to infinite models is robust as confirmed by using alternative techniques. One of the standard extrapolation techniques is the $1/N$ expansion [157]. However, the straightforward application of the $1/N$ rules often leads to insufficiently precise results, since small sizes of finite lattices typically used in exact diagonalization impede the asymptotic behavior. Thus, additional higher-order terms should

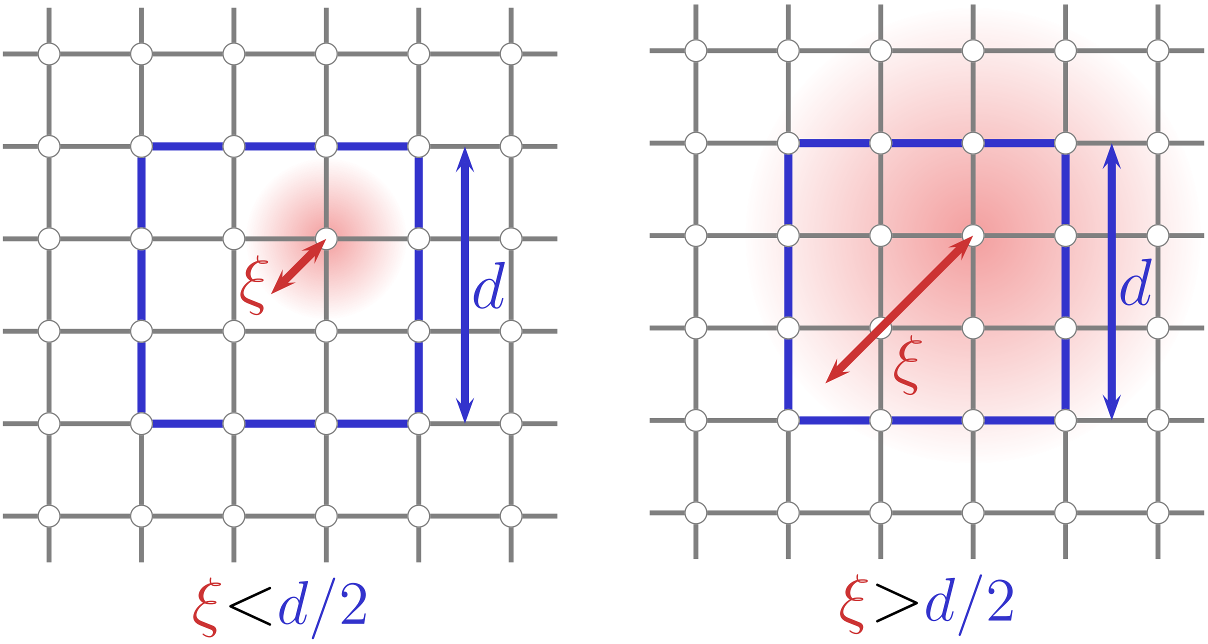

Figure 5.3: The correlation length ξ for finite lattices $d \times d$. For $\xi < d/2$, the physics of the finite lattice is in accord with the physics of the infinite system. On the contrary, in the case of $\xi > d/2$ the results for the finite lattice deviate from the respective infinite model.

be introduced [94]. Another example is the criterion for long-range magnetic ordering of an infinite model, based on the observation of the so-called Pisa tower of quasi-degenerate joint states (for finite lattices). Here, the normalized energy E/N is calculated for different S^z sectors. If the GS for each sector S^z is well-separated from the excited states, while E/N for the GS exhibits a linear dependence on $S^z(S^z+1)$, such situation is a fingerprint of long-range magnetic ordering of the respective infinite model [94].

Exact diagonalization of a Hamiltonian matrix yields all its eigenvalues and eigenvectors and therefore provides a *complete* description for the finite system under consideration. If this method were applicable for all models, there would have been no need for alternative approaches. However, for models with larger spins and/or larger number of spins, eigendecomposition of the respective Hamiltonian becomes computationally expensive: a HEISENBERG model for N spins $S = 1/2$ leads to a Hamiltonian matrix $H \in \mathbb{C}^{2^N \times 2^N}$. The exponential growth of the matrix dimensionality constitutes the basic drawback of the exact diagonalization as a method to solve quantum spin models. In particular, the “exponential wall” limits the feasible number of spins N in a model to approximately two dozens. There is one particularly spectacular example showing the power of the exponential wall. The first application of exact diagonalization to spin models was the solution of the HEISENBERG chain by BONNER and FISHER in 1964. The maximal finite lattice amounted to $N = 12$ spins $S = 1/2$ [158]. At present, almost a half-century later, the feasible size of the model is only doubled ($N = 24$).[2]

---

[2] The famous MOORE’s law states that the number of transistors per integrated circuit doubles every two years [159]. Assuming the same scaling for the calculational time, the improvement of computational facilities

With the development of alternative methods, such as quantum Monte Carlo (Sec. 5.3), it became eventually evident that for many models, except 1D, full diagonalization in general does not account for thermodynamics at even moderate temperatures $T \sim J$. The computational limitation to small N is apparently too tight for the majority of realistic models, and calls for optimization of the procedure. Since many problems are focused on the low-temperature limit, the knowledge of the full spectrum is not a prerequisite. Instead, it is enough to address its low-energy sector or, ultimately, only the GS ($T = 0$). Therefore, it is enough to calculate few lowest eigenvalues of the reduced Hamiltonian matrix. This can be done, for instance, within the numerically efficient Lanczos algorithm, yielding enormous reduction of the CPU time with respect to full diagonalization.

To illustrate the gain in performance, the present-day limits for full and Lanczos diagonalization of $S = 1/2$ models can be compared. While modern full diagonalization codes and computational facilities are limited to $N = 24$ spins $S = 1/2$ [160], Lanczos algorithm makes diagonalization of finite lattices up to $N = 42$ sites feasible [161]. Additional performance can be gained from further restrictions: for instance, in the high magnetic field limit (the sector of large S^z), a square lattice of $N = 64$ spins can be treated [162].

Lanczos diagonalization

In 1950, Lanczos presented an iterative procedure to obtain the extreme eigenvalues for Hermitian matrices [163]. The basic idea of this procedure is to construct a special basis space, in which the matrix A is transformed into a tridiagonal form (T-matrix). Each new state u_j of this basis is constructed by repeatedly applying the A-matrix to an initial arbitrary state $u_1 : \;\; u_1 \;\; = 1$ and subsequently orthogonalized with respect to other states $u_i : i \in [1, j-1]$. A step-by-step description of the algorithm is given in Sec. A1.

The Lanczos procedure is especially efficient for sparse matrices, hence it is intensively used for solving model Hamiltonians (see, e.g. the review for $S = 1/2$ gapped systems in Ref. 164). At present, finite lattices containing about $N \quad 40$ spins $S = 1/2$ can be treated. The values of N differ for particular spin models, since the symmetry of the finite lattice used for diagonalization should be compatible with the symmetry of the respective infinite lattice. Therefore, the maximal size of a finite lattice used for diagonalization typically varies between $N = 36$ for the kagome lattice (see Ref. 165 and references therein) and $N = 42$ for the star lattice [161].

A specific drawback of the Lanczos algorithm is the emergence of so-called "spurious states", caused by finite precision of numerical operations. These states can be detected by using additional heuristic algorithms [166].

A repeated application of the Lanczos algorithm to evaluate the low-energy eigenvalues,

---

required to advance from $N = 12$ to $N = 24$ should take approximately $2\log_2[(2^{24})^3/(2^{12})^3] = 72$ years, which is in good agreement with the facts. Thus, for a $N = 50$ sites problem, one has to take some $2\log_2[(2^{50})^3/(2^{24})^3] = 156$ years in consideration.

yields a rather accurate approximation for the low-temperature properties of the system. This method, commonly regarded as the "finite-temperature LANCZOS method", has been successfully applied for certain spin models, e.g. the frustrated square lattice [167]. Unfortunately, the related loss of performance compared to the standard LANCZOS procedure strongly reduces its advantage over the full diagonalization.

5.3 Quantum Monte Carlo

As discussed in the previous section, exact diagonalization can be applied only to a rather small finite systems. The general idea of QMC is to rewrite the partition function Z in a form that would allow to treat it by powerful stochastic algorithms. At present, most popular algorithms are the path-integral formulation and the stochastic series expansion.

In order to map a quantum model onto onto a classical statistical problem, a weight function W is used. Quantities simulated by stochastic methods contain the sums of W as well as the sum of the products of W and estimators of the measured quantity. This scheme can be applied only if W is positive definite. In the opposite case, the absolute value of W should be used. As a result, the average sign enters the expression for the simulated quantity. Typically, increase of the system size and/or decrease of temperature lead to a drastic decrease of the average sign and consequently, large statistical errors. This is known as the "sign problem" [168].

For HEISENBERG models, the sign problem arises only if the respective spin lattice is not bipartite. This can be understood as follows. Flipping two AFM coupled spins gives rise to a minus sign in the path integral. Thus, if the total number of spin flips is odd, the overall sign will be negative [168]. In fact, this scenario corresponds to a magnetically frustrated model. This is easy to illustrate, since such spin models feature closed loops formed an odd number of AFM couplings and an arbitrary number (including zero) of FM couplings.

QMC simulations provide excellent performance even for rather large systems and practically eliminate the influence of finite size effects. However, they are not applicable for the strict GS, since the computational time steeply increases for $T \to 0$. QMC simulations are extensively used for comparisons between the microscopic magnetic models and experiments discussed in Chapter 6.

5.4 Density-matrix renormalization group

Although DMRG is a relatively recent development [169], it is one of the most popular simulation techniques. Its obvious advantages are excellent performance and accuracy. Unlike QMC, DMRG can be applied to frustrated systems. Moreover, different algorithms allow to treat finite as well as infinite systems [170]. However, this method has a serious limitation: its application is restricted to 1D systems.[3] Since non-frustrated 1D models can be efficiently treated by modern QMC codes (excluding the precise $T = 0$ case), the primary playground of DMRG are frustrated 1D systems. Since none of systems discussed in the present work can be referred to this group, DMRG is not used here. Nevertheless, the basics of DMRG are briefly discussed for the sake of completeness.

DMRG inherits the basic ideas of the RG approach [173]. In particular, the system is subdivided into finite blocks. For the two neighboring blocks, the problem is solved exactly by diagonalization. Then, according to some criterion, the basis is truncated and the block is doubled, to complete a step of the iterative procedure. For the truncation criterion, RG utilizes energy of a certain state: this way, only the low-energy states are kept. Such approach works fine if the interactions between the blocks decays, as for instance, the KONDO model [173]. However, this is not the case for spin Hamiltonians [170].

DMRG employs a different strategy for the truncation [169]. First, the problem is solved not for a single block, but for a set of several adjacent blocks—a superblock. Second, the density matrix of the superblock is computed. The largest eigenstates of this density matrix are the states kept. This way, the method yields excellent performance for 1D problems at $T = 0$.

Extensions of the DMRG method, in particular, transfer-matrix DMRG (TMRG) [174–176], can be used to address finite temperature properties. At present, it is the method of choice for frustrated 1D systems, such as, e.g. the frustrated chain model [177, 178].

5.5 Bridge to experiments

Simulations yield quantities that are typically referred as “reduced”: reduced magnetic susceptibility, reduced magnetization etc. A comparison between the simulated quantities and the experimental data is possible only after a proper scaling. The simplest case is the multiplication of the simulated quantity by some constant, e.g. the leading exchange coupling J_i. In general, the procedure is more complicated, and often requires the fitting of the simulated dependence to the respective experimental data by varying several parameters. In this section, the general strategies of such fitting are discussed for magnetic susceptibility and magnetization data.

Besides, the simulations of finite systems inevitably suffer from finite-size effects. For certain quantities, they largely influence the results. It is the case, e.g. for the evaluation of the magnetic ordering temperature and the order parameter (Sec 5.5.3).

---

[3] Very recent developments give hope for successful application of DMRG algorithms to 2D models, such as the kagome lattice [171] of the frustrated square lattice [172] model.

5.5.1 Magnetic susceptibility

Fitting the experimental magnetic susceptibility data with a simulated dependence is the essential part of the computational approach used in this work. For any system which magnetic properties are being investigated, magnetic susceptibility is the first probe. Therefore, $\chi(T)$ data for a system under investigation are typically common, and in many cases, the only experimental information on the magnetism. Disagreements between a theoretical model and the experimental $\chi(T)$ data should be carefully investigated. If no clear reason for the discrepancy can be found,[4] the theoretical model is likely not sound, and should be either modified or discarded.

Simulations yield the reduced magnetic susceptibility χ^* as a function of reduced temperature T^* that are related to the experimental χ and T:

$$\chi^* = \chi \left(\frac{k_\mathrm{B} \max\{|J_i|\}}{N g^2 \mu_\mathrm{B}^2} \right) \qquad T^* = \frac{T}{k_\mathrm{B} \max\{|J_i|\}}. \tag{5.4}$$

If the values of J_i and g are known, for instance, from DFT calculations and ESR, respectively, the scaling of the simulated curve is straightforward. Seemingly simple, such scaling typically yields a rather poor agreement between experiment and theory. First, error bars for the J_i values from DFT are typically on the order of 10 %. Such differences are clearly visible in the $\chi(T)$ plots. Second, ESR data are not always available, and a simple guess of the g value (for instance, based on the measurements for related systems) may result in a similar inaccuracy (10–15 %). Finally, material samples contain a certain amount of defects and impurities, not accounted for by simulations of simple magnetic models. Therefore, an alternative approach should be used.

It is not surprising that fitting the theoretical curve to the experimental one provides a much better agreement between the two than the simple scaling discussed before. Numerous examples of a successful application of the fitting procedure described below, provide an empirical evidence for the reliability of this approach.

The first problem concerns the transformations of χ^* into χ and T^* into T that both are governed by the overall energy scale $\max\{|J_i|\} / k_\mathrm{B}$, but in different ways, as follows from Eq. 5.4. If χ^* had been an analytical function of T^*, this would have caused no complications. However, both $\chi^*(T^*)$ and $\chi(T)$ are discrete and finite sets. The proposed solution to this problem is fitting the $\chi^*(T^*)$ by a rational function using Padé approximants a_i and b_j:

$$\chi^*(T^*) = \frac{\sum_{i=0}^{I} (T^*)^i a_i}{1 + \sum_{j=1}^{J} (T^*)^j b_i} \tag{5.5}$$

---

[4] For instance, the discrepancy between the magnetic susceptibility curve for $CuSe_2O_5$ in Fig. 3 of Ref. 179 and the theoretical 1D chain model is related to the sample quality (the magnetic properties of $CuSe_2O_5$ are extensively discussed in Sec. 6.1.1). However, discrepancies can have completely different origin. Thus, CuNCN also features a quasi-1D magnetic model [75], while the peculiar experimental dependence of its magnetic susceptibility (Fig. 4 in Ref. 74), which seemingly contrasts with the proposed magnetic model, originates from the unusually large energy scale set by the leading magnetic exchange coupling J_1 2500 K [75].

The number of PADÉ approximants (I and J) should be minimal provided that discrepancies between the two curves are negligibly small. This way, a continuous function that approximates $\chi^*(T^*)$ is evaluated.

The next problem in the fitting are extrinsic contributions to the experimental $\chi(T)$: χ_0 and C_{imp}/T (their nature has been discussed in Sec. 3.2.1). To account for these effects, the respective terms should be included into the fit. Finally, the following expression is fitted:

$$\chi(T) = \frac{N_{\text{A}}\, g^2\, \mu_{\text{B}}^2}{\max\{|J_{ij}|\}\, k_{\text{B}}}\, \chi^* \quad \frac{T}{k_{\text{B}} \max\{|J_{ij}|\}} \quad + \frac{C_{\text{imp}}}{T} + \chi_0, \tag{5.6}$$

If additional experimental information is available, this expression can be modified. For instance, the g-factor value can be adopted from ESR measurements and kept constant during the fitting. For high-quality samples, especially single crystals, the impurity term C_{imp}/T can be omitted. Special attention should be paid to magnetic transitions: while some simulation methods, e.g. QMC, can account for 3D magnetic ordering (provided that the respective magnetic model is 3D), ED results typically lack any transitions, mostly because of the reduced dimensionality of the model ($D < 3$). Moreover, the region of the magnetically ordered phase can be largely influenced by anisotropic effects, neglected in HEISENBERG models.[5] Therefore, a typical fitting temperature range should lie above the transition temperature.

5.5.2 Magnetization

The reduced magnetic field h can be converted to the experimentally measured field H:

$$H = \frac{k_{\text{B}} \max\{|J_{ij}|\}}{g\, \mu_{\text{B}}} \quad h. \tag{5.7}$$

Therefore, a fit of $M^*_{\text{sat}}(h)$ yields an optimal value of $\max\{|J_i|\}/g$ that can be compared to the estimates based on other techniques (e.g. $\chi(T)$ data).

Simulations yield magnetization in the units that are related to the saturation magnetization M^*_{sat}. Measurements in static field yield magnetization in absolute units, while the value M_{sat} for one mole of $S = 1/2$ amounts to $N_{\text{A}}\, \mu_{\text{B}} \quad 5.585$ emu. Pulsed field measurements yield typically unscaled data (Sec. 3.3). In the case the saturation field is small and can be reached experimentally, the scaling is straightforward. However, for most systems, saturation fields largely exceed the experimentally accessible range. An alternative possibility is to scale the pulsed field data using a lab measurement for the same material as a reference. However, this procedure is often impeded by the narrowness of the field range used for the scaling (thus insufficient statistics). In this case, the only option is to scale M^* to get a best fit to alternative experimental data. Apparently, this scaling factor is an arbitrary number which depends neither on $\max\{|J_i|\}$, nor on g.

---

[5] This problem is not related to the computational method, but rather results from a substantial change on the model level.

5.5.3 LRMO temperature and order parameter

As follows from the Mermin-Wagner theorem [32], a 3D magnetic coupling is a prerequisite for an LRMO transition. Therefore, for a 3D model, magnetic ordering transition can be simply traced, e.g. by a kink in the temperature dependence of magnetic susceptibility.

Among the simulation methods discussed, only QMC (Sec. 5.3) is capable of handling such models.[6] Still, magnetic ordering for 2D models can be studied by calculating $\langle m_s^4\rangle - \langle m_s^2\rangle^2$, called the Binder ratio of staggered magnetization m_s, for different finite lattice sizes N. The intersection of the $\left[\langle m^4\rangle - \langle m^2\rangle^2\right](T)$ curves calculated for different N can be taken as an accurate estimate for the magnetic transition temperature [180]. In an alternative approach, the spin stiffness ρ_s defined as the second derivative of the GS energy with respect to infinitesimal spin tilt, is calculated for different finite lattice sizes N. Here, the ordered temperature is estimated as the intersection of the $\rho_s N(T)$ curves for different N. Instructive examples can be found in Refs. 181 and 182.

The main effect of quantum fluctuations in the magnetically ordered GS is the reduction of the order parameter compared to its classical value. In the literature, several definitions of the order parameter can be found. According to Ref. 94, a universal definition can be used:

$$m = \frac{1}{N}\left(\sum_{i,j}^{N} |\langle \mathbf{S}_i \cdot \mathbf{S}_j \rangle|\right)^{1/2}. \tag{5.8}$$

Alternatively, the order parameter can be defined in terms of the structure factor $S(\vec{q})$:

$$m(\vec{q}) = \sqrt{\frac{3S(\vec{q})}{N}}; \qquad S(\vec{q}) = \frac{1}{N}\left(\sum_{i,j}^{N} \exp\{i\vec{q}\cdot(\vec{R}_i - \vec{R}_j)\}\langle \mathbf{S}_i \cdot \mathbf{S}_j\rangle\right). \tag{5.9}$$

The finite size scaling of $m(\vec{q},N)$ is discussed in [183]. The essential result of this study is that the $1/N$ expansion for the structure factor[7] is not accurate enough, and its extended version should be used instead:

$$m(\vec{q}) = \sqrt{\frac{3\cdot S(\vec{q})}{N} - \frac{m_1}{\sqrt{N}} - \frac{m_2}{N} - \frac{m_3}{\sqrt{N^3}}}. \tag{5.10}$$

In Sec. 6.3, this scaling scheme is applied to estimate the order parameter of dioptase $Cu_6Si_6O_{18}{\cdot}6H_2O$.

---

[6] As discussed in Sec. 5.2, no fundamental limitations preclude from applying ED to 3D models. It is the low performance ED that sets the practical limitation to $D \leq 2$.

[7] $\vec{q}$ in $S(\vec{q})$ is the propagation vector of the magnetically ordered structure.

Chapter 6

Model spin systems: challenging the computational approach

6.1 Uniform chains

The uniform $S = 1/2$ Heisenberg chain Hamiltonian is the simplest isotropic model which describes an infinite number of $S = 1/2$ spins, coupled to the two NNs each. Since all the couplings in this model are equivalent, the only model parameter is the NN coupling J_1. The magnetic GS has been evaluated by Bethe [184].[1] The magnetic excitation spectrum is continuous, and the spin correlations $\langle \mathbf{S}_0 \cdot \mathbf{S}_\mathrm{i} \rangle$ in the GS exhibit a power-law decay upon a linear increase in i [185, 186]. The elementary excitations are $S = 1/2$ spinons that can be created in pairs only [187].

Purely 1D systems[2] exhibit neither FM nor AFM order at finite temperature ($T > 0$), as proven by Mermin and Wagner [32]. Moreover, in 1D, strong quantum fluctuations impede LRMO even at $T = 0$ [188]. However, there is an empirical evidence that despite strong quantum fluctuations leading to $T_\mathrm{N} \quad J_1$, most of the real material realizations of this model exhibit AF LRMO. This seeming discrepancy is readily resolved recalling that LRMO is driven by interchain couplings, intrinsic for real materials that form a 3D crystal structure. However, the ordered local magnetic moment (order parameter) in such quasi-1D systems is strongly reduced with respect to the classical value for $S = 1/2$ ($1\,\mu_\mathrm{B}$), which complicates its experimental observation.

Finite-temperature properties of $S = 1/2$ Heisenberg chains, such as $\chi(T)$ [76, 87] and $C_\mathrm{magn}(T)$[87], as well as the magnetization process [189] are extensively studied theoretically. Therefore, the model assignment can be challenged by rather simple experiments that in many cases provide an accurate estimate for the exchange coupling J_1, e.g. from T_max at which the magnetic susceptibility exhibits a broad maximum, or the saturation field (the estimates are given below). In addition, the $\chi(T_{\max})T_{\max}$ product can be used to address the validity of the 1D NN chain model for a certain system, i.e. verify the model assignment [87].

---

[1] The GS of a NN chain is a scarce example of an exactly solvable Heisenberg model.

[2] "1D", "2D", and "3D" refer to the spatial dimensionality of the spin lattice, and should not be confused with the number of independent spin components (three in the Heisenberg model).

The lowest possible number of free parameters (one) and thorough theoretical understanding of the model make HEISENBERG chain compounds excellent reference model systems that provide multiple possibilities for a direct comparison between the experimentally observed quantity and its theoretical prediction. At present, a number of real material realizations of the $S = 1/2$ HEISENBERG chain model are known, the most studied are $KCuF_3$, $BaCu_2Si_2O_7$, Sr_2CuO_3, and Cu benzoate. The key results for these systems are summarized below.

$KCuF_3$ has a perovskite-type crystal structure [190]. The magnetic GS is AFM, with $T_N = 39$ K and the ordered moment of 0.5 μ_B per Cu atom [191]. The coupling J_1 amounts to ∼400 K, largely exceeding the leading interchain coupling of about −20 K [192]. Below ∼800 K the system is orbitally ordered [193, 194]. The nature of the orbital order is still controversially debated, in particular, whether the electronic (KUGEL–KHOMSKII) or the structural (JAHN–TELLER) mechanism plays a leading role [55, 56, 58, 59, 195, 196]. The orbital order drastically affects the magnetic properties and stabilizes a 1D magnetic coupling regime, as confirmed experimentally [78].

Extensive INS studies [192, 192, 197–201],[3] revealed pronounced 1D features in the magnetic excitation spectrum, such as unbound spinons [198] and a peculiar longitudinal mode [201]. However, further experimental investigation of this system disclosed several unusual features that could not be accounted for by the HEISENBERG chain model. For instance, the ESR data [202] could be interpreted only by considering the anisotropy of the exchange couplings, and in addition, a recent study disclosed their dynamical nature [203]. Furthermore, there are experimental signatures for a sizable coupling between spin and orbital degrees of freedom [193, 194]. Such complexity of $KCuF_3$ renders it as a very interesting system, but at the same time discredits it as a good realization of the $S = 1/2$ HEISENBERG chain model.

Another candidate model system, the pyrosilicate $BaCu_2Si_2O_7$, contains corner-sharing chains of CuO_4 plaquettes. The intrachain exchange J_1 amounts to 280 K, while the interchain coupling is about 5 K [204, 205]. The system exhibits a long-range AFM ordering at 9 K with the strongly reduced magnetic moment of 0.12 μ_B per Cu atom [204, 206]. The excitation spectrum has been extensively studied by INS [204, 206–209], and the results in general conform to the $S = 1/2$ HEISENBERG chain model. However, in magnetic field, $BaCu_2Si_2O_7$ exhibits a fascinating variety of phases and multiple spin-flop transitions, evidencing a substantial role of anisotropic effects [210–213].

The other two candidate materials, Sr_2CuO_3 and Cu benzoate, exhibit a variety of unusual features. In particular, charge-transfer excitations [214], ultrafast nonlinear optical response [215] and anomalies in the inelastic X-ray scattering [216] disclose a quite involved electronic structure for Sr_2CuO_3, while a field-induced gap [217] originating from the Dzyaloshinskii-Moriya interactions [218] reveals a more complex magnetic coupling in Cu benzoate.

---

[3] Noteworthy, the investigation of $KCuF_3$ was accompanied by an active development of INS as an experimental technique to study magnetism on a microscopic level. One can probably say that the studies of $KCuF_3$ largely contributed to the rise of INS as a method.

For the majority of candidate materials, a comprehensive analysis based on modern experimental as well as theoretical techniques, unravels a more complicated nature of their magnetic properties. Therefore, it is crucial to develop of a reliable method capable of disclosing this complexity. To be more precise, such method should account for the *individuality* of a certain real material system.

A special feature of quasi-1D systems is the presence of only one leading coupling J_1, which value can be precisely evaluated from the experiments. In particular, the $T_{\max}$ position of the broad maximum in the magnetic susceptibility readily yields the value of J_1:

$$J_1 \qquad 1.56\,T_{\max}. \tag{6.1}$$

For the systems with small J_1, the $\chi(T)$ maximum is often concealed by the impurity and/or defect contribution (Sec. 3.2.1). However, the small energy scale of the exchange couplings is advantageous for magnetization studies, since the saturation field H_{sat} is within the reach of pulsed-field measurements, or even in steady fields using a standard lab equipment. In this case, J_1 can be estimated via the saturation field H_{sat}:

$$J_1 \qquad 0.336\,g\,H_{\mathrm{sat}}. \tag{6.2}$$

Since J_1 can be precisely estimated from the experiments, there is typically no need to evaluate J_1 from DFT calculations. Instead, quasi-1D systems can be used for a fine tuning of the U_d parameter in the DFT+U methods, i.e. picking an optimal value of U_d, which yields the same J_1 as in the experiments. After such tuning is performed, DFT calculations become a powerful tool to evaluate the leading interchain couplings. Since these couplings are much smaller than J_1, their experimental evaluation is very challenging. However, they are relevant for the LRMO temperature and the structure of the magnetically ordered state. Therefore, DFT calculations for quasi-1D systems, followed by simulations of the respective microscopic magnetic model, are an excellent method to explore the magnetic GS and magnetic ordering.

In this section, three real material realizations of the $S = 1/2$ Heisenberg chain model, $CuSe_2O_5$, $[NO]Cu(NO_3)_3$, and $CaCu_2(SeO_3)_2Cl_2$, are systematically examined. As will be shown, the developed computational approach yields reliable parameterizations of magnetic models for these three compounds, in excellent agreement with the experiments. In particular, the ordering temperature is addressed in a comparative study. It is shown that frustration of the interchain couplings plays the key role for the magnetic ordering transition temperature.

6.1.1 $CuSe_2O_5$

$CuSe_2O_5$ is a $S = 1/2$ HEISENBERG system with isolated CuO_4 plaquettes. The studies on a powder sample [179] hinted at possible low-dimensional character of its magnetic properties, but the low-temperature data were strongly affected by defects or impurities (Fig. 3 in Ref. 179), impeding any conclusive or quantitative analysis.

Selenites are typically susceptible to chemical transport, thus the main advantage of $CuSe_2O_5$ as a model system is the potential to grow large single crystals of high quality. For instance, the chemical transport method used in the present study allowed to grow needle-like crystals with up to 5 mm length.

This section is focused on the evaluation of a quantitative microscopic model for $CuSe_2O_5$. The numerical results are challenged by comparison to the experimentally measured single-crystal $\chi(T)$ and $C_p(T)$ data. An excellent agreement between theory and experiment asserts the validity of the computational approach. Another valuable outcome of this study is its contribution to the insufficiently studied issue of LRMO in real material quasi-1D systems.

Crystal structure

The monoclinic crystal structure of $CuSe_2O_5$ features chains of isolated CuO_4 plaquettes along c (see Fig. 6.1). The neighboring in-chain plaquettes are bridged by Se_2O_5 polyanions, consisting of two SeO_3 pyramids that share an oxygen atom (see Fig. 6.1). The formation of SeO_3 pyramids is typical for the lone-pair cation Se^{4+}, giving rise to an effective separation of the spin chains. This structural peculiarity is reflected in the morphology of the synthesized crystals (see Appendix, Sec. A2): the needle-like shape with an elongation along [001] is a macroscopic feature arising from the structural chains along c (Fig. 6.1) formed by an alternation of CuO_4 plaquettes and Se_2O_5 polyanion groups.

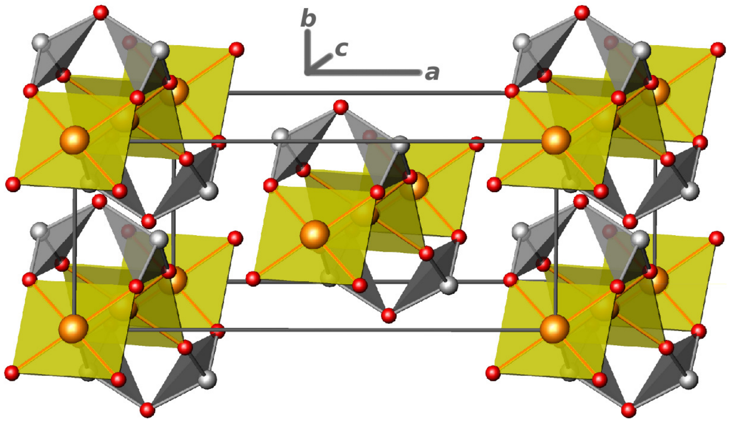

Figure 6.1: Crystal structure of $CuSe_2O_5$. The chains of isolated CuO_4 plaquettes run along c. Two neighboring SeO_3 pyramids share a corner and form Se_2O_5 polyanions that mediate the plaquettes. The neighboring in-chain plaquettes are tilted with respect to each other.

The experimental crystal structure [219] has been solved using X-ray diffraction on a single crystal. The low values of convergence factors ($R = 0.028$, $wR = 0.07$) and the reliable statistics ensured by a large number of observed reflections (655 reflections with $I > 2\sigma[I]$) compared to the number of refined parameters (40), are convincing arguments to credit the structural data and use them as an input for DFT calculations.

Experimental information

Single crystalline $CuSe_2O_5$ samples were grown by M. Schmidt, the X-ray diffraction analysis and EDXS measurements were carried out by Yu. Prots and P. Scheppan, respectively, the $\chi(T)$ and $C_p(T)$ dependencies were measured by W. Schnelle. For a detailed description of the experimental procedures, see Appendix, section A2. All experiments were carried out at MPI CPfS.

The magnetic susceptibility curves (Fig. 6.2, left panel) for both field orientations, parallel (H) and perpendicular ($H_{\perp}$) to [001], have a broad maximum at $T_{\max}$ 101 K and a finite value of χ at the lowest temperature measured (1.8 K), indicating the low-dimensional behavior and the absence of a spin gap. The high-temperature parts of the curves obey the Curie–Weiss law (Fig. 6.2, right panel; $T > 220$ K, H : θ $= 165$ K, $C = 0.51$ emu K mol^{-1}, $g = 2.32$; $H_{\perp}$: θ $= 170$ K, $C = 0.43$ emu K mol^{-1}, $g = 2.15$).[4] The positive value of θ evidences that the dominating couplings in $CuSe_2O_5$ are AFM (see Eq. 5.3 in Sec. 5.1). The shape of the experimental curve conforms to the $S = 1/2$ Heisenberg chain model, as revealed by fitting the experimental data with the parameterized solution from Ref. 87 (Fig. 6.2, left panel).

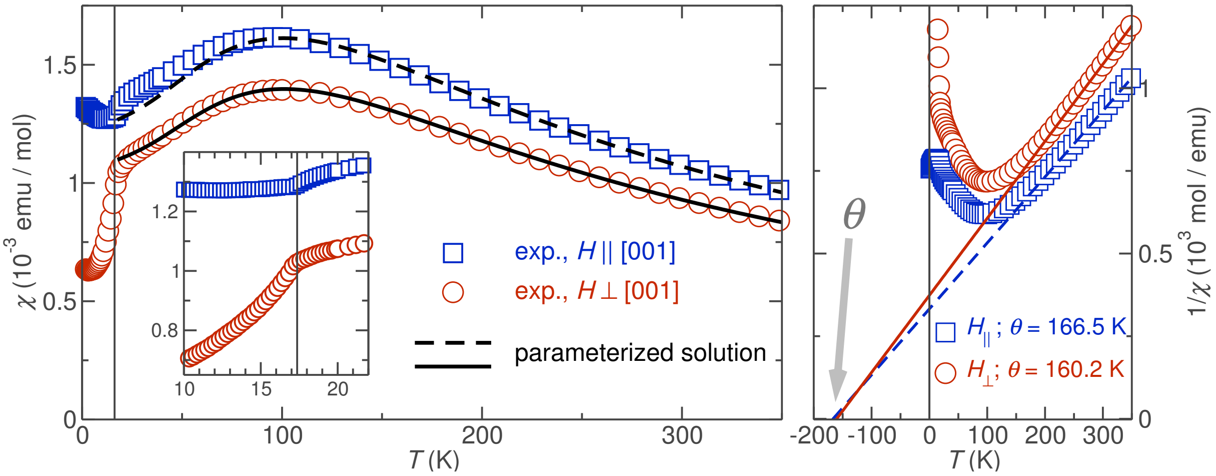

Figure 6.2: Left panel: magnetic susceptibility of $CuSe_2O_5$ as a function of temperature. The magnetizing field is 1 T. For the graphic presentation, only one of each five measured points is shown. The Bethe ansatz fits are shown with dashed ($J_1 = 157.1$ K, $g = 2.14$) and solid ($J_1 = 157.6$ K, $g = 2.00$) lines. Inset: the region around the magnetic ordering temperature is shown enlarged. Right panel: inverse magnetic susceptibility as a function of temperature. The Curie—Weiss fits (for $T > 230$ K) are shown with lines. The temperature-independent contribution χ_0 in the Curie—Weiss fits was set to zero.

To account for the deviation of the fitted curves from the experimental data, both curves were fitted independently, varying the temperature range used for the fitting. As a result, the magnetic susceptibility measured perpendicular to needle-like crystallites can be perfectly fitted by a consistent set of parameters ($J_1 = 157.6\,\mathrm{K}$, $g = 2.00$) in the whole temperature range down to the LRMO temperature, while the fit to the susceptibility measured parallel to the chains ($J_1 = 157.1\,\mathrm{K}$, $g = 2.14$) shows deviations at low temperatures (below T_{max}). This difference likely originates from a slight misalignment of microscopic plates in the needle-like crystallites, but its intrinsic nature (e.g. the presence of a substantial DZYALOSHINSKII-MORIYA coupling) can not be excluded.

---

[4] The slight disagreement of the θ values for different orientations of the magnetizing field is typical for single-crystal studies, see, e.g. Ref. 220.

A magnetic phase transition is observed at 17 K for both orientations of the magnetizing field. The nature of this transition can be understood by examination of the low-temperature part of the curve, below the transition. Due to the high quality of samples, the temperature range between the kink at 17 K down to 10 K is practically unaffected by defects (no appreciable CURIE tail). In this range, $\chi_{\perp[001]}$ exhibits a slight decrease only, while χ drops distinctly on cooling. For an ordered collinear antiferromagnet, linear spin wave theory predicts a T^2 decay and zero value at zero temperature for the magnetic susceptibility measured parallel to the direction of the local ordered magnetic moments [221, 222]. Although the extrapolated value of $\chi_{\perp[001]}(0)$ in $\mathrm{CuSe_2O_5}$ is nonzero, the decay of $\chi_{\perp[001]}$ below 17 K generally conforms to the anticipated behavior. Thus, the observed behavior suggest that the ordered magnetic moments in $\mathrm{CuSe_2O_5}$ are aligned almost perpendicular to the spin chain direction.

In contrast, the $\chi_{\ [001]}(T)$ behavior resembles the spin-wave result obtained by KUBO using higher-order corrections [221]. In particular, he concluded that the magnetic susceptibility measured perpendicular to the direction of the ordered moments should exhibit a slight increase upon cooling.[5] Exactly this behavior is observed in $\chi_{\ [001]}(T)$ for $\mathrm{CuSe_2O_5}$. Whether such behavior arises from the anticipated higher-order corrections or results from small misalignment of crystallites, or even related to defects and paramagnetic impurities, should be subject to future experimental studies.

To additionally verify the AFM ordering transition, $C_p(T)$ has been measured. The clear anomaly at 17 K (Fig. A1) and the linear behavior of $C_p\,T^{-2}(T)$ below this temperature are typical for antiferromagnets [224]. Thus, the $C_p(T)$ data confirm the transition to an AFM ordered state ($T_{\mathrm{N}}\ = 17\,\mathrm{K}$). Remarkably, the anomaly does not shift nor diminishes in magnetic fields up to $H = 9\,\mathrm{T}$. Unfortunately, for $\mathrm{CuSe_2O_5}$ the phonon and magnetic contributions to specific heat can not be disentangled due to the large energy scale of magnetic couplings. Besides, $\mathrm{ZnSe_2O_5}$ features a different crystal structure [225], and thus a different phonon spectrum, which renders it as an inappropriate non-magnetic reference system.

To summarize the experimental information, $\mathrm{CuSe_2O_5}$ exhibits a HEISENBERG chain-like magnetism with J_1 157 K. Since purely 1D systems can not order antiferromagnetically, the origin of the observed AFM ordering is further addressed by DFT calculations.

---

[5] Such behavior of $\chi_{\perp}$ (perpendicular to the direction of the ordered moment) is in agreement with the experiments on $\mathrm{MnF_2}$ [223]. In contrast, linear spin wave theory yields the temperature-independent $\chi_{\perp}$ [221].

DFT calculations

LDA yields a valence band of about 9 eV width formed mainly by Cu 3d, O 2p and Se 4p states (Fig. 6.3, right panel). The well-separated double-peak at the Fermi level contains two narrow, half-filled bands (Fig. 6.3, left panel). As expected, the LDA yields a metallic GS due to a strong underestimation of the electronic correlations. The orbital-resolved DOS shows that the two bands in the vicinity of ε_F originate from the antibonding $(dp)_\sigma$ orbital of a CuO$_4$ plaquette. For CuSe$_2$O$_5$, the antibonding $(dp)_\sigma$ orbital is well separated ($\Delta E \sim 0.5$ eV) from the lower lying Cu 3d and O 2p states, justifying the mapping onto an effective one-orbital model.

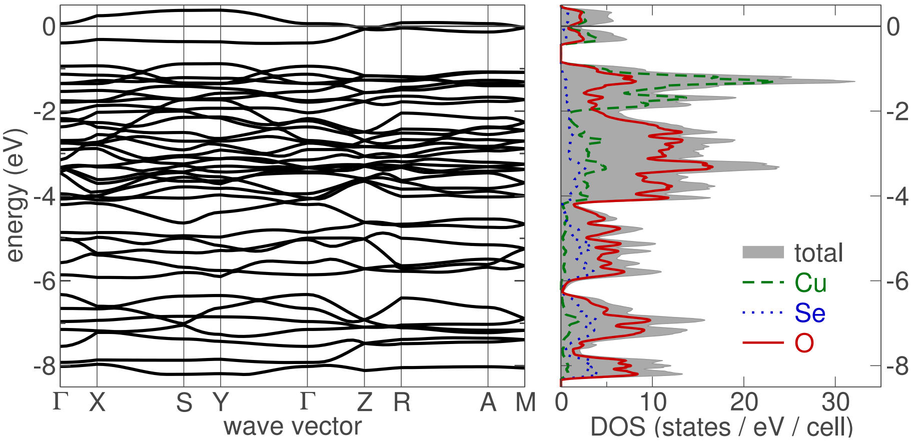

Figure 6.3: LDA band structure (left panel) and DOS (right panel) of CuSe$_2$O$_5$. Notation of $\vec{k}$-points: Γ=(000), X=($\frac{\pi}{a}$00), S=($\frac{\pi}{a}\frac{\pi}{b}$0), Y=(0$\frac{\pi}{b}$0), Z=(00$\frac{\pi}{c}$), R=($\frac{\pi}{a}0\frac{\pi}{c}$), A=($\frac{\pi}{a}\frac{\pi}{b}\frac{\pi}{c}$), M=(0$\frac{\pi}{b}\frac{\pi}{c}$).

For a quantitative analysis, an effective one-orbital TB Hamiltonian is constructed. The set of transfer integrals t_i was evaluated in order to get the best least-squares fit to the two LDA bands crossing ε_F. Since the TB fit procedure is sometimes insecure with respect to multiple solutions (Sec. 4.2.1), the WF technique was used as an alternative approach. The difference between the transfer integrals obtained by the WF method and by the TB fit is tiny and does not exceed 2 meV for individual t_i values (the average difference amounts to 0.2 meV). This deviation can be considered as an error margin for the mapping procedure. Thus, CuSe$_2$O$_5$ is a good example showing that for isolated bands the WF method should not be regarded more accurate than a direct TB fit, but rather as an independent alternative procedure [226–228]. The agreement of the results using the two independent mapping methods reflects the applicability of an effective one-band approach.

The resulting set of the transfer integrals (Table 6.1, first column) yields perfect agreement with the LDA bands (Fig. 6.4). To check the results for consistency, all t_i smaller than 10 meV were neglected and the fitting was repeated. The difference of the leading terms in both approaches did not exceed 10%. The hopping paths corresponding to the leading terms are shown in Fig. 6.4 (right panel).

Besides the leading NN intrachain coupling $t_1 = 165$ meV, only one of the short interchain

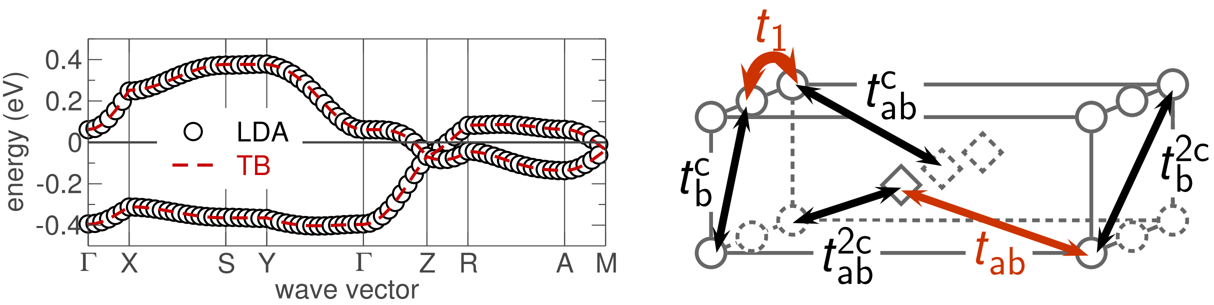

Figure 6.4: Left panel: the TB fit (red dashed line) to the LDA band structure [antibonding $(dp)_\sigma$ band, circles]. Right panel: the superexchange paths for the leading transfer integrals. The projection of the structure is the same as in Fig. 6.1.

Table 6.1: Leading transfer t_i (in meV) and exchange integrals J_i (in K) for $CuSe_2O_5$. The AFM exchange J_i^{AFM} is calculated via mapping the transfer integrals onto a Hubbard model ($U_{\mathrm{eff}} = 4.5$ eV) and subsequently onto a Heisenberg model. The FM exchange J_i^{FM} is evaluated as the difference between J_i and J_i^{AFM}.

path	t_i	J_i^{AFM}	J_i^{FM}	J_i
X_1	166	285	−120	165
X_{ab}	51	27	−7	20
X_b^{2c}	11	1.5	0	1.5
X_{ab}^{c}	10	1	0	1
X_b^{c}	10	1	0	<1
X_{ab}^{2c}	7	0.5	0	<1

couplings is sizable t_{ab} 45 meV (Table 6.1). The corresponding WFs for t_1 and t_{ab} are pictured in Fig. 6.5.

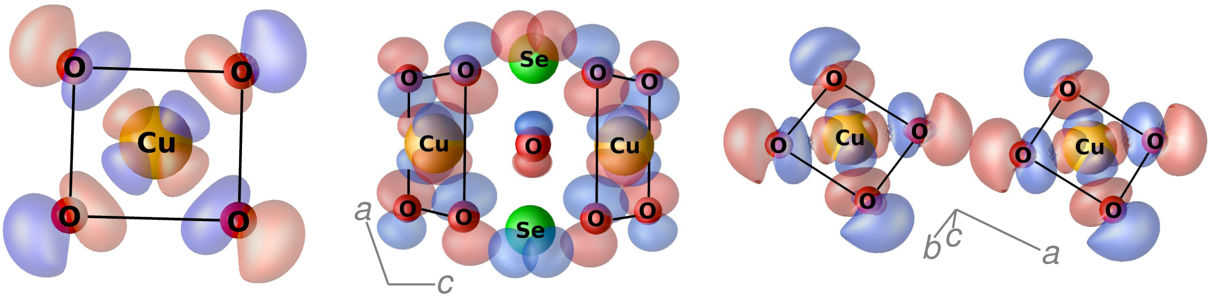

Figure 6.5: WFs for the Cu $3d_{x^2-y^2}$ orbital. Colors represent the sign of a WF. Left panel: the Cu $3d_{x^2-y^2}$ WF plotted on top of a CuO_4 plaquette, visualizing the σ-antibonding combination of Cu $3d_{x^2-y^2}$ and O $2p$ states, relevant for the magnetism. Central panel: the overlap of two WFs centered on the neighboring Cu atoms (corresponds to the NN intrachain coupling t_1). Right panel: the overlap of the WFs corresponding to the leading interchain coupling t_{ab}.

The mapping of the TB model onto a Hubbard model using $U_{\mathrm{eff}} = 4.5$ eV (the same value has been used for the related system $Sr_2Cu(PO_4)_2$ [229]), yields $J_1^{\mathrm{AFM}} = 285$ K for the NN intrachain exchange and $J_{ab}^{\mathrm{AFM}} = 27$ K for the largest interchain exchange. Other couplings yield values of AFM exchange less than 1.5 K (Table 6.1, second column) and will be neglected in further discussion.

The calculated leading magnetic exchange $J_1^{\mathrm{AFM}} = 285$ K is considerably larger than the Bethe ansatz fit estimate (155 K) based on the experimental $\chi(T)$ data. This discrepancy originates from FM contributions to the total magnetic exchange, which are neglected in the mapping procedure. To get a numerical estimate for the FM contribution, LSDA+U total energy calculations are performed for the wide range of $U_d = 6$–9 eV and $J_d = 1$ eV within AMF. The best agreement between the calculated value of the leading exchange coupling J_1 and its experimental estimate is obtained for $U_d = 6.5$ eV (Fig. 6.6). The resulting values for other exchange couplings are provided in Table 6.1.

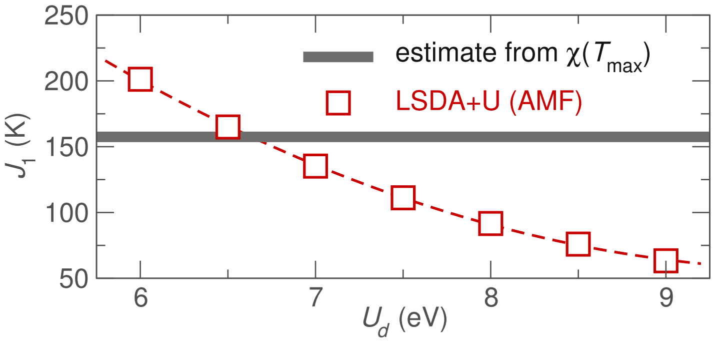

Figure 6.6: $CuSe_2O_5$: the NN coupling J_1 as a function of the parameter U_d (LSDA+U calculations). The AMF DCC has been used. The experimental estimate is based on the BETHE ansatz fit to the magnetic susceptibility data (Fig. 6.2).

Since the value of $U_d = 6.5$ eV is optimized with respect to J_1, it is worth to check other exchange integrals for consistency by performing additional calculations for different values of U_d. Besides the expected change of exchange integrals (0.5 eV increase of the U_d results in about 20 % decrease of J_i and vice versa), the ratio $\alpha \equiv J_{ab}/J_c$ of the leading exchange integrals ($\alpha = 0.121$ for $U_d = 6.0$ eV, $\alpha = 0.129$ for $U_d = 6.5$ eV, and $\alpha = 0.136$ for $U_d = 7.0$ eV) is rather stable with respect to the U_d value.

Considering the absence of edge-sharing connections of CuO_4 plaquettes, the $J_1^{FM} = -120$ K seems to be unusually large. A plausible explanation for the sizable FM contribution is the tilting of the plaquettes. As can be seen in Fig. 6.5, the tilting of the neighboring plaquettes gives rise to a sizable π-overlap of the WFs, and hence O $2p$ wave functions of the neighboring plaquettes, allowing for a considerable HUND's coupling. The large FM contribution may originate also from a destructive interference of coupling paths [230] or a strong coupling to ligands [231]. Which of these mechanisms plays a leading role in $CuSe_2O_5$ remains an open question.

Model simulations

Profiting from the non-frustrated nature of the spin model, QMC are applied to simulate the magnetic susceptibility with a subsequent comparison to the experimentally measured curves. The results of the simulations are given in Fig. 6.7 in comparison with the BETHE ansatz fits (where the interchain coupling is neglected). Obviously, the inclusion of the interchain coupling yields only a tiny improvement with respect to the BETHE ansatz fits. This fact demonstrates *a posteriori* the importance of a microscopic model for quasi-1D systems like $CuSe_2O_5$: apart from the microscopic modeling, there is no reliable way to account for the small interchain coupling directly from measurements of the magnetic susceptibility.

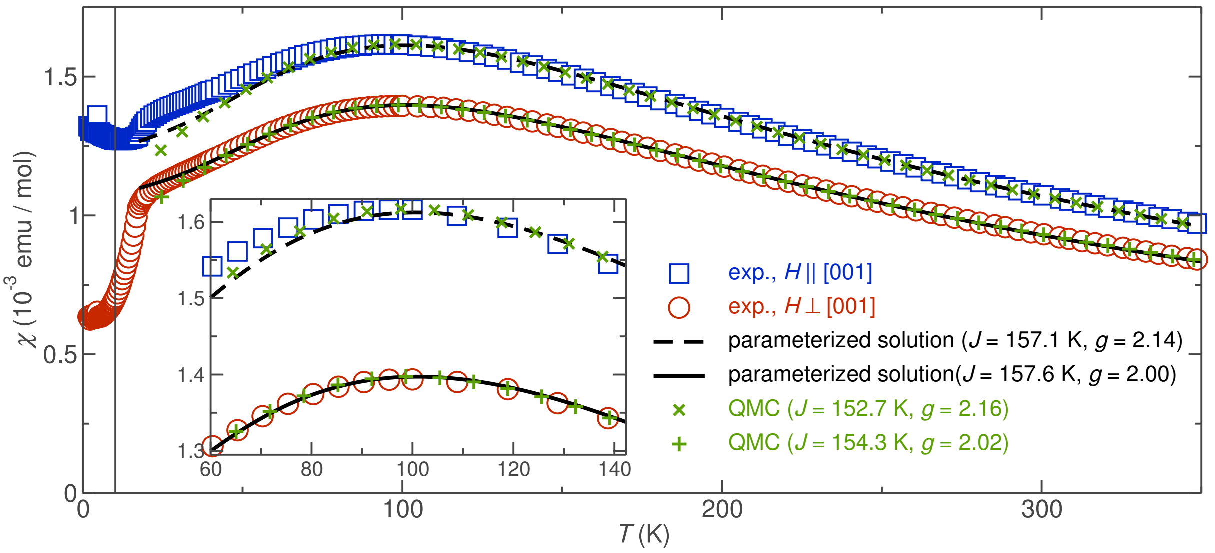

Figure 6.7: Comparison of BETHE ansatz and QMC fits to the experimental magnetic susceptibility. The temperature-independent contribution χ_0 in both fits was set to zero.

Discussion

The DFT calculations disclosed several advantages of $CuSe_2O_5$ as a model system. First, there is an unequivocal evidence from both theory and experiment that the magnetism is chain-like. Secondly, the microscopic analysis revealed that the second-neighbor intrachain coupling is practically absent, leading to a valuable simplification for a theoretical analysis. Finally, there is only one relevant interchain coupling, which couples the spin chains in a simple and non-frustrated way.

Since the uniform HEISENBERG chain model is well understood theoretically, several relevant quantities, such as the value of the leading exchange coupling, can be estimated directly from the experiment. In particular, the position of the wide maximum in the magnetic susceptibility corresponds to $\sim 0.64\,J_1$ [87], thus providing a possibility to adjust the U_d value used for LSDA+U calculations, and use this optimized value for other, more complex systems. However, the study of $CuSe_2O_5$ also demonstrates that not all experimental estimates can be used for as a reliable reference. For instance, using the value of θ 165 K to estimate the sum of the leading exchange couplings leads to unrealistically large $J_1 > 300$ K. Such behavior stems from the large value of the leading exchange coupling, whereas the magnetic susceptibility does not reach the CURIE–WEISS regime even for the highest temperature measured (compare Fig. 6.2 with Fig. 3.4).

There are several important issues which can not be accounted for based on the experimental data, only. The central issue is the AFM ordering temperature, which amounts to 17 K, seemingly high for a quasi-1D system. The extensive comparative analysis presented in Sec. 6.1.4 discloses the crucial role of magnetic frustration for the LRMO. For the non-frustrated system $CuSe_2O_5$, theoretical estimates for T_N provide excellent agreement with the experimentally observed value.

So far, the microscopic magnetic model fully accounts for the magnetic susceptibility data and the LRMO temperature (Sec. 6.1.4). However, the full understanding of the magnetic properties of even such a seemingly simple system as $CuSe_2O_5$ is still missing. For instance, the origin of the large J_1^{FM} can not be identified unambiguously. In addition, the nature of the kink in $C_p\,/\,T^2$ (T) (Fig. A1, inset) is also not clear. The kink is stable at least up to $H = 9\,\mathrm{T}$ and thus not related to defects. Intriguingly, a similar feature has been observed for the related system Bi_2CuO_4 (Fig. 3 in Ref. 232) favoring the intrinsic nature of the kink. To elucidate this unusual feature, further experimental studies on $CuSe_2O_5$ and similar systems as well as a careful theoretical analysis should be carried out.

6.1.2 $[NO]Cu(NO_3)_3$

Low-dimensional magnetism is characteristic to real materials with strong spatial anisotropy of exchange couplings.[6] On the structural level, such anisotropy is typically ruled by magnetically inactive atomic groups. The electronic structure of such groups disfavors any appreciable magnetic exchange, essentially confining the magnetic exchange to a 1D or 2D regime. Efficiency of the dimensional reduction strongly depends on the chemical nature of the non-magnetic groups. In $CuSe_2O_5$, the confinement of the magnetic properties to 1D is realized by Se_2O_5 groups, featuring lone pairs of the Se atoms. Another quasi-1D system, the compound $[NO]Cu(NO_3)_3$, also bears a special chemical feature, the nitrosonium $[NO]^+$ cation which forms a mixed salt with the magnetic $S = 1/2$ Cu^{2+}. As will be shown below, the nitrosonium cations effectively isolate the spin chains from each other, by a substantial reduction of the interchain exchange.

Recently, the magnetism of $[NO]Cu(NO_3)_3$ has been investigated in a combined experimental and theoretical study [233]. The experimental magnetic susceptibility can be well described by the Heisenberg uniform chain model with the leading magnetic exchange coupling J_1 exceeding 150 K. For the microscopic magnetic model, the authors of Ref. 233 put forward a 2D Nersesyan–Tsvelik model [234], which is also known as an anisotropic frustrated square lattice [235]. Based on the almost temperature-independent values of the g-factor, observed in ESR, and the lack of sharp anomalies in the specific heat, the absence of LRMO has been conjectured. To reconcile this with the large coupling J_1, the authors of Ref. 233 suggested that the interchain couplings J' and J_2 (Fig. 6.11) in the $[NO]Cu(NO_3)_3$ structure show an exactly 2:1 ratio, thus leading to strong frustration that inhibits LRMO.

The conjecture on the exact $J_2 : J' = 1 : 2$ ratio in $[NO]Cu(NO_3)_3$ is based on two tentative assumptions: i) the J_2 and J' couplings are running exclusively via [NO] groups; ii) the energies of these couplings are proportional to the number of bridging [NO] units (two for J' and one for J_2) [233]. Regarding the complexity of exchange interactions in general, such assumptions should be supported by a microscopic verification. In the following, the proposed phenomenological model is challenged by DFT calculations.

---

[6] This kind of anisotropy is related to the crystallographic directions and should not be confused with anisotropic J terms that describe the coupling of certain spin components, as in an Ising or an xy model.

Crystal structure

The monoclinic crystal structure of $[NO]Cu(NO_3)_3$ (Fig. 6.8) is formed by chains of isolated CuO_4 plaquettes running along the b direction. One type of the triangular $(NO)_3^-$ nitro-groups links the plaquettes within a chain, thus connecting to the two neighboring plaquettes. The nitro-groups of the second type are connected to one plaquette only. The chains stack along the a and c directions, whereas the $[NO]^+$ cations are located between the chains.

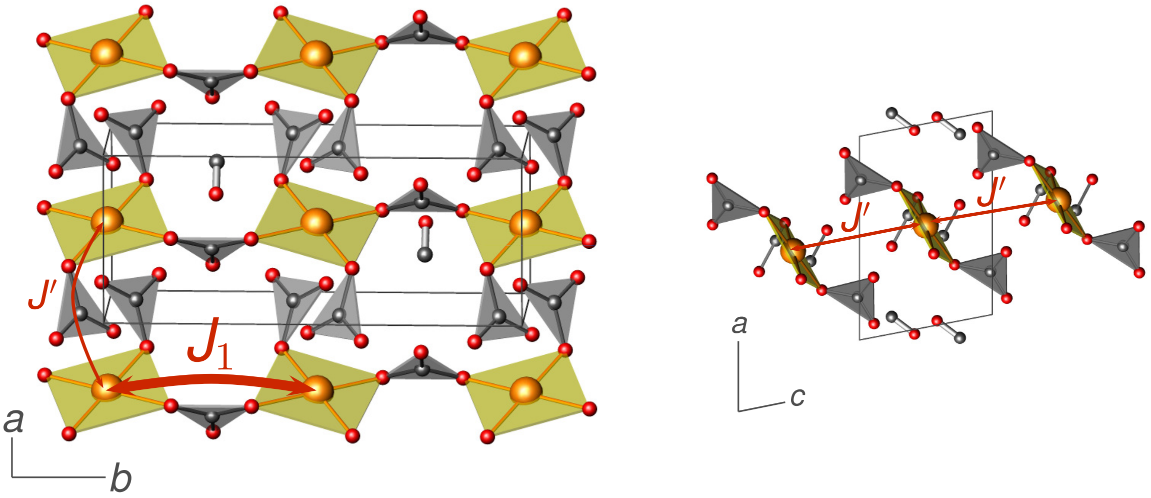

Figure 6.8: Crystal structure of $[NO]Cu(NO_3)_3$. The neighboring CuO_4 plaquettes are connected via NO_3 triangles and form chains along b (left panel). The chains are well separated by $[NO]^+$ cations. In the left panel, the nearly overlapping NO_3 triangles lie in different planes and remain disconnected (see also the right panel).

DFT calculations

Following the developed computational procedure, the LDA picture serves as a starting point. A sharp peak of [NO] states appearing at 1 eV above ε_F is a peculiar feature of $[NO]Cu(NO_3)_3$ related to the antibonding π^*-states of the $[NO]^+$ cation (two nearly degenerate orbitals for each [NO] group). Another peculiarity of $[NO]Cu(NO_3)_3$ is the enhanced width of the valence band, due to the low-lying bonding N–O states, separated from the rest of the valence band. However, similar to other cuprates, the valence band of $[NO]Cu(NO_3)_3$ exhibits dominant contribution of Cu 3d and O 2p states (Fig. 6.9). The well-separated DOS for the antibonding Cu–O bands at ε_F has two distinct maxima (van Hove singularities), characteristic of a 1D behavior. Assuming the Heisenberg chain scenario, the width W of the antibonding band readily yields the leading hopping term $t_1 = W/4$ 180 meV.

The strong hybridization of the σ-overlapping Cu $3d_{x^2-y^2}$ and O $2p_{x,y}$ orbitals (Fig. 6.9, bottom right) and their separation from the rest of the valence band allow to treat them as a whole within an effective one-orbital model. At first glance, the band structure (Fig. 6.9,

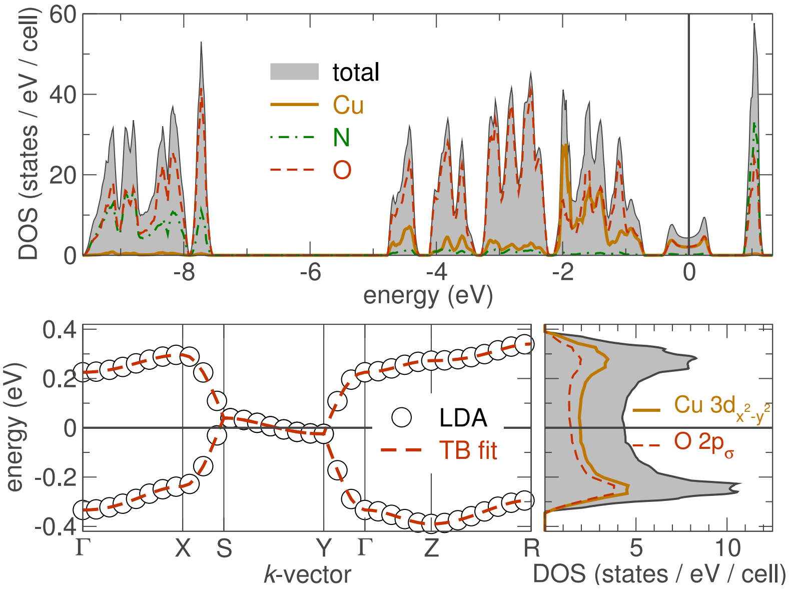

Figure 6.9: Top: the valence band of [NO]Cu(NO$_3$)$_3$. Bottom left: the band structure of the two-band $(dp)_\sigma$ complex at ε_F and the fit using the WF technique. Bottom right: the orbital-resolved DOS for the antibonding band.

bottom left) exhibits the predominant dispersion along X–S and Y–Γ. This corresponds to the crystallographic b direction and supports the proposed 1D scenario. To evaluate the hopping terms, the WF technique is used. This way, a perfect fit to the LDA band structure is obtained (Fig. 6.9, bottom left). The resulting WFs highlight the Cu–O–O–Cu superexchange path (Fig. 6.10).

The WFs yield $t_1 = 150$ meV for the leading NN intrachain hopping and a small non-frustrated interchain hopping $t' = 17$ meV, while other hoppings are smaller than 10 meV. In particular, the previously proposed t_2 (Fig. 6.11) appeared to be as small as 2 meV, disfavoring the model with the frustrated interchain couplings. The couplings J_1 and J' form layers (Fig. 6.11), whereas the leading hopping in the perpendicular direction is $t_\perp = 6$ meV.

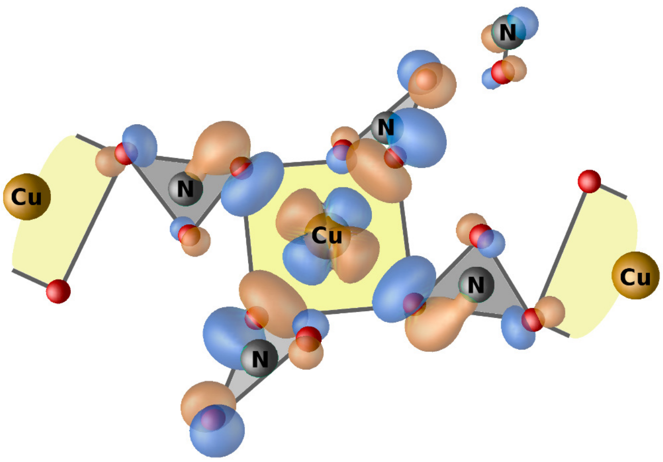

Figure 6.10: The WF for the Cu 3$d_{x^2-y^2}$ orbital in [NO]Cu(NO$_3$)$_3$. The underlying polyhedra constitute a fragment of the HEISENBERG chain.

J_i^{AFM} are estimated by mapping the leading hoppings onto a HUBBARD model with the effective on-site Coulomb repulsion U_{eff}. Adopting $U_{\mathrm{eff}} = 4.5$ eV yields $J_1^{\mathrm{AFM}} = 230$ K and $J'^{\mathrm{AFM}} = 3$ K. The frustrating coupling J_2^{AFM} 0.04 K is negligible. The interlayer coupling is $J_\perp^{\mathrm{AFM}} = 0.4$ K.

LSDA+U total energy calculations were carried out for $U_d = 6.5 \pm 1$ eV and $J_d = 1$ eV within AMF and $U_d = 8.5 \pm 1$ eV and $J_d = 1$ eV within FLL. The experimental $J_1 = 150$ K, evaluated from the $\chi(T)$ data, can be reproduced within AMF by setting U_d to 7.5 eV, exceeding the value $U_d = 6.5$ eV optimized for $CuSe_2O_5$ (Sec. 6.1.1). The larger value of U_d in $[NO]Cu(NO_3)_3$ may be related to the complex chemical nature of this system, which manifests itself in particular features of the LDA valence band, or to structural transformations at low temperatures that were not studied experimentally. In additional, J_1 exhibits a rather strong dependence on in both AMF (J_1 200 ± 50 K for $U_d = 6.5 \mp 1$ eV) and FLL (J_1 240 ± 40 K for $U_d = 8.5 \mp 1$ eV). Although AMF seems to be a more appropriate choice, the absence of low-temperature structural data poses certain difficulties for using $[NO]Cu(NO_3)_3$ as a reference system to pick up the optimal value of U_d. Thus, further experimental structural studies are highly desirable.

The LSDA+U results for J' are below 1 K, disregarding the calculational parameters, such as DCC and U_d. Therefore, the model and the LSDA+U approaches consistently describe $[NO]Cu(NO_3)_3$ as a quasi-1D system with the leading exchange coupling of about 200 K and a small non-frustrated interchain coupling.

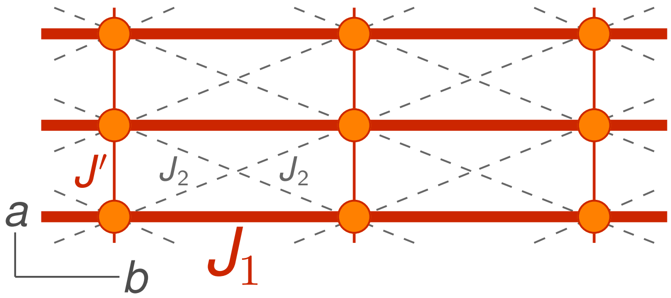

Figure 6.11: Microscopic magnetic model for $[NO]Cu(NO_3)_3$. The projection is the same as in the left panel of Fig. 6.8.

The interchain coupling J' runs via the [NO] groups, as evidenced by small tails of π^* [NO] molecular orbitals in the Cu-based WFs (Fig. 6.10). Nevertheless, the hoppings depend on the mutual orientation of the WFs, hence a simple counting of the bridging [NO] units neglects a basic ingredient of the superexchange mechanism. In contrast, the DFT calculations suggest J_2 J' and do not support the earlier conjecture on the exact $J' : J_2 = 2 : 1$ ratio [233]. In conflict with Ref. 233, $[NO]Cu(NO_3)_3$ is an essentially non-frustrated 1D spin system, while the absence of LRMO is an effect of strong quantum fluctuations. It is rather similar to other 1D Cu^{2+} compounds with CuO_4 plaquettes separated by non-magnetic groups. The J_1 value of 150–250 K is typical for the Cu–O–O–Cu superexchange, e.g. in the uniform-spin-chain compounds $M_2Cu(PO_4)_2$ ($M =$ Sr, Ba) [229].

Model simulations and discussion

In the following, the experimental data for $[NO]Cu(NO_3)_3$ are reconsidered in light of the non-frustrated 1D spin model suggested by the DFT calculations. First, the specific heat data were reported in a narrow temperature range, only (1.8–10 K) [233]. The experimental curve exhibits a minimum around 5 K with an increase towards lower temperatures interpreted as a Schottky anomaly (although the characteristic maximum was not observed) and a typical increase towards higher temperatures due to the phonon contribution $\propto T^3$. Since J_1 150 K, the magnetic specific heat exhibits a maximum around 70 K [87], hence the experimental data in this temperature range (along with the proper non-magnetic reference to estimate the phonon contribution) could be helpful. Regarding the Schottky anomaly, its intrinsic origin has not been proven.

Next, the bulk magnetic susceptibility data are considered. In the $\chi(T)$, the characteristic maximum at ~100 K is almost wiped out by the large impurity and/or defect contribution. The attempts to describe the magnetic susceptibility within the uniform chain model [87], supplied with the temperature-independent term χ_0 and the impurity contribution C_{imp}/T, yields a remarkably good fit down to 2 K with $\chi_0 = 7.7 \cdot 10^{-5}$ emu mol^{-1}, $C_{\text{imp}} = 0.015$ emu K mol^{-1} (4 % of $S = 1/2$ impurities), $J_1 = 150$ K, and $g = 2.12$. Since the same model poorly fits the intrinsic susceptibility from ESR below 80 K, it is likely that the ESR bears a systematic error that causes the underestimate of χ at low temperatures (probably, due to the separation of the intrinsic and the impurity signal in the spectra). To resolve this puzzling issue, additional experimental studies, such as susceptibility measurements on single crystals or NMR, are highly desirable.

Finally, it is worth to reconsider the possibility of LRMO in $[\text{NO}]\text{Cu}(\text{NO}_3)_3$, which was rejected in Ref. 233. The upturn in the specific heat, interpreted as a Schottky anomaly in Ref. 233, may conceal a weak transition anomaly below 5 K. The weakness of the anomaly is a natural consequence of T_{N} J_1, which results in a significantly small amount of entropy released at T_{N} (see Sec. 3.2.2). Further on, the ESR intensities diverge below 10 K and might also indicate the onset of LRMO.

To summarize, $[\text{NO}]\text{Cu}(\text{NO}_3)_3$ is a good realization of a Heisenberg chain model with the intrachain exchange J_1 150 K. The chains are coupled in a non-frustrated way, and the interchain coupling topology is the same is in CuSe_2O_5 (anisotropic square lattice). Deviations of the ESR line width and the low-temperature specific heat from the expected behavior are likely extrinsic and should be addressed by further studies on higher quality samples.

6.1.3 $\text{CaCu}_2(\text{SeO}_3)_2\text{Cl}_2$

So far, DFT calculations yield reliable numerical values for the microscopic magnetic couplings. However, a statement that in both CuSe_2O_5 and $[\text{NO}]\text{Cu}(\text{NO}_3)_3$, the uniform Heisenberg chain scenario could be guessed by a bare look at the crystal structure, is not far off the mark. The next compound, $\text{CaCu}_2(\text{SeO}_3)_2\text{Cl}_2$, shows an instructive example of a structurally involved system, where the leading superexchange path is highly nontrivial. Moreover, the interchain coupling is realized by two independent exchange couplings, which make the system magnetically frustrated. The complex magnetic model of $\text{CaCu}_2(\text{SeO}_3)_2\text{Cl}_2$ could be a valuable contribution for further theoretical developments in the field of quasi-1D quantum magnets.

Crystal structure

In contrast to the previously discussed compounds, the crystal structure of $CaCu_2(SeO_3)_2Cl_2$ (Fig. 6.12) comprises two nonequivalent Cu positions: Cu(1) and Cu(2). The Cu(1) atoms show a slightly distorted square-planar $Cu(1)O_4$ environment, typical for Cu^{2+} oxides. In contrast, Cu(2) is six-fold coordinated, with four O and two Cl forming an octahedron, squeezed along Cu(2)–O1 (Table A2). Although such octahedral coordination is rather unusual, it still conforms to a square-planar-like CF splitting of 3*d* levels and the conventional non-degenerate $3d^9$ orbital GS with the half-filled $3d_{x^2-y^2}$ orbital, confined to the plane of a $Cu(2)O_2Cl_2$ plaquette (Fig. 6.12).[7] This plaquette is formed by two Cu(2)–Cl bonds and two Cu(2)–O1 bonds. The formation of the plaquette can be qualitatively understood in terms of different ionic radii for O and Cl: the larger size of the Cl atoms makes their effect on the Cu 3*d* orbitals comparable to the effect of O1 with shorter distances to Cu. The resulting CF splitting resembles that of a CuO_4 plaquette and drives one of the atomic *d* orbitals half-filled. This scenario is *a posteriori* confirmed by the DFT calculations.

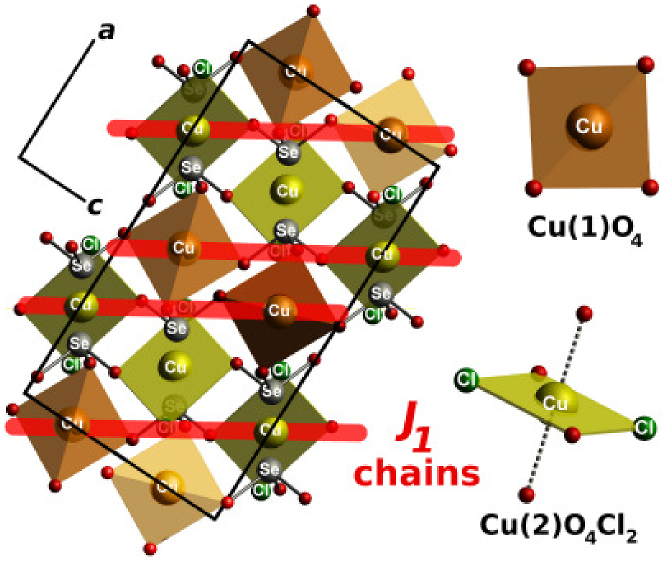

Figure 6.12: Left: crystal structure of $CaCu_2(SeO_3)_2Cl_2$. The structural chains run along $[10\bar{1}]$ (not shown), whereas the magnetic chains range along ~[201], as shown by red lines. Red unlabeled spheres denote O atoms. Right: local environment of Cu(1) and Cu(2). The magnetically active $Cu(1)O_4$ and $Cu(2)O_2Cl_2$ plaquettes are highlighted.

The formation of CuO_2Cl_2 plaquettes is a casual phenomenon for Cu oxychlorides [236, 237]. A special feature of $CaCu_2(SeO_3)_2Cl_2$ is the presence of two longer Cu(2)–O3 bonds which are similar to the Cu(2)–Cl bonds in terms of interatomic distances but are essentially inactive with respect to the magnetism.

The $Cu(1)O_4$ plaquettes and the $Cu(2)O_4Cl_2$ octahedra share corners and form chains along $[10\bar{1}]$. However, the bridging O3 atoms do not belong to the $Cu(2)O_2Cl_2$ plaquettes, hence a simple Cu(1)–O3–Cu(2) superexchange is unlikely. Instead, the leading exchange couplings should run via SeO_3 trigonal pyramids which join the plaquettes into a framework.

---

[7] In this local coordinate system, x corresponds to the axis, along which the CuO_6 octahedra are squeezed. Consequently, the z axis runs toward O3 atoms.

Experimental information

The powder sample of $CaCu_2(SeO_3)_2Cl_2$ was prepared in the group of P. S. Berdonosov at the Moscow State University. The $\chi(T)$ dependencies for various magnetic fields were measured by A. Tsirlin at MPI CPfS. The high-field magnetization has been measured in HZDR HLD by Y. Skourski.

The $\chi(T)$ dependence (Fig. 6.13) shows a broad maximum at 83 K and a pronounced increase below 30 K. The susceptibility maximum evidences the low-dimensional behavior, while the low-temperature upturn is caused by the paramagnetic contribution of defects and/or impurities. Above 230 K, the data can be fitted with the modified Curie–Weiss law (Eq. 3.6). The fit yields the temperature-independent contribution $\chi_0 = 6(1)\cdot 10^{-5}$ emu (mol Cu)$^{-1}$, the Curie constant $C = 0.42(1)$ emu K mol^{-1}, and $\theta = 93(5)$ K. The positive θ indicates predominant AFM interactions in the system. The expressions Eqs. 3.7 and 3.8 yield the resulting effective magnetic moment $\mu_{\mathrm{eff}} = 1.83(1)\,\mu_{\mathrm{B}}$ and the g-factor $g = 2.11(1)$, typical for $S = 1/2$ Cu^{2+}.

The whole $\chi(T)$ dependence can be described by the expression for the uniform $S = 1/2$ chain [87]. The temperature range 2–380 K fits to the validity condition of this parameterization $0 \leq T \leq 5J_1$. To account for temperature-independent and the low-temperature impurity contribution to $\chi(T)$, the intrinsic chain susceptibility χ_{HC} is supplemented with the temperature-independent and Curie contribution:

$$\chi(T) = \chi_0 + \frac{C_{\mathrm{imp}}}{T} + \frac{N_{\mathrm{A}}\, g^2\, \mu_{\mathrm{B}}^2}{J_1}\, \chi_{\mathrm{HC}} \quad \frac{T}{J_1} \quad . \tag{6.3}$$

The fit yields $J_1 = 133(1)$ K, $g = 2.11(1)$, and $\chi_0 = 3(1)\cdot 10^{-5}$ emu (mol Cu)$^{-1}$. This χ_0 value is almost twice smaller than the value obtained from the Curie–Weiss fit. The reason for this discrepancy is the additional term C_{imp}/T in Eq. 6.3. Since this term is of the same order as χ_0 in the high-temperature region, and both χ_0 and C_{imp}/T are positive, χ_0 from the Curie–Weiss fit is substantially larger than χ_0 from Eq. 6.3. The fitted $C_{\mathrm{imp}} = 0.005(1)$ emu K (mol Cu)$^{-1}$ corresponds to about 1% of $S = 1/2$ impurities. To check the applicability of the Heisenberg chain model to the system, the quantity $\chi_{\mathrm{HC}}(T_{\mathrm{max}})\, T_{\mathrm{max}}\, g^{-2}$ was calculated. According to Eq. 31 from Ref. 87, it should amount to 0.0353229(3) emu K (mol Cu)$^{-1}$ for a Heisenberg chain system, independent of J_1. For $CaCu_2(SeO_3)_2Cl_2$, $\chi_{\mathrm{HC}}(T_{\mathrm{max}})\, T_{\mathrm{max}}\, g^{-2} = 0.0345(8)$ emu K (mol Cu)$^{-1}$ deviates only by few percent from the ideal value, justifying the model assignment.

The observed linear $M(H)$ dependence shown in the inset of Fig. 6.13 (the magnetization is measured in arbitrary units, as explained in Sec. 3.3) is also consistent with the proposed uniform-chain behavior, since the accessible field range is well below the saturation field of $H_s = 188$ T for $J_1 = 133$ K and $g = 2.11$.

The extrinsic nature of the low-temperature Curie tail in $\chi(T)$ is supported by its suppression in magnetic field (Fig. A2). The temperature derivative of magnetic susceptibility

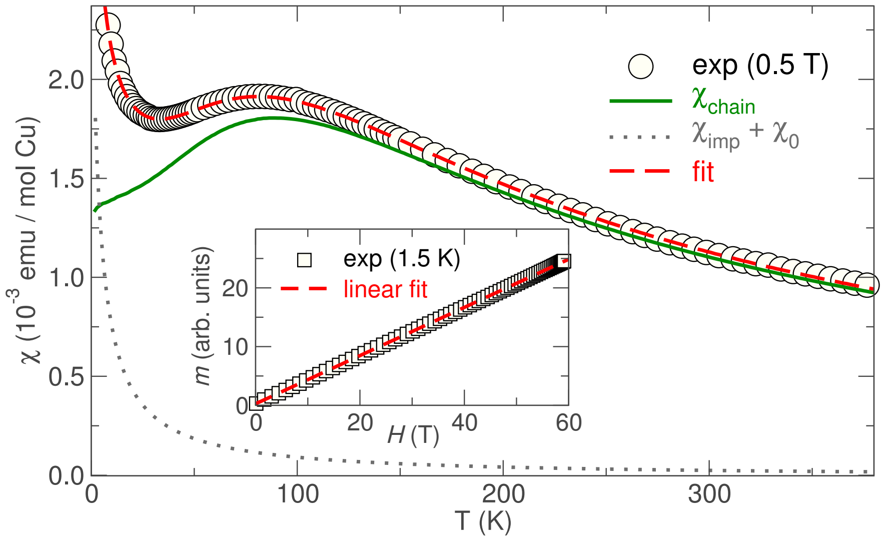

Figure 6.13: Magnetic susceptibility (black circles) and the fit with Eq. 6.3 (dashed red line). HEISENBERG chain (solid green line) and impurity (gray line) contributions to the fitted curve are shown. Inset: high-field magnetization curve (squares) with a linear fit (red line).

exhibits a kink at 6 K, which is likely a signature of an AFM ordering. This issue will be later discussed in context of the microscopic spin model.

DFT calculations

The LDA valence band (Fig. 6.14, top) is clearly split into two parts: the region between −8 and −5.5 eV is dominated by Se 4p and O 2p states, while the rest of the valence band is formed by Cu, O, and Cl states.

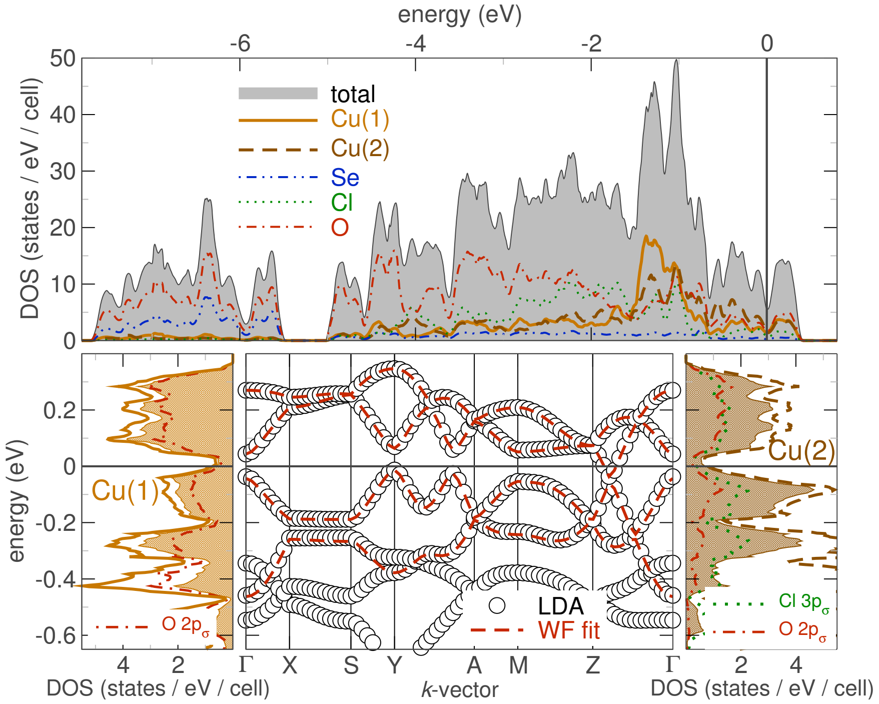

Figure 6.14: Top: total and atom-resolved DOS for $CaCu_2(SeO_3)_2Cl_2$. Bottom center: LDA band structure (circles) and the WF fit (red line). Bottom left and right: orbital-resolved DOS for Cu(1) and Cu(2). Shaded regions show the $3d_{x^2-y^2}$ contribution.

Typical for cuprates, the σ-overlapped Cu $3d_{x^2-y^2}$ and O 2p states are confined to the vicinity of the FERMI level. However, $CaCu_2(SeO_3)_2Cl_2$ lacks a separated band complex around ε_F reflecting the octahedral coordination for Cu(2), and thus necessitates a detailed analysis of the magnetically active orbitals.

Table 6.2: Interatomic Cu–Cu distances d (in Å), transfer integrals t_i (in meV), as well as J^{AFM} and J^{FM} contributions to the total exchange integrals J_i (in K) for the leading couplings in $\mathrm{CaCu_2(SeO_3)_2Cl_2}$. For notation of the paths, see Fig. 6.15. J_{nn} stands for the NN coupling, along the structural chains (not shown in Fig. 6.15).

path	atoms	d	t_i	J_i^{AFM}	J_i^{FM}	J_i
J_{nn}	Cu(1), Cu(2)	3.84	19	4	–	4
J_{ic1}	Cu(1), Cu(1)	4.13	47	25	−15	10
J_1	Cu(1), Cu(2)	6.19	139	200	−55	145
J_{ic2}	Cu(2), Cu(2)	7.33	30	10	–	10

To evaluate the relevant states, the DOS is projected onto a set of local orbitals. The $3d_{x^2-y^2}$ contribution dominates the Cu(1) DOS at ε_{F} (Fig. 6.14, left bottom). For the Cu(2) atom, the situation is less trivial, since the local environment of this atom implies two short Cu(2)–O bonds as well as four long [two Cu(2)–O and two Cu(2)–Cl] almost equidistant bonds, making the choice of the local coordinate system ambiguous. However, the analysis of local DOS for different situations readily yields the correct choice of the local axes and evidences that the two short Cu(2)–O and two Cu(2)–Cl bonds form a plaquette with the Cu $3d_{x^2-y^2}$ magnetically active orbital. The local DOS of this orbital clearly dominates the states at ε_{F} (Fig. 6.14, right bottom) and conforms to the standard cuprate scenario.

The effective one-orbital TB model for $\mathrm{CaCu_2(SeO_3)_2Cl_2}$ is described by a 4×4 matrix, due to the four magnetic magnetic Cu atoms in a unit cell: two Cu(1) and two Cu(2). The model is parameterized using the WF technique, which yields a dispersion in excellent agreement with the LDA bands (Fig. 6.14, bottom). The effective one-orbital TB model yields three relevant couplings (Table 6.2): t_1 running along Cu(1)-Cu(2) chains almost parallel to the [201] direction (Fig. 6.15), the short-range interchain coupling t_{ic1} which connects Cu(1) atoms, as well as the long-range interchain coupling t_{ic2} connecting Cu(2) atoms along $[10\bar{1}]$. The clearly dominant t_1 amounts to 139 meV, while t_{ic1} and t_{ic2} are found to be 47 and 30 meV, respectively. Due to the particular orientation of the magnetically active orbitals, the hopping t_{nn} along the "structural chains" is apparently small, and likely has a minor influence on the magnetic GS, as will be shown later.

Next, the TB model is mapped onto a HUBBARD model with an effective on-site Coulomb repulsion U_{eff}, to obtain the estimates for J_i^{AFM}. Adopting a typical value $U_{\mathrm{eff}} = 4.5$ eV yields $J_1^{\mathrm{AFM}} = 200$ K, $J_{\mathrm{ic1}}^{\mathrm{AFM}} = 25$ K and $J_{\mathrm{ic2}}^{\mathrm{AFM}} = 10$ K.

Based on structural considerations only, an appreciable FM contribution might be expected for the short-range coupling J_{ic1} and the NN coupling J_{nn}, whereas J_1 and J_{ic2} are rather long-range, and their FM contributions should be small. To challenge this conjecture, supercell LSDA+U calculations are preformed. Combining the LSDA+U results with J_i^{AFM} estimates from the HUBBARD model, the FM contributions J_i^{FM} are evaluated.

Adopting the AMF DCC with $U_d = 6.5$ eV and $J_d = 1$ eV, $J_1 = 145$ K is obtained, in excellent agreement with the experimental J_1 133 K from the fit to the $\chi(T)$. In accordance with the expectations, the long-range interchain coupling J_{ic2} has a tiny FM contribution only, while for the short-range coupling J_{ic1} the FM contribution reaches $J_{\mathrm{ic1}}^{\mathrm{FM}} = -15\,\mathrm{K}$ (see Table 6.2). At first glance, the rather large $J_1^{\mathrm{FM}} \sim -55\,\mathrm{K}$ may look surprising. However, in $\mathrm{CuSe_2O_5}$, the leading intrachain coupling J_1 runs also via two corner-sharing $\mathrm{SeO_3}$ pyramids and the FM contribution J_1^{FM} to this coupling amounts to even $-100\,\mathrm{K}$ (Sec. 6.1.1). Therefore, such high FM contributions are likely intrinsic to the superexchange realized via $\mathrm{SeO_3}$ pyramids. In contrast to $\mathrm{CuSe_2O_5}$, this superexchange results from the overlap of oxygen orbitals, while the Se states have only a minor contribution to the WF, as can be seen in Figs. 6.5 and A4.

The last remark concerns the short-range coupling between the NN Cu(1) and Cu(2) atoms that form the structural chains. The WFs analysis yields a negligible t_{nn} associated with this coupling path. Still, the respective interatomic distance (3.84 Å) is relatively small, which could give rise to an FM coupling. Therefore, it is important to obtain the value of J_{nn} using the LSDA+U calculations. The resulting exchange of 4 K is in excellent agreement with the TB estimate (4 K), evidencing a negligible FM contribution and justifying the restriction to the three couplings J_1, J_{ic1}, and J_{ic2} for a minimal model.

Model simulations and discussion

The DFT-based microscopic magnetic model of $\mathrm{CaCu_2(SeO_3)_2Cl_2}$ is depicted in Fig. 6.15. Its key element are the Cu(1)–Cu(2) chains running almost parallel to the [201] direction, which differs from the structural chains. The chains are coupled by two nonequivalent exchange interactions: J_{ic1} is short-range and links the Cu(1) atoms of the two neighboring chains, while the long-range J_{ic2} bridges the Cu(2) atoms of the fourth-neighbor chains. Another difference between J_{ic1} and J_{ic2} is that the former is responsible for a 3D coupling [connects Cu(1) atoms belonging to different layers, see Fig. 6.15], whereas the latter is confined to the *ac* plane. Either of interchain couplings *alone*, J_{ic1} or J_{ic2}, leads to a 3D or 2D non-frustrated model, respectively. However, the *combination* of the two interchain couplings gives rise to magnetic frustration, evidenced by an odd number of AFM bonds (seven) along the closed, hourglass-shaped loop shown in Fig. 6.15.

The complex interchain coupling regime impedes an accurate estimation of the LRMO transition temperature. In general, the 3D coupling regime should rise T_{N}. On the other hand, the interchain coupling is frustrated, which certainly suppresses the magnetic ordering. The interplay of the 3D coupling regime and the frustration should result in a moderate T_{N} of $\mathrm{CaCu_2(SeO_3)_2Cl_2}$, comparable to that of $\mathrm{CuSe_2O_5}$. Indeed, the kink of magnetic susceptibility at 6 K in Fig. A2 fits well to the energy scale of the anticipated LRMO in $\mathrm{CaCu_2(SeO_3)_2Cl_2}$ (compare to $T_{\mathrm{N}} = 17\,\mathrm{K}$ in $\mathrm{CuSe_2O_5}$ with non-frustrated interchain couplings). The comparative analysis of T_{N} for $\mathrm{CuSe_2O_5}$, $\mathrm{[NO]Cu(NO_3)_3}$ and $\mathrm{CaCu_2(SeO_3)_2Cl_2}$ is presented later in this section.

Magnetic frustration is one of the leading mechanisms that give rise to complex magnetic structures. It is therefore interesting to address the structure of the anticipated magnetically ordered GS of $\mathrm{CaCu_2(SeO_3)_2Cl_2}$. First, the low-energy sector of a classical HEISENBERG model

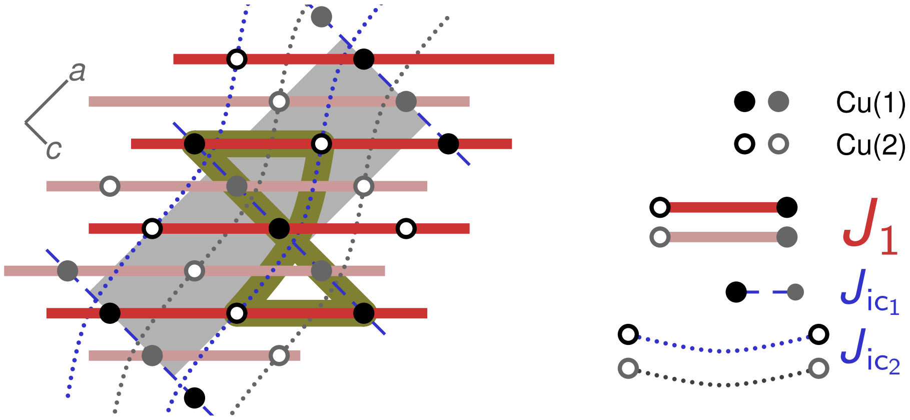

Figure 6.15: Microscopic magnetic model for $CaCu_2(SeO_3)_2Cl_2$. Filled and empty circles show the Cu(1) and Cu(2) positions. Bold lines and circles denote the exchange couplings and the spins (the same notation applies to Table 6.2) in the front plane, whereas gray circles and shaded lines correspond to the atoms lying in the back plane. The planes are connected by J_{ic1} couplings, only. A closed loop (dark-yellow line) having an odd number of AFM couplings evidences the frustrated character of the spin model. The crystallographic unit cell is depicted by the gray rectangle.

is studied on finite lattices of 16 coupled chains. For each chain, a condition of the ideal AFM arrangement of the neighboring spins is imposed. This condition makes the chains effectively infinite, since the number of possible states for each chain amounts to two: a certain spin can be up or down, which governs the arrangement of all other spins in the chain, independent of the chain length.

To keep the problem computationally feasible, only collinear spin arrangements are addressed. The magnetic GS is evaluated as a state with minimal energy. Adopting the ratios of the leading exchange couplings from our LSDA+U calculations (Table 6.2, last column), yields an AFM GS, with the magnetic unit cell doubled along a and quadrupled along c with respect to the crystallographic unit cell, i.e. the propagation vector is $(^1/_2, 0, ^1/_4)$. To understand the particular way the frustration is lifted, the products $-4[\vec{S}_i \cdot \vec{S}_j](J_{ij}/|J_{ij}|)$ for all (i, j) spin pairs in a unit cell are computed. This way, the satisfied couplings can be distinguished from the unsatisfied ones: for collinear configurations, such a product amounts either to 1 (a satisfied coupling) or to -1 (an unsatisfied coupling). For a certain type of exchange coupling, the sum of such products can be divided by the total number of couplings of this type in the unit cell (which is larger than unity). Then, the fraction of satisfied couplings can be estimated. Such analysis yields that 100 % of J_1 (as imposed by the constraint) and J_{ic2}, but only 75 % of J_{ic1} couplings are satisfied in the proposed $(^1/_2, 0, ^1/_4)$ GS.

Taking into account the restriction to collinear states, it is worth to address the stability of this GS using alternative techniques. Thus, classical Monte Carlo simulations yield diagonal spin correlations $\langle S_i^z S_j^z \rangle$, where i and j are spins coupled by a particular magnetic exchange. The resulting correlations amount to $-0.24452(1)$, $-0.16716(1)$ and $-0.23056(3)$ for the J_1, J_{ic1} and J_{ic2} couplings, respectively. These numbers should be compared to $\langle S_i^z S_j^z \rangle = -0.25$

for a perfect AFM arrangement. Despite the small deviations from this ideal number, the spins coupled by J_1 and J_{ic2} can be regarded as antiferromagnetically arranged, corroborating the classical energy minimization result. On the contrary, the value for J_{ic1} is substantially smaller, yielding the average angle of $\arccos(0.16716\,S^{-2})$ 48° between the respective spins. The resulting angle is very close to $\pi/4$, hence the spins in the fourth-neighbor chains are almost antiparallel to each other (the angle amounts to π). This is in accord with the almost antiparallel arrangement of spins coupled by J_{ic2} couplings (coupling between the fourth-neighbor chains).

In the classical model, the exotic regime of frustrated interchain couplings leads to a rather complex magnetic ordering in $\mathrm{CaCu_2(SeO_3)_2Cl_2}$: the classical energy minimization yields the collinear $(1/2, 0, 1/4)$ state, while the classical Monte Carlo simulations are in favor of a non-collinear magnetic GS. However, these two GSs differ only by the mutual arrangement of spins coupled by J_{ic1}.

Since for quasi-1D systems quantum fluctuations are crucial, the respective quantum model should be addressed. However, the study of a magnetic ordering for a 3D frustrated quantum model is a challenging task, since standard methods are either not applicable (DMRG due to the high dimensionality, QMC due to frustration) or do not account for the thermodynamic limit (ED). Moreover, $\mathrm{CaCu_2(SeO_3)_2Cl_2}$ features a non-negligible magnetic impurity contribution, as evidenced by the low-temperature upturn in $\chi(T)$ (Fig. 6.13). At low temperatures, these impurities can give rise to strong internal fields and possibly alter the GS.[8] Therefore, the magnetic ordering in $\mathrm{CaCu_2(SeO_3)_2Cl_2}$ deserves additional investigation using alternative techniques, both from experimental as well as theoretical side.

Despite the unexpected complexity of the magnetic model, the nontrivial structural organization of $\mathrm{CaCu_2(SeO_3)_2Cl_2}$ has an important advantage. In particular, the Cl and Br atoms are known to be easily substitutable owing to their similar chemical nature. Such substitution can be used to create bond randomness and to access the exotic behavior of partially disordered spin systems [239, 240]. In the case the Cl states participate in the superexchange, the chemical substitution inevitably affects the geometry of the superexchange pathways, and gives rise to drastic changes in the magnetic properties. On the contrary, in $\mathrm{CaCu_2(SeO_3)_2Cl_2}$, the Cl atoms lie away from the leading superexchange pathway. Thus, partial Cl/Br substitution will alter the relevant microscopic parameters (such as the CF splitting) without changing the superexchange geometry.

A peculiar arrangement of magnetic plaquettes makes $\mathrm{CaCu_2(SeO_3)_2Cl_2}$ a good realization of the $S = 1/2$ HEISENBERG chain model with an intrachain exchange coupling of ~133 K and frustrated interchain couplings realized via two nonequivalent superexchange paths. Simulations of the microscopic model suggest two states—the collinear $(1/2, 0, 1/4)$ state and a closely related non-collinear state as the candidates for the magnetically ordered GS. A kink in the magnetic susceptibility at 6 K hints at an LRMO transition, which is subject to future experimental verification.

---

[8] Similar effect was recently discussed for the anisotropic triangular lattice model in the one-dimensional limit, see Ref. 238.

6.1.4 Magnetic frustration as a key to the LRMO temperature

1D systems exhibit sizable quantum fluctuations, inhibiting LRMO [188]. In addition, the absence of LRMO at any nonzero temperature is assured by the MERMIN–WAGNER theorem. In contrast, real quasi-1D magnetic systems feature small interchain couplings that typically drive the system into a magnetically ordered state. The temperature of the magnetic ordering transition depends on several quantities (the value of intrachain and interchain couplings, topology of the interchain couplings) and can vary in a wide range.

The issue of magnetic ordering in quasi-1D systems has been extensively studied theoretically [241–247]. To keep the problem feasible, all these theories proceed from the mean-field approach. Moreover, typically only simple interchain coupling topologies are considered, such as an anisotropic square lattice, anisotropic cubic lattice or recently, anisotropic triangular lattice. Such restrictions limit the applicability of these theories to real material systems, where the interchain coupling can be of a rather complex nature, as for instance in $CaCu_2(SeO_3)_2Cl_2$.

A comparison between the experimental T_N and its estimate using theoretical expressions and exchange integrals from a DFT-based model is further impeded by additional peculiarities of quasi-1D systems. The most relevant is the spatial anisotropy of exchange couplings present in a system. For instance, the leading interchain coupling in both $CuSe_2O_5$ and $[NO]Cu(NO_3)_3$ couples a certain chain with only two neighboring chains. Thus, the couplings to the other neighboring chains are considerably smaller, resulting in the spatial exchange anisotropy. Moreover, the number of neighboring chains can be larger than four. Unfortunately, there is no unique solution to this problem. To allow for a comparative study, a generalized approach should be used. The simplest scheme is to restrict the analysis to the relevant interchain couplings, only. In this way, the coordination number z [Fig. 6.16, (a)–(d)] is defined as the number of the neighboring chains coupled by relevant interchain couplings J_{ic}. Thus, the zJ_{ic} product serves as the effective interchain coupling. Although such approach violates the MERMIN–WAGNER theorem [32],[9] it is justified empirically, as will be shown below.

The second problem is the anisotropy in the spin space. In the computational approach, the isotropic HEISENBERG model is presumed, thus the anisotropic effects are neglected. Although the microscopic model generally conforms to the macroscopic behavior, the spin anisotropy is inevitably present, as evidenced, e.g. for $CuSe_2O_5$ by the strong dependence of the g-factor on the orientation of magnetizing field (Fig 6.2). In a common sense approach,

---

[9] Such approach yields a finite LRMO temperature even for a purely 2D model ($z = 2$).

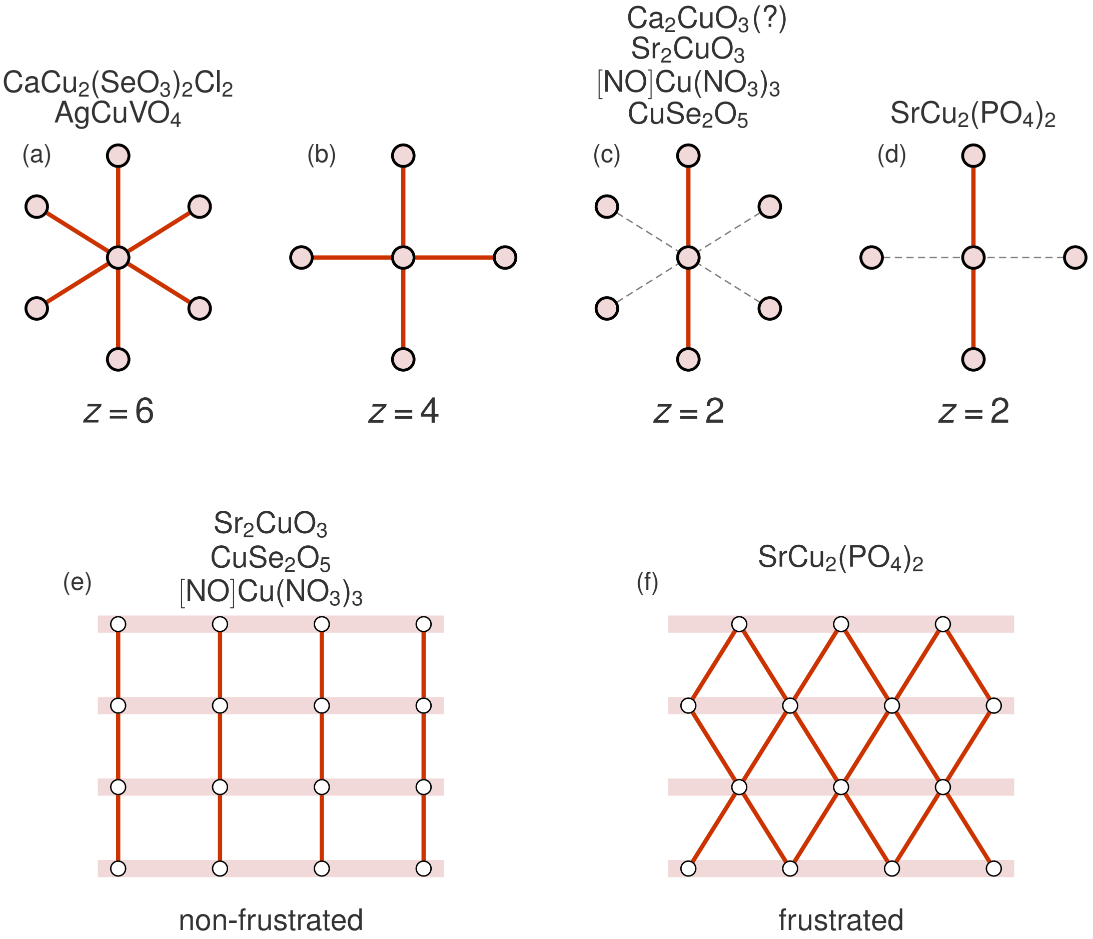
$CaCu_2(SeO_3)_2Cl_2$
$AgCuVO_4$
Ca_2CuO_3(?)
Sr_2CuO_3
$[NO]Cu(NO_3)_3$
$CuSe_2O_5$
$SrCu_2(PO_4)_2$
(a)
(b)
(c)
(d)
$z = 6$
$z = 4$
$z = 2$
$z = 2$
(e)
Sr_2CuO_3
$CuSe_2O_5$
$[NO]Cu(NO_3)_3$
(f)
$SrCu_2(PO_4)_2$
non-frustrated
frustrated

Figure 6.16: Top panel: the coordination number z for different interchain coupling regimes (a)–(d). Spin chains denoted by filled circles run in the direction perpendicular to the projection plane. Relevant interchain J_{ic} couplings are shown by solid red lines. Compounds featuring a certain interchain coupling topology are listed above the sketches. The question mark for Ca_2CuO_3 is explained on page 102. Bottom panel: non-frustrated (e) and frustrated (f) interchain coupling topologies. Broad pale lines denote spin chains, the thin bright lines are interchain couplings. The individual spins are shown with empty circles. Note the triangular tiling in the right panel.

Table 6.3: Exchange integrals (in K, columns 2 and 3), coordination number z (column 4) as well as experimental (column 6) and theoretically calculated (columns 7–9) ordering temperatures T_N (in K) for quasi-one-dimensional cuprates. The ordering temperatures T_N were calculated using Eqs. 6.4–6.6 and the exchange integrals from columns 2 (NN intrachain coupling J_1) and 3 (the interchain coupling J_ic), as well as the z value from column 4. Column 10 shows (T_N calc. / T_N exp.) ratios. Here, for the theoretical estimate, the value from column 9 (the expression from Ref. 245) is adopted. Note that the interchain couplings are not frustrated in the first three systems [Sr_2CuO_3, $CuSe_2O_5$ and $[NO]Cu(NO_3)_3$], partly frustrated in the next three compounds [Ca_2CuO_3, $AgCuVO_4$, and $CaCu_2(SeO_3)_2Cl_2$], while $Sr_2Cu(PO_4)_2$ features fully frustrated interchain couplings.

compound	J_1	J_ic	z	Ref.	T_N exp. [Ref.]	T_N calc. Eqs. 6.4	6.5	6.6	T_N calc. / T_N exp.
Sr_2CuO_3	2200	9	2	[26]	5 [33]	15.0	11.7	11.2	2.2
$CuSe_2O_5$	165	20	2		17	24.5	19.6	18.0	1.1
$[NO]Cu(NO_3)_3$	150	3	2		<4 (?) [233]	4.4	3.5	3.3	~1 (?)
Ca_2CuO_3	1850	42	2	[26]	9 [33]	61.1	48.2	45.6	5.1
$AgCuVO_4$	280	3	6	[88]	2.5 [88]	12.7	10.1	9.5	3.8
$CaCu_2(SeO_3)_2Cl_2$	140	10	6		6	34.3	27.7	25.0	4.2
$Sr_2Cu(PO_4)_2$	187	3	2	[229]	0.085 [248]	4.5	3.5	3.4	400

the spatial exchange anisotropy is expected to lower T_N, while the spin anisotropy raises it. However, it is tricky to estimate how these two effects are balanced in real systems.

The following analysis is an empirical attempt to estimate the influence of frustration onto the magnetic ordering. For this purpose, the LRMO temperatures for several quasi-1D magnetic compounds are compared in a systematic way. To calculate T_N, three different expressions (Eqs. 6.4–6.6) were used. The calculated T_N are given in the three last columns of Table 6.3.

$$\text{Eq. 13 from Ref. 242:} \quad T_\mathrm{N} = 0.32\,|J_\mathrm{ic}|\,z\ \overline{\ln(5.8\,J_1\,T_\mathrm{N}^{-1})}. \tag{6.4}$$

$$\text{Eq. 21 from Ref. 243:} \quad T_\mathrm{N} = 0.23\,|J_\mathrm{ic}|\,z\ \overline{\ln(5.8\,J_1\,T_\mathrm{N}^{-1}) + {}^{1}\!/_{2}\ln\ln(5.8\,J_1\,T_\mathrm{N}^{-1})}. \tag{6.5}$$

$$\text{Eq. 8 from Ref. 245:} \quad T_\mathrm{N} = 0.233\,|J_\mathrm{ic}|\,z\ \overline{\ln(2.6\,J_1\,T_\mathrm{N}^{-1}) + {}^{1}\!/_{2}\ln\ln(2.6\,J_1\,T_\mathrm{N}^{-1})}. \tag{6.6}$$

First, the two well studied quasi-1D cuprates Sr_2CuO_3 and Ca_2CuO_3 are commonly referred as model systems in most theoretical studies regarding the T_N problem. These two systems are essentially different from the other cuprates considered, due to the presence of corner-sharing connections of CuO_4 plaquettes with Cu–O–Cu angle of 180°, giving rise to a large NN coupling of the order of 2000 K. In addition, there is an evidence for an appreciable second-neighbor coupling [26]. Nevertheless, they are referred here for the sake of completeness. For Sr_2CuO_3, the calculated T_N overestimate the experimental values by about a factor of two. Considering the large energy scale of the magnetic couplings and appreciable scattering of their numerical estimates (see Table I in Ref. [26]), the agreement for Sr_2CuO_3 is rather good. For Ca_2CuO_3, the experimental T_N is considerably lower than all theoretical estimates. This origin of this discrepancy will be discussed later.

Similar to Sr_2CuO_3 and Ca_2CuO_3, the structure of $AgCuVO_4$ comprises the corner-sharing chains of CuO_4 plaquettes [249]. However, a sizable bucking of these chains reduces the Cu–O–Cu angle down to 113°, which in turn diminishes the respective AFM superexchange by almost an order of magnitude [88]. There are at least four appreciable interchain couplings [88] that form a rather complex spin lattice: in the bc plane, two relevant interchain couplings form a non-frustrated network, while the two couplings J_{ic1}^{ab} and J_{ic2}^{ab} in the ab plane form J_{ic1}^{ab}–J_1–J_{ic2}^{ab} frustrated triangles. It is difficult to estimate the absolute values of these couplings precisely, but the averaged coupling of about 3 K is claimed to be a reasonable guess [88]. Theory overestimates T_{N} for $AgCuVO_4$ by a factor of four (Table 6.3).

The structural implementation of spin chains in $Sr_2Cu(PO_4)_2$ is essentially different. Here, CuO_4 plaquettes are isolated, and the superexchange is mediated by a double bridge of PO_4 tetrahedra. Special features of such chains can be illustrated by a comparison to the chains of edge-sharing plaquettes. In this way, the spin chains in $Sr_2Cu(PO_4)_2$ can be mapped onto edge-sharing chains, where every second plaquette is cut out [229]. As a result, the new NN coupling (in an edge-sharing chain, it corresponds to the second-neighbor coupling) is still appreciable, while the second-neighbor coupling is negligibly small (the fourth-neighbor coupling in an edge-sharing chain). The interchain coupling regime in $Sr_2Cu(PO_4)_2$ is strongly frustrated due to the presence of triangular units formed by J_1 and two J_{ic} couplings [Fig. 6.16, (f)], which contrasts to the non-frustrated square units in the other compounds. Quite remarkably, the discrepancy between the theoretical estimates and the experimental value of T_{N} for $Sr_2Cu(PO_4)_2$ is especially large: theory yields T_{N} that is more than two orders of magnitude larger than the experimentally observed (Table 6.3).

The microscopic magnetic models for $CaCu_2(SeO_3)_2Cl_2$, $CuSe_2O_5$, and $[NO]Cu(NO_3)_3$ are discussed above. For $CaCu_2(SeO_3)_2Cl_2$, a compound with a complex and partially frustrated interchain coupling regime, theory overestimates the ordering temperature by a factor of four (Table 6.3). In contrast, $CuSe_2O_5$ lacking any appreciable frustration of interchain couplings, shows an excellent agreement between theory and experiment (Table 6.3). Unfortunately, the issue of magnetic ordering in $[NO]Cu(NO_3)_3$ is still under debate [233, 250] and lacks experimental verification.

All the compounds discussed so far can be split into three distinct groups. The first group comprises Sr_2CuO_3, Ca_2CuO_3, $CuSe_2O_5$, and $[NO]Cu(NO_3)_3$, featuring a non-frustrated magnetic model. The compounds with partially frustrated interchain couplings, $AgCuVO_4$ and $CaCu_2(SeO_3)_2Cl_2$, form the second group. Finally, the fully frustrated $Sr_2Cu(PO_4)_2$ should be singled out.

The compounds of the first group, except for Ca_2CuO_3, show good agreement between the experimental T_{N} and its theoretical estimate. To analyze the origin of the large (T_{N} calc./T_{N} exp.) for Ca_2CuO_3, auxiliary DFT calculations were carried out. A preliminary analysis using WFs shows that in addition to the leading interchain coupling t_{ic} ($t_{\perp}$ in the notation of Ref. 26), there is another relevant interchain coupling t_{ic2}. Since $|t_{\mathrm{ic2}}|$ $0.5|t_{\mathrm{ic}}|$, this coupling can play a substantial role in the magnetic properties. Most important, t_{ic2} together with the intrachain coupling t_1, form a spin lattice topologically equivalent to the lattice in Fig. 6.16 (f). Therefore, the actual spin model of $\mathrm{Ca_2CuO_3}$ should be described by Fig. 6.16 (a) rather than (c), while the compound should be placed to the second group (partially frustrated interchain couplings). In contrast, similar analysis performed for $\mathrm{Sr_2CuO_3}$ yields $|t_{\mathrm{ic2}}|$ $0.25|t_{\mathrm{ic}}|$, leading to a factor of 16 difference for J_i^{AFM}. Thus, the spin model of $\mathrm{Sr_2CuO_3}$ can be treated as non-frustrated in good approximation.

As follows from the last column in Table 6.3, the compounds from the second group (with partially frustrated interchain couplings) exhibit sizable deviations between the experimental T_{N} and the theoretical estimates. However, the most remarkable failure of the theoretical approaches manifests itself for the case of $\mathrm{Sr_2Cu(PO_4)_2}$. Taking into account the variety of spin chain types and interchain coupling topologies considered, it is unlikely that the disagreement between theoretical and experimentally observed T_{N} values for $\mathrm{Sr_2Cu(PO_4)_2}$ originates from the neglect of spin anisotropy effects.

Finally, only the magnetic frustration is left to be the dominant reason for a huge discrepancy between theory and experiment. The present analysis reveals that frustrated interchain couplings play a crucial role for the magnetic ordering. This fact explains why theoretical schemes fail to predict T_{N} for frustrated systems. In addition, this observation is fully consistent with the fact, that for systems with partially frustrated interchain couplings [$\mathrm{CaCu_2(SeO_3)_2Cl_2}$, $\mathrm{AgCuVO_4}$, and likely, $\mathrm{Ca_2CuO_3}$], theory works still much better than for the fully frustrated case of $\mathrm{Sr_2Cu(PO_4)_2}$.

In the existing theoretical approaches, a parameter controlling the frustration caused by interchain couplings is missing. Therefore, new theories which would treat magnetic frustration as one of the key issues for the magnetic ordering, are especially needed. On the other hand, there is a lack of information from the experimental side, resulting in a very limited number of systems that challenge the theoretical predictions. Thus, experimental verification of LRMO in $\mathrm{[NO]Cu(NO_3)_3}$ and the measurement of T_{N} could be very helpful to challenge the conjecture on the key role of frustration. Besides, synthesis and investigation of new systems with structural features favoring quasi-1D magnetism, are highly desirable.

6.2 2D models with dimer-like couplings

As demonstrated in the previous section, spin chain compounds have good potential to provide accurate experimental estimates for the leading exchange coupling J_1. This property can be used to challenge DFT-based methods in general, since it provides a reliable scaling for free parameters, such as U_d in the DFT+U methods. However, good reference systems do not necessarily feature a quasi-1D magnetic model. The true prerequisite is distinct separation of the energy scales between the leading magnetic coupling $J = \max(J_i)$ and the other couplings J_i. Thus, the computational approach is further tested for the quasi-2D systems α-$Cu_2P_2O_7$ and $CdCu_2(BO_3)_2$, featuring a single dominant coupling.

Compared to spin chain systems, quasi-2D magnets have certain advantages. From the experimental side, the suppression of quantum fluctuations (compared to the 1D case) leads to a less pronounced reduction of the ordered magnetic moment, facilitating its experimental observation. In addition, the intrinsic contribution typically dominates the experimental $\chi(T)$ behavior of quasi-2D magnets, since such systems are more robust to impurities and defects (compared to the 1D case where every single defect breaks the spin chain). Suppression of quantum fluctuations is advantageous for numerical studies, since purely 2D models can order at $T = 0$, in contrast with the 1D case [94].

This section focuses on the quasi-2D systems with a dominant dimer-like coupling J. The latter term implies the situation where each spin is coupled by J to *at most one* other spin. In the limit of infinitesimal interdimer couplings, the system resides in the singlet (dimerized) GS. However, seemingly small couplings between the dimers can substantially alter the magnetic GS and the excitation spectrum, e.g. stabilizing an LRMO.

Recent vibrant research on dimerized models and systems is largely inspired by their potential to exhibit a peculiar many-body effect—the Bose–Einstein condensation of magnons. This effect has been observed for several $S = 1/2$ Heisenberg magnets, among which the most studied are $TlCuCl_3$ [45], Cs_2CuCl_4 [251] and $BaCuSi_2O_6$ [252, 253].

Following the reasoning of Ref. 254, the Bose–Einstein condensation of magnons can be interpreted as follows. The dimerized magnetic GS is characterized by a gap in the magnetic excitation spectrum: the GS is a singlet, and the lowest lying excitation is a triplet. In magnetic field, the triplet splits into three branches due to the Zeeman effect. The energy of the lowest branch decreases linearly upon increase of the field strength. At some critical field H_c, this branch crosses the energy of the singlet state (unaffected by magnetic field), and becomes the new GS. If the dimers are isolated, the magnetization exhibits a jump from zero (singlet) to the saturation value. However, the interdimer couplings, intrinsic for real materials, give rise to a finite dispersion of the triplet branch. Consequently, the transition to the saturated state occurs continuously between the two critical fields H_{c1} and H_{c2} that correspond to the situations when the bottom and the top of the magnon branch, respectively, cross the GS energy.

The interesting BEC physics is enclosed into the field range between H_{c1} and H_{c2}. At H_{c1}, the system already attains a LRMO. Microscopically, this results in the long-range ordering of $S^{x,y}$ components of the constituent spins. In this ordered state, the elementary excitations are $S = 1$ triplons. The amount of triplons is controlled by the magnetic field, which then plays the role of the chemical potential. Due to their bosonic nature, triplons can occupy the same state, allowing for a formation of BEC.

The experimental verification of BEC is far from being straightforward. One of possible ways is to measure the critical fields as a function of temperature, and this way obtain the critical exponents (e.g. Ref. 252). However, this method requires a large number of measurements and strongly suffers from the absence of sharp transitions. Another solution is to search for characteristic features in the magnetic excitation spectrum, using INS (e.g. Refs. 251 and 255). In most cases, neither of the two experiments can be carried out in a standard lab. Therefore, for a BEC candidate system, it is crucial to learn as much as possible prior to performing $M(H,T)$ or INS measurements.

Dimer formation is a casual structural feature found in numerous magnetic materials. However, by far not every compound from this class exhibits a dimer-like magnetism. Moreover, structural dimers do not necessarily coincide with magnetic dimers. The latter situation is often difficult to identify, since macroscopic measurements do not provide the relevant information on the microscopic model. Even local probes may suffer from ambiguous interpretation, as revealed by extensive studies of the dimer system $CuTe_2O_5$ [43, 256]. In contrast, the DFT-based approach is truly microscopic, and thus free from this shortcoming. Moreover, simulations of the resulting microscopic model are capable to distinguish between gapped and gapless spectra. Finally, the potential to exhibit the BEC behavior can be estimated within this purely computational approach [257].

For challenging the DFT-based approach, an additional advantage of the quasi-2D magnetic systems with dimer-like features is the their proximity to the quantum phase transition between the singlet and LRMO phases. This transition is ruled by the J_i/J ratios of the interdimer couplings and the intradimer coupling. The two resulting GS can be safely distinguished experimentally. Thus, the resulting magnetic GS of the simulated model can be used as an additional criterion to test the computational approach.

6.2.1 $Cu_2A_2O_7$ ($A=$P, As, V)

The dimer-like structures characteristic to the family of $Cu_2A_2O_7$ ($A=$P, As, V) oxosalts, are an excellent playground for studying the interplay between subtle structural details and magnetism. In particular, different AO_4 anionic groups drastically alter the magnetic behavior: coupled dimers in α-$Cu_2P_2O_7$ and alternating chains in α-$Cu_2As_2O_7$ contrast to a honeycomb lattice in β-$Cu_2V_2O_7$. As will be shown, DFT calculations not only provide quantitative microscopic magnetic models for the three systems, but also disclose the origin of the qualitative difference in their coupling regime.

The experimental information on the magnetism of $Cu_2A_2O_7$ ($A=$P, As, V) systems is utterly uneven. The magnetism of β-$Cu_2V_2O_7$ is extensively characterized experimentally. Previous studies generically put forward the essentially 1D magnetism [258–260]. However, the starting point of these studies—the model of spin chains formed by distorted CuO_6 octahedra—is in sharp contrast with the orientation of the magnetically active orbitals. DFT calculations readily refute this model, and propose an unexpected 2D honeycomb lattice model, which allows for a consistent interpretation of all available experimental data. The experimental information on α-$Cu_2P_2O_7$ is scarce: an AFM ordering observed at 27 K was discussed within a tentative model of the magnetic structure established from neutron diffraction [261] and NMR [262], but without any microscopic insight. The magnetism of α-$Cu_2As_2O_7$ was addressed by $\chi(T)$, $C_p(T)$, ESR, NMR measurements in a very recent study [263].

Crystal structure

$Cu_2A_2O_7$ compounds have several polymorph modifications. In the following, the α modifications of $Cu_2P_2O_7$ and $Cu_2As_2O_7$, isostructural to the β modification of $Cu_2V_2O_7$, will be considered.

The building blocks of the structure are Cu_2O_6 dimers, formed by two edge-sharing CuO_4 plaquettes, as well as the A_2O_7 pyro-groups comprising two corner-sharing AO_4 tetrahedra. With respect to the magnetic properties, the structure is essentially 2D, since the magnetic layers (Fig. 6.17, top left) are coupled only by the pyro-groups (Fig. 6.17, top right), and the respective magnetic superexchange is rather small, as confirmed *a posteriori* by the DFT calculations. The structural organization of the magnetic layers in $Cu_2A_2O_7$ systems bears strong similarities to $S = 1/2$ vanadates, such as $(VO)_2P_2O_7$, $VO(HPO_4)\cdot 0.5H_2O$, $KZn(H_2O)(VO)_2(PO_4)_2(H_2PO_4)$ and CsV_2O_5 [264].

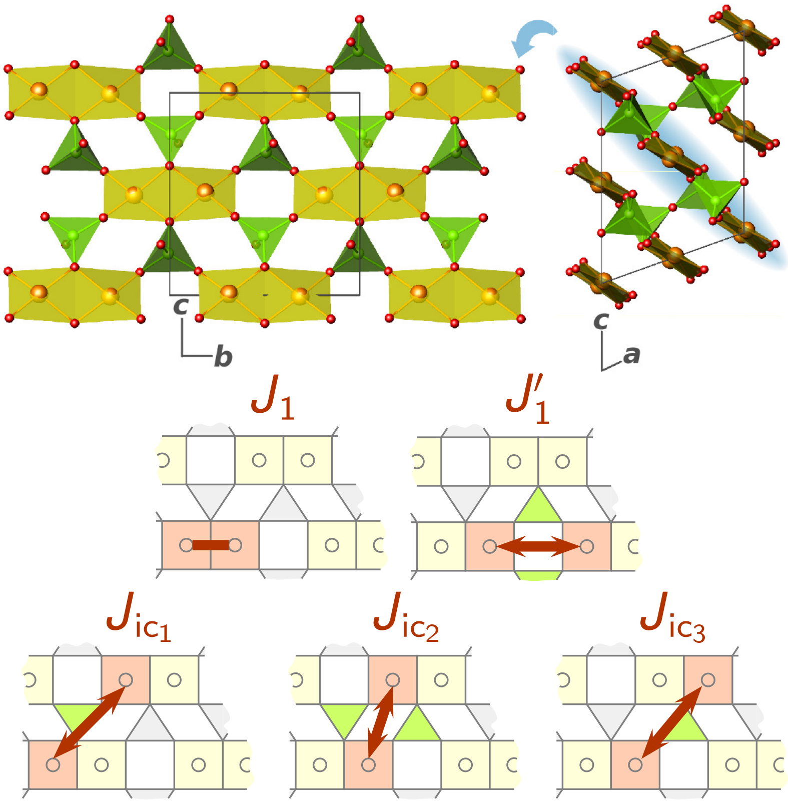

Figure 6.17: Top: magnetic layers (left) in the crystal structure (right) of $Cu_2A_2O_7$. Bottom: five leading exchange couplings in $Cu_2A_2O_7$: intrachain couplings within (J_1) and between (J'_1) the structural dimers. The couplings J_{ic1}, J_{ic2}, and J_{ic3} connect the chains to each other, forming a 2D magnetic layer.

DFT calculations

To evaluate the leading exchange couplings, DFT band structure calculations are performed. For α-$Cu_2P_2O_7$ and α-$Cu_2As_2O_7$, LDA yields a valence band with a width of 10 eV (Fig. 6.18), larger than typical values for cuprates. In contrast, the valence band complex in β-$Cu_2V_2O_7$ is much narrower. A naked-eye comparison of the valence bands hints at similarity of the electronic structures of α-$Cu_2P_2O_7$ and α-$Cu_2As_2O_7$ and unlikeness of both to β-$Cu_2V_2O_7$.

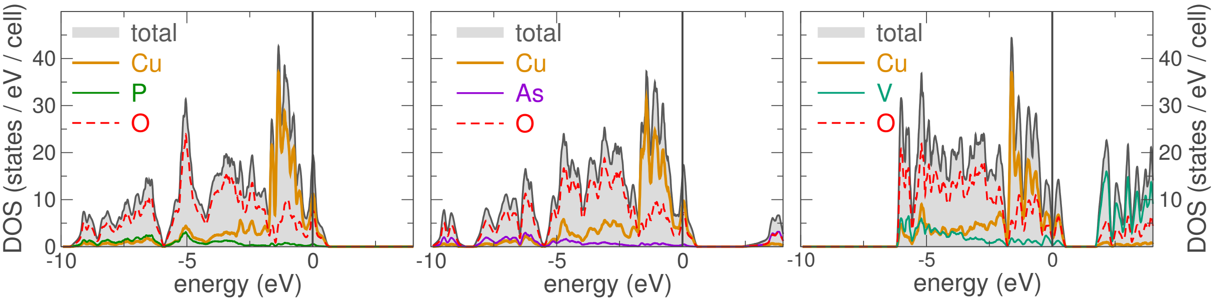

Figure 6.18: LDA DOS for $Cu_2A_2O_7$ ($A=$P, As, V). Note the pronounced difference in the structure of the valence band of α-$Cu_2P_2O_7$ and α-$Cu_2As_2O_7$ on one hand, and β-$Cu_2V_2O_7$ on the other hand.

For all three systems, nonzero DOS at ε_F evidences a metallic GS, in contrast with their insulating nature, but in agreement with the studies discussed in Sec. 6.1, since the LDA systematically underestimates the correlation effects. The structure of the DOS in the vicinity of ε_F is again notably different for α-$Cu_2P_2O_7$/α-$Cu_2As_2O_7$ on one hand, and β-$Cu_2V_2O_7$ on the other hand.

Typical for cuprates, the states at ε_F have the $3d_{x^2-y^2}$ character. The relevant couplings were identified using WFs for the Cu $3d_{x^2-y^2}$ states. The resulting fits are in excellent agreement with the LDA bands (Fig. 6.19) and yield five relevant in-plane couplings. Two of them—the couplings within the structural dimer t_1 and between the structural dimers t_1' (Fig. 6.17, middle)—form alternating chains along the b axis. The chains are connected by two types of interchain couplings: t_{ic1} and t_{ic3} run through a single AO_4 tetrahedron, whereas t_{ic2} connects two Cu atoms with a double bridge of AO_4 tetrahedra (Fig. 6.17, bottom). Together with t_1 and t_1', these interchain couplings form the magnetic layers, parallel to (101), as shown in Fig. 6.17. The interlayer coupling is realized via A_2O_7 pyro-groups and amounts to 30 meV in α-$Cu_2P_2O_7$, 35 meV in β-$Cu_2V_2O_7$, and 40 meV in α-$Cu_2As_2O_7$. Since these couplings are substantially smaller than the leading intraplane terms, they can be neglected in the minimal model.

Numerical values of t_i's are summarized in Table 6.4. A mere comparison of the transfer integrals t_i for the three $Cu_2A_2O_7$ systems suffices to disclose the substantial difference in the coupling regimes. First, the coupling t_1 within the structural dimer is essentially the same in α-$Cu_2P_2O_7$ and β-$Cu_2V_2O_7$, while in α-$Cu_2As_2O_7$ it is substantially larger. In contrast, the interdimer coupling t_1' is almost equal in α-$Cu_2P_2O_7$ and α-$Cu_2As_2O_7$, and much smaller in β-$Cu_2V_2O_7$. Yet, the difference in the interchain coupling regime is even more pronounced: α-$Cu_2P_2O_7$ and β-$Cu_2V_2O_7$ have sizable t_{ic1} and t_{ic3} with negligibly small t_{ic2}, while for β-$Cu_2V_2O_7$ the situation is exactly the opposite. This is in line with the clearly different band dispersions in α-$Cu_2P_2O_7$/α-$Cu_2As_2O_7$ and β-$Cu_2V_2O_7$ (Fig. 6.19).

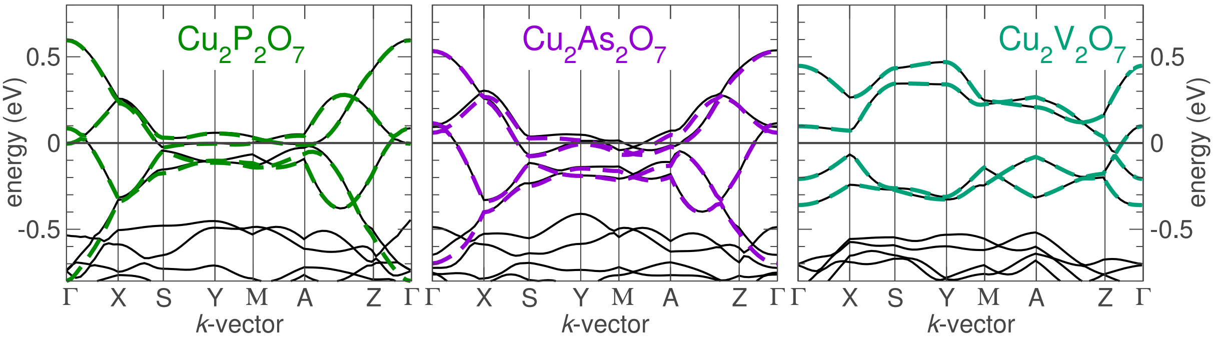

Figure 6.19: WF fits (dashed lines) to the LDA band structure (solid lines) for $Cu_2A_2O_7$. The different dispersion of α-$Cu_2P_2O_7$ and α-$Cu_2As_2O_7$ compared to β-$Cu_2V_2O_7$ hints at different magnetic coupling regimes in these systems. Notation of $\vec{k}$-points: $\Gamma=(000)$,$X=(\frac{\pi}{a}00)$, $S=(\frac{\pi}{a}\frac{\pi}{b}0)$, $Y=(0\frac{\pi}{b}0)$,$M=(0\frac{\pi}{b}\frac{\pi}{c})$, $A=(\frac{\pi}{a}\frac{\pi}{b}\frac{\pi}{c})$, $Z=(00\frac{\pi}{c})$.

Table 6.4: Transfer (t_i, in meV) and exchange (J_i, in K) integrals for α-$Cu_2P_2O_7$, α-$Cu_2As_2O_7$ and β-$Cu_2V_2O_7$. J_i are calculated using LSDA+U, AMF, $U_d = 6.5$ eV and $J_d = 1$ eV. See Fig. 6.17 for path notation.

path	α-$Cu_2P_2O_7$			α-$Cu_2As_2O_7$			β-$Cu_2V_2O_7$		
	t_i	J_i^{AFM}	J_i	t_i	J_i^{AFM}	J_i	t_i	J_i^{AFM}	J_i
X_1	156	251	34	170	298	168	148	226	5
X_1'	103	109	102	104	112	126	−84	73	61
X_{ic_1}	83	71	46	76	60	49	18	3	–
X_{ic_2}	−12	1	–	34	12	–	97	97	87
X_{ic_3}	79	64	41	77	61	48	−15	2	–

The AFM exchange integrals (Table 6.4), evaluated via mapping onto a HUBBARD, and subsequently, onto a HEISENBERG model, apparently sharpen the trends outlined for t_i's. Still, the magnetic model is incomplete, since the Cu–O–Cu angles within the structural dimers are close to 90°, and a sizable FM contribution could be expected at least for J_1. Therefore, LSDA+U calculations are performed using the relevant range of U_d parameters.[10] As in the case of 1D cuprates, discussed in the previous section, $U_d = 6.5$ eV and $J_d = 1$ eV within AMF seems to be an optimal choice. The resulting J_i's calculated are provided in Table 6.4.

The LSDA+U results are in accord with the estimates based on the model approach. In α-$Cu_2As_2O_7$, the rather large value of J_1', which exceeds the respective $J_1'^{\text{AFM}}$ value, likely originates from subtle differences in the way the CuO_4 plaquettes are distorted. However, the 14 K difference between the two values is considerably smaller than the exchange energy scale in this system. Moreover, a slight increase of U_d readily remedies the problem.[11]

LSDA+U calculations yield substantial FM contributions for the intradimer couplings J_1 in all three systems. However, their impact on the magnetic model is different. For α-$Cu_2P_2O_7$ and β-$Cu_2V_2O_7$, a sizable FM contribution of $J_1^{\text{FM}} \sim -220$ K drastically reduces the coupling within the structural dimers, while in α-$Cu_2As_2O_7$, a somewhat smaller FM exchange contribution does not suffice to render J_1 inactive, and it even remains the leading coupling.

---

[10] The relevant range is evaluated based on the studies of quasi-1D systems (Sec. 6.1).

[11] The value of U_d is sensitive to geometrical characteristics of the magnetic plaquettes, such as the Cu–O distances and O–Cu–O angles.

As expected, the interdimer couplings J_1' have negligible FM contributions. In addition, they are only moderately dependent on the nature of the AO_4 groups: α-$Cu_2As_2O_7$ exhibits the largest coupling $J_1' = 126$ K, while it is slightly smaller (102 K) in α-$Cu_2P_2O_7$, and twice smaller (61 K) in β-$Cu_2V_2O_7$.

The interchain coupling regime is essentially different in α-$Cu_2P_2O_7$/α-$Cu_2As_2O_7$ and β-$Cu_2V_2O_7$: for the former systems, J_{ic1} and J_{ic3} are the leading terms, while J_{ic2} is negligibly small. For β-$Cu_2V_2O_7$, it is the other way round. WFs for the magnetically active orbitals elucidate the origin of this difference (Fig. 6.20): for α-$Cu_2P_2O_7$/α-$Cu_2As_2O_7$, essentially no P or As contributions are visible, while the Cu–O–O–Cu paths (Fig. 6.20, left and middle), favor t_{ic1} and t_{ic3} couplings, and consequently, the respective AFM exchange integrals. In contrast, the WF of β-$Cu_2V_2O_7$ shows sizable weight on V atoms, exhibiting a shape reminiscent of the $3d_{3z^2-r^2}$ orbital. These V states hybridize with the nearby O orbitals, thus forming the effective superexchange path Cu–O–V–O–Cu. The V–O hybridization drastically alters the interchain coupling regime, now favoring the J_{ic2} exchange via a double bridge of VO_4 tetrahedra (Fig. 6.20, right).

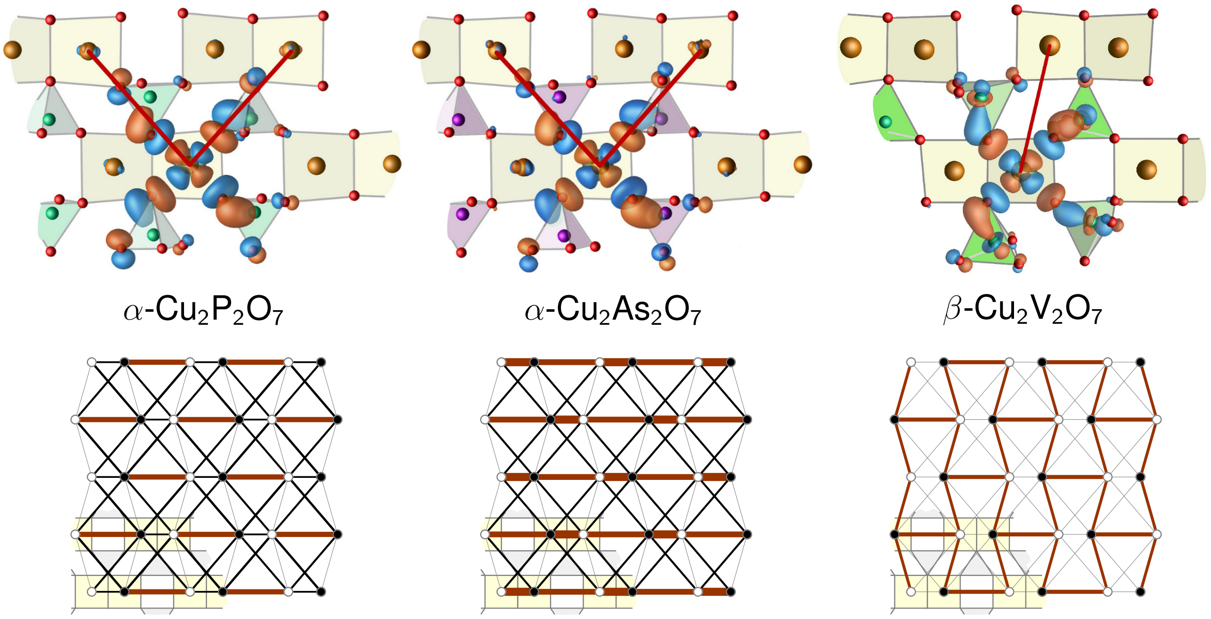

Figure 6.20: Top: WANNIER functions for Cu $3d_{x^2-y^2}$ states with the relevant interchain couplings (lines). Bottom: the spin models for $Cu_2A_2O_7$ compounds. The thickness of a line reflects the magnitude of the respective coupling. Filled and empty circles represent up and down spins in the antiferromagnetically ordered state.

The resulting microscopic magnetic models of $Cu_2A_2O_7$ compounds are remarkably different (Fig. 6.20, bottom). The magnetism of α-$Cu_2P_2O_7$ is dominated by J_1, seemingly favoring a dimer-like behavior, with magnetic dimers formed in between the structural ones. However, as will be shown in the next paragraphs, the interdimer couplings are strong enough to impede the formation of a singlet GS. In α-$Cu_2As_2O_7$, the strong intrachain couplings J_1 and J_1' suggest a quasi-1D magnetic behavior. In α-$Cu_2P_2O_7$, interchain and interlayer couplings again give rise to an LRMO state, although the ordering temperature is considerably lower (11 K versus 27 K in α-$Cu_2P_2O_7$). β-$Cu_2V_2O_7$ exhibits the most nontrivial magnetism. In first approximation, the numerical estimates for the two nonequivalent couplings J_1' and J_{ic2} are similar enough to be considered equal. Such assumption leads to a 2D honeycomb topology of the underlying spin lattice. Since the simulations (next section) suggest that the small anisotropy arising from the two nonequivalent couplings has only a minor impact on the GS, β-$Cu_2V_2O_7$ can be regarded as a good realization of the honeycomb lattice HEISENBERG model.

Simulations

β-$Cu_2V_2O_7$ The spin models of $Cu_2A_2O_7$ are 2D and non-frustrated, hence efficient QMC algorithms can be used. A. TSIRLIN showed that the isotropic honeycomb lattice yields a perfect description to the experimental magnetic susceptibility [265]. Moreover, taking the interlayer coupling into account yields a reasonable estimate for T_N [265]. However, the DFT-model yields two nonequivalent couplings J_1' and J_{ic2} that form an *anisotropic* honeycomb lattice. To evaluate the influence of spatial exchange anisotropy, the ordered magnetic moment as well as the diagonal spin correlations were estimated.

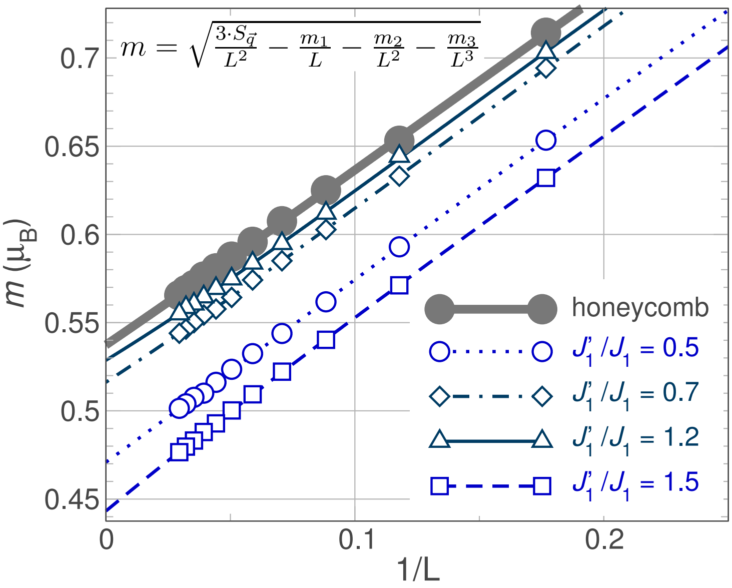

Figure 6.21: Finite size scaling of the ordered magnetic moment m for anisotropic honeycomb lattice, $L = \sqrt{N}$, $\vec{q}$ is the propagation vector of the magnetically ordered state.

As discussed in Sec. 5.5.3, the $1/N$ expansion for the order parameter (ordered magnetic moment) bears sizable inaccuracies. However, a higher-order expansion (the expression is given in Fig. 6.21) yields very accurate results [183]. The results of such scaling for the anisotropic honeycomb lattice model are presented in Fig. 6.21. Although the spatial exchange anisotropy reduces the ordered moment,[12] for the range of ratios $0.7 \leq J_1'/J_1 \leq 1.2$, relevant for β-$Cu_2V_2O_7$, only a minor influence is expected.

---

[12] Such behavior conforms to the enhancement of 1D properties in the anisotropic model.

Another important characteristic of the GS are spin correlations. To address the correlations in the anisotropic honeycomb lattice model, $\langle S_0^z S_i^z \rangle$ were computed for various J_1'/J_1 ratios. Again, the spin correlations for $0.7 \leq J_1'/J_1 \leq 1.2$ are hardly distinguishable from those of the ideal honeycomb lattice (Fig. 6.22). Therefore, the magnetism of β-$Cu_2V_2O_7$ can be effectively described by a HEISENBERG honeycomb lattice model, making this compound a promising model system.

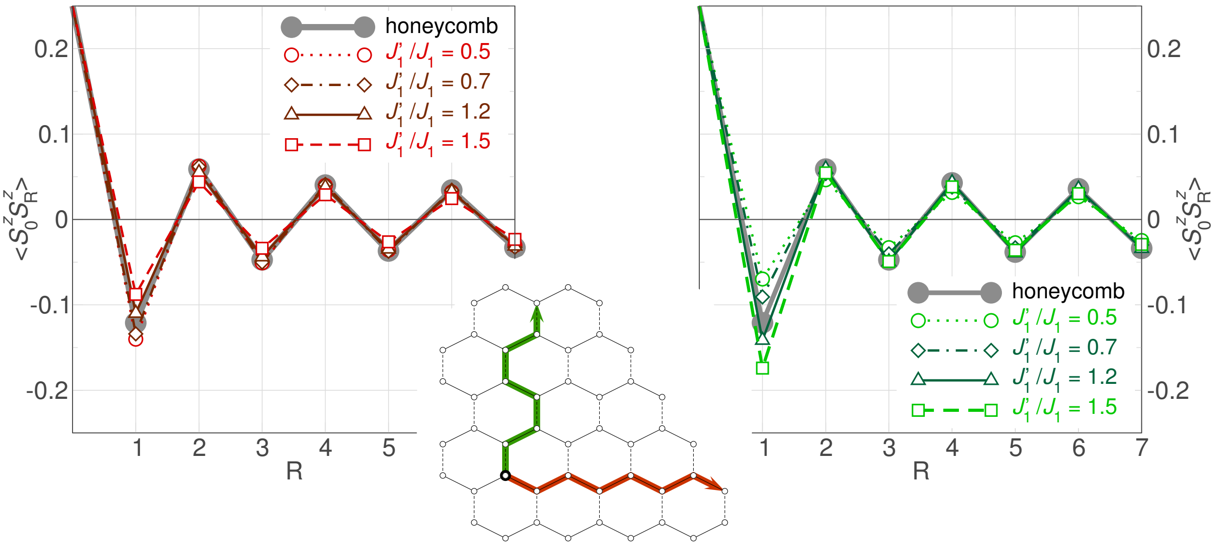

Figure 6.22: Diagonal spin correlations for an anisotropic honeycomb lattice with two nonequivalent NN couplings J_1 and J_1' that correspond to J_1' and J_{ic2} in β-$Cu_2V_2O_7$ (Fig. 6.17), respectively. Bold lines are the results for an ideal (regular) honeycomb lattice. R denotes the coordination sphere. The sketch in the middle panel shows the respective arrangement of S_0 and S_R spins, coupled by J_1 (solid line) and J_1' (dashed line).

α-$Cu_2P_2O_7$ Considering the lack of experimental information on the magnetism of α-$Cu_2P_2O_7$, the DFT-based theoretical study was accompanied by experimental investigation. Powder samples of α-$Cu_2P_2O_7$ were synthesized and characterized [including $\chi(T)$ measurements] by A. TSIRLIN at MPI CPfS. ESR measurements were performed by J. SICHELSCHMIDT (MPI CPfS). High-field magnetization has been measured by F. WEICKERT and YU. SKOURSKI in HZDR HLD.

Magnetic susceptibility has been simulated using QMC for the DFT-based model comprising four relevant terms $J_1' : J_1 : J_{ic1} : J_{ic3} = 1 : 0.33 : 0.45 : 0.40$. The best agreement with the experimental curve is obtained for $J_1' = 79$ K and $g = 2.21$ (Fig. 6.23, top panel), which is in reasonable agreement with $J_1' = 109$ K from LSDA+U (AMF, $U_d = 6.5$ eV) and the powder-averaged $g = (2g_\perp + g\ )/3 = 2.18$.

The simulated magnetization curve (Fig. 6.23, bottom panel) is scaled adopting $J_1' = 79$ K and $g = 2.21$ from the fit to the magnetic susceptibility. The overall agreement with the experiment is rather good, while the residual discrepancy can be ascribed to the imperfect scaling of the experimental high-field curve (Fig. 6.23, inset, bottom panel).

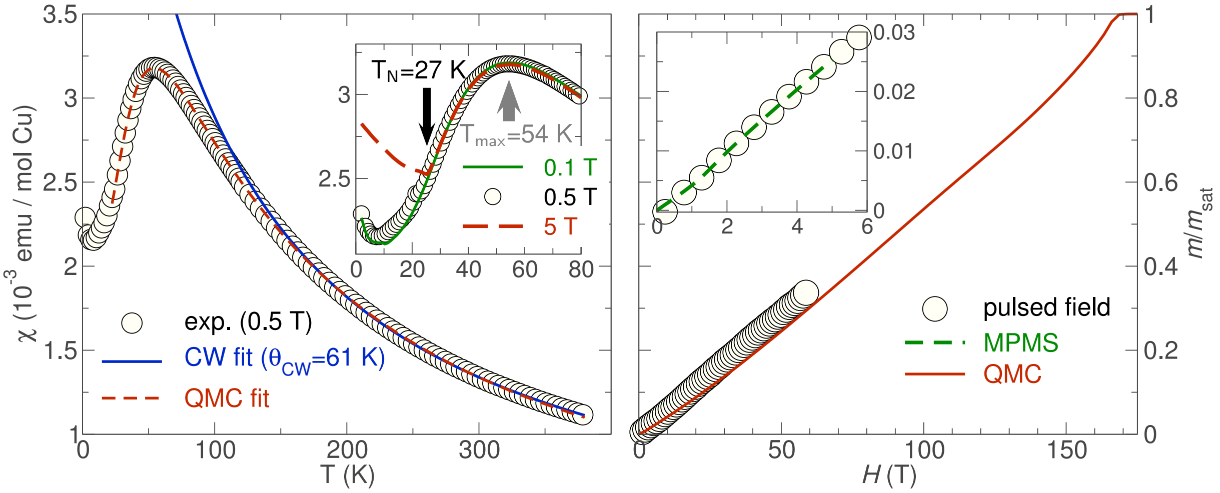

Figure 6.23: Top: QMC and CURIE–WEISS fits to the experimental $\chi(T)$ of α-$Cu_2P_2O_7$. Inset: the field dependence of $\chi(T)$, evidencing a magnetic transition at 27 K and a spin-flop transition between 0.5 and 5 T. Bottom: Experimental magnetization in comparison with the QMC-simulated dependence. The simulated curve was scaled using J and g values from the fit to $\chi(T)$. Inset: the scaling of the high-filed curve using the low-field MPMS data.

α-$Cu_2As_2O_7$ Various experimental probes, such as $\chi(T)$, $M(H)$, ESR and NMR unambiguously resolve LRMO in α-$Cu_2As_2O_7$ [263]. However, the DFT-based model is dominated by J_1 and J_1', and their difference is seemingly large enough to prevent LRMO and drive the system into the singlet GS. To prove the existence of LRMO in the magnetic model of α-$Cu_2As_2O_7$, the spin stiffness ρ_S is evaluated using QMC. At the quantum critical point, the product quantity $\rho_S N$ is independent of N [182]. In this way, the transition between the singlet and the magnetically ordered state can be traced.

The ratio of the leading couplings $J_1 : J_1' = 0.6$ was adopted from the DFT calculations. In addition, $J_{\text{ic1}} = J_{\text{ic3}}$ was assumed. The resulting plots of $\rho_S N$ versus J_{ic1}/J_1 evidence a quantum phase transition at J_{ic1}/J_1 0.18, separating the gapful and gapless GSs. Since this value is slightly smaller than the DFT estimate (0.28), the expected GS is long-range ordered, but T_{N} should be strongly reduced. This conclusion is in excellent agreement with the experiments.

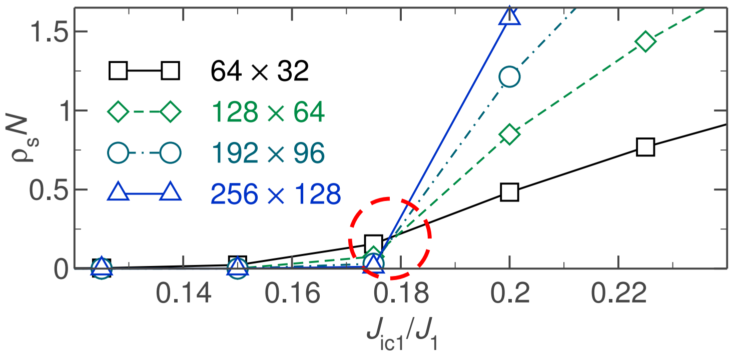

Figure 6.24: Spin stiffness ρ_S multiplied by the finite lattice size N (given in the legend) versus J_{ic1}/J_1 ratio. QMC simulations have been performed for the spin model of α-$Cu_2As_2O_7$ ($J_1' = 0.6\,J_1$, $J_{\text{ic3}} = J_{\text{ic1}}$) at $T = 0.0125\,J_1$. The fingerprint of a quantum phase transition is marked by the red circle. The lines are guides to the eye.

Discussion

Although the $Cu_2A_2O_7$ systems are isostructural, their magnetic properties are very different. It is reasonable to start the discussion with the structure and properties of the magnetic GS. Although all three systems order antiferromagnetically, the difference in the microscopic magnetic models gives rise to different propagation vectors: α-$Cu_2P_2O_7$ and α-$Cu_2As_2O_7$ retain the C-centering of the unit cell, while the magnetic structure of β-$Cu_2V_2O_7$ breaks it (see black and white circles for spin up and down in Fig. 6.20). The magnetic models of α-$Cu_2P_2O_7$ and α-$Cu_2As_2O_7$ comprise the same set of exchange couplings, and yet they are different: α-$Cu_2P_2O_7$ should be regarded as a system of strongly coupled dimers, while the alternating chain description is more appropriate for α-$Cu_2As_2O_7$. The spin correlations in β-$Cu_2V_2O_7$ —an anisotropic version of a honeycomb lattice, hint at a minor influence of the spatial exchange anisotropy, thus the ideal honeycomb lattice HEISENBERG model should properly account for the magnetic excitation spectrum.

So far, α-$Cu_2P_2O_7$ and α-$Cu_2As_2O_7$ reveal strong similarity to each other. However, the LRMO temperature in α-$Cu_2P_2O_7$ (27 K) is very close to that of β-$Cu_2V_2O_7$ (26 K), but in α-$Cu_2As_2O_7$ it is substantially smaller (11 K). The small value of the transition temperature can be explained by a proximity to a quantum critical point. In particular, the alternating HEISENBERG chain exhibits a gapped magnetic spectrum. Interchain couplings reduce the value of the spin gap, and at some critical value drive the system into a magnetically ordered state. The estimated value for the critical interchain coupling ($J_{\mathrm{ic1}}/J_1 \quad 0.18$) is only slightly larger than the respective DFT-based estimate for α-$Cu_2As_2O_7$ (0.28).

To summarize, the computational approach disclosed the fascinating variety of magnetic models realized in $Cu_2A_2O_7$ compounds. α-$Cu_2P_2O_7$ is a system of strongly coupled dimers, which surprisingly exhibits an LRMO. β-$Cu_2V_2O_7$ is a rare example of a system with the honeycomb lattice magnetism. The proximity to a quantum critical point makes α-$Cu_2As_2O_7$ an interesting model system, which magnetism can be possibly tuned by pressure or chemical partial substitution. For all three systems, the LSDA+U calculations for $U_d = 6.5$ eV and $J_d = 1$ eV within AMF yield rather accurate numerical estimates (±20%) for the leading exchange couplings.

6.2.2 $CdCu_2(BO_3)_2$

A natural way to attack a complex problem is to account for its simplified variant first. Not surprisingly, this approach is widely used for interpretation of the experimental results: to start with a simple model, which would describe major features, and subsequently refine it by considering more subtle peculiarities. Provided that the initial, crude model is essentially correct, its further refinement can be done by applying more precise experimental techniques. However, a wrong initial guess can largely impede the interpretation and lead to incorrect conclusions.

Concerning the latter case, the magnetism of $CdCu_2(BO_3)_2$, controversially discussed during the last six years, is very instructive. With respect to its chemical composition, this compound is strongly related to the well-studied SHASTRY–SUTHERLAND (Fig. 6.25, left panel) system $SrCu_2(BO_3)_2$ [46]. However, the smaller ionic radius of Cd^{2+} compared to Sr^{2+} (0.95 Å versus 1.26 Å [266]) leads to a symmetry reduction and alters the crystal structure, giving rise to two independent Cu sites.

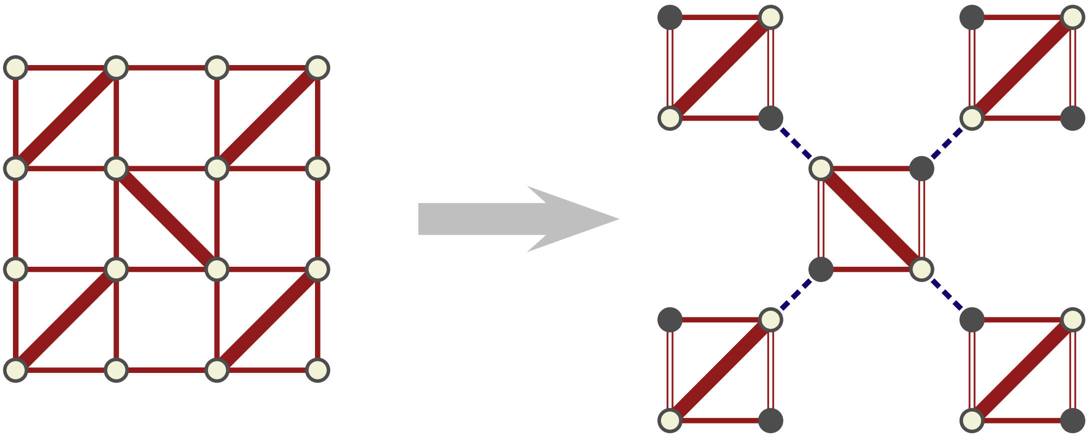

Figure 6.25: Left panel: the original SHASTRY–SUTHERLAND model with the dimer-like coupling J (thick lines) and the coupling J' (thin lines) along the edges of the square lattice. Right panel: the decorated anisotropic SHASTRY–SUTHERLAND model in $CdCu_2(BO_3)_2$. The horizontal and vertical couplings (J' in the original model) are not equivalent, leading to J_{t1} (double line) and J_{t2} (single line). In addition, the coupling J_{it} (dashed line) tiles the lattice into four-spin units (tetramers). Filled circles denote the "decoration" spins.

The initial guess of the magnetic model was based on $\chi(T)$, $C_p(T)$ and $M(H)$ measurements. In particular, the authors of Ref. 267 conjectured that pairs of Cu(1) atoms form magnetic dimers, while Cu(2) sites build spin chains, and these two subsystems (chains and dimers) are decoupled. This model seemingly accounts for the magnetization plateau observed at one-half of the saturation magnetization (the spin chains fully polarized, the dimers retain the singlet state). However, the QMC simulations of this tentative model did not properly account for the experimental data. Sizable deviations of the experimental and the simulated curves made the model assignment questionable [268]. Finally, the ND studies revealed that both Cu(1) and Cu(2) atoms bear a nonzero magnetic moment in the magnetically ordered state, strongly disfavoring the "dimers + chains" picture [269].

A closer look to the crystal structure of $CdCu_2(BO_3)_2$ helps to recognize the drawbacks of the proposed magnetic model. In particular, the mutual arrangement of the magnetic $Cu(1)O_4$ and $Cu(2)O_4$ plaquettes hints at a more complex scenario of magnetic couplings. As will be shown below, DFT calculations disclose the complexity of the underlying magnetic model, which includes three AFM and one FM exchange coupling. Interestingly, the actual magnetic model strongly resembles that of $SrCu_2(BO_3)_2$, yet it is more intricate and less frustrated. Subsequent simulations of the microscopic magnetic model yield excellent agreement with the experiments.

Crystal structure

$CdCu_2(BO_3)_2$ is monoclinic, space group $P2_1/c$, with two independent Cu and B sites, in contrast with $SrCu_2(BO_3)_2$ [46]. The crystal structure of $CdCu_2(BO_3)_2$ was first studied by XRD [270], and later refined at 1.5 and 15 K using ND [269]. No structural transitions were observed in the temperature range between 1.5 and 298 K.

The crystal structure of $CdCu_2(BO_3)_2$ is shown in Fig. 6.26. The local coordination of Cu(1) and Cu(2) is plaquette-like, the $Cu(2)O_4$ plaquettes are tetrahedrally-distorted. The neighboring Cu(1) plaquettes share common edges and form $Cu(1)_2O_6$ structural dimers. These dimers share common corners with $Cu(2)O_4$ plaquettes ("monomers"). BO_3 triangles are pairwise connected by sharing an oxygen atom. $Cu(1)_2O_6$ dimers, $Cu(2)O_4$ monomers, and BO_3 triangles form magnetic layers, almost parallel to $(\bar{1}02)$. Large cavities within the layers accommodate the Cd atoms.

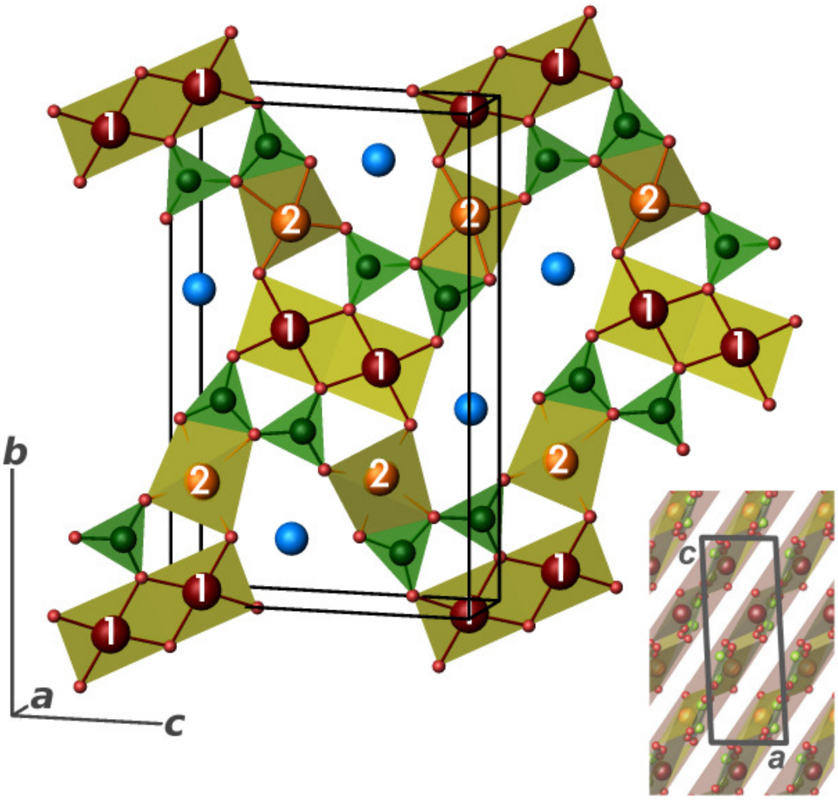

Figure 6.26: Crystal structure of $CdCu_2(BO_3)_2$. Main panel: the magnetic layers. The two types of Cu atoms, "dimer" and "monomer", are denoted by "1" and "2", respectively. BO_3 triangles and Cd atoms are shown green and blue, respectively. Right bottom: position of the magnetic layers (shown shaded) in the crystal structure.

Although the experimental structural data [269, 270] defined at several temperatures correspond to the same structural type, the individual bond lengths and angles are different. As repeatedly discussed in this thesis, magnetic properties are especially sensitive to subtle changes in Cu–O–Cu angles that alter the superexchange along these paths. Thus, in $CdCu_2(BO_3)_2$ the Cu(1)–O–Cu(1) angles within the structural dimers as well the Cu(1)–O–Cu(2) angle between a "dimer" and a "monomer" atom, should be carefully analyzed. The experimentally defined values for the two angles are given in Table 6.5. To evaluate the relation between structural details and magnetism, DFT calculations were performed for all three structural data sets (1.5 K, 15 K and 295 K).

T, K	method	$\widehat{\text{Cu(1)–O–Cu(1)}}$, °	$\widehat{\text{Cu(1)–O–Cu(2)}}$, °	Ref.
1.5	ND	98.2	117.5	269
15	ND	98.5	117.4	269
295	XRD	99.3	118.4	270

Table 6.5: Experimental Cu–O–Cu angles in the crystal structure of $CdCu_2(BO_3)_2$ as a function of temperature.

DFT calculations

LDA yields a valence band with a dominant contribution of Cu and O states (Fig. 6.27, top). The well-separated DOS in the vicinity of ε_F comprises eight bands, as expected for four Cu(1) and four Cu(2) atoms in the unit cell. However, only four of the eight bands cross ε_F, while the other four bands are either empty or filled (Fig. 6.27, bottom left). This situation is a fingerprint of a strong dimer-like coupling.[13] The atomic resolved DOS reveals that the filled and empty bands are dominated by Cu(1) states, hinting at a strong coupling within the structural dimers.

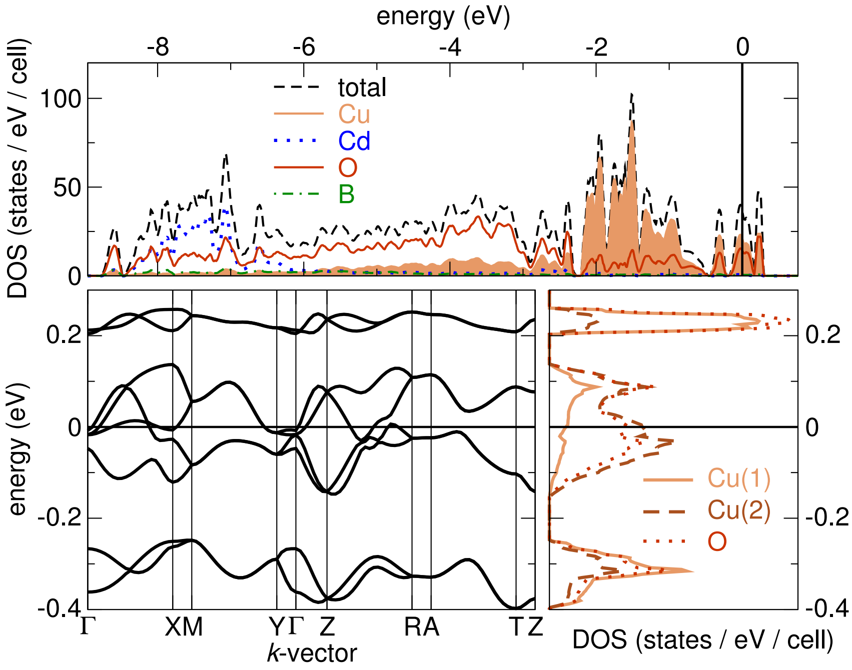

Figure 6.27: Top: LDA DOS for $CdCu_2(BO_3)_2$. Bottom left: $(dp)_\sigma$ bands in the LDA band structure. Bottom right: atom-resolved DOS for the states relevant for magnetism.

The effective one-orbital model has been parameterized using WFs for $3d_{x^2-y^2}$ states of both Cu(1) and Cu(2). The resulting WFs are presented in Fig. 6.28. Besides the apparently present intradimer coupling, sizable weight of the WFs on the O atoms suggests an appreciable coupling via the Cu–O–O–Cu paths. Numerical evaluation of the leading transfer integrals yields the intradimer coupling $t_d = 221$ meV (thick red-black line in Fig. 6.28), two nonequivalent couplings $t_{t1} = 78$ meV (red-white-red lines in Fig. 6.28) and $t_{t2} = 87$ meV (red lines in Fig. 6.28), connecting two Cu(1) and two Cu(2) atoms that form a tetramer, and a coupling between the tetramers $t_{it} = -51$ meV realized via Cu(1)–O–Cu(1) paths (blue

---

[13] Roughly, the splitting between the bands is governed by the leading energy scale (the intradimer coupling), while the band dispersions are ruled by interdimer couplings that are considerably smaller.

Table 6.6: LSDA+U exchange integrals (in K) for $CdCu_2(BO_3)_2$ as a function of DCC and U_d.

DCC	AMF			FLL		
U_d	5.5 eV	6.5 eV	7.5 eV	7.5 eV	8.5 eV	9.5 eV
J_d	297	146	70	356	271	202
J_{t1}	42	30	19	44	36	29
J_{t2}	84	61	48	74	68	57
J_{it}	−61	−45	−34	−181	−160	−135

lines in Fig. 6.28). The second largest intertetramer coupling t_{it2} (not shown in Fig. 6.28) amounts to 40 meV.

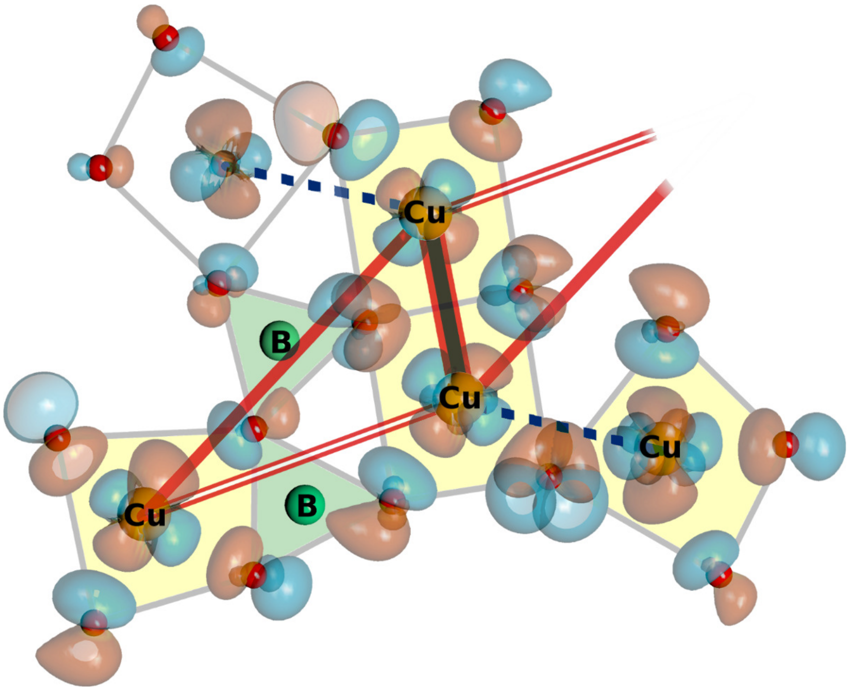

Figure 6.28: Four WFs for $3d_{x^2-y^2}$ states (two "dimer" and two "monomer" Cu atoms) of $CdCu_2(BO_3)_2$. Note the Cu–O–O–Cu superexchange via a double bridge of BO_3 triangles.

Mapping of the effective TB model onto a HUBBARD and a HEISENBERG model yields the substantially large J_d^{AFM} 500 K. The edge-sharing geometry typically gives rise to a sizable FM contribution, therefore the actual spin model should be evaluated from the supercell approach. Moreover, since $CdCu_2(BO_3)_2$ features both edge- and corner-sharing connections of the magnetic plaquettes, the applied DCC scheme is expected to have a substantial influence on the results (see Refs. 15 and 265 for instructive examples). To evaluate the influence of the DCC scheme as well as U_d, the LSDA+U calculations have been performed for a range of U_d between 5.5 and 7.5 eV for AMF and between 7.5 and 9.5 eV for FLL.

In accord with the expected reduction of the magnetic exchange for the edge-sharing geometry, LSDA+U calculations yield considerably reduced values of J_d in comparison with J_d^{AFM} estimates, disregarding the DCC scheme used. As expected for the $J_i^{AFM} \propto t_i^2$ dependence, a rather small value of $|t_{t1} - t_{t2}| = 11$ meV develops into a more substantial difference between J_{t1} and J_{t2}. A less trivial result is the FM nature of J_{it}. Even more surprising is the low value of J_{it2}. This coupling runs between the tetramers, connecting Cu(1) and Cu(2) via Cd atoms. The situation largely resembles the FM system CdVO_3, where the Cd states are responsible for the FM coupling between the spin chains [271]. The sizable $J_{\text{it2}}^{\text{FM}}$ in $\text{CdCu}_2(\text{BO}_3)_2$ is likely caused by a small admixture of Cd 5*s* states. This FM contribution compensates $J_{\text{it2}}^{\text{AFM}}$, and practically renders the respective exchange inactive. Therefore, the minimal magnetic model can be confined to four relevant couplings: J_{d}, J_{t1}, J_{t2} and an FM J_{it}.

The main difference between the AMF and FLL results is the strongly increased absolute value of J_{it} for the latter DCC scheme. This leads to the picture of linear tetramers, where the ultimate Cu(2) atoms are ferromagnetically coupled to one of Cu(2) atoms that form a dimer. This scenario is unlikely, because ED of the respective model Hamiltonian with $J_{\text{d}} + |J_{\text{it}}| \quad J_{\text{t1}} + J_{\text{t2}}$ yields a gapped magnetic excitation spectrum (next section), in contrast with the experiments [269]. On the contrary, the AMF results are in accord with an AFM LRMO, observed experimentally. Therefore, the AMF scenario looks more plausible.

The microscopic magnetic model is plotted in Fig. 6.29. The elementary units are square-like tetramers, formed by two Cu(1) and two Cu(2) spins. Within the tetramer, the Cu(1) are strongly coupled by J_d, while the coupling between Cu(1) and Cu(2) is realized by two inequivalent J_{t1} and J_{t2} running via Cu(1)–O–O–Cu(2) superexchange paths. Since all three couplings are AFM, their competition gives rise to frustration. However, the sizable difference between the numerical values of J_{t1} and J_{t2} largely lifts this frustration. The intertetramer exchange J_{it} is FM, and it couples the tetramers into a magnetic layer.

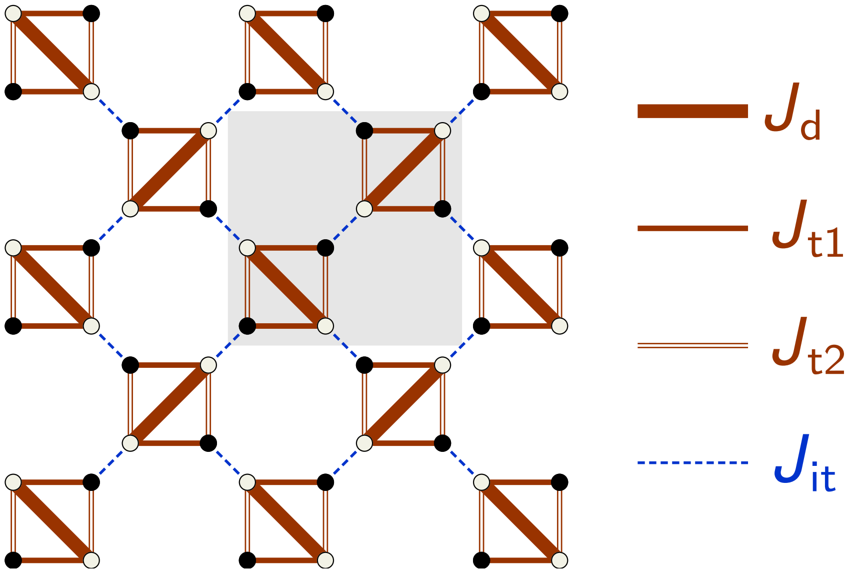

Figure 6.29: Microscopic magnetic model for $\text{CdCu}_2(\text{BO}_3)_2$. Red and blue lines denote AFM and FM couplings, respectively. Line thickness corresponds to the strength of a particular coupling.

Simulations

The microscopic magnetic model is 2D and frustrated, thus ED is a method of choice for simulations. As mentioned in the previous section, the model based on the FLL results exhibits a sizable spin gap, which is too large to be a finite-size effect. Since the gapped spectrum contrasts with the experiments, in the following the AMF-based model is analyzed. The spin correlations for the magnetic GS are depicted in Fig. 6.30. As expected for the strong coupling J_d, spin correlations within the structural dimers are substantial. The absence of a rapid decay of spin correlations, for large R, hints at LRMO.

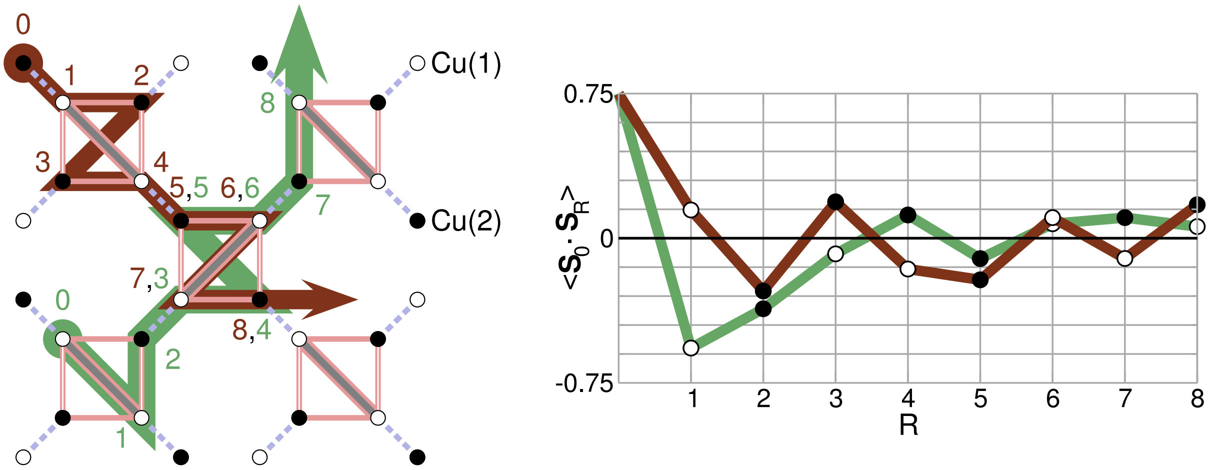

Figure 6.30: Spin correlations in the GS of $\mathrm{CdCu_2(BO_3)_2}$ (right panel). The leading exchange couplings are adopted from the LSDA+U calculations, AMF DCC, $U_d = 6.5$ eV and $J_d = 1$ eV. The paths are given in the left panel.

A peculiar feature of the magnetic GS of $\mathrm{CdCu_2(BO_3)_2}$ is the experimentally observed difference in the values of the ordered magnetic moments localized on Cu(1) and Cu(2) atoms [269]. A crude estimate for the ordered magnetic moment can be obtained from the spin correlations of the maximally separated spins on a finite lattice. Although finite size ($N = 32$ sites) effects impede direct comparison to the experimentally measured magnetic moments, the $\langle \mathbf{S}_0 \cdot \mathbf{S}_8 \rangle$ correlations (Fig. 6.30) of Cu(1) and Cu(2) can be compared to each other. ED yields $\langle \mathbf{S}_0 \cdot \mathbf{S}_8 \rangle[\mathrm{Cu(1)}] = 0.060$ and $\langle \mathbf{S}_0 \cdot \mathbf{S}_8 \rangle[\mathrm{Cu(2)}] = 0.174$, for Cu(1) and Cu(2), respectively. In the simplest picture, the ratio $\sqrt{\langle \mathbf{S}_0 \cdot \mathbf{S}_8 \rangle[\mathrm{Cu(1)}]} : \sqrt{\langle \mathbf{S}_0 \cdot \mathbf{S}_8 \rangle[\mathrm{Cu(2)}]} = 0.59$ should be close to the ratio of the magnetic moments. Although the results may be considerably affected by finite-size effects, a comparison to the experimental [269] $m_{\mathrm{Cu(1)}} : m_{\mathrm{Cu(2)}} = 0.45 : 0.83 = 0.54$ reveals surprisingly good agreement between theory and experiment.

Magnetic susceptibility has been simulated on $N = 16$ sites finite lattice for different $J_\mathrm{d} : J_\mathrm{t1} : J_\mathrm{t2} : J_\mathrm{it}$ ratios, and subsequently fitted to the experimental curve (Fig. 6.31). The best fit is obtained for $1 : 0.2 : 0.45 : -0.2$, which is quite close to $1 : 0.2 : 0.4 : -0.3$ yielded by LSDA+U calculations for AMF DDC with $U_d = 6.5$ eV and $J_d = 1$ eV. The fit yields $g = 2.19$ and $J_\mathrm{d} = 152$ K, in excellent agreement with $J_\mathrm{d} = 146$ K obtained from LSDA+U.

For the $1 : 0.2 : 0.45 : -0.3$ ratio, the GS magnetization has been simulated for $N = 32$ sites finite lattices and scaled using the values of J_d and g from the fit to $\chi(T)$. The resulting curve together with the experimentally measured dependence are shown in Fig. 6.32. Taking into account different temperatures of the simulation (0 K) and the experiment (1.5 K), the agreement between the scaled $M^*(h)$ and the experimental $M(H)$ curve is very good.

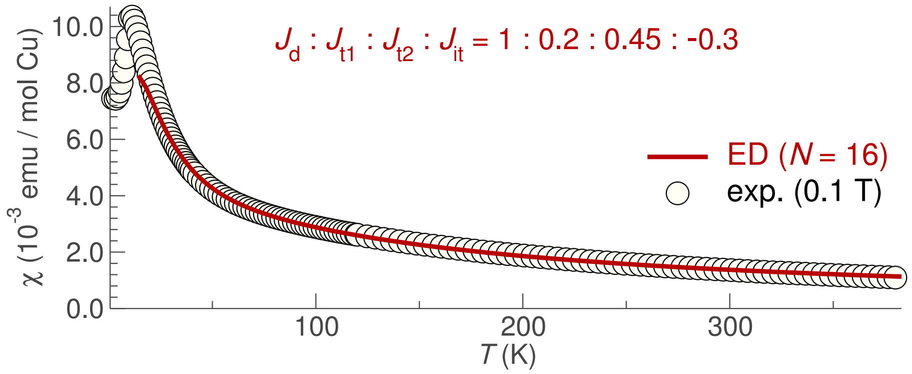

Figure 6.31: Fit to the experimental [269] magnetic susceptibility of $CdCu_2(BO_3)_2$. $\chi^*(T^*)$ was simulated on $N = 16$ sites finite lattices using periodic boundary conditions.

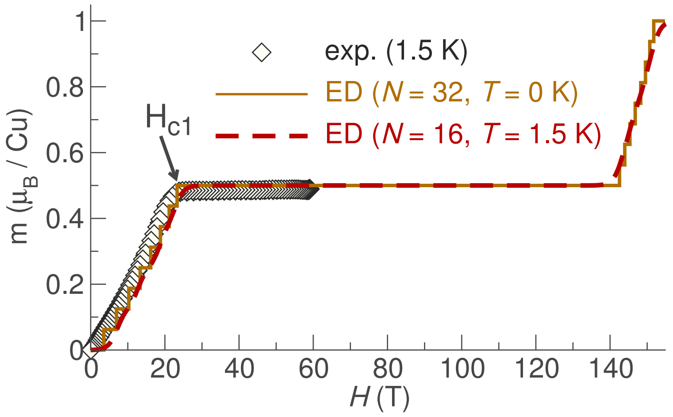

Figure 6.32: Comparison the ED-simulated $M^*(h)$, scaled using J and g from the fit to magnetic susceptibility (Fig. 6.31), with the experimental magnetization curve.

Discussion

The DFT calculations readily refute the initially proposed the "dimers + chains" model, and disclose a more complex 2D frustrated magnetism with four relevant microscopic magnetic couplings. Although the dimer-like coupling J_d is strongly dominant, the competing inter-dimer couplings J_{t1} and J_{t2} as well as the FM coupling J_{it} promote LRMO. The experimental magnetic susceptibility can be well reproduced by the $J_d : J_{t1} : J_{t2} : J_{it}$ ratios derived from the LSDA+U calculations (AMF, $U_d = 6.5$ eV, $J_d = 1$ eV). Remarkably, the overall energy scale (J_d) which can be reliably defined from the experimental magnetic susceptibility, reveals an excellent agreement between experiment and theory.

Although the ED simulations inevitably suffer from finite size effects, the presence of a magnetization plateau at one-half of the saturation magnetization can be safely established. Moreover, the pronounced difference in the strength of Cu(1)–Cu(1) and Cu(2)–Cu(2) spin correlations at the maximal separation on the finite lattices, conforms to the different ordered magnetic moments on Cu(1) and Cu(2), as observed experimentally. The good agreement of $J_d = 152$ K, obtained from the fit to the magnetic susceptibility, and the LSDA+U-derived (AMF DCC, $U_d = 6.5$ eV, $J_d = 1$ eV) $J_d = 146$ K evidence excellent accuracy of the numerical approach.

The main features of the spin model are the strong coupling J_d within the structural dimers, competing intratetramer couplings J_{t1} and J_{t2}, and the FM intertetramer coupling J_{it}. Using the conventional terminology, the microscopic magnetic model of $CdCu_2(BO_3)_2$ can be described as an *anisotropic decorated* SHASTRY–SUTHERLAND lattice (Fig. 6.25, right panel). Although the non-equivalence of J_{t1} and J_{t2} largely reduces magnetic frustration, a potential advantage of $\mathrm{CdCu_2(BO_3)_2}$ is the possibility to explore the phase diagram of this model by tuning the $J_{\mathrm{t2}}\,/\,J_{\mathrm{t1}}$ ratio, e.g. in high-pressure experiments.

6.3 3D model with 1D features in dioptase $\mathrm{Cu_6Si_6O_{18}{\cdot}6H_2O}$

Despite the pronounced differences in the chemical composition and structural organization, all systems discussed so far are low-dimensional magnets. Such low-dimensional behavior manifests itself by distinct experimental features, like for instance, a characteristic broad maximum in the magnetic susceptibility. Interestingly, similar behavior can observed in the systems featuring even a 3D microscopic magnetic model. Obviously, strong quantum fluctuations are a prerequisite in this case. The question is then, what can be the source of quantum fluctuations in a 3D model. The following study of the mineral dioptase provides an unambiguous evidence that a small coordination number of the underlying spin lattice invokes low-dimensional behavior despite the 3D character of the spin lattice itself. It is an instructive example showing that the low-dimensional magnetism is not confined to the low-dimensional magnetic models, but rather to a broader class of models that are either low-dimensional or bear small coordination numbers, or both.

Dioptase $\mathrm{Cu_6Si_6O_{18}{\cdot}6H_2O}$ is a well-known mineral, which typically occurs as dark green crystals. Its similarity to emerald led to considerable confusion and gave rise to a popular belief in its special mystical powers that grant an owner of this gemstone the ability to understand the language of birds or to talk to trees.

Even the magnetic properties of dioptase were cloaked in mystery for a long time. In particular, several experimental studies yielded quantitatively controversial results [272–276]. Besides the discrepancies that are likely related to dioptase samples originating from different locations, the experimental studies essentially converge in the description of dioptase as an antiferromagnet with a rather low Néel temperature (T_{N} 15 K) compared to the Curie–Weiss temperature of about 45 K [276]. The ordered magnetic moment ($m = 0.55\,\mu_{\mathrm{B}}$ [276]) is considerably reduced with respect to the classical value of $1\,\mu_{\mathrm{B}}$. In order to account for the experimental behavior of dioptase, the authors of Ref. 16 suggested a microscopic model with two relevant AFM exchange couplings: the coupling J_{c} along the spiral chains and the coupling J_{d} within the structural $\mathrm{Cu_2O_6}$ dimers. This study places the compound in proximity to a quantum critical point due to a competition between chain-like ordering favored by J_{c} and magnetic dimer formation caused by J_{d}. Although this model conforms to the rather low values of T_{N} and the ordered moment, it yields only a rather poor fit to the experimental magnetic susceptibility, as revealed by the QMC simulations for a wide range of $J_{\mathrm{d}}/J_{\mathrm{c}}$ ratios (Fig. 4 in Ref. 16).

In the following, a new microscopic magnetic model for dioptase is established. The resulting minimal model contains the AFM coupling J_{c} and the FM coupling J_{d}, as was suggested before based on the ND results for the related compound — anhydrous black dioptase [274]. Subsequent QMC simulations of this model evidence that the FM nature of J_d resolves all mentioned controversies and yields an excellent agreement with the experiments.

6.3.1 Crystal structure

The crystal structure is trigonal, space group $\bar{3}$. The general structural organization of dioptase is depicted in Fig. 6.33 (left). In the mineralogical textbooks, dioptase is typically considered as a ring silicate, with isolated $[Si_6O_{18}]^{12-}$ rings as the key element of the crystal structure. However, for the magnetic properties of dioptase, these rings play only a minor role, and the magnetic couplings regime is governed by the mutual connection of magnetic units. Typical for cuprates, these units are slightly distorted CuO_4 plaquettes. Water molecules reside in the vertices of elongated $CuO_4(H_2O)_2$ octahedra.

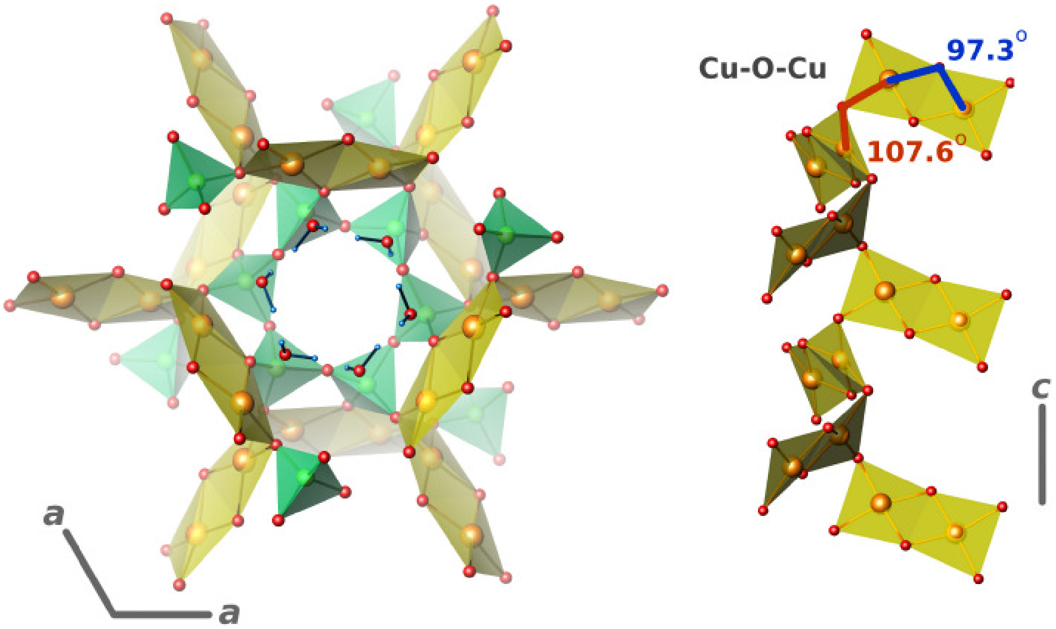

Figure 6.33: Crystal structure of dioptase $Cu_6Si_6O_{18}\cdot 6H_2O$. Left: projection perpendicular to the c axis. The structure is formed by Cu_2O_6 dimers (yellow), SiO_4 tetrahedra (green) and water molecules (O atoms with two blue O–H bonds). The fading corresponds to different distances between the respective polyhedra and the projection plane (darker means closer). Right: the spiral chains along c formed by corner-sharing connections of the structural dimers.

Each plaquette shares a common edge with one of the neighboring plaquettes forming a Cu_2O_6 structural dimer, and has two corner-sharing connections with the plaquettes belonging to the neighboring dimers (Fig. 6.33, right). Despite only two types of connections, the resulting 3D openwork motive is rather complex and does not represent any archetype topology. The Cu–O–Cu angles amount to 97.3° and 107.6° for the edge- and corner-sharing connections, respectively.

6.3.2 DFT calculations

The LDA atom-resolved DOS depicted in the top panel of Fig. 6.34 reveals a rather unusual structure of the valence band. In addition to the typically dominant Cu and O states, the sizable H_2O contribution originates from the apical position of the crystal water in the distorted $CuO_4(H_2O)_2$ octahedra, and thus rather short Cu–O_{H_2O} distances of 2.51 and 2.66 Å. The width of the valence band is about 9 eV, slightly larger than in other cuprates. The well-separated density at ε_F is formed by Cu–O $(dp)_\sigma$ states.

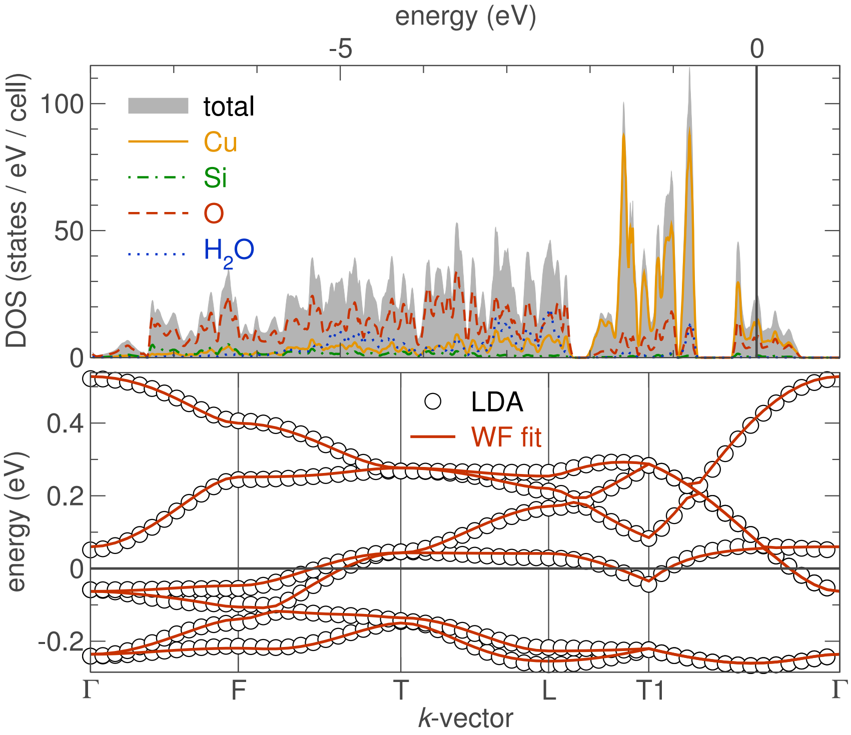

Figure 6.34: Top: LDA total and atom-resolved DOS. "H_2O" is the sum of the water-molecule H and O_{H_2O} states. Consequently, to avoid the double counting, the "O" states do not contain the contribution of the O_{H_2O} atom. Bottom: band structure and the WF fit within the effective one-band model. Notation of $\vec{k}$-points: Γ=(000), F=$(\frac{\pi}{a}0-\frac{\pi}{c})$, T$(\frac{\pi}{a}\frac{\pi}{b}-\frac{\pi}{c})$, L=$(0\frac{\pi}{b}0)$, T_1=$(\frac{\pi}{a}\frac{\pi}{b}\frac{\pi}{c})$.

The well-separated DOS at ε_F is formed mainly by Cu and O states. A projection onto a set of local orbitals readily yields the dominant $3d_{x^2-y^2}$ character of the Cu states. However, the peculiar non-coplanar orientation of the neighboring plaquettes impedes a straightforward evaluation of the orbital character of the relevant O states. In particular, the orbital-resolved DOS for the O states shows a mixture of $2p_{x,y}$ and $2p_z$ states. This can be illustrated by addressing the orbital-resolved DOS for individual atoms. The states corresponding to the O atoms bridging two Cu atoms in a dimer show a clearly planar character. For the O atoms linking two neighboring dimers, the O $2p_x$ and O $2p_z$ contributions are comparable, because the O $2p_z$ states correspond to the O $2p_x$ states of the neighboring dimer, while the O $2p_y$ contribution is negligible. Thus, although the O $2p_z$ contributions are unusually high and seemingly hint at sizable O $2p_\pi$ contributions, the states at ε_F are clearly dominated by Cu–O $(dp)_\sigma$ states. Since the number of bands forming the band complex coincides with the number of plaquettes in the unit cell, the magnetic properties of the compound can be described by an effective one-orbital TB model.

The WF fit yields two relevant transfer integrals: $t_c = 126$ meV, running along the spirals of dimers (in the c direction), and $t_d = 104$ meV, the intradimer coupling. Other hoppings are smaller than 25 meV and thus can be neglected in the minimal model. The mapping onto a Hubbard and a Heisenberg model delivers $J_c^{AFM} = 164$ K and $J_d^{AFM} = 112$ K. Since exchange integrals $J_{ij}^{AFM} \propto t_{ij}^2$, all further exchanges are smaller than 6 K (less than 4 % of the leading exchange).

The examples of $Cu_2A_2O_7$ (Sec. 6.2.1) and $CdCu_2(BO_3)_2$ (Sec. 6.2.2) evidence that the edge-sharing-plaquettes geometry can give rise to sizable J_i^{FM} for the coupling within the structural Cu_2O_6 dimers. For dioptase, J_d^{FM} even outgrows the respective AFM contribution and renders this coupling FM. In particular, the calculation adopting $U_d = 6.5$ eV within the AMF DCC scheme yields $J_c = 110$ K and $J_d = -66$ K. Thus, the FM contributions amount to $J_c^{FM} = 54$ K and $J_d^{FM} = -178$ K, respectively.

To challenge the FM nature of J_d, LSDA+U calculations have been performed for a wide range of U_d, using both AMF and FLL DCC. The results for the individual couplings J_c and J_d, as well as for their ratio J_d/J_c are presented in Fig. 6.35. Although the individual values of the exchange couplings depend on the value of U_d, the J_d coupling is FM disregarding the parameters used.

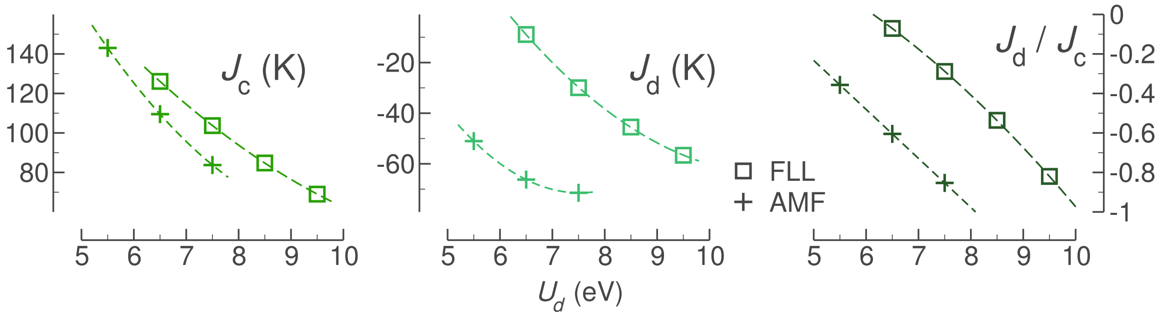

Figure 6.35: LSDA+U results for J_c, J_d and J_d/J_c ratio in dioptase $Cu_6Si_6O_{18}{\cdot}6H_2O$. Note that for J_d/J_c AMF and FLL yield qualitatively similar results, with a constant shift U_d^{AMF} $(U_d^{FLL} - 2\,\text{eV})$.

Supporting the conclusions of Refs. 16 and 274, the microscopic analysis yields only two relevant magnetic couplings in $Cu_6Si_6O_{18}{\cdot}6H_2O$. These two couplings build a complex 3D network formed by J_c chains that are coupled to each other by FM J_d (Fig. 6.36). In contrast with Ref. 16, the LSDA+U calculations evidence the FM nature of J_d, with consequently different physics. The sizable dependence of the J_d/J_c ratio on the value of U_d (Fig. 6.35) makes an extensive analysis of the resulting J_c–J_d model necessary.

6.3.3 Simulations

The non-frustrated nature of the magnetic model allows to use QMC algorithms. QMC simulations performed for the relevant parameter range $-1 \leq J_d/J_c \leq -0.2$ of the J_c–J_d model, evidence that the J_d/J_c ratio can be varied in a rather wide range between -0.8 and -0.4, yielding a very good fit to the experimental $\chi(T)$ above T_N. Therefore, the fitting of $\chi(T)$ alone does not suffice to provide an accurate estimate for J_d/J_c.

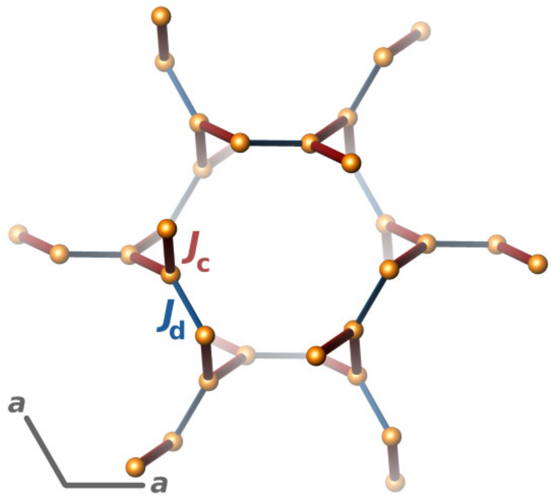

Figure 6.36: Microscopic magnetic model for dioptase $Cu_6Si_6O_{18}{\cdot}6H_2O$. AFM J_c couplings (red thick lines) form spiral chains coupled together by FM J_d couplings (blue thinner lines). The projection perpendicular to the c axis is shown (same as in the left panel of Fig. 6.33). The fading corresponds to different distances between the respective couplings and the projection plane (sharper means closer).

To improve the refinement of J_d/J_c, the magnetic ordering temperature T_N is traced by a distinct kink in the simulated curves. The reference to T_N yields J_d/J_c close to -0.5. The respective fit is shown in the top panel of Fig. 6.37. The resulting $J_c = 78$ K agrees well with the DFT estimates: 110 K for $U_d = 6.5$ eV and $J_d = 1$ eV within AMF ($J_d/J_c = -0.6$) and even better with 85 K at $U_d = 8.5$ eV in the FLL scheme ($J_d/J_c = -0.55$). Moreover, the resulting $g = 2.26$ and $\chi_0 = -6.9 \cdot 10^{-5}$ emu (mol Cu)$^{-1}$ are consistent with the estimates from the CURIE–WEISS fit [2.30 and $-7.2 \cdot 10^{-5}$ emu (mol Cu)$^{-1}$, respectively].

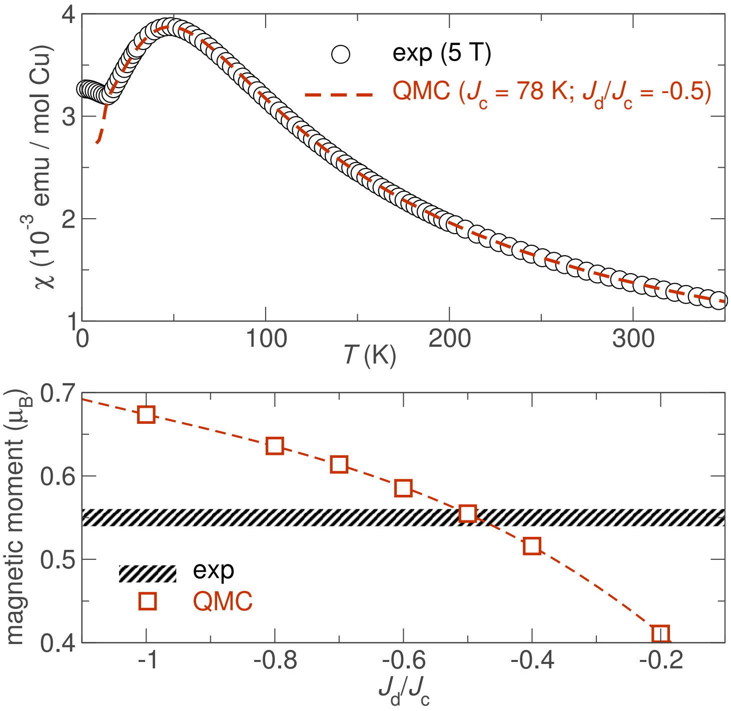

Figure 6.37: QMC simulations for the J_c–J_d magnetic model of dioptase $Cu_6Si_6O_{18}{\cdot}6H_2O$. Upper panel: fit to the magnetic susceptibility. Lower panel: comparison of the simulated and the experimental value for the ordered magnetic moment.

For a further test of the microscopic model, the magnetic GS properties are considered. First, the propagation vector $\vec{q}$ of the AFM ordered GS coincides with the experimentally observed $\vec{q} = (0, 0, {}^{2\pi}/_{3})$ [276] in the whole range $-1 \leq J_d/J_c \leq -0.2$. In this GS, the neighboring spins along the spiral chains (J_c) align antiferromagnetically, while the ordering within the edge-shared dimers (J_d) is FM. This justifies the validity of the microscopic model, but does not allow for a more accurate refinement of the $J_\mathrm{d}/J_\mathrm{c}$ ratio.

For a further comparison, the ordered magnetic moment $m = 0.55(1)\,\mu_\mathrm{B}$ [276] is considered. The simulated value of m is estimated from the finite-size scaling of the static structure factor (Eq. 5.10 on page 76), taken for the propagation vector of the ordered structure. The results of the simulations for various $J_\mathrm{d}/J_\mathrm{c}$ ratios are shown in the bottom panel of Fig 6.37. Remarkably, the theoretical m for $J_\mathrm{d}/J_\mathrm{c} = -0.5$ is in good agreement with the experimental value.

6.3.4 Discussion

The DFT-based analysis reveals a peculiar microscopic magnetic model in dioptase: the spin lattice is 3D and non-frustrated, hence any references to the frustrated spin chain model should be precluded. As in the case of $\mathrm{Cu}_2A_2\mathrm{O}_7$ systems (Sec. 6.2.1), the AMF DCC with $U_d = 6.5$ eV and $J_d = 1$ eV yield numerically accurate results for the leading couplings. It is important to note that the magnetic model in dioptase is very different from the star lattice. Such confusion can arise from a specific projection of the spin lattice, where the segments of the spiral chains look like flat frustrated triangles (Fig. 6.36).

Instead, the spin lattice in dioptase can be described in terms of AFM spin chains running along the c direction that are arranged on the honeycomb lattice, i.e. each chain is coupled to the three neighboring chains, and the system is geometrically 3D (Fig. 6.33).

The experimental data for dioptase give evidence for strong quantum fluctuations: the broad susceptibility maximum at $T_\mathrm{max}/J_\mathrm{c}$ 0.64, the low Néel temperature ($T_\mathrm{N}/J_\mathrm{c}$ 0.2), and the reduced magnetic moment $0.55\,\mu_\mathrm{B}$. The magnetic moment is even lower than $0.6\,\mu_\mathrm{B}$ found for the Heisenberg model on the 2D square lattice geometry, thus quantum fluctuations in the dioptase spin lattice are even stronger than in the square lattice. Quantum fluctuations in a 3D spin system can arise from magnetic frustration (e.g., Ref. 82), but the dioptase spin lattice is neither low-dimensional, nor frustrated, hence its quantum behavior has a different origin. Thus, it is the low coordination number of the lattice that reduces the exchange energy (which stabilizes the ordered GS), and thus is solely responsible for the observed low-dimensional behavior.

Dioptase is often called “green dioptase”, to distinguish it from the “black dioptase” $\mathrm{Cu_6Si_6O_{18}}$,[14] which exhibits similar magnetic properties [274, 277]. The substitution of Si with Ge leads to the new compound $\mathrm{Cu_6Ge_6O_{18}\cdot 6H_2O}$, isostructural to green dioptase [278]. Dehydration or chemical substitution of side groups is a promising route to tune the magnetism of dioptase toward more interesting phases. Besides the quantum critical point, discussed for the case of two AFM couplings [16], a strong J_d may lead to an exotic hyperkagome lattice of effective $S = 1$ spins [279]. This issue deserves further investigation.

---

[14] Strictly speaking, “black dioptase” is not a mineral and therefore should not be called dioptase at all. However, this term is already deeply implanted in scientific literature (e.g. Refs. 274 and 277), which makes it at least worth mentioning.

Interestingly, while neither the dioptase crystal structure, nor its spin model look low-dimensional, the essential physics is governed by strong quantum fluctuations, typical for low-dimensional magnets. The above considerations should stimulate further studies of dioptase-structure-like materials and the respective spin model.

6.4 Summary

The developed computational approach has been successfully applied to several cuprate materials exhibiting low-dimensional magnetic behavior. For all the systems, simulations of the DFT-based magnetic models accurately reproduce the available experimental data.

Although standard parameterizations of the exchange and correlation potential (LDA and GGA) yield a wrong electronic ground state due to underestimation of the correlation effects, they provide an accurate description of kinetic processes (virtual electron hoppings). Adding the missing part of electronic on-site correlations (HUBBARD model) leads to a reliable quantitative magnetic model describing the leading AFM couplings.

The FM part of the magnetic exchange can be evaluated using the DFT+U approach. For the compounds with decoupled magnetic CuO_4 plaquettes, extensive comparisons between the simulated and the measured quantities suggest that the DFT+U method as implemented in `FPLO` (version 6 and later) yields generally accurate estimates for the leading exchange integrals using AMF DCC with $U_d = 6.5$ eV. However, in the case the edge- and/or corner-sharing connections of CuO_4 plaquettes are present, DFT+U calculations can show a nontrivial dependence of the resulting J_i's on U_d and especially, the DCC scheme.

Since experimental evaluation of small interchain or interplane couplings is at best nontrivial and challenging, DFT calculations seem to be a natural alternative to attack this problem. Originally designed to account for the leading exchange couplings, the computational method reveals surprisingly good numerical accuracy even for the couplings one or two orders of magnitude smaller than the leading energy scale. The studies of quasi-1D systems evidence that DFT can safely distinguish between small, but relevant, and practically absent couplings, providing a unique possibility to explore small interchain and interplane magnetic couplings.

Chapter 7

Kagome lattice compounds

7.1 Introduction

Onsager's exact solution of the Ising model on a square lattice published in 1944 [280] has spurred scientific activity in the field of model magnetism. Subsequent studies extended this approach to other spin lattice topologies. Not surprisingly, the highly symmetrical lattices with possibly simple topology were addressed first. The class of Archimedean lattices, that are comprised of regular polygons, perfectly matches these criteria (the square lattice itself is indeed an Archimedean lattice).

Particularly simple lattices are formed by equivalent polygons of just one type: these are, besides the square lattice, the triangular and the honeycomb lattice. On the next level of complication, lattices comprising two types of polygons can be considered, such as the star lattice, composed of dodecagons and triangles; two lattices composed of triangles and squares as well as two lattices comprising regular triangles and hexagons. By virtue of a particularly simple topology, one of the latter two soon became a subject of theoretical investigation. Only after decades, it became gradually evident that this specific lattice exhibits the most exotic magnetic properties among the whole class of Archimedean lattices.

The name "kagome" was introduced in 1951 by Itiro Syôzi[1], who first addressed the issue of magnetic ordering of Ising spins in this geometry [282]. In his analysis, Syôzi considered the FM as well as AFM coupling. For the latter case, he concluded that magnetic ordering should be suppressed. Two years later, a different method applied to the problem confirmed this conjecture [283].

The activity on the kagome model had been gradually dying out, until the first candidate materials were found in early 1970's. These were minerals from the jarosite group ("jarosites") with the formula $R\mathrm{Fe}_3(\mathrm{OH})_6(\mathrm{SO}_4)_2$ [$R = (\mathrm{NH}_4)$, Na or K] [284], exhibiting a non-collinear AFM GS state (e.g., Ref. 285). Later, it has been found that the substitution of $S = 5/2$ Fe^{3+} by $S = 3/2$ Cr^{3+} led to a different magnetic behavior caused by more pronounced quantum fluctuations in the latter case [286].

---

[1] Ref. 281 reserves the idea to christen the lattice for Kodi Husimi, the leader of the group in which Itiro Syôzi worked.

The first system proposed to be a good realization of a $S = 3/2$ kagome HEISENBERG antiferromagnet was $SrCr_8Ga_4O_{19}$ [287]. Followed by the experimental studies (e.g. magnetization [288, 289], μSR [290] and NMR [291, 292] measurements), the discovery of the material has revived interest to the kagome model itself.

The central problems actively debated in the literature were the structure of the magnetic GS and the issue of magnetic ordering. Mean-field theory predicts the absence of long-range magnetic ordering [293]. On the classical level, the GS of the kagome HEISENBERG model is infinitely degenerate [294, 295]. This degeneracy can be lifted, at least partially, by thermal [296] or quantum [297] fluctuations. In particular, thermal fluctuations tend to select coplanar GSs, following the mechanism known as "order-by-disorder" [298].

On the kagome lattice geometry, two coplanar GSs with different propagation vectors can be realized: the $\vec{q} = (0,0)$ (or shortly, $q = 0$) state for which the magnetic cell coincides with the unit cell, and the $\vec{q} = (2\sqrt{3}\pi, 2\sqrt{3}\pi)$ (typically regarded as "$\sqrt{3} \times \sqrt{3}$") state with the magnetic cell three times larger than the unit cell [299]. Linear spin-wave theory and series expansions reveal a subtle interplay between $q = 0$ and $\sqrt{3}\times\sqrt{3}$ phases in the presence of the second- and third-neighbor couplings [300]. In a recent study, L. MESSIO *et al.* systematically examined the classical HEISENBERG model on a kagome lattice, by taking second- and third-neighbor interactions into account [301]. Their variational approach delivers, in addition to the $q = 0$ and $\sqrt{3} \times \sqrt{3}$ phase, also three non-coplanar states: two cuboctahedral states and an octahedral state. These states are regular, i.e. they depend on the symmetries of the model and do not scale with the model parameters J_i.

While the classical GS on the kagome lattice is an explored territory, the structure of the respective quantum GS is still far from being understood. At present, there is no doubt that the GS lacks LRMO, but its properties are actively debated. In particular, the series expansion studies [302, 303] as well as the recent multiscale entanglement renormalization ansatz (MERA) analysis [304] favor the valence bond crystal (VBC) magnetic GS, suggested also for the spin-1/2 frustrated square lattice [305] and the pyrochlore lattice [306]. The VBC GS is formed by long-range ordering of spin singlets and is characterized by broken translational symmetry and a finite gap in the excitation spectrum.

Other studies propose the emergence of a spin liquid GS on the kagome lattice. However, there is still no consensus, whether this spin liquid is topological and has a gapped excitation spectrum [307] or it is gapless and critical (algebraic) [308].[2] At present, state-of-the-art DMRG calculations are in favor of the former scenario [311]. A crucial present-day task is to ascertain, which of the two GSs (if any) is realized in real $S = 1/2$ kagome materials.

ED of finite kagome lattices with up to $N = 36$ sites reveals a peculiar excitation spectrum with a large number of singlets filling the spin gap (in particular, 153 singlets for a $N = 27$

---

[2] Topological spin liquids got their name from the specific type of ordering (topological), which emerges in systems featuring both a degenerate GS and a spin gap [309]. Critical spin liquids, also called algebraic, exhibit a power-law decay of the spin correlations, while the respective exponent is universal [310].

sites lattice [83] and 210 singlets for a $N=36$ sites lattice [312]) and no separated Pisa tower of quasi-degenerate joint states.[3] Interestingly, static impurities induce sizable dimer-dimer correlations and lower the number of low-lying singlets considerably [313]. Further peculiarities of the excitation spectrum are extensively discussed in Refs. 83, 314, and 165.

Similar to the nature of the GS, the spin gap issue is still under active debate. Thus, the extrapolation of ED results to the thermodynamic limit yields a very small, albeit nonzero spin gap, which amounts to ∼5% of the exchange coupling constant J_1 [83], and zero order parameter. A mean-field decoupling of the effective Hamiltonian corroborates this result [315]. Alternative techniques, such as numerical contractor renormalization (CORE) [316], series expansions [302, 303] or MERA [304] do not provide a fully conclusive answer to the question whether the spin gap survives in the thermodynamic limit. Recently, the comparison with ED-computed spectra for other lattices showing gapless behavior, and a careful analysis of the energy scales inside each S^z sector rendered the spin gap in the kagome model as an extrinsic property [165]. Experimental verification of this conjecture is still missing.

The magnetization process of the kagome model has been addressed in several works [94, 317–319]. Typical features are a plateau at $1/3$ of the saturation magnetization and a steep slope of $M(H)$ close to the saturation field $H_{\text{sat}}=3J_1\,k_{\text{B}}\,g^{-1}\mu_{\text{B}}^{-1}$. The structure of the plateau state is discussed in Ref. 320.

The thermodynamical behavior of the kagome model was investigated using ED on finite lattices up to $N=24$ sites [321, 322], HTSE for $\chi(T)$ [153] and $C_{\text{magn}}(T)$ [153, 155] as well as the GREEN's functions technique [323]. Since an experimental measurement of $C_p(T)$ and especially $\chi(T)$ is a routine task, the applicability of the theoretical model can be challenged by a direct comparison between theory and experiment.

The discovery of the first spin-1/2 kagome system herbertsmithite $Cu_3Zn(OH)_6Cl_2$ [54] inspired unprecedented activity from both experimental (discussed in Sec. 7.2) and theoretical side. Since the basics of the kagome physics were already known, new studies aimed to find a consistent description for the experimentally observed features, such as the influence of anisotropic DM interactions [324, 325], non-magnetic impurities [325] as well as additional couplings beyond NNs [314]. Thus, at a sufficiently large DM coupling (>10 % of J_1), the kagome model undergoes a quantum phase transition from the moment-free GS to the NÉEL phase [324], even in the presence of static impurities [325]. Besides, the second-neighbor coupling J_2, tends to stabilize a $\sqrt{3}\times\sqrt{3}$-type GS [314].

Herbertsmithite is the most familiar, albeit not unique candidate for the realization of the $S=1/2$ kagome HEISENBERG model. Even prior to the discovery of herbertsmithite, another mineral, volborthite $Cu_3[V_2O_7](OH)_2{\cdot}2H_2O$, has been suggested to imply the kagome physics, despite the monoclinic distortion of the magnetic layers [326]. An oxygen-free system, $Rb_2Cu_3SnF_{12}$ contains non-ideal kagome-like magnetic layers of corner-sharing

---

[3] This terms implies a quasilinear dependence between S^z and the GS energy in the respective S^z sector. See, e.g., Figs. 2.6(a), 2.9, and 2.11 in Ref. 94.

CuF_4 squares [327, 328]. Two isostructural minerals—kapellasite $Cu_3Zn(OH)_6Cl_2$ [329] and haydeeite $Cu_3Mg(OH)_6Cl_2$ [330]—with the crystal structure closely resembling that of herbertsmithite, contain perfect kagome layers of $S = 1/2$. Another promising candidates are the metal-organic system Cu(1,3-bdc) [331] and the Mg-counterpart of herbertsmithite [332, 333]. Since the field of kagome physics is vibrant, new materials are expected to be synthesized within the next few years.

Experimental investigation of the candidate $S = 1/2$ materials is very appealing, since it could resolve the remaining controversies regarding the magnetic properties of this geometrically frustrated model. However, prior to comparisons between theory and experiments, the applicability of the kagome model should be addressed. In this Chapter, the microscopic approach is applied to explore the magnetic models of herbertsmithite $Cu_3Zn(OH)_6Cl_2$ (Sec. 7.2), kapellasite $Cu_3Zn(OH)_6Cl_2$ and haydeeite $Cu_3Mg(OH)_6Cl_2$ (Sec. 7.3), as well as volborthite $Cu_3[V_2O_7](OH)_2{\cdot}2H_2O$ (Sec. 7.4) on the microscopic level. These DFT-based studies disclose several relevant features beyond the simple kagome model, such as additional couplings that have not been considered so far. Subsequent models studies reveal the importance of these features with respect to the magnetic GS and the lowest-lying excitations.

7.2 Herbertsmithite $Cu_3Zn(OH)_6Cl_2$

Herbertsmithite $Cu_3Zn(OH)_6Cl_2$ was described as a new mineral species in 2004 [334]. Only one year later, the material was proposed to imply the spin liquid physics, since the temperature dependence of its magnetic susceptibility showed no sign of a magnetic ordering transition down to 2 K, despite the large $\theta = 314$ K [335]. The measurements were carried out using the newly synthesized powder samples.

The first report on the magnetism of herbertsmithite [335] was immediately followed by a number of studies, predominantly from the experimental side. In particular, the NN coupling $J_1 = 190$ K [54] was estimated based on HTSE for the magnetic susceptibility [153]. One of the most difficult tasks was to distinguish between the extrinsic contribution of defects and impurities, and the intrinsic contribution of $S = 1/2$ kagome planes. Detailed magnetization [336], μSR [337], and NMR [338, 339] studies revealed the absence of LRMO at least down to 50 mK. Surprisingly, the temperature dependence of the magnetic susceptibility did not conform to the theoretical estimates for an ideal $S = 1/2$ kagome HEISENBERG antiferromagnet [322, 340]. To understand the origin of this discrepancy, additional experimental and theoretical studies were carried out.

The ND study in Ref. 341 reported sizable Cu–Zn intersite disorder: about 6% of Cu positions within the kagome planes were claimed to be occupied by Zn, and consequently, about 18% of Zn positions between the kagome planes to be occupied by Cu. At the same time, the ESR study in Ref. 342 disclosed the presence of anisotropic DM couplings, amounting to ∼0.08 of the NN coupling J_1. From the theoretical side, the problems of the antisite Cu/Zn disorder and the DM anisotropy were in the focus of several ED studies. In particular, the $|D|/J_1$ ratio in herbertsmithite was claimed to be close to the quantum critical point ($|D|/J_1 \sim 0.1$), separating a moment-free spin liquid and a Néel phase [324]. Intraplane non-magnetic (Zn) impurities were studied in Ref. 313. The main effect is dimerization, which develops at the magnetic sites in the vicinity of the non-magnetic impurity. The presence of DM couplings suppresses this tendency, but moderate values of $|D|/J_1$ exhibit only a minor effect [325].

Synthesis of single crystal samples [343] and subsequent experiments considerably improved understanding of the involved magnetic properties of herbertsmithite. First, anomalous X-ray dispersion studies refuted the earlier conjecture of intersite disorder. Instead, it was found [344] that there are almost no Zn impurities within the kagome layers, but about 15 % of Zn atoms are replaced by Cu. Thus, the correct chemical formula for herbertsmithite is $Cu_3(Zn_{0.85}Cu_{0.15})(OH)_6Cl_2$. Subsequent μSR studies disclosed, in addition to sizable DM anisotropy, also the relevance of the anisotropic exchange: $J_1^{x,y} \neq J_1^z$ [345].

Although it is very difficult to account for the exchange anisotropy, experimentally indicated confinement of defects to the interlayer position opens up new avenues for DFT-based studies. In particular, it becomes computationally feasible to estimate the effect of a magnetic interlayer impurity on the local environment. This DFT-based study comprises two parts. First, a microscopic magnetic model is evaluated for the idealized structure of herbertsmithite, neglecting the Cu–Zn disorder completely. In the second part, the influence of a single interlayer impurity on the microscopic magnetic couplings is studied. Finally, the experimentally observed decoupling of the kagome planes and the interlayer magnetic impurities, is explained by the frustrated nature of the interlayer couplings.

7.2.1 Crystal structure

The crystal structure is trigonal rhombohedral (space group $R\bar{3}m$) and features magnetic layers of corner-sharing CuO_4 plaquettes (Fig. 7.1, left) and ZnO_6 octahedra residing in the interlayer space (Fig. 7.1, right bottom). Magnetic Cu^{2+} atoms form regular kagome layers parallel to (111). The O atoms that bridge the neighboring CuO_4 plaquettes, are bonded to H atoms, with the O–H bonds directed toward the Cl atoms (located in the interlayer space). The neighboring layers are rotated by 120° and shifted with respect to each other forming an ...–I–II–III–I–II–III–...-type stacking (Fig. 7.1, right top).

CuO_4 plaquettes in herbertsmithite are planar with the Cu–O bond length of 1.97 Å. The Cu–O–Cu angle between the neighboring plaquettes is 120°, hinting at a sizable AFM exchange.

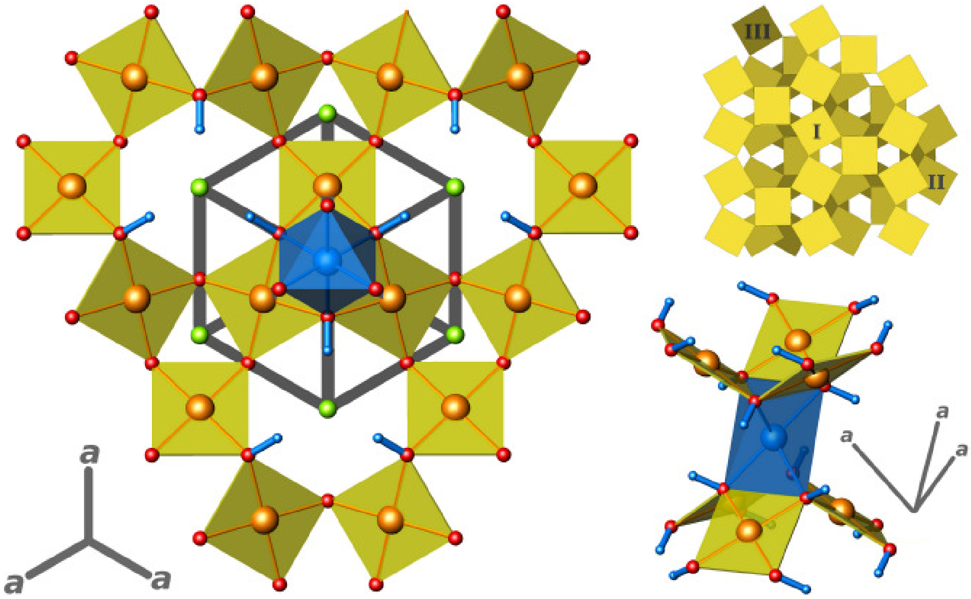

Figure 7.1: The trigonal rhombohedral crystal structure of herbertsmithite $Cu_3Zn(OH)_6Cl_2$ comprises magnetic layers formed by $Cu(OH)_4$ plaquettes and Cl atoms, as well as $Zn(Mg)O_6$ octahedra located in the interlayer space. Left: a kagome layer. Right top: stacking of the three neighboring kagome layers (I, II, and III). Right bottom: buckling and connection of the neighboring layers.

7.2.2 DFT calculations

Modeling of the Cu-Zn structural disorder in herbertsmithite on the DFT level is a challenge, since there is no universal way to take this issue into account. However, keeping in mind that the effect of structural disorder should be minor and short-ranged (as evidenced by recent NMR studies on single crystals [346]), the idealized (fully ordered) structure of herbertsmithite seems to be an appropriate starting point.

For the lattice constants and atomic coordinates, the data from Refs. 347 and 335, respectively, were used (see also Table A5). To cross-check the results, the structural model from Ref. 335 as well as two alternative sets of lattice constants were adopted from Refs. 343 and 347. All four experimental data sets yield almost indistinguishable band dispersions. The internal atomic coordinates were defined using X-ray diffraction, thus the positions of light atoms are subject to careful verification. Therefore, the internal atomic coordinates of the H atoms were optimized by relaxation in LDA (the resulting coordinates are given in Table A5). Optimization in the GGA yields a marginally different structure (the difference in the O–H bond length is $\sim$0.01 Å). In the following, unless otherwise mentioned, the DFT calculations will be carried out using the LDA-optimized crystal structure.

On the LDA level, the electronic structure of herbertsmithite does not feature any peculiarities beyond the standard cuprate scenario: the low-lying states of the valence band are dominated by Zn and O states, while the higher lying states are mainly of Cu, O and Cl character (Fig. 7.2, top). Typical for cuprates, the well-separated density at ε_F is formed by Cu and O states. This energy range comprises three bands (Fig. 7.2, bottom), in accord with three Cu atoms in a unit cell.

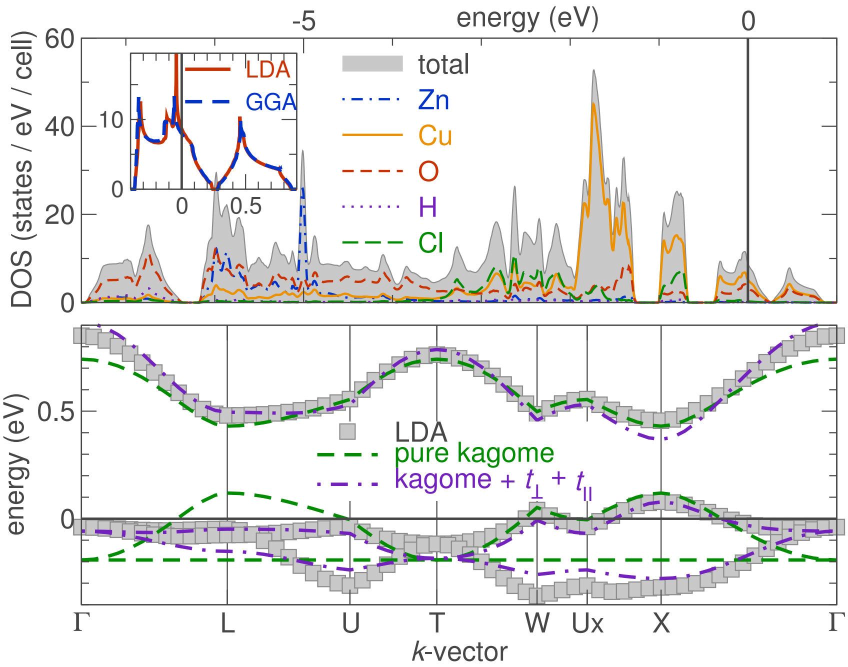

Figure 7.2: LDA DOS (top) and band structure (bottom) of herbertsmithite $Cu_3Zn(OH)_6Cl_2$. The crystal structure is optimized beforehand within LDA. Ideal ordering of Cu and Zn atoms is presumed. Inset: comparison between LDA and GGA. Bottom panel: TB fits using two models: (i) with t_1 only (pure kagome) and (ii) with three transfer integrals t_1, $t_\perp$ and t (for notation, see Fig. 7.4).

Prior to evaluation of relevant couplings, the accuracy of the band dispersions should be estimated. One of the key parameters affecting the band dispersions is the parameterization of the exchange and correlation potential. To evaluate this influence, non-magnetic calculations have been performed in LDA as well as in GGA. The resulting electronic structures are practically indistinguishable. In particular, the change in the width of the band complex at ε_F is about 0.01 eV (Fig. 7.2, top inset), corresponding to a relative difference below 1 %. The difference between LDA and GGA is negligibly small compared to other sources of numerical inaccuracies.

Much more pronounced is the difference between the experimental and the LDA-optimized crystal structure (Fig. 7.3). Since the experimental atomic coordinates lead to unusually short O–H bonds of 0.82 Å, more credit should be given to the optimized structure, with plausible O–H distances of 1.01 Å.

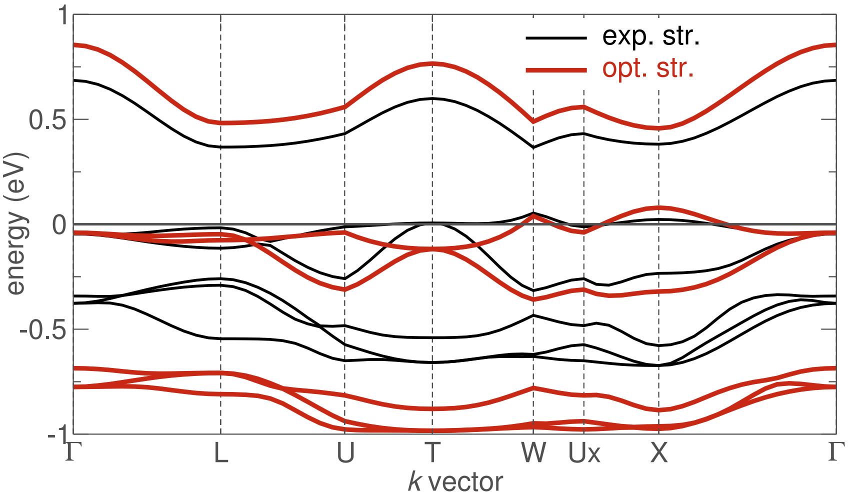

Figure 7.3: LDA band structures of herbertsmithite $Cu_3Zn(OH)_6Cl_2$ calculated using the experimental (exp. str.) and the LDA-optimized crystal structure (opt. str.). Atomic coordinates for the both structures are presented in Table A5.

Similar to the DFT-based studies described in Chapter 6, the WFs for Cu $3d_{x^2-y^2}$ orbitals provide an excellent description to the three isolated bands at ε_F. Three relevant transfer integrals are found: the dominant NN coupling $t_1 = 163$ meV, the interlayer coupling $t_\perp = 37$ meV as well as the long-range coupling $t\ \ = 23$ meV within the kagome plane. Further couplings are smaller than 10 meV and can be neglected for the minimal model.

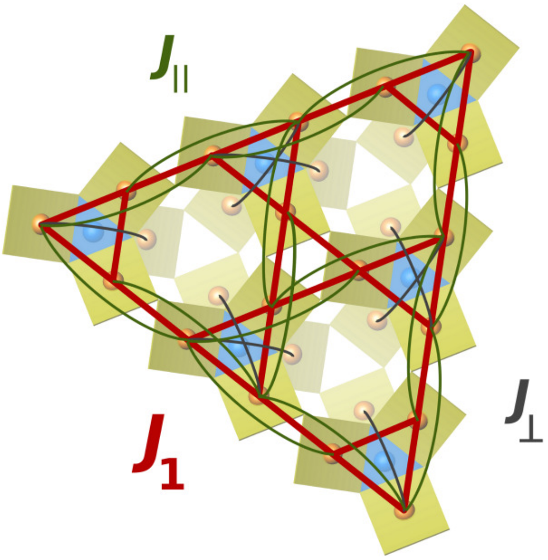

Figure 7.4: Microscopic magnetic model for the idealized (no Cu-Zn disorder) structure of herbertsmithite $Cu_3Zn(OH)_6Cl_2$. Three relevant couplings, the nearest-neighbor coupling J_1, the third-neighbor coupling J and the interlayer coupling $J_\perp$ are shown. The CuO_4 plaquettes are depicted as yellow squares.

The relevance of t_1 fully conforms to the experimental findings. Adopting a standard value of U_{eff} yields $J_1^{\text{AFM}} = 274$ K, largely overestimating the experimental $J_1 = 190$ K. This deviation points to a sizable FM contribution to the respective magnetic exchange J_1. The relevance of the two additional couplings $t\ \ $ and $t_\perp$ is less trivial. Similar to t_1, the $t\ \ $ coupling is confined to the kagome planes, and can be regarded as a second-neighbor coupling with respect to t_1 (Fig. 7.4). However, in terms of Cu–Cu distances within the kagome planes, this coupling is third-neighbor. In addition, there is another, nonequivalent third-neighbor coupling running through hexagonal voids of the kagome lattice, which corresponds to the same Cu–Cu distance. In herbertsmithite, this coupling is substantially smaller than $t\ \ $ (in contrast, the related materials kapellasite $Cu_3Zn(OH)_6Cl_2$ and haydeeite $Cu_3Mg(OH)_6Cl_2$ feature a sizable coupling running through hexagonal voids, see Sec. 7.3). The interlayer coupling $t_\perp$ leads to $J_\perp^{\text{AFM}} = 14$ K. Although this coupling is substantially smaller than J_1, it exceeds the upper estimate for a possible magnetic ordering temperature (~ 50 mK) by several orders of magnitude.

Numerical values for the leading exchange couplings are evaluated using the LSDA+U method. Here, the experimental $J_1 = 190$ K gives an opportunity to adjust the DCC scheme and the U_d value, in order to get precise estimates for $J\ \ $ and $J_\perp$. In this way, the experimental J_1 is reproduced for $U_d = 7.0$ eV in AMF [for the $J_1(U_d)$ dependence, see Fig. A5] and $U_d = 9.0$ eV in FLL. The values of U_d agree with the previous estimates (Chapter 6).

The estimates for $J\ \ $ and $J_\perp$ are evaluated using the optimized values for U_d. As expected, the difference in $t_\perp$ and $t\ \ $ gets even more pronounced when resorting to the exchange integrals: DFT+U yields $J_\perp = 6$–7 K and a very small $J\ \ $ of about 0.5–1 K. The applicability of the NN kagome HEISENBERG model apparently depends on $J_{\perp}/J_1$ and $J\ /J_1$. The DFT+U analysis for the fully ordered structure suggests that these ratios are as small as $J_{\perp}/J_1 = 0.035$ and $J\ /J_1 = 0.005$, and compared to the large DM coupling of about $0.08J_1$ [342], their effect on the magnetic GS should be of minor importance.

After evaluation of the magnetic model for the fully ordered structure, the effect of interplane magnetic impurities should be considered. The major difficulty is to model a random distribution of impurities. In the strict sense, a random distribution of atoms violates periodic boundary conditions, thus standard DFT tools are not applicable. However, the experiments suggest that the magnetic impurities in herbertsmithite alter the local environment, only [346], and do not give rise to any long-range effects. Profiting from the well-established localized nature of the impurity effects, a randomly distributed impurity can be modeled using fully ordered structures. Such approach is exploited in the present study.

In the simplest interplane magnetic impurity model, all Zn atoms can be replaced by Cu, leading to the hypothetical Zn-free herbertsmithite $Cu_3Cu(OH)_6Cl_2$.[4] This configuration conforms to the initial trigonal symmetry, thus the minimal magnetic supercell can be used. For the first step, the impact on the additional Cu atom should be studied on the LDA level. It would be natural to compare the band dispersions for the fully ordered and the Zn-free herbertsmithite. However, the different number of relevant bands (three and five,[5] respectively), and an additional renormalization of the FERMI level impede a direct comparison. Therefore, it is more instructive to compare the transfer integrals, evaluated using the WF procedure. In this way, the t_1 coupling is found to be almost unaffected by the additional Cu atom. The $t\ $ and $t_{\perp}$ couplings are 15% and 35% reduced in comparison to the fully ordered $Cu_3Zn(OH)_6Cl_2$. Due to the presence of two relevant orbitals for an impurity Cu atom, there are two different hopping terms (one for each orbital). Thus, the t_{imp} coupling between intraplane and impurity electrons amounts to 97 meV and 56 meV for the $3d_{3z^2-r^2}$ and $3d_{x^2-y^2}$ orbitals of the impurity atom, respectively. For the intraplane spins, only the $3d_{x^2-y^2}$ electrons enter the minimal low-energy model. Apart from the additional t_{imp} term, no further couplings exceed 15 meV. Therefore, the analysis can be restricted to only four leading terms: t_1, $t\ $, $t_{\perp}$ and t_{imp}.

From the analysis of the idealized structure, the couplings J_1, $J\ $, and $J_{\perp}$ were estimated. In the next step, the exchange coupling J_{imp} is evaluated within the LSDA+U approximation by stabilizing magnetic configurations with parallel and antiparallel mutual alignment intraplane (kagome) and interplane (impurity) spins, and comparing their total energies. In this way, $J_{\mathrm{imp}} = -16$ K and -56 K are found in AMF and FLL, respectively.

Besides promoting the additional coupling J_{imp}, the presence of an interplane magnetic impurity can alter the leading intraplane coupling J_1. In order to estimate this effect, the initial trigonal symmetry is lowered to the triclinic, while keeping the metrics of the unit cell intact. The LSDA+U calculations for such supercells suggest that the magnetic interplane impurity gives rise to an appreciable enhancement of J_1: this exchange coupling amounts to 254 K in AMF and 231 K in FLL. In addition to this effect, the AMF calculations done for the triclinic supercell yield $J_{\text{imp}} = -27$ K, which contrasts with $J_{\text{imp}} = -16$ K, obtained for the rhombohedral cell.[6] The origin of this discrepancy can be revealed by comparing the occupation matrices. Thus, the trigonal symmetry imposes the degeneracy of $3d_{x^2-y^2}$ and $3d_{3z^2-r^2}$ orbitals, leading to equal occupation numbers. In contrast, the triclinic symmetry lifts this degeneracy, hence the occupation numbers can be different. Indeed, the occupation for the $3d_{x^2-y^2}$ orbital is about factor of two larger than that of the $3d_{3z^2-r^2}$ orbital.

---

[4] Although the chemical composition of the Zn-free herbertsmithite is the same as in the mineral botallackite $Cu_2(OH)_3Cl$ [348], their crystal structures are different.

[5] Five bands originate from the $3d_{x^2-y^2}$ orbitals of the three intraplane Cu atoms, as well as the $3d_{x^2-y^2}$ and $3d_{3z^2-r^2}$ orbitals of the impurity Cu atoms.

The different occupations of the $3d_{3z^2-r^2}$ and $3d_{x^2-y^2}$ orbitals even in the geometrically regular octahedral coordination hint at possible relevance of the CF effects. Interestingly, this issue has not been discussed in the literature so far, and therefore deserves an additional commentary. In Sec. 2.1.1, the CF effect was presented as one of the leading driving forces for the magnetism in cuprates. In fact, among the large number of cuprate crystal structures, there are still no examples of a regular octahedral coordination for the magnetic Cu^{2+} ions. Non-occurrence of regular CuO_6 octahedra in real materials naturally puts forward the idea that the replacement of Zn by Cu in herbertsmithite should be accompanied by a distortion of the local environment, in order to lift the orbital degeneracy.

The orbital degeneracy can be lifted by stabilizing one of the two orbital GSs, $3d_{x^2-y^2}$ or $3d_{3z^2-r^2}$. The calculational approach provides a unique possibility to model both scenarios by setting an initial orbital occupation matrix and relaxing the internal atomic coordinates within DFT+U. Not surprisingly, if an electron hole is initially localized in the $3d_{x^2-y^2}$ orbital, the "4+2" structural distortion (four short bonds and two long Cu–O bonds) is stabilized. In contrast, using the $3d_{3z^2-r^2}$ solution as a starting point stabilizes the opposite "2+4" distortion (two short bonds and four long Cu–O bonds). Both scenarios are schematically depicted in Fig. 7.5 (top panel).

The resulting LSDA+U total energies are presented in Table 7.1. For the "$|\downarrow\uparrow\uparrow\rangle$ + $|\text{imp: } 3d_{3z^2-r^2}\rangle$" configurations (the first ket denotes the intraplane spin arrangement, the second ket stands for the magnetically active orbital of the impurity atom), the convergence could not be reached due to the reversal of orbital occupations: the impurity spin changes its orbital character from the initially set $3d_{3z^2-r^2}$ to $3d_{x^2-y^2}$. For all other configurations, the forces were minimized down to 0.01 eV/Å. In agreement with the expectations, the orientation of the impurity spin has a minor influence on the GS energy. The influence of the intraplane spin configuration, ferromagnetic $|\uparrow\uparrow\uparrow\rangle$ or ferrimagnetic $|\downarrow\uparrow\uparrow\rangle$, is substantially larger.

The energy difference between the $|\text{imp: } 3d_{x^2-y^2}\rangle$ and $|\text{imp: } 3d_{3z^2-r^2}\rangle$ configurations (~350 K) is on the same scale as the difference between $|\downarrow\uparrow\uparrow\rangle$ and $|\uparrow\uparrow\uparrow\rangle$ (~400 K). The

---

[6] The FLL values bear a small (2 K) difference, which does not exceed the error bars.

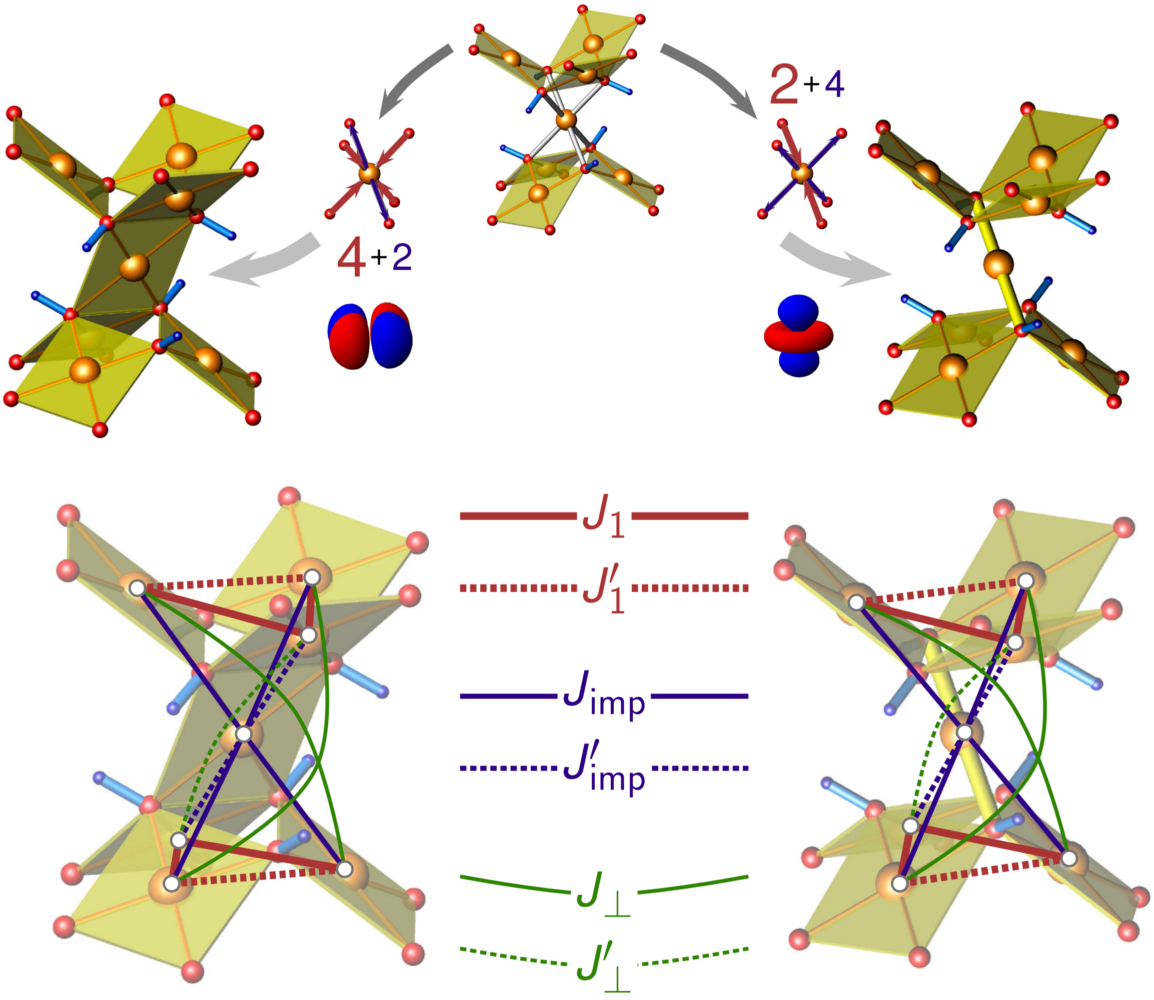
2+4
4+2
J_1
J_1'
J_{imp}
J_{imp}'
$J_\perp$
$J_\perp'$

Figure 7.5: Two possible types of a structural distortion in the hypothetical Zn-free herbertsmithite $Cu_3Cu(OH)_6Cl_2$. Left panel: formation of a CuO_4 plaquette (the "4+2" scenario). Right panel: formation of two short Cu–O bonds (the "2+4" scenario). Bottom panel: the structural distortions lead to nonequivalent exchange couplings: J_1 and J_1', J_{imp} and J_{imp}', $J_\perp$ and $J_\perp'$.

Table 7.1: Total energy (in K) of fictitious Zn-free herbertsmithite $Cu_3Cu(OH)_6Cl_2$ as a function of the orbital of the impurity spins ($|\mathrm{imp}\colon 3d_{3z^2-r^2}\rangle$ or $|\mathrm{imp}\colon 3d_{3z^2-r^2}\rangle$), the spin of the interplane Cu atom (up $|{\uparrow_{\mathrm{imp}}}\rangle$ or down $|{\downarrow_{\mathrm{imp}}}\rangle$), and the arrangement of the intraplane Cu spins (ferromagnetic $|{\uparrow\uparrow\uparrow}\rangle$ or ferrimagnetic $|{\downarrow\uparrow\uparrow}\rangle$). The GS is at zero energy. For the non-converged energies ("–"), see text. The LSDA+U calculations were performed for a low-symmetry supercell, using $U_d = 7.0$ eV within the AMF DCC.

		$|\mathrm{imp}\colon 3d_{x^2-y^2}\rangle$	$|\mathrm{imp}\colon 3d_{3z^2-r^2}\rangle$
$|{\uparrow\uparrow\uparrow}\rangle$:			
	$|{\uparrow_{\mathrm{imp}}}\rangle$	416.9	744.7
	$|{\downarrow_{\mathrm{imp}}}\rangle$	449.8	801.1
$|{\downarrow\uparrow\uparrow}\rangle$:			
	$|{\uparrow_{\mathrm{imp}}}\rangle$	19.6	–
	$|{\downarrow_{\mathrm{imp}}}\rangle$	0	–

present LSDA+U results (Table 7.1) suggest the $|\ \mathrm{imp}\colon 3d_{x^2-y^2}\rangle$ configuration is energetically favorable, thus the impurity leads to a "4+2" distortion of the $Cu_{\mathrm{imp}}O_6$ octahedra. However, the 400 K difference between the two types of distortion is far too small for a robust conclusion. It should be kept in mind that this difference can be further altered by (i) the parameterization of the exchange and correlation potential, (ii) the type of DCC, and (iii) the value of U_d. Therefore, the "2+4" distortion can not be excluded. In the following, both types of distortions are considered.

Moreover, the similar energy scales of orbital and spin degrees of freedom[7] render the possibility of their decoupling questionable. Instead, the scenario of sizable spin-orbital coupling looks more plausible, while the physics might be accounted for by the KUGEL–KHOMSKII Hamiltonian [55], rather than the HEISENBERG approach. Therefore, the scenarios discussed below might be substantially altered by considering the orbital excitations. This issue deserves an additional analysis, beyond the scope of this study.

Quite remarkably, even an infinitesimal structural distortion of either type, "4+2" or "2+4", has far-reaching effects on the magnetic properties, leading to a way more involved model with several non-equivalent J_1 and J_{imp}. First, the shift of the O atomic position affects the Cu–O–Cu angles and leads to the two non-equivalent NN couplings J_1 and J_1' (Fig. 7.5, bottom panel). Second, localization of the impurity spin in a particular orbital gives rise to non-equivalence of the impurity couplings, J_{imp} and J_{imp}'. Finally, also the interplane couplings $J_\perp$ and $J_\perp'$ become non-equivalent (Fig. 7.5).

Parameterization of such a complicated magnetic model requires evaluation of large magnetic supercells. On the other hand, the energy scale of the relevant couplings (except for J_1) is close to the limits of resolution attainable by the present-day DFT codes. To keep the problem solvable, the leading couplings J_1, J_1', J_{imp}, and J_{imp}' are evaluated, while $J_\perp$ and $J_\perp'$ are assumed to be equal. Such an assumption allows to evaluate the four couplings J_1, J_1', $J_\perp$, and $J_\perp'$ using a computationally feasible supercell.

---

[7] The similarity of the two energy scales in herbertsmithite is quite unusual. For instance, in the spin-liquid candidate volborthite $Cu_3[V_2O_7](OH)_2{\cdot}2H_2O$, the orbital excitation energies largely exceed the energy scale of magnetic excitations (Sec. 7.4).

The results of extensive LSDA+U calculations are summarized in Table. 7.2. Surprisingly, for both types of structural distortion ("4+2" or "2+4"), the averaged NN coupling $\overline{J_{\text{imp}}} \equiv {}^2\!/_3 J_1 + {}^1\!/_3 J_1'$ is very close to 190 K. However, there is a substantial difference between the NN couplings J_1 and J_1', which amounts to surprisingly large 20–40% of the averaged coupling $\overline{J_1}$. Therefore, magnetic impurities, albeit confined to interplane sites, considerably alter the local exchange couplings in the kagome planes.

Table 7.2: Leading exchange integrals (in K) in the Zn-free herbertsmithite $Cu_3Cu(OH)_6Cl_2$. The average couplings are evaluated as $\overline{J_1} = {}^2\!/_3 J_1 + {}^1\!/_3 J_1'$ and $\overline{J_{\text{imp}}} = {}^2\!/_3 J_{\text{imp}} + {}^1\!/_3 J_{\text{imp}}'$. Interplane (imp) spins are characterized by their orbital state ($3d_{x^2-y^2}$ or $3d_{3z^2-r^2}$). The LSDA+U calculations were carried out for $U_d = 7.0$ eV using AMF DCC.

	J_1	J_1'	$\overline{J_1}$	J_{imp}	J_{imp}'	$\overline{J_{\text{imp}}}$
$\lvert \text{imp}: 3d_{x^2-y^2}\rangle$	150	275	192	−23	17	−10
$\lvert \text{imp}: 3d_{3z^2-r^2}\rangle$	213	135	187	−12	−33	−19

The magnetic coupling between the intraplane and impurity spins strongly depends on the type of structural distortion. Thus, for $\lvert \text{imp}: 3d_{x^2-y^2}\rangle$, J_{imp} and J_{imp}' are similar, but have opposite signs. Quite unusual, the edge-sharing connections of CuO_4 and $Cu_{\text{imp}}O_4$ plaquettes give rise to an AFM exchange. This unexpected result can be explained by a rather large value of the respective Cu–O–Cu angle ($\sim 99.4^\circ$), which suffices to compensate the large HUND's coupling (FM) on the O sites by AFM superexchange. In contrast, $\lvert \text{imp}: 3d_{3z^2-r^2}\rangle$ leads to exclusively FM couplings between the kagome and impurity spins.

Different local-probe experiments generally agree that the kagome layers and interplane magnetic impurities in herbertsmithite are largely decoupled. This experimental fact seemingly contrasts with the large values of J_{imp} (orders of magnitude larger than possible long-range magnetic ordering temperature), evaluated using the LSDA+U calculations. In the next section, the origin of this discrepancy is addressed by evaluation of spin correlations in the magnetic GS.

7.2.3 Simulations

For the idealized structure of herbertsmithite $Cu_3Zn(OH)_6Cl_2$, DFT calculations yield a relatively simple model with only two relevant exchange couplings J_1 and $J_\perp$, with $J_1 \quad J_\perp$. However, the replacement of nonmagnetic Zn by magnetic Cu atoms leads to rather complicated microscopic model comprising J_1, J_1', J_{imp}, J_{imp}', $J_\perp$, and $J_\perp'$. The model is frustrated, thus numerically efficient QMC techniques can not be used. In addition, the 3D nature of this model impedes using DMRG as well. Therefore, among the standard simulation methods, only ED can be used.

ED can not account for the thermodynamical limit due to small sizes of feasible finite lattices (Sec. 5.2). Especially for a 3D magnetic model, this limitation drastically reduces the

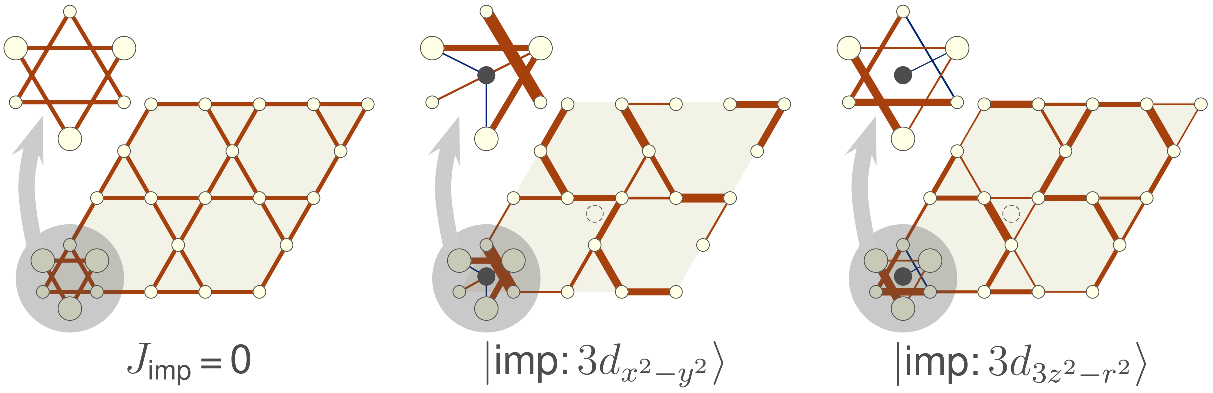
$J_{\text{imp}} = 0$
$|\text{imp}: 3d_{x^2-y^2}\rangle$
$|\text{imp}: 3d_{3z^2-r^2}\rangle$

Figure 7.6: NN spin correlations in the GS of Zn-free herbertsmithite $Cu_3Cu(OH)_6Cl_2$ (ED on $N = 26$ sites finite lattices). The width of the line corresponds to the size of the respective spin correlation, the red and blue color correspond to a negative and a positive correlation, respectively. Marginal correlations $|\langle \mathbf{S}_i \cdot \mathbf{S}_j \rangle| < 0.02$ are not shown. In each panel, only one kagome plane is shown. The impurity (interlayer) spins are shown with the filled (above the reference plane) and the dashed-lined (below the reference plane) circles. Insets: spin correlations between the kagome (small empty circles) and impurity (filled circles) spins, as well as interlayer correlations (the spins of the neighboring kagome layer are denoted by large empty circles).

applicability of the method. A possible way to sidestep the problem is to use small clusters instead of finite lattices. For instance, the seven-spin clusters depicted in the bottom panel of Fig. 7.5, are seemingly suits for simulations of a local impurity effect. However, isolated triangles are a rather poor approximation for the kagome lattice. Therefore, it is more appropriate to consider a small finite lattice of $N = 26$ spins: two kagome layers featuring 12 spins each, and two interlayer impurity spins. In this configuration, $1/4$ of all spin triangles are coupled to an interlayer spins.

First, the finite lattice is challenged by simulation of the pure kagome model with J_1, only (Fig. 7.6, left panel). In this way, the NN diagonal spin correlations $\langle S_0^z S_1^z \rangle$ are evaluated. The two-double layer $N = 26$ finite lattice (featuring two kagome layers of $N = 12$ sites) yields $\langle S_0^z S_1^z \rangle = -0.07562$, very close to the state-of-the-art $N = 36$ sites result for the kagome lattice $\langle S_0^z S_1^z \rangle = -0.07306$ [349]. However, for the correlations between the second neighbors are poorly described: the $N = 26$ double-layer lattice yields sizable FM correlation $\langle S_0^z S_2^z \rangle = 0.02958$, while the $N = 36$ sites kagome lattice yields negligibly small FM correlation of 0.00386 [349]. Thus, the $N = 26$ finite lattice provides a reasonable description for the NN correlations, only.

After establishing the applicability range of the $N = 26$ finite lattice, the models from Table 7.2 are simulated. The NN correlations for the $|\text{imp}: 3d_{x^2-y^2}\rangle$ and $|\text{imp}: 3d_{3z^2-r^2}\rangle$ cases are shown in Fig. 7.6, middle and right panel, respectively. Both solutions exhibit rather involved correlations, with no clear physical picture, such as, for instance, dimerization around the impurity sites.

To account for the origin of such involved physical picture, the simulations were repeated for a simpler model without the $J_\perp$ coupling. As expected, the interplane correlations are substantially altered, since for $J_\perp = 0$, the interplane coupling is not frustrated. However, the impact of $J_\perp$ on the intraplane spin correlations is marginal (below 2%), hence they can not give rise to the complicated patterns in the middle and right panel of Fig. 7.6.

7.2.4 Discussion

The cumulative experimental evidence for the kagome physics in herbertsmithite is fully supported by the band structure calculations: the NN exchange J_1 is clearly dominant, and the next strongest intraplane coupling is about two orders of magnitude smaller. The coupling between the layers is approximately $J_\perp$ 7 K, which exceeds the possible LRMO temperature by several orders of magnitude. Thus, the absence of LRMO in herbertsmithite is the pure effect of frustration.

To account for the magnetic impurity effect, a microscopic magnetic modeling has been carried out for a hypothetical Zn-free herbertsmithite $Cu_3Cu(OH)_6Cl_2$. In this hypothetical structure, the $Cu_{imp}O_6$ polyhedra are regular. The substitution of Zn by Cu does not affect the geometry, thus leaving the regularity intact. However, regular $Cu_{imp}O_6$ octahedra would feature orbital degeneracy, and at the same time, have only one hole in the $3d$ shell, hence they are expected to be unstable against distortion of the local environment. In fact, such distortion takes place in all known cuprate materials. This argument definitely favors the distorted scenario, and consequently, gives rise to a complicated microscopic magnetic model with several non-equivalent intra- and interplane couplings, as well as the couplings between the kagome and impurity spins. However, the simulations of such microscopic models (for both types of distortion, "4+2" or "2+4") suggest the emergence of rather complicated spin correlations, with a barely perceptible tendency for dimerization. In general, the DFT calculations and simulations suggests a sizable impact of the magnetic impurities onto the intraplane magnetism.

In contrast, such tendencies are not observed in the experiments, rendering the distorted scenario to a certain extent implausible. In the alternative scenario, the inheritance of the orbital degeneracy leads to a sizable FM coupling between the kagome and impurity spins J_{imp} -35 ± 20 K. The simulations evidence that for the relevant range $0.1J_1 \leq |J_{imp}| \leq 0.3J_1$, the correlations between the intraplane and impurity spins are still marginal. This conforms to the experimentally observed decoupling of the magnetic subsystems. In addition, recent unpublished ESR experiments suggest a pronounced reduction of the g-factor for the impurity atoms. This indirectly supports the orbital degeneracy, which would give rise to an unquenched orbital moment.

In summary, there is no experimental evidence for a sizable alteration of the kagome lattice model. Still, future experiments should focus on the presence of the impurity-induced structural distortion, and in the case such distortion takes place, its type ("4+2" or "2+4") should be determined. Moreover, more precise structural data, especially the H position, are highly desirable.

7.3 Kapellasite $Cu_3Zn(OH)_6Cl_2$ and haydeeite $Cu_3Mg(OH)_6Cl_2$

Kapellasite (a metastable polymorph of herbertsmithite), as well as its isostructural Mg-counterpart haydeeite, comprise ideal (non-distorted) kagome lattices of magnetic Cu^{2+} atoms, thus they are regarded as spin liquid candidate materials.

Interestingly, both materials were first discovered as minerals [329, 330]. However, small size and insufficient quality of natural crystals impede experimental studies of these interesting systems. Therefore, the results of this DFT-based study are mostly a theoretical prediction which is subject to a future experimental confirmation. Several months after the present DFT study has been published [350], the first successful synthesis of powder samples of kapellasite was reported [351]. Unfortunately, the measured bulk magnetic susceptibility contains too large impurity and/or defect contributions for the conclusive comparison with the DFT-based predictions. Very recently, powder samples of haydeeite were obtained, and the crystal structures of the both materials were refined using ND [352].

Well-characterized samples open up new vistas for investigation of kapellasite and haydeeite. In particular, NMR [353] and ND studies for kapellasite are already underway. Therefore, a deeper experimental insight into the magnetism of these systems can be expected in the nearest future.

7.3.1 Crystal structure

The trigonal (space group $P\bar{3}m1$) crystal structure of kapellasite [329] and haydeeite [330] features magnetic layers formed by CuO_4 plaquettes and $Zn(Mg)O_6$ octahedra (Fig. 7.7, left), and the interlayer space is filled with Cl and H atoms. The neighboring CuO_4 plaquettes share corners and form a regular kagome layer of magnetic ions. Magnetic layers are considerably buckled (Fig. 7.7, right top), leading to the Cu–O–Cu angle of 105.9° (105.0°) for kapellasite (haydeeite).

Owing to the identical chemical composition and the presence of similar structural units, it is instructive to compare the crystal structures of kapellasite and herbertsmithite. Thus, the rhombohedral unit cell of herbertsmithite (space group $R\bar{3}m$) contrasts with the primitive trigonal cell of kapellasite/haydeeite (space group $P\bar{3}m$). As a consequence, the stacking of the kagome layers is realized in a different way: the neighboring layers in herbertsmithite are shifted and rotated with respect to each other (Fig. 7.1, top right panel), while the stacking of the kagome layers in kapellasite is not accompanied by a parallel shift or rotation. Second, despite the corner-sharing of CuO_4 plaquettes in both compounds, the magnetic layers in kapellasite are less buckled than in herbertsmithite (Fig. 7.8), which results in a strongly reduced value of the Cu–O–Cu angle ($\sim$106° in kapellasite versus $\sim$120° in herbertsmithite), hinting at a smaller AFM coupling.

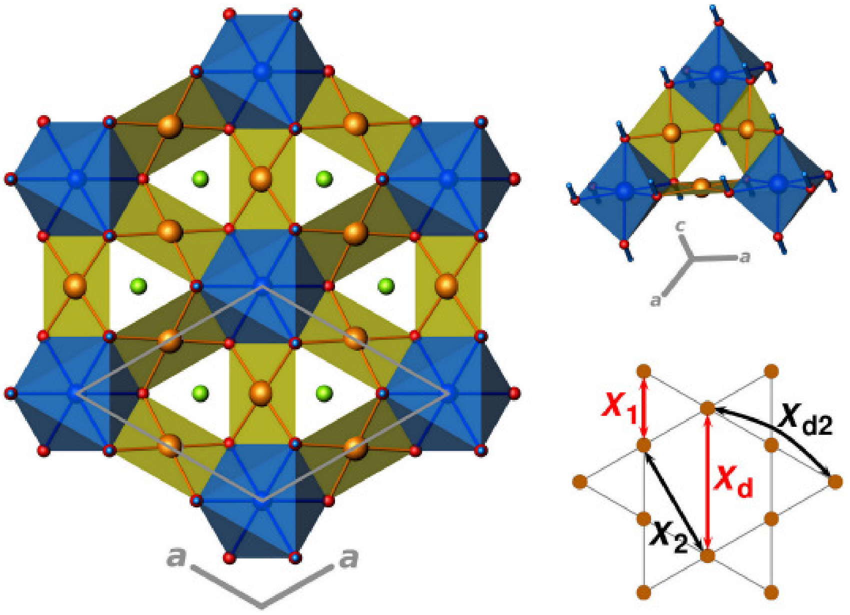

Figure 7.7: Crystal structure of kapellasite $Cu_3Zn(OH)_6Cl_2$ [329] and haydeeite $Cu_3Mg(OH)_6Cl_2$ [330]. CuO_4 plaquettes and non-magnetic $Zn(Mg)O_6$ octahedra are shown yellow and blue, respectively. Cl atoms are green spheres, O–H bonds are depicted by blue sticks. Left: a kagome layer. Right top: buckling of a kagome layer. Right bottom: superexchange paths for the leading couplings.

As a result of stronger buckling in kapellasite, the octahedral voids become small enough to accommodate Zn atoms with a concomitant formation of six Zn–O bonds (in herbertsmithite, the respective Zn–O distances would be too large to form a chemical bond). Consequently, there is no space left for the Cl atoms within the magnetic layers. Therefore, Cl atoms are squeezed to the interlayer space. Thus, on the simplest level, the transition between herbertsmithite and kapellasite can be described as the rotation and the shift of the neighboring magnetic layers, accompanied by the exchange of Zn and Cl atoms.

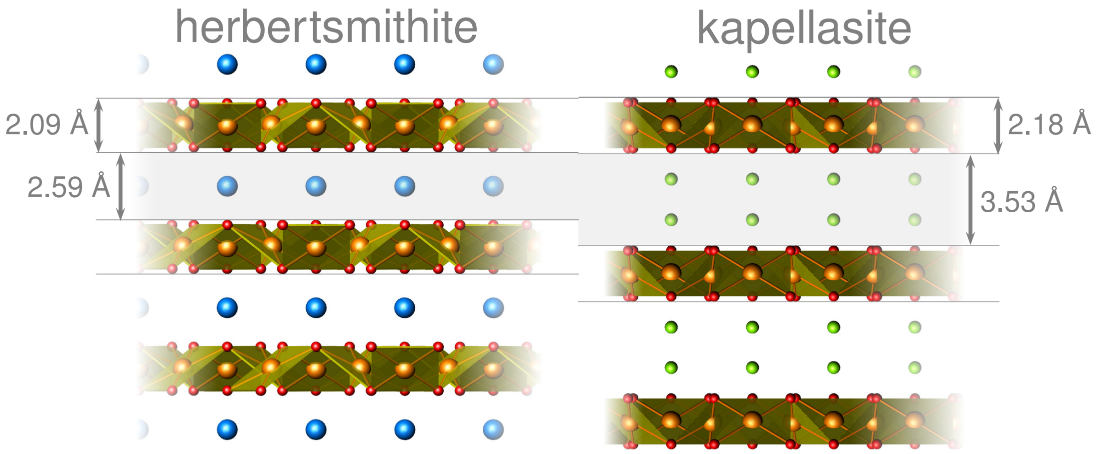

Figure 7.8: Thickness of the magnetic kagome layers (a measure of buckling) and the interlayer separation in the crystal structures of herbertsmithite $Cu_3Zn(OH)_6Cl_2$ (left) kapellasite $Cu_3Zn(OH)_6Cl_2$ (right). Interlayer space is filled by Zn atoms (large blue spheres) in herbertsmithite and by Cl atoms (small green spheres) in kapellasite.

The next remark concerns the interlayer separation, which is considerably larger for kapellasite (Fig. 7.8). The DFT studies (Sec. 7.2) reveal a sizable interlayer coupling for herbertsmithite, since largely covalent O–Zn–O junctions strongly favor the superexchange. In contrast, essentially ionic H–Cl bonds impede the superexchange along these paths in kapellasite and haydeeite. These empirical considerations are confirmed by the DFT calculations, described below.

Similar to herbertsmithite, the atomic coordinates for H atoms should be carefully analyzed. Since the precise structural data for the two materials were published only very recently [352], the DFT study was based on the previous structural studies, where the experimental H position was either missing (haydeeite, Ref. 330), or led to the short O–H bond lengths of 0.78 Å [329]. Compared to a typical O–H bond length (1 ± 0.05 Å), this value looks largely underestimated. Keeping in mind experimental problems with the precise determination of the H position (Sec. 3.1.1), it has been relaxed within the LDA.[8] The optimized (equilibrium) positions yield the O–H distance very close to 1 Å for both systems. In addition, the O–H distances were found to play a crucial role for the magnetism, while the Cu–O–H angle appeared to be less important (Sec. 7.3.2).

At present, the optimized H positions can be compared to the experimental ones, precisely defined using ND on deuterated samples [352]. The resulting O–D distances amount to 1 Å and 0.98 Å for kapellasite and haydeeite, respectively; in excellent agreement with the DFT-based estimates.

7.3.2 DFT calculations

For both compounds, LDA yields similar valence bands with a total width of 6–7 eV, dominated by Cu and O states (Fig. 7.9). The only pronounced difference is the presence of Zn states (for kapellasite) at the lower bound of the valence band, while no appreciable density of Mg states is found in haydeeite. This difference originates from a more covalent character of Zn–O bonds compared to essentially ionic Mg–O bonds.

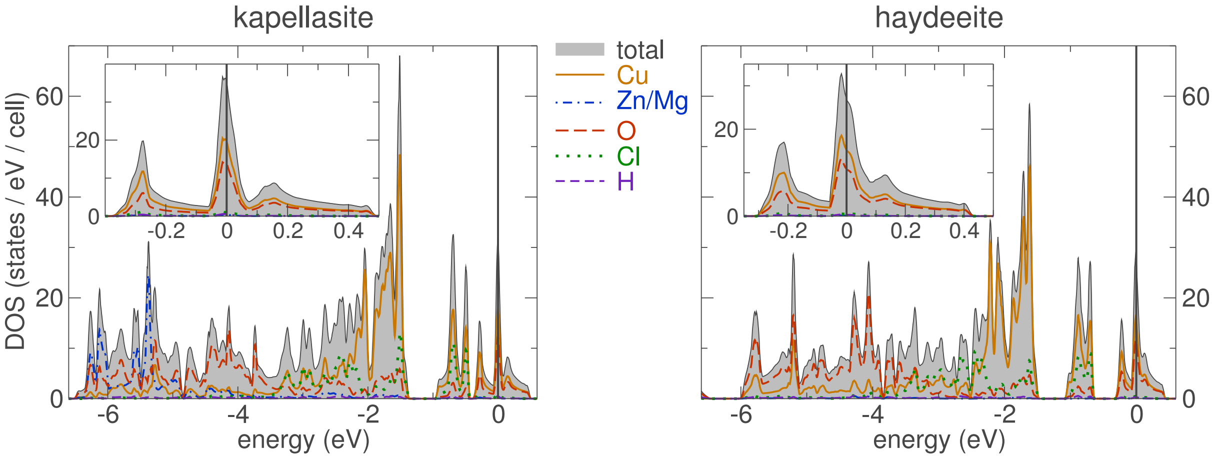

Figure 7.9: DOS for kapellasite $Cu_3Zn(OH)_6Cl_2$ (left) and haydeeite $Cu_3Mg(OH)_6Cl_2$ (right). The Fermi level ε_F is at zero energy. Insets: the $(dp)_\sigma$ band complexes at ε_F.

The states relevant for magnetism are confined to a close vicinity of ε_F. To evaluate the orbital characters of these states, the local coordinate system of a CuO_4 plaquette is considered. Projecting the DOS onto a set of local orbitals yields a dominant contribution of Cu $3d_{x^2-y^2}$ orbitals (Fig. 7.10, upper panel), as for most cuprates. The analysis of the relevant ligand states is more tricky. Thus, in addition to the expected O $2p_\sigma$ states, $2p_\pi$ and $2p_z$ show sizable contribution to O states around ε_F (Fig. 7.10, lower panel). This effect is caused by the peculiar buckling of magnetic layers and the corner-sharing connections of the neighboring CuO_4 plaquettes (Fig. 7.9). As a result, O $2p_\sigma$ states in the coordinate system of a certain plaquette turn into a combination of different O $2p$ states in the local system of the neighboring plaquette, i.e. the local coordinate systems of the neighboring plaquettes are non-orthogonal. Therefore, the seemingly large O $2p_\pi$ contribution (Fig. 7.10) does not invalidate the effective one-orbital approach (similar to dioptase, Sec. 6.3), typically used for cuprate systems.

---

[8] The experimental H position reported for kapellasite served as a staring point for the relaxation of both kapellasite and haydeeite.

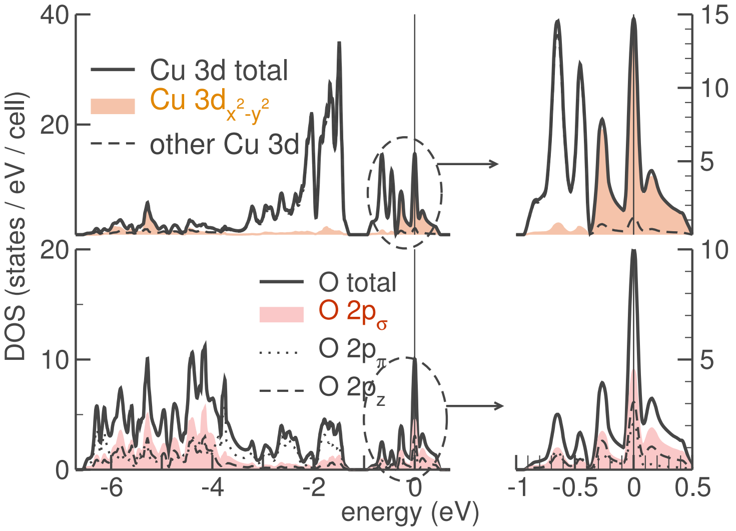

Figure 7.10: Orbital-projected DOS of Cu $3d$ and O $2p$ orbitals in kapellasite $Cu_3Zn(OH)_6Cl_2$. Left panel: the valence band. Right band: $(dp)_\sigma$ states are dominant in the vicinity of ε_F. The sizable contribution of O $2p_z$ states is explained in the text.

Next, the LDA band structure is considered. Here, the well separated DOS at ε_F is formed by a three-band complex (Fig. 7.11). Since the number of bands is the same as the number of Cu atoms in a unit cell, there is no necessity to consider other Cu orbitals.

The two band structures bear strong resemblance to each other, hinting at similar coupling regimes. Yet, the bandwidth of the three-band complex is slightly larger for kapellasite (0.86 eV versus 0.73 eV in haydeeite). Since the bandwidth is directly related to the magnitude of transfer integrals t_i, the leading couplings in kapellasite are expected to be slightly enhanced compared to haydeeite.

To evaluate the relevant couplings, an effective one-orbital TB model is parameterized in order to get the best fit to the LDA bands. A steepest descent procedure for the transfer integrals, corresponding to the ten smallest Cu–Cu distances, yields consistent solutions that are in excellent agreement with the LDA bands (Fig. 7.11). Since only four of ten couplings exceed 10 meV ($\sim$10$-$15 % of the leading coupling), the stability of the leading terms was checked by a subsequent reduction of the number of parameters in the model. These results suggest that the leading t_i terms bear less than 10% uncertainty.

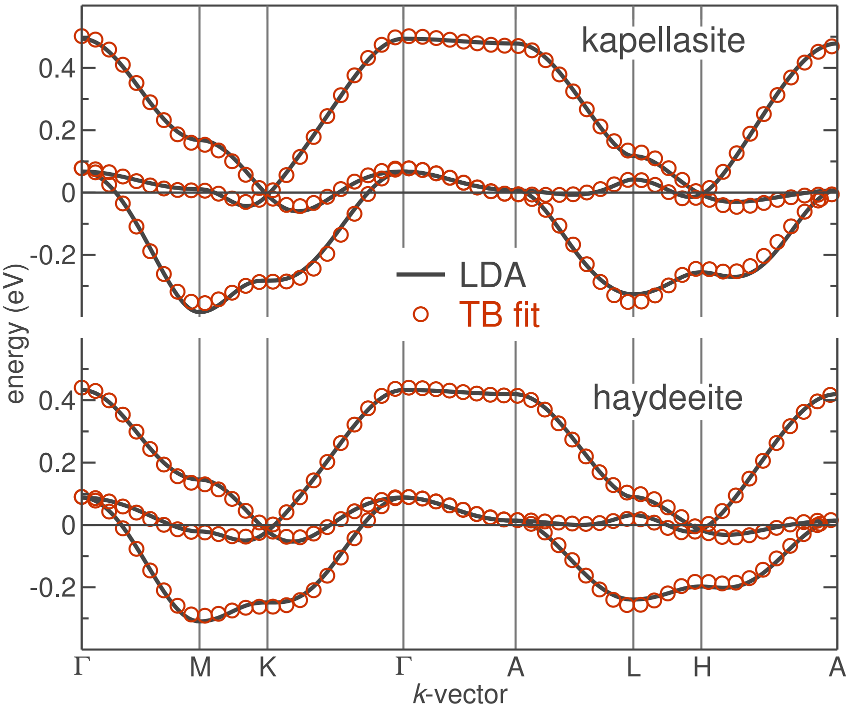

Figure 7.11: Band structure of kapellasite $Cu_3Zn(OH)_6Cl_2$ (top) and haydeeite $Cu_3Mg(OH)_6Cl_2$ (bottom). LDA bands as well as tight-binding (TB) fits are shown.

The four relevant terms are the NN coupling t_1, the two nonequivalent second-neighbor couplings t_2 and t_{d2}, as well as the third-neighbor coupling t_d running along the diagonals of voids on a kagome lattice (Fig. 7.7, right bottom; Table 7.3, third column). In order to include the missing part of electronic correlations, the TB model is mapped onto a HUBBARD model and subsequently onto a HEISENBERG model (Sec. 4.2), yielding the AFM part of the exchange (Table 7.3, fourth column). The values of the total exchange (Table 7.3, last column) are derived from the LSDA+U calculations. Since for the both systems, J_2 and J_{2d} are significantly smaller than the leading terms J_1 and J_d, the following analysis is confined to the latter two exchange couplings.

Table 7.3: Leading couplings in kapellasite $Cu_3Zn(OH)_6Cl_2$ and haydeeite $Cu_3Mg(OH)_6Cl_2$: Cu–Cu distances (in Å), transfer integrals t_i (in meV), the AFM J_i^{AFM} and the FM J_i^{FM} contributions to the total exchange J_i (in K).

kapellasite $Cu_3Zn(OH)_6Cl_2$

path	Cu–Cu	t_i	J_i^{AFM}	J_i^{FM}	J_i
X_1	3.151	87	78	−48	30
X_2	5.458	−10	1	–	<1
X_{2d}	6.302	20	4	−3	<1
X_d	6.302	49	25	−15	10

haydeeite $Cu_3Mg(OH)_6Cl_2$

path	Cu–Cu	t_i	J_i^{AFM}	J_i^{FM}	J_i
X_1	3.137	73	55	−46	9
X_2	5.433	−9	1	−1	<1
X_{2d}	6.273	22	5	−4	<1
X_d	6.273	42	18	−9	9

The NN exchange coupling J_1 in kapellasite and, especially, haydeeite is substantially smaller than the constituent AFM and FM contributions, J_1^{AFM} and $|J_1^{\mathrm{FM}}|$, respectively, disclosing a competition between the superexchange and the HUND's rule exchange. Thus, even a small alteration of the Cu–O–Cu can affect the resulting J_1. At the same time, only a marginal effect could be expected for J_d due to the long-range nature of this coupling. The physically relevant quantity α is crucially dependent on fine details of the crystal structure, such as Cu–O–Cu bond angles and O–H distances. Thus, to define the exact location of kapellasite and haydeeite in the phase diagram of the J_1–J_d model, precise structural data are necessary.

In contrast, the J_1–J_d model (Fig. 7.12) itself is a robust result. On the structural level, the relevance of J_d is can be ascribed to the parallel arrangement of the respective plaquettes, which favors the superexchange. On the other hand, the largely non-coplanar arrangement of the second-neighbor plaquettes explains the absence of any appreciable J_2.

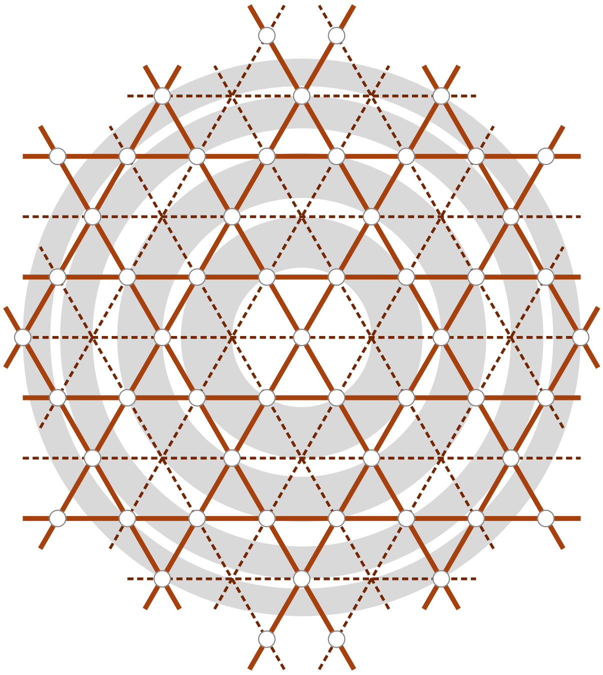

Figure 7.12: Magnetic J_1–J_d model on a kagome lattice. J_1 and J_d couplings are shown with bold solid and thin dashed lines, respectively. The first eight coordination spheres are depicted by concentric circles.

7.3.3 Spin model and simulations

The resulting microscopic magnetic model is depicted in Fig. 7.12. To evaluate the impact of the additional diagonal coupling J_d onto the magnetic GS and the excitation spectrum, the classical GS of the J_1–J_d model is addressed. Since the essential physics of the model is governed by the ratio of the two leading couplings, the ratio $\alpha \equiv J_\mathrm{d}/J_1$ is introduced to simplify the following discussion. The numerical simulations were performed by J. RICHTER at the University of Magdeburg.

The classical GS for $\alpha = 0$ (the pure kagome model) case is known to be highly degenerate [295, 296, 354]. The additional diagonal coupling J_d drastically reduces this degeneracy and selects non-coplanar GSs with 12 magnetic sublattices. These GSs are characterized by a perfect antiparallel spin alignment along the chains formed by diagonal couplings J_d and by a 120° spin arrangement on each triangle formed by the NN J_1 couplings (Fig. 7.13). As a result, every two spin-sublattices are antiparallel to each other and these two sublattices are perpendicular to one other group of two antiparallel sublattices. Noteworthy, such GSs are selected by an infinitesimal α. In a very recent study, such states were derived in a systematic way by considering classical GSs of a modified kagome model (extended by taking the second- and third-neighbor couplings into account) [301].

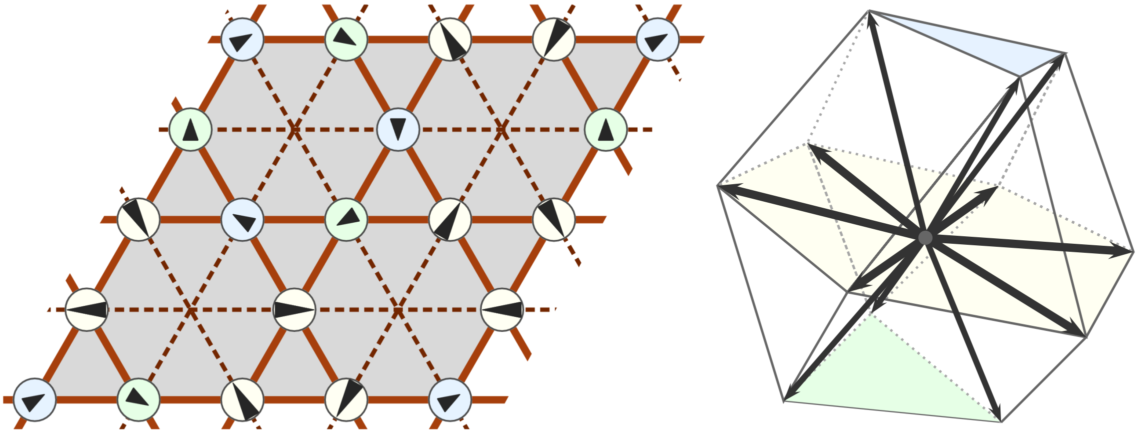

Figure 7.13: The classical 12-sublattice state of the AFM J_1–J_d model in the kagome geometry. Arrows denote the orientation of the spins vectors. The neighboring spins form 120° angles, the spins coupled by J_d are antiparallel. Yellow circles correspond to six in-plane spins (longer arrows), blue and green circles are out-of-plane spins (shorter arrows). The color notation is explained in the right panel.

The low spin value of $S = 1/2$ and the 2D nature of the spin model hint at the relevance of quantum fluctuations and call for an investigation of the quantum model. For this purpose, the GS spin correlations and the lowest-lying excitations were computed using Lanczos diagonalization (Sec. 5.2) on a finite lattice of $N = 36$ sites with periodic boundary conditions. This finite lattice fits to the magnetic structure of the classical GS.

The results for the calculated spin correlations $\langle \mathbf{S}_0 \cdot \mathbf{S}_R \rangle$ are presented in the right panel of Fig. 7.14. For comparison, the spin correlations for the pure kagome model ($\alpha = 0$) are shown. Obviously, the spin correlations in the quantum GS are drastically altered by J_d. While for $\alpha = 0$ the decay of the spin correlation function is extremely rapid, a well pronounced short-range order is found for $\alpha = 0.36$ and $\alpha = 1.0$, corresponding to the spin models of kapellasite and haydeeite, respectively. The short-range order corresponds to the classical magnetic structure. This leads to the conclusion that even in the quantum model the GS has a non-coplanar magnetic structure giving rise to enhanced chiral correlations.

Another important difference from the pure kagome system concerns the low-temperature thermodynamics. For $\alpha = 0$, the spin gap is filled by 210 singlets [83, 312] leading to different low-temperature behavior of the C_p (power-law in T) and χ (exponential decay). By contrast, for $\alpha = 1$ ($\alpha = 0.36$) there are no (only a few) singlets within the spin gap.

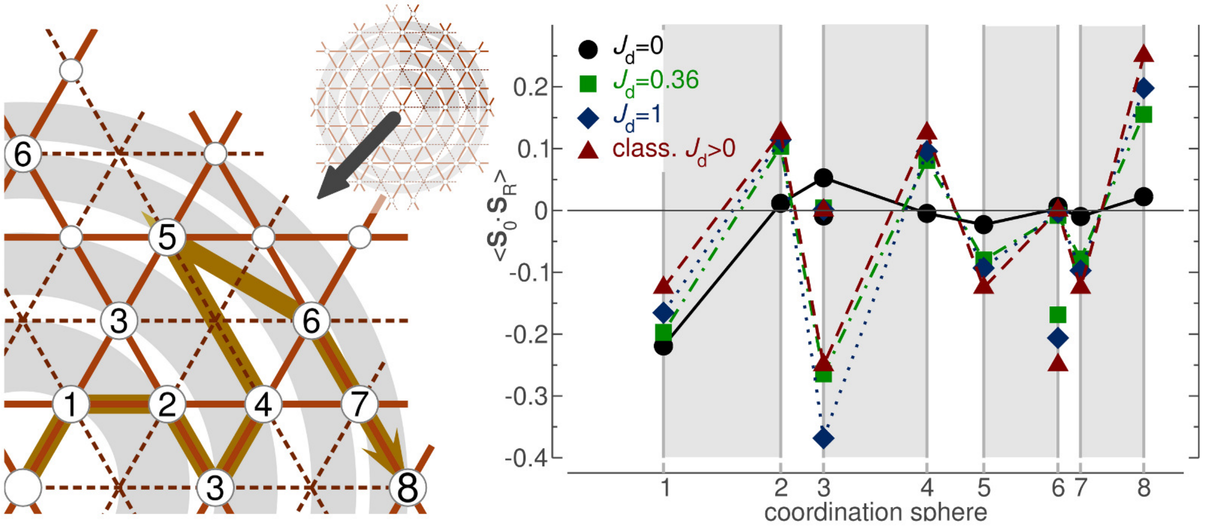

Figure 7.14: Left panel: the spin model for kapellasite $Cu_3Zn(OH)_6Cl_2$ and haydeeite $Cu_3Mg(OH)_6Cl_2$ with the leading J_1 (bold solid lines) and J_d (dashed lines) couplings. Concentric circles denote coordination spheres. Right panel: spin correlations on a $N = 36$ sites finite lattice using periodic boundary conditions. Note that for R = 3 and R = 6, two nonequivalent spin separations exist. The lines are guides for the eyes and correspond to the path depicted in the left panel. The strong correlations for one of the sets at R = 6 originate from finite-size effects.

Therefore, no essential difference between the low-temperature behavior of C_p and χ is expected.

7.3.4 Discussion

Geometrical considerations A common feature of all cuprates bearing an ideal kagome arrangement of Cu^{2+} ions and corner-sharing of the magnetic CuO_4 plaquettes is a strong buckling of the magnetic layers. This issue is related to both geometry and crystal chemistry, and deserves a detailed explanation. Thus, a typical polyhedron of Cu^{2+} is a flat CuO_4 plaquette with the $3d_{x^2-y^2}$ half-filled (magnetically active) orbital. Corner-sharing CuO_4 plaquettes can be indeed arranged in planar fashion, with Cu^{2+} atoms forming a kagome lattice. This arrangement can be described as an Archimedean lattice of O atoms, composed of regular squares (with a Cu atom in the center), triangles (empty) and hexagons (empty). In a real crystal structure, hexagons have to be filled by cations M to keep the charge balance. However, there are no cations known that would bear a planar 6-fold coordination. On the other hand, the octahedral coordination, topologically identical to a planar hexagon, is typical for many cations, for instance Zn^{2+} and Mg^{2+}. Moreover, the M–O distances on the planar Archimedean lattice have to match the O–O distances in a CuO_4 plaquette (~2.8 Å), whereas Zn–O and Mg–O bonds are considerably shorter (about 2.1 Å). Therefore, buckling of the kagome layer is a unique solution in order (i) to restore the octahedral coordination of Zn/Mg cations and (ii) shorten Zn/Mg–O distances to allow for a formation of a chemical bond. Noteworthy, this buckling does not break the three-fold rotational symmetry, essential for an ideal kagome layer.

How to control the buckling or even keep the planar Archimedean lattice intact and consequently, retain a perfect planar kagome layer? As discussed above, filling the planar O hexagons with cations is a prerequisite. Although there are no cations with such planar coordination, real structures are always 3D. Therefore, any coordination with six ligand atoms lying in a plane would match the requirements. Obviously, this is possible only if the total coordination number is large enough (for instance, twelve). In fact, such large coordination numbers are common for large cations forming essentially ionic bonds with oxygen. The next problem to solve is the large negative charge which such a structure would have. The compensation can be achieved within a layered structure, where the magnetic kagome planes would alternate with positively charged layers. Although synthesis of a material featuring such structure is at best challenging, the magnetism of the resulting compounds could be extremely interesting, since large Cu–O–Cu angles (compared to the buckled geometry) are expected to enhance the NN superexchange. This could be helpful to prove (or disprove) the theoretical prediction of a small (∼5% of J_1) spin gap in the $S = 1/2$ kagome HEISENBERG model.

Magnetism DFT calculations evidence that the magnetic properties of kapellasite and haydeeite can be effectively described within a J_1–J_d model on a kagome lattice. Since this model has been neither reported for any known systems, nor studied as a purely geometrical model, it is worth to discuss its properties in more detail. Presuming the AFM nature of the both couplings, the limiting cases of the J_1–J_d model are the pure kagome model ($\alpha = 0$) and the model of decoupled chains ($\alpha = \infty$). Although the GSs for these two limits are completely different, both of them lack LRMO. In contrast, for finite values of α corresponding to the cases of kapellasite ($\alpha = 0.36$) and haydeeite ($\alpha = 1$), sizable spin correlations evidence a magnetic order which is at least short-range. To investigate the onset of this order, spin correlations are calculated for various values of α. The results shown in Fig. 7.15 indicate a drastic enhancement of correlations in the range $\alpha = 0.1$–0.3.

Although the largest finite lattice size ($N = 36$) is too small and its shape is considerably anisotropic for an accurate study of the decoupled chains limit (large α), even moderate values of α show chain-like features of the GS. Thus, as follows from Fig. 7.14 and especially Fig. 7.15, the magnetic correlations along the chains built by J_d couplings (in Fig. 7.14 that is for R = 3 and 8, and additionally R = "+" in Fig. 7.15) are strongest, indicating that the low-energy excitations might be $S = 1/2$ spinons causing an effectively 1D low-temperature physics. Interestingly, such effect has been discussed for other 2D models: the crossed-chain model [355], the anisotropic triangular lattice [356] as well as the anisotropic SHASTRY–SUTHERLAND lattice [357].

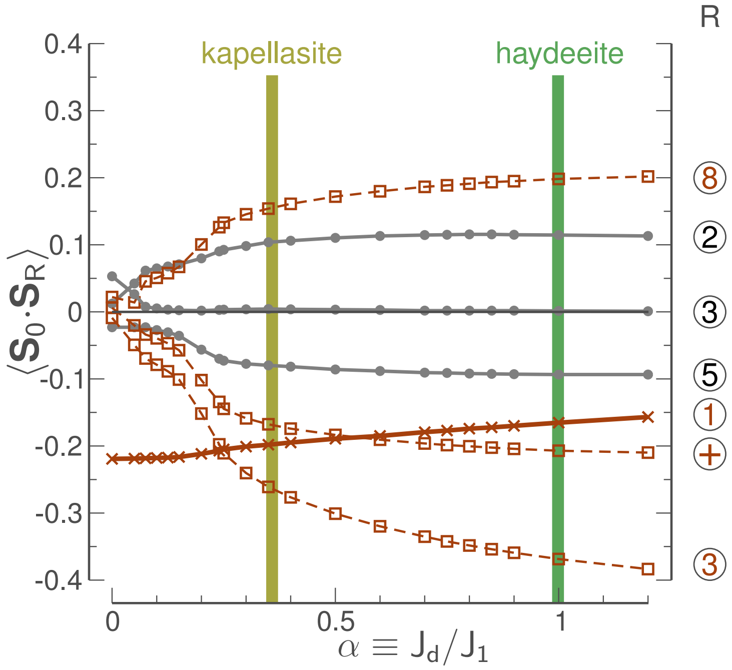

Figure 7.15: Spin correlations in the J_1–J_d model at various J_d/J_1 ratios. For the notation of spins, see the left panel of Fig. 7.14. The spin "+" is the next spin in the J_d chain running through 0, 3 and 8.

7.4 Volborthite $Cu_3[V_2O_7](OH)_2{\cdot}2H_2O$

The mineral volborthite $Cu_3[V_2O_7](OH)_2{\cdot}2H_2O$ was found in the Ural mountains (Russia) in 1838 and named after the Russian-German paleontologist Alexander von Volborth [358]. Initially, it was described as a vanadic acid containing copper oxide, subsequent studies revealed the presence of hydroxyl groups and crystal water.

The crystal structure of volborthite was repeatedly investigated in the last 40 years, thus several controversial structural models are presently available. The inaccuracies of the experimental crystal structure may have crucial impact on the DFT-based magnetic models, hence a substantial part of the computational study aimed to obtain a reliable structural input.

Although the material is known for more than 150 years, the magnetism of volborthite remained unexplored till 2001. Then, the authors of Ref. 326 carried out an extensive experimental study of the magnetic properties of volborthite, in particular, magnetic susceptibility (up to 400 K), specific heat (up to 70 K), low-field magnetization (up to 5 T), and ^{51}V NMR experiments, including the Knight shift and $1/T_1$ measurements. Based on (i) a good fit of $\chi(T)$ using HTSE for the pure kagome model [153], (ii) the lack of long-range magnetic ordering down to 1.8 K despite the large value of the Weiss temperature $\theta = 115$ K, and (iii) seemingly small monoclinic distortion of the kagome layers, they concluded that volborthite might be a realization of an $S = 1/2$ Heisenberg kagome antiferromagnet.

For about 8 years, the magnetic properties of volborthite were studied mainly by resonance techniques. In particular, X-band and high-field (up to 16 T) ESR measurements revealed a strong decay of the ESR signal at ~5 K, which is likely a fingerprint of a short-range order at lower temperatures [359]. μSR studies, carried out on the pure and Znsubstituted (diluted) samples of volborthite, showed slow spin fluctuations persistent down to 50 mK [360]. Later on, ^{51}V NMR experiments revealed the existence of a frozen magnetic state with the frozen moment on Cu atoms amounting to 0.4 μ_B [361]. The authors of Ref. 361 suggested the short-range order similar to be similar to the $\sqrt{3}\times\sqrt{3}$ state of the pure kagome model [354].

The development of a new synthesis procedure helped to improve the quality of volborthite samples, that were subsequently used for the new ^{51}V NMR measurements focusing on the field-induced transitions [362]. The NMR experiments revealed a rather involved phase diagram with an anomalous low-field phase exhibiting slow dynamics and showing two distinct energy scales, as well as the high-field phase, with the transition between the two phases at ∼5 T [362].

The high-field behavior has been further investigated by magnetization in pulsed fields up to 55 T [363]. The improved sample quality allowed to resolve peculiar transitions at 4, 25 and 46 T, called magnetization steps [363]. The presence of these successive transitions indicates an even more complicated phase diagram. Very recent high-field measurements up to 70 T reveal the diminishing slope of the magnetization between 60 and 70 T pointing to the onset of a magnetization plateau [364].

Polarized and inelastic neutron scattering experiments revealed a flat band of excitations [365]. In addition, fingerprints of the short-range magnetic ordering are visible even at high temperatures of ∼15 K. In a very recent $C_p(T)$ measurement, a clear kink has been observed at 1 K, indicative of the ordering transition [366]. Based on these measurements, the GS has been characterized as gapless and less ordered than the high-field phase (>5 T).

To sum up the experimental findings, the magnetic properties of volborthite turned out to be very complicated. Not surprisingly, these controversies attracted attention of theoretical physicists, resulting in several attempts to find a consistent description for the magnetism of volborthite from the theoretical side. Since the kagome layers in volborthite are slightly distorted and the experimentally observed features are definitely not accounted for by the pure kagome model, the theoretical studies focused on the GS [367–370] and thermodynamic properties [160] of the anisotropic kagome model, which comprises two nonequivalent nearest-neighbor interactions. These studies contributed significantly to the understanding of the model itself, but attempts to reach consistency with the experimental data by varying the degree of anisotropy were not successful so far. Perhaps, the most striking disagreement is the deviation of the magnetic susceptibility from the theoretically predicted behavior even at rather high temperatures of ∼100 K [160].

In this DFT-based study, the microscopic magnetic model for volborthite is evaluated and the origin of the puzzling disagreement between the experiments and the previously suggested theoretical models is resolved. In particular, it is shown that the seemingly small distortion of the kagome lattice is an incorrect starting point for modeling. Instead, subtle structural features lead to a completely different frustrated magnetic model with three exchange couplings J_{ic}, J_1, and J_2, whereby J_1 is FM. Subsequent simulations of this microscopic model evidence an improved agreement with the experimental data.

7.4.1 Crystal structure

The monoclinic (space group $C2/m$) crystal structure of volborthite has been investigated by several XRD studies [371–373] as well as a combined XRD and ND study [374].

Table 7.4 summarizes these studies and reports the structural parameters relevant for the magnetism. Large scattering of these parameters can be explained by a poor quality of the single crystals used for the experimental studies. In addition, the chemical composition of volborthite hampers structural studies due to the considerable content of H and V atoms, which are poor scatterers of X-rays and neutrons, respectively (for details, see Sec. 3.1.1 and 3.1.2). However, despite sizable deviations of individual bond lengths and angles, the layered structural motive (Fig. 7.16) is the same in all the experimental studies.

The structure of volborthite comprises magnetic layers formed by two (three in the model of Ref. 373) independent Cu atoms with essentially different local environment: Cu(1) has two short and four long Cu(1)–O bonds, while Cu(2) bears a typical Cu^{2+} coordination with four short and two long Cu(2)–O bonds (see Table 7.4). In Fig. 7.16, the crystal structure is depicted in terms of short-bonded polyhedra, i.e. the dumbbells for Cu(1) and the plaquettes for Cu(2). These polyhedra form edge-sharing chains of $Cu(2)O_4$ plaquettes, coupled by $Cu(1)O_2$ dumbbells (Fig. 7.16, right). Already on this purely descriptive level, these magnetic polyhedra are hardly reminiscent of a kagome layer.

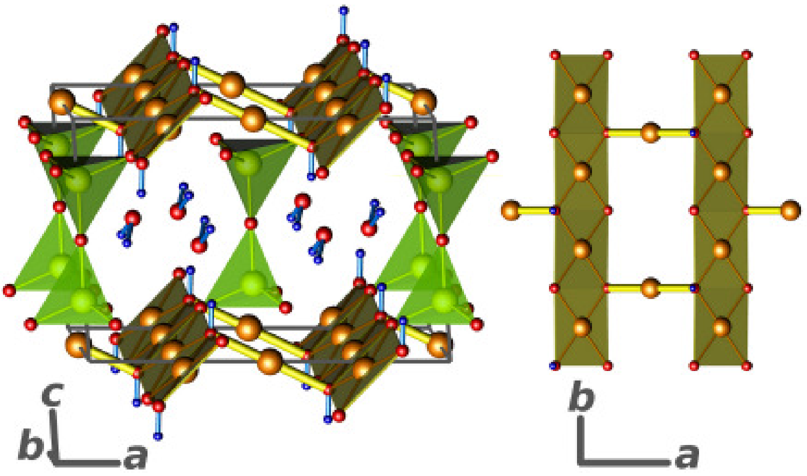

Figure 7.16: Monoclinic crystal structure of volborthite $Cu_3[V_2O_7](OH)_2{\cdot}2H_2O$ (left). The structure contains magnetic layers (right) formed by chains of edge-sharing $Cu(2)O_4H_2$ plaquettes, connected by $Cu(1)(OH)_2$ dumbbells. The interlayer space is filled with pyrovanadate V_2O_7 groups and water molecules (left).

A reliable structural input is a prerequisite for microscopic modeling based on DFT calculations. Since even a small change of Cu–O–Cu angle can lead to drastic changes in the magnetic properties. After a careful consideration of the available structural data sets, the structural model based on the joint XRD and ND from Ref. 374 has been chosen, since such combination improves the reliability of the resulting data. However, the number of observed reflections (340 in the X-ray and 102 in the ND study [374]) is not sufficient for fully conclusive results. Therefore, a structural optimization relaxing the atomic coordinates and minimizing the forces (for details, see Sec. 7.4.2), has been carried out. To evaluate the influence of the different structural models, the calculations are performed for the experimental as well as for the optimized structure.

Table 7.4: Selected bond lengths and angles from different structural data sets for volborthite. In Ref. 371, H positions have not been reported. Ref. 374 provides two data sets, based on XRD and ND studies. Ref. 373 implies a different structural model, which results in a symmetry reduction and thus increased number of nonequivalent bonds. The last column corresponds to the optimized structure (see Sec. 7.4.2).

structural model (Ref.)					
[371]	[372]	[374] XRD	[374] ND	[373]	this study, optimized
Cu(1)–O distances, Å					
2.046	1.945	1.926	1.905	1.914	1.912
2.084	2.172	2.165	2.158	2.000/2.369	2.143
Cu(2)–O distances, Å					
2.032	1.922	1.913	1.900	1.927/1.942	1.907
2.048	2.031	2.052	2.048	2.044/2.058	1.991
2.295	2.413	2.438	2.379	2.454/2.322	2.423
Cu(2)–O–Cu(2) angles (intrachain), °					
91.49	92.43	91.37	91.40	93.59/92.25	95.06
92.38	99.47	100.30	101.00	101.22/97.90	100.72
Cu(1)–O–Cu(2) angle(s) (interchain), °					
95.54	103.24	104.30	105.57	102.17/100.53	105.06
O–H distance(s), Å					
–	1.008	0.886	0.921	0.871/1.179	1.029

7.4.2 DFT calculations

The valence band of volborthite is formed predominantly by Cu and O states, with a minor admixture of V states (Fig. 7.17, top). Unlike kapellasite and haydeeite (Fig. 7.9), the DOS of volborthite lacks a separated density peak at ε_{F}. The $\vec{k}$-resolved picture of the energy region corresponding to the magnetic excitations yields an empty, a half-filled and a filled band, in agreement with three Cu atoms per cell (Fig. 7.17, bottom). However, three additional bands in the vicinity of ε_{F} hint at possible orbital mixing and call for a careful evaluation of the orbital states.

To evaluate the relevant orbitals, the DOS is projected onto local orbitals of the two structurally independent Cu atoms, Cu(1) and Cu(2). The resulting orbital-resolved DOS is shown in Fig. 7.18. The $3d_{x^2-y^2}$ and $3d_{3z^2-r^2}$ orbitals exhibit sizable energy overlap, while other $3d$ states lie at lower energies for the both Cu atoms. The LDA yields an essentially different filling of the orbitals: for Cu(1) the $3d_{3z^2-r^2}$ is close to half-filling and the $3d_{x^2-y^2}$

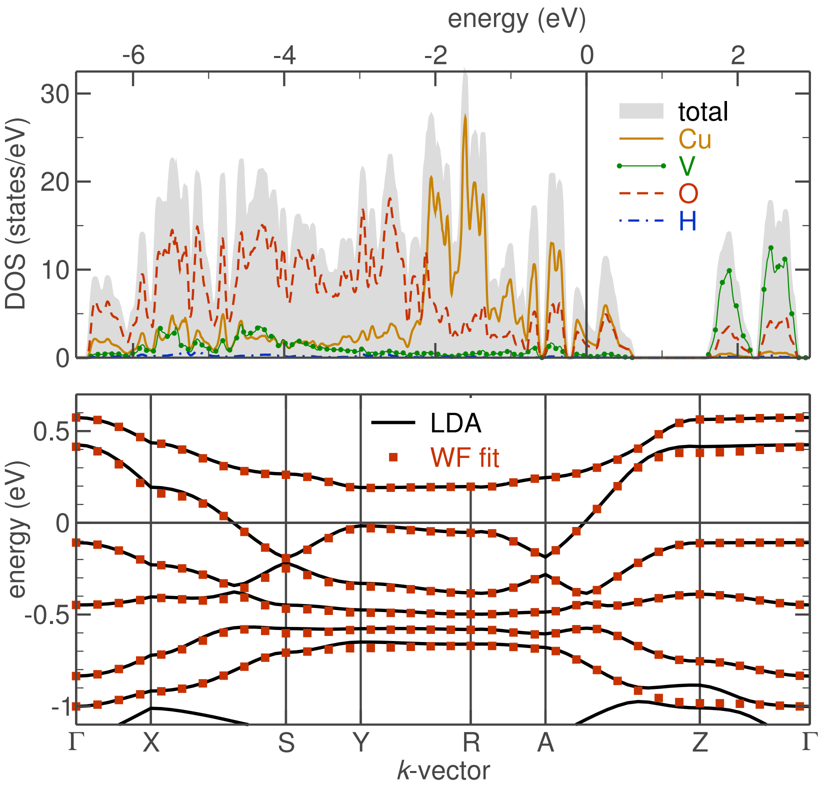

Figure 7.17: Top: total and atom-resolved DOS for volborthite $Cu_3[V_2O_7](OH)_2{\cdot}2H_2O$. Bottom: LDA band structure and the Wannier functions fit for an effective two-orbital model.

orbital is almost filled (Fig. 7.18, left), while for Cu(2) it is the other way round (Fig. 7.18, right).

The closer proximity to half-filling is still insufficient to judge whether the respective orbital is magnetically active or not. Thus, in the LDA picture for $CuSb_2O_6$, the $3d_{x^2-y^2}$ orbital is closer to half-filling. However, if the $3d_{x^2-y^2}$ orbitals were magnetically active, the magnetism of $CuSb_2O_6$ would be essentially 2D, in sharp contrast to the experimentally observed 1D behavior [375]. The reason for this failure of the LDA is the underestimation of strong correlations intrinsic for the $3d^9$ electronic configuration (Sec. 2.1). A typical solution to the problem is switching to the LSDA+U approximation that remedies this drawback. In particular, for $CuSb_2O_6$, LSDA+U yields the correct 1D magnetism with the $3d_{3z^2-r^2}$ magnetically active orbital [376].

To evaluate the GS orbitals for volborthite, the approach previously used for $CuSb_2O_6$ [376], is applied. Thus, the solutions comprising different orbital occupations are compared with respect to their total energies, in order to evaluate the GS configuration. Since only $3d_{x^2-y^2}$ and $3d_{3z^2-r^2}$ orbitals contribute to the states in the vicinity of ε_F (Fig. 7.18), the analysis is restricted to these two orbitals. Two independent Cu atoms give rise to four states in the resulting model (Fig. 7.19). The LSDA+U calculations using the AMF DCC with $U_d = 6$ eV and the FM spin arrangement yield an orbitally-ordered GS comprising Cu(1) $3d_{3z^2-r^2}$ and Cu(2) $3d_{x^2-y^2}$ orbitals, which follows the LDA result.

Next, the stability of this solution is addressed. The energy separation (orbital gap) between the orbital GS and the first excited orbital state exceeds 0.6 eV (Fig. 7.19) or $\sim$7000 K, which is roughly two orders of magnitude larger than the leading couplings.

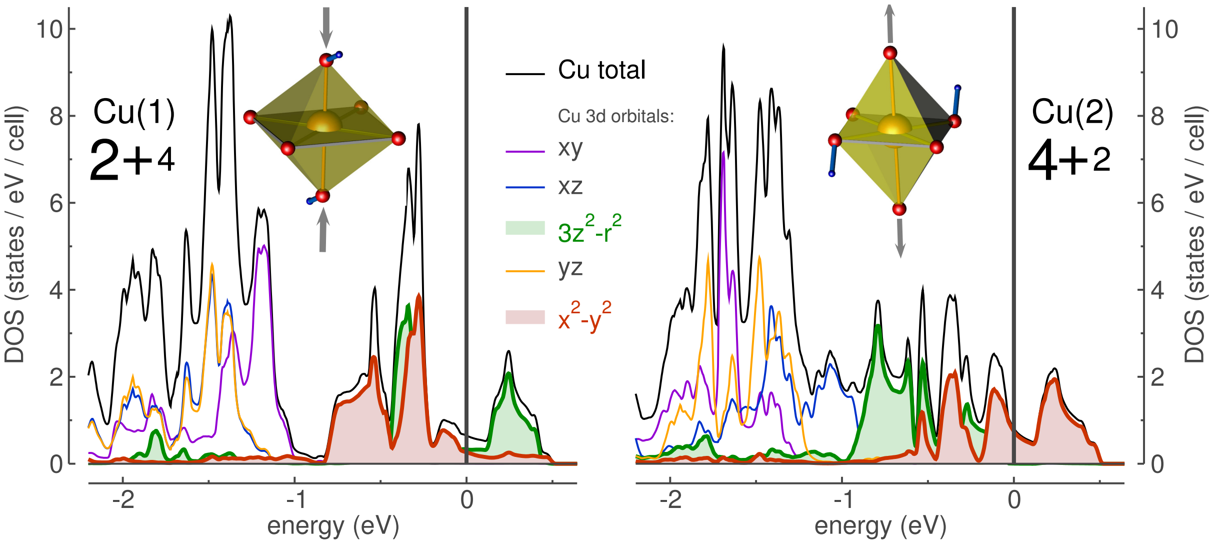

Figure 7.18: Orbital-resolved DOS in the LDA for Cu(1) and Cu(2) atoms in volborthite $Cu_3[V_2O_7](OH)_2{\cdot}2H_2O$. Insets: distortion of the local environment of Cu(1) (left) and Cu(2) (right).

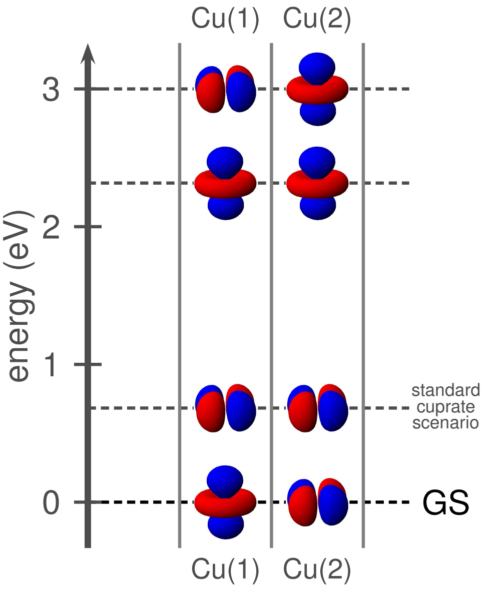
Cu(1)
Cu(2)
energy (eV)
3
2
1
0
standard cuprate scenario
GS
Cu(1)
Cu(2)

Figure 7.19: Energy separation between the orbital GS and excited states, as yielded by LSDA+U calculations (AMF, $U_d = 5$ eV, FM spin alignment). The orbitals were plotted using `Orbital Viewer` [377].

Such a large energy separation, in sharp contrast with herbertsmithite (Sec. 7.2), evidences that orbital and spin degrees of freedom are decoupled and can be analyzed separately. To cross-check the results, additional calculations are performed for the FLL DCC using $U_d = 8$ eV for the FM as well as for the AFM spin arrangements. The difference between the AMF and the FLL results amounts to 5%. As expected for the different energy scales, the orbital gap is not affected by spin arrangements (<1% difference between the FM and AFM configurations). Therefore, the orbital order of Cu(1) $3d_{3z^2-r^2}$ and Cu(2) $3d_{x^2-y^2}$ is well established for the whole relevant temperature range.

The relevant couplings are evaluated within a minimal three-orbital model (one orbital per Cu site) comprising Cu(1) $3d_{3z^2-r^2}$ and Cu(2) $3d_{x^2-y^2}$ states, only. Unfortunately, the overlapping orbital contributions impede an accurate fit to the LDA bands, hence it is reasonable to extend the model by including the lower-lying Cu(1) $3d_{x^2-y^2}$ and Cu(2) $3d_{3z^2-r^2}$ states explicitly. Such an extension leads to a six-orbital TB model, which was solved using the Wannier functions technique (Sec. 4.2.3). The perfect fit to the LDA bands (Fig. 7.17, bottom) justifies this solution.

The TB model contains hoppings between six [two for Cu(1) and four for Cu(2)] different orbitals for the three Cu atoms in the unit cell. However, only three of the six orbitals are magnetically active. Therefore, the following analysis is confined to the three-orbital sector describing to the hoppings between the GS orbitals Cu(1) $3d_{3z^2-r^2}$ and Cu(2) $3d_{x^2-y^2}$. Here, the leading terms are the NN couplings t_1 connecting Cu(2) atoms and t_{ic} running between Cu(1) and Cu(2) (Fig. 7.20). These NN terms correspond to the t and t' couplings in the anisotropic kagome model [367–370]. Quite unexpectedly, one of the second-neighbor couplings t_2 (Fig. 7.20) is also sizable. Further couplings are smaller than 30 meV (20 % of the leading coupling t_{ic}) and can be neglected in the minimal model.

As discussed in Sec. 7.4.1, insufficient sample quality and the specific chemical composition of volborthite may give rise to sizable uncertainties for the atomic coordinates (especially, for H atoms). The rather high values of forces, calculated in the LDA, corroborate this concern. To minimize the forces, an optimization of the crystal structure is performed within LDA. The optimized structure inherits all major structural peculiarities of volborthite and, in the first place, preserves the essentially different local arrangement of Cu(1) and Cu(2) atoms (Table 7.4, last column). Still, the changes in the Cu–O–Cu angles and the O–H distance alter the magnetism. Since the optimized structure yields 0.8 eV lower total energy (per cell) than the experimental one, more credit should be given to the optimized structure.

In order to evaluate the influence of the structural model, the couplings are calculated for the both structures using LDA as well as GGA. The results are summarized in Table 7.5. The main trend clearly visible in the data is the increased value of t_1 for the optimized structure, while the values of t_{ic} and t_2 are almost unaffected by the structural model. In addition, the LDA and GGA results practically coincide (Table 7.5). It is important to note that this coincidence is specific to volborthite and should not be generalized even for closely

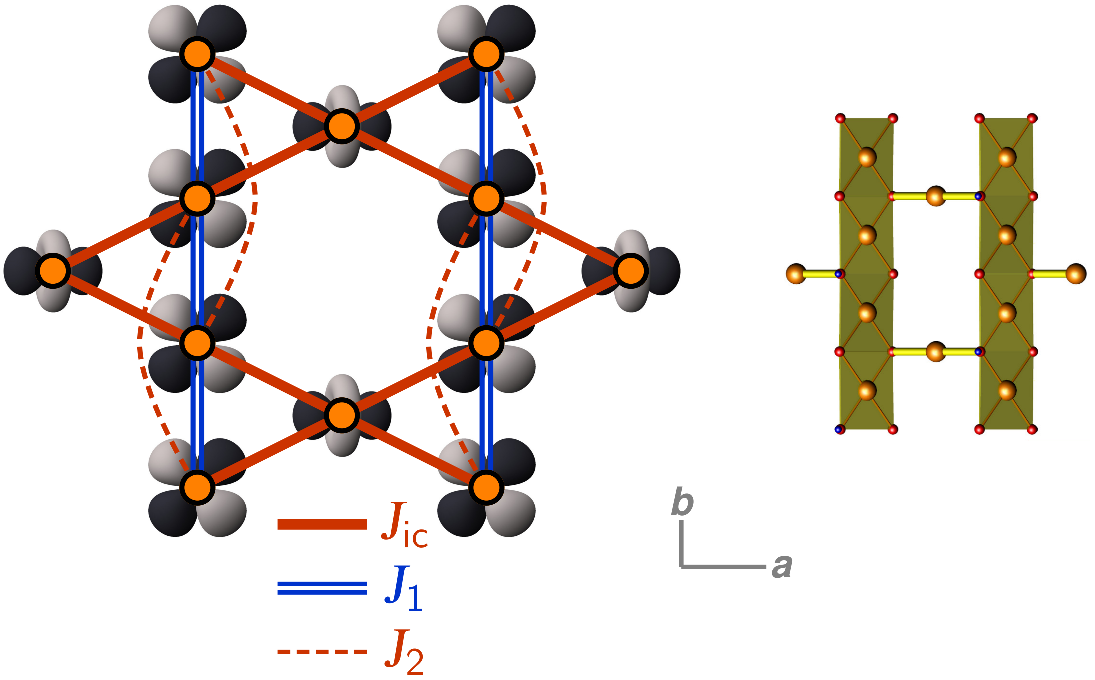

Figure 7.20: The microscopic magnetic model for volborthite $Cu_3[V_2O_7](OH)_2{\cdot}2H_2O$. Left: the magnetically active orbitals and the leading couplings. Cu atoms are depicted as orange circles. The orbitals were plotted using `Orbital Viewer` [377]. Right: the structural unit (see also Fig. 7.16) for which the magnetic model in the left panel is drawn.

Table 7.5: Transfer integrals t_i (in meV) and AFM exchange integrals J_i^{AFM} (in K) for the leading couplings in volborthite $Cu_3[V_2O_7](OH)_2{\cdot}2H_2O$ for the experimental and the optimized crystal structure.

path (Fig. 7.20)	experimental [374]				optimized (Table A7)			
	LDA		GGA		LDA		GGA	
	t_i	J_i^{AFM}	t_i	J_i^{AFM}	t_i	J_i^{AFM}	t_i	J_i^{AFM}
X_{ic}	156	251	156	251	155	248	157	254
X_1	91	85	93	89	117	141	119	146
X_2	59	36	57	33	64	42	62	42

related systems (β-$Cu_2V_2O_7$ is an instructive counterexample [265]).

To account for the correlation effects, the transfer integrals t_{ic}, t_1 and t_2 are mapped onto a Hubbard model with the effective Coulomb repulsion $U_{\text{eff}} = 4.5$ eV. This way, the AFM contributions for the leading exchange interactions can be estimated (Table 7.20). The energy scale set by the leading exchange coupling $J_{\text{ic}}^{\text{AFM}}$ 250 K largely exceeds the experimental θ 115 K. This discrepancy originates from the minimal character of the effective six-orbital model, which does not account for the Hund's coupling on ligand O atoms, being the major source of FM exchange in cuprates (Sec 4.2.7). For volborthite, sizable FM contributions to the NN couplings J_{ic}, and especially J_1 (due to the edge-sharing of the neighboring plaquettes) can be expected.

The values of the total exchange, containing the AFM and FM contributions, are evaluated based on LSDA+U calculations for various spin arrangements within the orbital

GS, which comprises the Cu(1) $3d_{3z^2-r^2}$ and the Cu(2) $3d_{x^2-y^2}$ magnetic orbitals. Due to the aforementioned uncertainties for the atomic coordinates in the experimental crystal structure as well as the orbitally-ordered GS, the evaluation of the leading couplings in volborthite is a nontrivial task. First, the resulting values of exchange integrals depend on the structural model, which can been traced even on the LDA level by comparing the respective values of J_i^{AFM} (Table. 7.5). Second, the total exchange integrals depend on the U_d value used in the LSDA+U scheme. Last but not the least, the LSDA+U calculations evidence strong dependence of the total exchange integrals on the DCC scheme. Depending on all these parameters, $J_1 = -80 \pm 10\,\mathrm{K}$, $J_2 = 35 \pm 15\,\mathrm{K}$ and $J_{\mathrm{ic}} = 100 \pm 60\,\mathrm{K}$ are evaluated for the experimental structure. The calculations of the optimized structure yield $J_1 = -65 \pm 15\,\mathrm{K}$, $J_2 = 45 \pm 15\,\mathrm{K}$ and $J_{\mathrm{ic}} = 100 \pm 60\,\mathrm{K}$. The ratios of the leading couplings $J_{\mathrm{ic}}/|J_1|$ and $J_2/|J_1|$ are graphically summarized in Fig. 7.21.

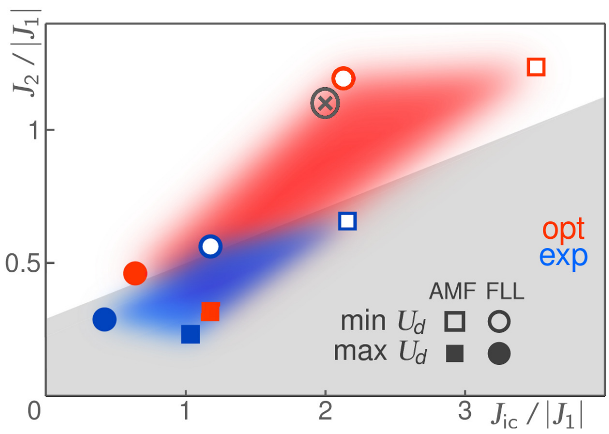

Figure 7.21: LSDA+U exchange integrals for volborthite $Cu_3[V_2O_7](OH)_2{\cdot}2H_2O$ as a function of the structural model (opt or exp), the LSDA+U DCC scheme (AMF or FLL) and U_d (min U_d, max U_d) on the phase diagram of the J_1–J_2–J_{ic} model. The white and gray fields correspond to the singlet and the ferrimagnetic phases, respectively. The red- and blue-shaded areas depict possible values of exchange couplings for the both structural models. The ED results yield the best agreement for $J_{\mathrm{ic}}/|J_1| = 2$, $J_2/|J_1| = 1.1$, depicted by a encircled cross.

The substantially FM nature of J_1, in accord with the small values of the respective Cu–O–Cu angles (Table 7.4), and the relatively small uncertainties of its strength disregarding the parameters used give strong evidence that the pure kagome model is totally inappropriate for volborthite. The anisotropic kagome model hardly remedies the situation, since the NN couplings—an FM J_1 and an AFM J_{ic}—do not compete with each other, thus the model is not frustrated. Indeed, the GS of a system with an FM J_1 and an AFM J_{ic} is ferrimagnetic, with an FM arrangement of spins in the J_1–J_2 chains and antiparallel arrangement of spins between the chains (dangling spins). Since the number of intrachain spins is two times larger than the number of dangling spins, the total magnetic moment of the GS amounts to one-third of the saturation magnetization. Such GS is in striking contrast with the experiments, unequivocally evidencing a moment-free GS [326]. Therefore, the anisotropic kagome model also does not account for the magnetism of volborthite.

The microscopic insight evidences that the appropriate model to describe the magnetic properties of volborthite is the J_1–J_2–J_{ic} model with a FM J_1. In this model, frustration is governed by the second-neighbor exchange J_2, which competes with both J_1 and J_{ic}. The properties of this model will be discussed in the next section (Sec. 7.4.3).

Localization of volborthite in the phase diagram of the J_1–J_2–J_{ic} model is rather challenging. As can be seen from the large color-shaded fields in Fig. 7.21, the results of the LSDA+U calculations do not provide a fully conclusive answer. Therefore, additional and complementary methods have to be used (Sec. 7.4.3). Still, the results of LSDA+U calculations allow to strongly delimit the relevant region in the phase space of the J_1–J_2–J_{ic} model (red- and blue-shaded area in Fig. 7.21). First, J_1 is FM disregarding the parameters used for both structural models. Next, the LSDA+U results render J_{ic} as the leading coupling in volborthite. However, the ratios J_{ic}/J_1 and J_2/J_1, crucial for the magnetism, can not be determined precisely enough. Instead, two general trends can be established. First, the optimized structure has an enhanced $J_2/|J_1|$ ratio compared to the experimental structure. Second, FLL yields considerably smaller J_{ic} and somewhat larger values for J_2 than AMF. Still, for a fully conclusive quantitative analysis, precise experimental structural input is highly desirable.

7.4.3 Ground state and thermodynamics of the J_1–J_2–J_{ic} model

For this discussion, the signs for the leading couplings adopted from the DFT calculations (Sec. 7.4.2), in particular, the AFM J_{ic} and J_2 as well as the FM J_1. First, the limiting cases of this model are discussed. Thus, for $J_2 = 0$ the model is non-frustrated and the classical GS is ferrimagnetic, with the moment equal to $1/3$ of the saturation value. In the case of $J_{\text{ic}} = 0$, the model is reduced to a frustrated HEISENBERG chain in an effective magnetic field induced by the dangling spins. Interestingly, a similar model (but with AFM J_1) has been discussed with regard to volborthite [378]. To discuss the intermediate situations, it is convenient to introduce the ratios $J_{\text{ic}}/|J_1|$ and $J_2/|J_1|$.

Phase diagram DFT calculations yield $0.5 \leq J_{\text{ic}}/|J_1| \leq 3.5$ and $0.25 \leq J_2/|J_1| \leq 1.25$, corresponding to the color-shaded regions in Fig. 7.21. Following the strategy employed for kapellasite and haydeeite (Sec. 7.3.3), the classical model is analyzed and afterwards quantum fluctuations are introduced by calculating the spectra of finite lattices. Since the exact solution for a 2D classical J_1–J_2–J_{ic} model is at best nontrivial, the model is simplified by considering the zig-zag chains running along b in volborthite. In these zig-zag chains, J_{ic} plays the role of NN coupling, J_1 is the second-neighbor coupling and J_2 is the fourth-neighbor coupling. Presuming that the GS of this 1D model is the same as for an isolated chain, two states are readily obtained: a ferrimagnetic (collinear) GS and a spiral state, with the phase transition between the two states given by $J_2^{\text{class, 1D}} = 0.25\,|J_1| + 0.125\,J_{\text{ic}}$.

The LSDA+U estimates for J_2 are higher than this critical value, disregarding the parameters used. Therefore, all LSDA+U solutions correspond to the classical spiral GS. Such GS has no net magnetic moment, in accord with the experiments [379]. On the next level of complication, a more realistic 2D classical model on a finite lattice of $N = 36$ spins is considered using periodic boundary conditions [379]. The simulations were performed by J. RICHTER at the University of Magdeburg. The boundary effects and the interpenetration of the zig-zag chains modify the expression for the phase transition and extend the stability range for the ferrimagnetic phase [379]:

$$J_2^{\text{class}} = \frac{|J_1|}{2.9} + \frac{J_{\text{ic}}}{6.0}. \tag{7.1}$$

Finally, the quantum model on the same lattice is investigated. Quantum fluctuations further stabilize the ferrimagnetic collinear state, yielding [379]:

$$J_2^{\text{quant}} = \frac{|J_1|}{3.3} + \frac{J_{\text{ic}}}{5.0}. \tag{7.2}$$

The stability ranges of the ferrimagnetic as well as the spiral phases set by Eq. 7.2 are depicted in Fig. 7.21 with gray and white regions, respectively. The LSDA+U solutions for the experimental structure (the blue-shaded region in Fig. 7.21) largely fall into the region of the ferrimagnetic phase. In contrast, the solutions for the optimized structure (the red-shaded region in Fig. 7.21) lie either in a close vicinity to the phase boundary or in the region corresponding to the spiral phase. Since the ferrimagnetic solutions contrast with the experiments [326], in the following only the spiral phase above the phase boundary given by Eq. 7.2, is analyzed.

Magnetic ground state The structure of the GS is generally probed by spin correlations. The correlation functions for volborthite are presented in Fig. 7.22. Discussing the results is more convenient in terms of the J_1–J_2 chains, corresponding to the edge-sharing chains of Cu(2)O_4 plaquettes (Fig. 7.16), and the dangling spins of Cu(1). Thus, the correlations between the J_1–J_2 chains (Fig. 7.22, top left) exhibit a rapid decay reminiscent of the pure kagome HEISENBERG antiferromagnet. In contrast, the correlations along the J_1–J_2 chains (Fig. 7.22, bottom right) are much stronger, and exhibit no clear signature of decay. In fact, these intrachain correlations fit to a spiral state with a pitch angle very close to the classical model. Hence, the simulations reveal well-pronounced intrachain spiral correlations together with weaker interchain correlations. It is important to note that these statements are restricted to short-range correlations.

Since correlations along the chains are strongest, one could argue that the model exhibits an effectively 1D low-temperature physics as has been discussed previously for the 2D models such the J_1–J_d model for kapellasite and haydeeite as well as other models mentioned in Sec. 7.3.3. Further studies of the model should focus on this issue.

Excitation spectrum The experimental investigation of the magnetic GS of volborthite is still far from being settled. Instead, thermal behavior of the magnetic susceptibility and the response in a magnetic field are rather well studied, and therefore can be a crucial test for the applicability of the J_1–J_2–J_{ic} model to volborthite. Thus, the respective properties are simulated and compared to the experimental $M(H)$ [363, 364] and $\chi(T)$ [364] data.

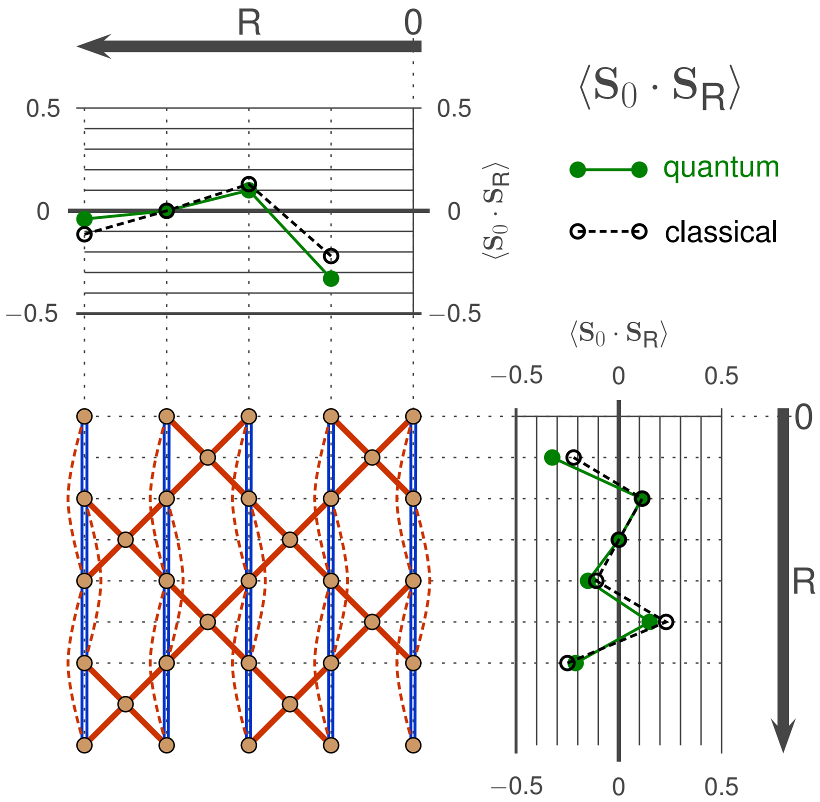

Figure 7.22: GS spin correlations for volborthite $Cu_3[V_2O_7](OH)_2{\cdot}2H_2O$. For the exchange integrals, the solution $J_{ic}/|J_1| = 2$, $J_2/|J_1| = 1.1$ depicted by the cross in Fig. 7.21, is used. The spin correlations between the J_1–J_2 chains decay rapidly (top), while the correlations along the chains are strong and considerably deviate from the pure kagome model.

First, adding the magnetic field term to the HEISENBERG Hamiltonian yields the $M^*(h)$ dependence. For the boundary of the ferrimagnetic and the spiral GSs (Eq. 7.2), a wide $^1/_3$-magnetization plateau is found, which starts at zero field $H_{1/3} = 0$. However, enhancement of J_2 and lowering $|J_1|$ and J_{ic}, according to the limits set by the DFT calculations, leads to a significant increase of $H_{1/3}$ and to a drastic diminishing of the plateau width. Close to the DFT-boundary ($J_{ic}/|J_1| = 2$, $J_2/|J_1| = 1.1$, $J_{ic} = 100$ K), $H_{1/3} = 22$ T (Fig. 7.23, left), still underestimating the tentative experimental $H_{1/3}$ 60 T.

This deviation originates from the minimalistic character of the model and sizable finite size effects. Nevertheless, a slightly modified ratio $J_2/|J_1| = 1.6$ yields $H_{1/3} = 55$ T (Fig. 7.23, left) in excellent agreement with the experiment [364]. It should be mentioned that the nature of spin correlations in the $^1/_3$-magnetization plateau phase is substantially different compared to the pure kagome model [320]. Unfortunately, small magnetization jumps seen experimentally [363] can not be resolved with present lattice sizes and might be even related to anisotropic exchange, beyond the HEISENBERG model.

Finally, the finite-temperature properties are addressed by calculating the temperature dependence of magnetic susceptibility $\chi^*(T^*)$ using two different lattices[9] of $N = 24$ spins. The simulations were carried out by P. SINDZINGRE at the PIERRE and MARIE CURIE university (Paris). It is possible to obtain a good fit down to 50 K (Fig. 7.23, right), while the resulting $g = 2.16$ and $J_{ic} = 100.5$ K are in excellent agreement with ESR experiments [359] and the estimates from DFT.

---

[9] The lattices are shown in Appendix, Fig. A7.

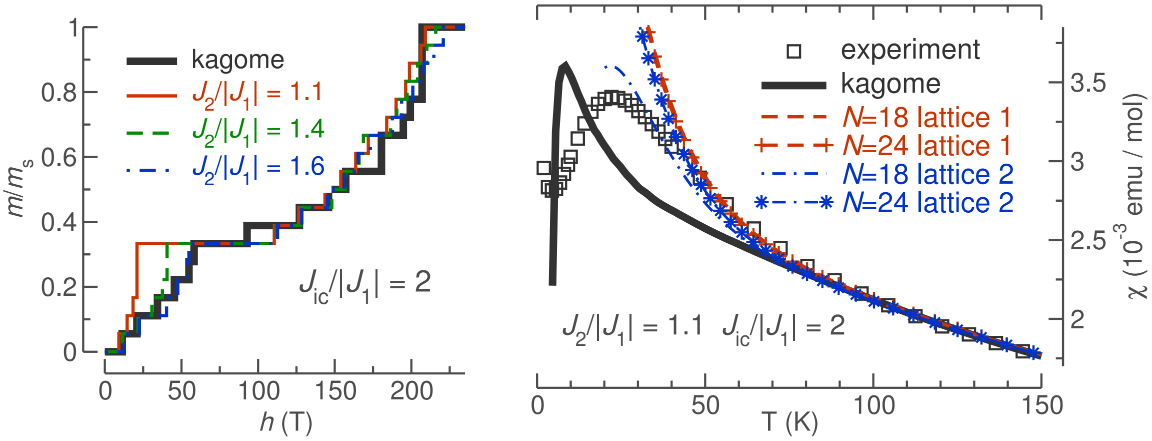

Figure 7.23: Top: fits to the experimental $\chi(T)$ [364] for volborthite $Cu_3[V_2O_7](OH)_2{\cdot}2H_2O$. The finite lattices, used for the calculation, are shown in Appendix (Fig. A7). The solution of the J_1–J_2–J_{ic} model yields a significantly improved description down to 50 K from the pure kagome model ($J_1 = J_{ic}$) (bold line). Bottom: magnetization curves ($N = 36$ sites) for different solutions of the J_1–J_2–J_{ic} model in comparison to the pure kagome model.

Chapter 8

Summary and outlook

The principal goal of this study was to establish a reliable and universal procedure, capable of evaluating a quantitative microscopic magnetic model for $S = 1/2$ HEISENBERG systems. The presented results evidence that the combination of full potential density-functional theory (DFT) band structure calculations and model simulations demonstrates excellent performance and accuracy for the basic characteristics of the magnetic ground state and the low-energy spectrum of spin systems.

The real material studies presented in Chapters 6 and 7 render the computational approach as an appealing alternative, complementary to an experimental characterization. In the following, its advantages are discussed in a systematic way. First, such approach allows to *distinguish between different microscopic models* that yield similar macroscopic behavior for several physical properties. Strictly speaking, this advantage is not unique to the computational approach, hence such a distinction can be done experimentally, e.g. by precise measurements of magnon dispersions in an inelastic neutron scattering experiment. However, such measurements require high-quality samples and can be performed only using large-scale facilities. In contrast, the computational procedure is less time consuming and can be carried out using conventional computer equipment.

Recent DFT-based studies refuted a surprisingly large number of empirical magnetic models. One of the most remarkable example is volborthite $Cu_3[V_2O_7](OH)_2{\cdot}2H_2O$, initially described as an anisotropic kagome lattice. In contrast, extensive DFT studies (Sec. 7.4) reveal that this compound features strongly coupled frustrated spin chains, thus a completely different type of magnetic frustration is realized. Very recent inelastic neutron scattering experiments corroborate this theoretical model [365].

The second advantage is the capability to provide accurate estimates for the leading magnetic couplings, and consequently, *reliably parameterize the microscopic Hamiltonian*. This is especially important for models featuring several relevant exchange couplings. In such a case, the magnetic phase diagram typically comprises several phases that are microscopically different, but often indistinguishable in the bulk experiments (e.g. in the temperature dependence of magnetic susceptibility). This widespread effect is caused by internal symmetries of the underlying model. Unfortunately, in many cases this ambiguity is carelessly overlooked, and the incorrect scenario is chosen. Consequently, the strength and even the sign of the leading exchange couplings can be erroneous. Dioptase $Cu_6Si_6O_{18}\cdot 6H_2O$ (Sec. 6.3) is an instructive example showing that the microscopic theoretical approach eliminates this ambiguity and reliably yields the correct parameterization.

The recent development of new computational techniques and facilities boosted the performance of the DFT-based approach. Still, many present-day studies put forward or rely on tentative magnetic models. This lingering type of modeling is based on a set of empirical rules that link the magnetic exchange couplings to the relevant structural parameters, such as bond angles. As a natural consequence of its unbeatable simplicity, such analysis is sometimes blindly applied, without even considering the key ingredients of the superexchange, such as the orientation of the magnetically active orbitals. In this way, a quasi-1D magnetic model was suggested for β-$Cu_2V_2O_7$ [259]. Moreover, even formally correct application of empirical GOODENOUGH–KANAMORI rules may yield incorrect results, as shown for $CdCu_2(BO_3)_2$ (Sec. 6.2.2). In contrast, the computational approach provides a microscopic insight, correctly disclosing the quasi-2D magnetism for the honeycomb lattice system β-$Cu_2V_2O_7$ (Sec. 6.2.1) as well as for the anisotropic decorated SHASTRY–SUTHERLAND model in $CdCu_2(BO_3)_2$ (Sec. 6.2.2).

In addition, many tentative magnetic models are based on a common belief that the magnetism is solely ruled by the mutual orientation of magnetic structural units. Again, this approach is oversimplified and can be largely misleading. For instance, the $Cu_2A_2O_7$ (A = P, As, V) are isostructural, thus the replacement of the non-magnetic groups should play a minor role for the magnetic properties. In contrast with this conjecture, the family of $Cu_2A_2O_7$ compounds shows a surprising variety of magnetic behaviors: coupled dimers in α-$Cu_2P_2O_7$, the honeycomb lattice model in β-$Cu_2V_2O_7$, and the quasi-1D model of alternating spin chains in α-$Cu_2As_2O_7$. Such striking dissimilarity of the magnetic properties is governed by non-magnetic AO_4 groups. The DFT-based analysis not only discloses this dissimilarity, but also *accounts for the microscopic mechanism* responsible for the different magnetic properties of these seemingly similar systems.

Among the variety of low-dimensional magnets, frustrated systems exhibit particularly interesting magnetic properties. The commonly used experimental indication for magnetic frustration is the small value of T_N/θ, where T_N is the long-range magnetic ordering temperature and θ is the WEISS temperature. Yet, it is difficult to distinguish between frustrated and low-dimensional systems, since both frustration and low-dimensionality generally reduce T_N/θ. Thus, the low T_N/θ in $[NO]Cu(NO_3)_3$ motivated the authors of Ref. 233 to put forward the anisotropic frustrated square lattice model for this compound. However, the DFT-based analysis (Sec. 6.1.2) discloses inconsistency of this model, and demonstrates that the low T_N/θ results from the quasi-1D nature of the microscopic model, while frustration effects are marginal. Since the effects of low-dimensionality and frustration are typically entwined, and their disentanglement in the experiment is at best challenging, the computational DFT-based approach should be regarded as a relevant alternative, complementary to the experimental studies.

The next issue to discuss is the accuracy of the computational approach. Based on the results of the present study and numerous DFT-based studies published in the literature, the error bars for the leading couplings can be estimated on the order of 10–15%. However, the ratios of the leading couplings are typically evaluated with higher precision. The studies of quasi-1D spin chain compounds (Sec. 6.1) evidence excellent performance of the computational approach. In particular, relevant interchain couplings can be distinguished from essentially inactive superexchange pathways. Thus, $CuSe_2O_5$ and $CaCu_2(SeO_3)_2Cl_2$, despite the similar energy scale of the leading intrachain coupling, feature very different interchain coupling regime: the spin chains in $CuSe_2O_5$ are coupled in a simple square-lattice-like manner (Sec. 6.1.1), while two relevant interchain couplings in $CaCu_2(SeO_3)_2Cl_2$ (Sec. 6.1.3) lead to an involved spin model with magnetic frustration.

Even numerical estimates for the relevant interchain couplings are rather precise, although they are one or two orders of magnitude smaller in strength than the leading intrachain exchange. Hence, band structure calculations provide a unique possibility to address the interchain or interplane coupling regime, essential for the magnetic ground state, but hardly directly perceptible in the experiment, due to the different energy scales. The excellent accuracy renders DFT calculations as the method of choice for studying the interchain (interplane) coupling regime in quasi-1D (quasi-2D) magnets.

Besides the apparent advantages of the computational approach, considering it as a panacea would be an apparent exaggeration. Especially for practical applications of the method, its limitations should be extensively discussed. The first limitation is the strong influence of the structural input. Since even subtle structural details can considerably alter the magnetic properties, the consistency of the experimental crystal structure should be carefully studied. The influence of the structural parameters is especially large for the compounds featuring small Cu–Cu distances, where the magnetic CuO_4 units share common edges or corners. This is the case for kagome-lattice systems (Chapter 7). The strong competition of antiferromagnetic superexchange and ferromagnetic HUND's coupling on the O sites in kapellasite $Cu_3Zn(OH)_6Cl_2$ and haydeeite $Cu_3Mg(OH)_6Cl_2$ makes them especially sensitive to the fine details of their crystal structures. Although the microscopic J_1–J_d model is qualitatively robust, the ratio of the two leading couplings can be considerably affected by the structural model (Sec. 7.3).

The second limitation is related to the model assignment. The developed approach is based on the HEISENBERG scenario (isotropic coupling), and presuming this picture is applicable, yields accurate numerical estimates for the individual magnetic couplings. However, real materials are never free from anisotropies. For cuprates, the ESR experiments typically yield about 10% anisotropy of the g-factor, hinting at the non-equivalence of the couplings between the different spin components. This anisotropy is likely too small to alter the magnetic ground state, but it definitely affects the long-range magnetic ordering temperature in quasi-1D and quasi-2D magnets.

Besides the anisotropy effects, real materials inevitably bear a certain amount of structural defects. Modeling the structural disorder within DFT is a challenging task, thus structural defects are typically neglected. Such approximation is well justified for the majority of materials, yet structural disorder can substantially influence the magnetism of certain compounds, thus the impurity effects can not be completely neglected. However, even a simplified treatment of impurity effects leads to several non-equivalent magnetic couplings and rather involved magnetic models. The increased complexity largely impedes simulations, hampering comparisons with the experiments. To illustrate this effect, the study of herbertsmithite (Sec. 7.2) is very instructive. Here, even a rather simple treatment of a magnetic impurity leads to a model with eight relevant couplings, while only two couplings suffice to describe the magnetism of the idealized compound (featuring a fully ordered crystal structure).

At this point, it is natural to proceed to extensions of the computational approach. The DFT-based study of herbertsmithite provides valuable information on the influence of magnetic interplane impurities onto the magnetic coupling regime. Still, the approximations used to model the impurity effects are likely too crude for a quantitative modeling. In particular, an adequate description for the structural defects within DFT would largely remedy the problem. Therefore, the extension of the DFT-based approach for the case of structurally disordered strongly correlated systems is highly desirable.

Recent theoretical studies evidence a substantial influence of anisotropic Dzyaloshinskii-Moriya interactions onto the magnetic properties (e.g., Ref. 324). For a very limited range of compounds, the Dzyaloshinskii-Moriya couplings were evaluated directly from band structure calculations [146]. Although the pioneering studies evidence excellent potential of such approach, an universal computational scheme is still missing. The extension of the developed approach to the case of anisotropic coupling is a relevant, albeit arduous task.

Another substantial development could be the extension of the method to take finite temperature into account. Combining quantum magnetism and molecular dynamics can lead to a better understanding of the complex interplay of magnetic and lattice degrees of freedom in frustrated systems.

In this thesis, only cuprate materials were considered, yet the computational approach can be readily applied to other $S = 1/2$ systems, such as V^{4+}, Cr^{5+} or Ti^{3+} compounds. Moreover, with minor modifications, it can be extended to other metallates with higher value of spin. However, it should be kept in mind that within the class of 3d metallates, the electronic correlations can vary in a rather broad range, thus the simplified treatment of electronic correlations within the DFT+U methods can become critical. At this point, replacement of the DFT+U approach by more sophisticated DFT+DMFT schemes seems to be a natural extension. In this way, even metal-insulator transitions could be investigated on a microscopic level.

Further extensions can be envisaged, yet the computational approach in its present version is a powerful tool that can be directly applied to any particular compound from the vast family of $S = 1/2$ HEISENBERG magnets. The real-material studies described in Chapters 6 and 7 evidence not only the excellent performance of the computational approach, but also its relevance: for all the systems under consideration, the DFT-based studies not barely reproduced the experimental data, but instead delivered *new valuable information on the magnetic properties for each particular compound.*

Beyond any doubt, further computational studies will yield new interesting and surprising results, such as the ferromagnetic nature of the couplings that were previously considered antiferromagnetic, unexpected long-range couplings, or the subtle balance of antiferromagnetic and ferromagnetic contributions that can "switch off" the respective magnetic exchange. In this way, dozens of potentially interesting systems can acquire quantitative microscopic magnetic models.

The results of this work evidence that elaborate experimental methods and the DFT-based modeling are of comparable reliability and complement each other. In this way, the advantageous combination of theory and experiment can advance the research in the field of low-dimensional quantum magnetism. For practical applications, the excellent predictive power of the computational approach can largely alleviate designing materials with specific properties.

In future, a closer collaboration of theory and experiment is expected, yet for a concise outlook, which is given below, it is reasonable to differentiate between them. From the experimental side, a more precise determination of the crystal structure is desired, especially for the light atoms. High-field measurements should become more and more relevant by reaching higher magnetic fields. A very promising way of altering the structure and consequently the magnetic properties is application of external pressure. Although at present, the applicability of standard probes for magnetism in a high-pressure experiment is limited, a constant improvement of the equipment gives hope for a future boom of such studies. The continuous improvement of synthesis methods will ensure better sample quality, and consequently, further progress in the accuracy of the experimental data. Besides improving the accuracy, it is important to extend the experimentalist's toolbox, i.e. to increase the diversity of the experimental methods. Without a doubt, the magnetic resonance techniques presently experience a golden age. Taking into account that ESR, NMR and especially μSR are relatively new developments, emergence of new spectroscopic methods can not be excluded. Reaching even lower temperatures could also be advantageous for development of new experimental techniques. Recent progress of in the field of cold atoms evidences excellent potential of this sector.

The vibrant development of new computational methods aiming to provide an even more realistic description for strongly correlated systems, should enable a more accurate determination of crucial parameters such as the HUBBARD U_d or the HUND'S exchange on the ligand site. The ongoing extension of the computational techniques, in order to account for anisotropic magnetic exchange couplings, should resolve a number of long-standing puzzles, especially for frustrated systems. Finally, many real compounds are characterized by appreciable coupling of their magnetism to the lattice or orbital degrees of freedom. Providing an adequate DFT-based description for such complicated cases is one of the most crucial and challenging present-day tasks. Due to its relevance for various technological applications, considerable progress in this field can be expected in near future.

A reliable microscopic model is vital to provide a correct interpretation of an experimental measurement. Even more important, a microscopic model provides a link between different experimental results and transforms them into what is typically called as a physical picture. Flashed by such an enlightening picture, the mind can realize with a contentment: "I do understand".

Appendix

A1 Exact diagonalization

Simplest example: a $S = 1/2$ Heisenberg dimer

The Heisenberg dimer is a system of two coupled spins i and j, described by the Heisenberg Hamiltonian:

$$\hat{H} = \mathbf{S}_i \cdot \mathbf{S}_j. \tag{A1}$$

Since each spin $S = 1/2$ has only two possible states, $|\uparrow\rangle$ and $|\downarrow\rangle$, the construction of a basis set for this system is trivial and readily yields four states spanning the Hilbert space: $|\uparrow\uparrow\rangle$, $|\uparrow\downarrow\rangle$, $|\downarrow\uparrow\rangle$ and $|\downarrow\downarrow\rangle$. Next, the Hamiltonian matrix can be constructed by means of Dirac's spin exchange operator $\hat{P}$:

$$\mathbf{S}_i \cdot \mathbf{S}_j = 2\hat{P} - 1. \tag{A2}$$

Thus,

$$\begin{aligned}
\hat{H}\,|\uparrow\uparrow\rangle &= 2\,|\uparrow\uparrow\rangle - |\uparrow\uparrow\rangle = |\uparrow\uparrow\rangle \\
\hat{H}\,|\uparrow\downarrow\rangle &= 2\,|\downarrow\uparrow\rangle - |\uparrow\downarrow\rangle \\
\hat{H}\,|\downarrow\uparrow\rangle &= 2\,|\uparrow\downarrow\rangle - |\downarrow\uparrow\rangle \\
\hat{H}\,|\downarrow\downarrow\rangle &= 2\,|\downarrow\downarrow\rangle - |\downarrow\downarrow\rangle = |\downarrow\downarrow\rangle,
\end{aligned} \tag{A3}$$

leading to a 4×4 Hamiltonian matrix with six nonzero matrix elements:

$$H = \frac{1}{4}\begin{array}{ccccc}
|\uparrow\uparrow\rangle & |\uparrow\downarrow\rangle & |\downarrow\uparrow\rangle & |\downarrow\downarrow\rangle & \\
1 & & & & |\uparrow\uparrow\rangle \\
 & -1 & 2 & & |\uparrow\downarrow\rangle \\
 & 2 & -1 & & |\downarrow\uparrow\rangle \\
 & & & 1 & |\downarrow\downarrow\rangle
\end{array}.$$

Eigendecomposition of this matrix yields the singlet ground state $\frac{|\uparrow\downarrow\rangle - |\downarrow\uparrow\rangle}{\sqrt{2}}$ with energy

-0.75 and three degenerate excited states (triplet) $\frac{|\uparrow\downarrow\rangle+|\downarrow\uparrow\rangle}{\sqrt{2}}$, $|\uparrow\uparrow\rangle$ and $|\downarrow\downarrow\rangle$ with energy 0.25. This is the complete spectrum of the model. The thermodynamic average $\langle A\rangle$ of any observable A can be evaluated using the partition function Z:

$$\langle A\rangle = \frac{1}{Z}\sum_{i=1}^{4} A_i \exp \quad -\frac{E_i}{k_{\mathrm{B}}T} \quad \text{, where } Z = \sum_{i=1}^{4} \exp \quad -\frac{E_i}{k_{\mathrm{B}}T} \quad , \tag{A4}$$

where E_i and A_i denote the energy and the value of A in the state i, respectively. This way, a theoretical model can be challenged by comparing to the experimentally observed values of A.

Lanczos algorithm

The Lanczos algorithm is typically used to evaluate the extreme eigenvalues of sparse matrices. After the initialization (Eq. A5), a tridiagonal T-matrix (Eq. A6) is constructed within the iterative j-step procedure (Eq. A7). The extreme eigenvalues of this $j\times j$ matrix rapidly converge to the extreme eigenvalues of the A-matrix. Typically, j 100 is enough to reach the accuracy of 10^{-14} for the ground state energy [166].

$$A \in \mathbb{C}^{n\times n}, A = A^{\dagger};\; j=1;\; \alpha_j,\beta_j \in \;^{1};\; u_j, w_j \in \mathbb{C}^{n\times 1};\; u_0 = 0;\; u_1 :\; u_1 \;= 1;\; \beta_1 = 0 \tag{A5}$$

$$T \in \;^{j\times j} \qquad T = \begin{pmatrix} \alpha_1 & \beta_1 & & & & \\ \beta_1 & \alpha_2 & \beta_2 & & & \\ & \beta_2 & \ddots & \ddots & & \\ & & \ddots & \ddots & \ddots & \\ & & & \ddots & \ddots & \beta_{j-1} \\ & & & & \beta_{j-1} & \alpha_j \end{pmatrix} \tag{A6}$$

$$\begin{aligned} w_j &= A\cdot u_j - \beta_j u_{j-1} \\ \alpha_j &= u_j^{\dagger}\cdot w_j \\ w_j &= w_j - \alpha_j u_j \\ \beta_{j+1} &= \;\; w_j \\ u_{j+1} &= w_j(\beta_{j+1})^{-1} \\ j &= j+1 \end{aligned} \tag{A7}$$

A2 Details of the experimental studies (Chapter 6)

$CuSe_2O_5$

The experiments were carried out at MPI CPfS by M. Schmidt (synthesis of single crystals), Y. Prots (X-ray diffraction), P. Scheppan (EDXS measurements), and W. Schnelle (thermodynamical measurements). Single crystals of $CuSe_2O_5$ were grown by chemical vapor transport using $TeCl_4$ as a transport agent. Using a microcrystalline powder of $CuSe_2O_5$ (obtained from a mixture of CuO and SeO_2 at 723 K) as a source, the transport experiments were carried out in an endothermic reaction of T_2 (source) 653 K to T_1 (sink) 553 K.

The obtained crystals had a green color and form strongly elongated (along [001]) plates, which macroscopically look like needles. The typical length of a needle is 5–10 mm and the width does not exceed 1 mm, while for most of crystallites it is considerably smaller. The slight disorientation of plates forming a needle intricates a precise X-ray diffraction measurement on single crystals. Thus, the samples were characterized by X-ray powder diffraction and EDXS experiments. The lattice parameters of the synthesized crystals are similar to those reported for $CuSe_2O_5$ (Table A1). The results of the EDXS analysis (Cu 32.78 ± 0.31 %, Se 67.14 ± 0.23 %) for 13 points (2 crystals) yield Cu:Se 0.488 ± 0.006, very close to the ideal ratio of 0.5. Thus, the obtained single crystals represent an almost pure $CuSe_2O_5$ phase.

Table A1: Comparison of the measured lattice parameters a, b, c, the monoclinic angle β and the unit cell volume V of $CuSe_2O_5$ with the published data.

parameter	Ref. 219	Ref. 380	this work
a (Å)	12.3869	12.254	12.272
b (Å)	4.8699	4.858	4.856
c Å)	7.9917	7.960	7.975
β (°)	109.53	110.70	110.91
V (Å^3)	447.13	443.27	443.95

Magnetization was measured in a SQUID MPMS magnetometer (1.8–350 K) in magnetic fields up to 1 T. Heat capacity (1.8–100 K) was determined by a relaxation method up to $H = 9$ T.

$CaCu_2(SeO_3)_2Cl_2$

The samples of $CaCu_2(SeO_3)_2Cl_2$ were grown by P. S. Berdonosov at the Moscow State University. Calcium selenite $CaSeO_3$ was prepared via solution synthesis. The solutions of calcium nitrate $Ca(NO_3)_2$ (chemically pure) (6.214 g) and selenous acid H_2SeO_3 (98 %) (4.886 g) in a minimal amount of hot distilled water were mixed. The ammonia 1:5 water solution was added to fix pH of the solution in the range 7−8. The fine white powder was obtained as a precipitate. The precipitate was then dried at 150 °C. According

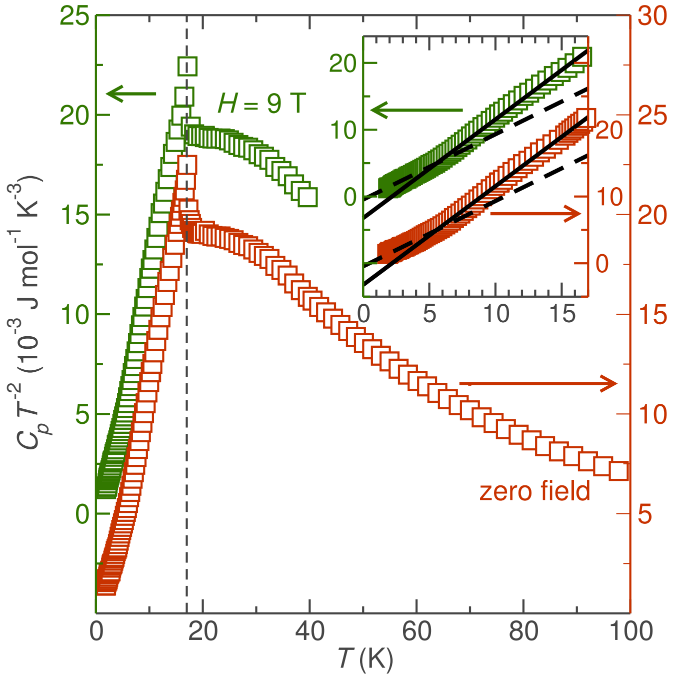

Figure A1: C_p/T^2 of $CuSe_2O_5$ as a function of temperature and magnetic field. The Néel temperature is marked with a dashed line. Inset (ordered phase region): the $C_p \propto T^3$ behavior predicted by theory is complicated by a clear kink at 7 K.

to X-ray powder diffraction (XRPD), the obtained powder was identified as a hydrate $CaSeO_3{\cdot}H_2O$. The hydrate was further calcined on a gas burner in a ceramic plate for 30 min. The resulting product was identified as a single phase $CaSeO_3$ [space group $P2_1/n$, $a = 6.399(5)$ Å, $b = 6.782(4)$ Å, $c = 6.682(8)$ Å, $\beta = 102.84(6)$ °].

SeO_2 was obtained from H_2SeO_3 by its decomposition under vacuum at 60 °C and the sublimation of the resulting substance in a flow of anhydrous air and NO_2. CuO (ultra pure) and $CuCl_2$ (Merck, >98 %) were used. The dark-greenish powder sample of $CaCu_2(SeO_3)_2Cl_2$ was obtained from a stoichiometric mixture of $CaSeO_3$, $CuCl_2$, CuO, and SeO_2. The mixture (about 0.5 g total) was prepared in Ar-filled camera, sealed in a quartz tube, and placed into the electronically controlled furnace. The sample was heated from room temperature to 300 °C for 12 hours, exposed at 300 °C for 24 hours, heated up to 500 °C for 12 hours, and exposed at 500 °C for 96 hours.

The resulting samples were single-phase, as confirmed by powder x-ray diffraction (STOE STADI-P diffractometer, $CuK_{\alpha 1}$ radiation, transmission geometry). The powder pattern was fully indexed in the monoclinic space group $C2/c$ with lattice parameters $a = 12.752(3)$ Å, $b = 9.036(2)$ Å, $c = 6.970(1)$ Å, $\beta = 91.02(1)$ °. $CaCu_2(SeO_3)_2Cl_2$ is rather stable in air, although a prolonged exposure of about 3 months led to a partial decomposition towards crystalline $CuSeO_3{\cdot}2H_2O$ and possible amorphous products.

Magnetic susceptibility was measured by A. A. Tsirlin at MPI CPfS with an MPMS SQUID magnetometer in the temperature range 2–380 K in magnetic fields of 0.5, 2, and 5 T. The high-field magnetization of $CaCu_2(SeO_3)_2Cl_2$ was measured by Y. Skourski (HZDR HLD) in pulsed magnetic fields up to 60 T at a constant temperature of 1.5 K.

Table A2: Selected interatomic distances d (bond lengths) in the $CaCu_2(SeO_3)_2Cl_2$ structure.

bond			d (Å)	bond			d (Å)
Ca	–	O1	2.362(2)	Cu(1)	–	O2	1.920(2)
		O2	2.458(3)			O3	2.012(2)
		Cl	2.827(1)				
		Cl	2.948(1)	Cu(2)	–	O1	1.891(2)
Se	–	O1	1.705(2)			O3	2.455(2)
		O2	1.707(2)			Cl	2.404(1)
		O3	1.684(3)				

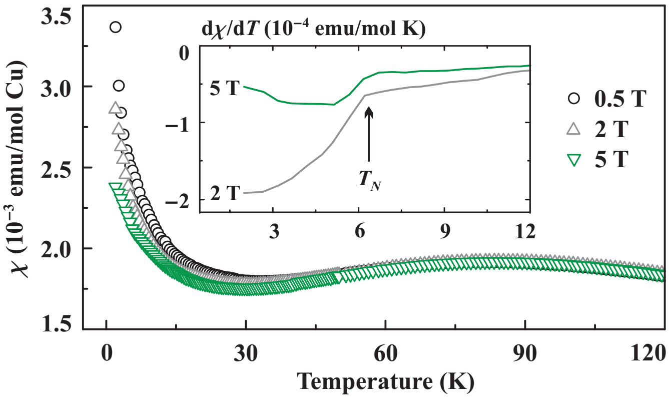

Figure A2: (after A. A. Tsirlin) Magnetic susceptibility of $CaCu_2(SeO_3)_2Cl_2$ measured in magnetic fields of 0.5 T, 2 T, and 5 T. The increase in the field leads to suppression of the low-temperature paramagnetic upturn. The inset shows the derivative of the magnetic susceptibility and a kink around 6 K, likely evidencing long-range magnetic ordering.

$Cu_2A_2O_7$

The synthesis and sample characterization were carried out by by A. Tsirlin at MPI CPfS, ESR spectra were measured by J. Sichelschmidt (MPI CPfS), high-field magnetization measurements were done by Y. Skourski at the HZDR HLD.

A single-phase powder sample of α-$Cu_2P_2O_7$ was prepared by a solid-state reaction of CuO and $NH_4H_2PO_4$. A stoichiometric mixture of the reagents was fired at 250 °C for 6 hours in air to remove ammonia and water. The sample was further placed into a sealed quartz tube and heated at 800 °C for 12 hours. The resulting light-gray powder was analyzed by X-ray diffraction (Huber G670 Guinier camera, $CuK_{\alpha 1}$ radiation, image plate detector, 3–100° angle range). A Rietveld refinement confirmed the formation of α-$Cu_2P_2O_7$ and did not show any traces of impurity phases (in particular, the admixture of β-$Cu_2P_2O_7$ can be ruled out). In contrast, a high-temperature annealing in air always produced a $Cu_3(PO_4)_2$ impurity.

Magnetic susceptibility was measured with an MPMS SQUID magnetometer in the temperature range 2–380 K in applied fields up to 5 T. High-field magnetization measurements (at $T = 1.4$ K) were performed in pulsed fields up to 60 T.

The ESR spectra of a powder sample of α-$Cu_2P_2O_7$ were recorded at X-band frequencies (9.4 GHz) for temperatures 5–300 K. The spectra were fitted with a powder average of two Lorentzian lines corresponding to two (effective) components of the g-tensor in axial symmetry: $g_\perp$ and g .

A3 Details of the DFT band structure calculations (Chapters 6 and 7)

Al, Si and NaCl

Calculations have been performed using `fplo9.00-37` [126]. For scalar relativistic calculations, the exchange-correlation potential of PERDEW and 28 WANG [99] has been used. The lattice constants were adopted from Refs. 381, 382, and 383 for Al, Si, and NaCl, respectively. E_0 in Fig. 4.1 are the total energies computed for the largest $\vec{k}$-meshes: 22776, 5216, and 145 for Al, Si, and NaCl, respectively (the numbers refer to the irreducible wedge).

$CuSe_2O_5$

Band structure calculations were carried out using `fplo7.00-27` [126] for the experimental structural parameters [219]. The standard basis set and the PERDEW–WANG parameterization of the exchange-correlation potential were used [99]. For the LDA calculations, a $\vec{k}$-mesh of $12\times12\times9$ $\vec{k}$-points (355 points in the irreducible wedge) was used, for LSDA+U calculations, $8\times8\times7$ ("1" in Fig. A3, space group $P\bar{1}$, equivalent to the primitive cell of the conventional C-centered cell), $3\times8\times4$ ("2" in Fig. A3, space group $P\bar{1}$, metrically equivalent to the conventional C-centered cell) and $4\times4\times2$ ("3" in Fig. A3, space group $P1$, equivalent to the primitive cell doubled along c) supercells were chosen. The convergence with respect to $\vec{k}$-meshes has been carefully checked.

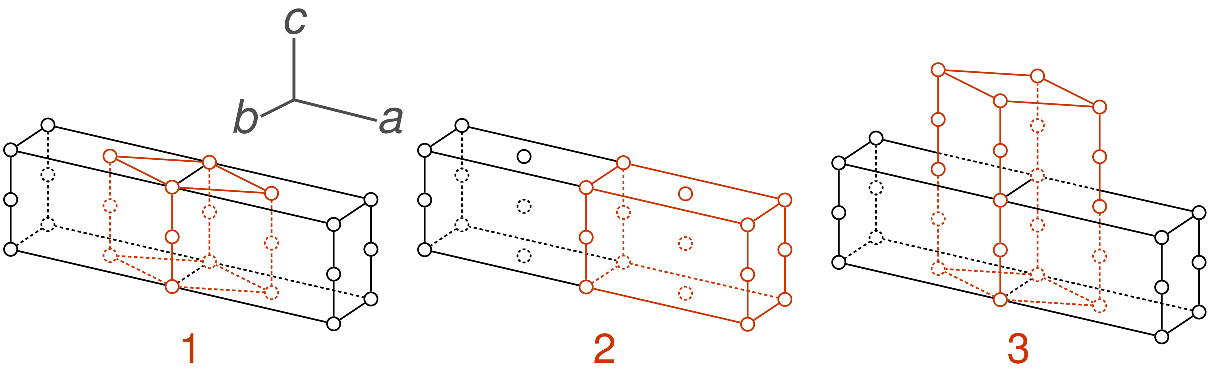

Figure A3: Supercells (red lines) used for LSDA+U calculations of $CuSe_2O_5$. For the numbering, see text. In each panel, two neighboring conventional C-centered cells are depicted (black lines). The crystallographic axes correspond to the conventional cell. Empty spheres denote magnetic (Cu) atoms.

$[NO]Cu(NO_3)_3$

For DFT band structure calculations, the experimental crystal structure from Ref. 384 was used. Since the structural data are not easily available [the journal does not provide an online access to the publication, while the structure is absent in the Inorganic Crystal Structure Database (ICSD)], the structural information is given in Table A3.

Table A3: Experimental crystal structures of $[NO]Cu(NO_3)_3$ from Ref. 384 $Cu_3Zn(OH)_6Cl_2$. Space group $P2_1/m$, $a = 4.6580(10)$ Å, $b = 11.102(3)$ Å, $c = 7.009(2)$ Å, $\beta = 100.83(2)°$.

atom	x/a	y/b	z/c
Cu	1/2	1/2	1/2
N	0.3694(5)	1/4	0.4333(3)
N	0.0126(3)	0.56051(14)	0.2136(2)
N	0.2433(9)	3/4	−0.0837(5)
O	0.4393(3)	0.34617(12)	0.3536(2)
O	0.2445(5)	1/4	0.5699(3)
O	0.2825(3)	0.58883(12)	0.2807(2)
O	−0.1067(3)	0.48171(14)	0.2952(2)
O	−0.1100(3)	0.61442(13)	0.0673(2)
O	0.4148(6)	3/4	0.0218(4)

The scalar-relativistic DFT calculations were performed using `fplo9.00-33` [126]. For the LDA, the Perdew–Wang parameterization [99] of the exchange-correlation potential was chosen. LDA calculations were done on a converged mesh of 16×10×12 $\vec{k}$-points (588 in the irreducible wedge). The band dispersions were cross-checked by GGA calculations, using the parameterization of Perdew, Burke and Ernzerhof [100]. The resulting differences between LDA and GGA for the relevant bands are negligible (1 %).

For LSDA+U calculations, a 6×3×4-points supercell (100 $\vec{k}$-points in the irreducible wedge, space group $P\bar{1}$, metrically equivalent to the conventional unit cell) and a 2×2×3-points supercell (space group $P1$, doubled along a) have been used. The LSDA+U results for AMF DCC $U_d = 6.5$ eV were cross-checked using GGA+U. The latter yielded ∼25 % smaller value for the leading exchange J_1.

$CaCu_2(SeO_3)_2Cl_2$

Band structure calculations have been performed using `fplo9.00-31` [126]. For the exchange and correlation potential, the parameterization of Perdew and Wang [99] has been chosen. The LDA calculations were performed on a $\vec{k}$-mesh of 10×10×12 points was used. For spin-polarized supercell LSDA+U calculations, the $\vec{k}$-meshes of 4×4×4 (space group $P1$, equivalent to the primitive cell, which volume amounts to one half of the conventional C-centered cell) and 4×4×2 points (space group $P1$, equivalent to the primitive cell doubled along c) were used.

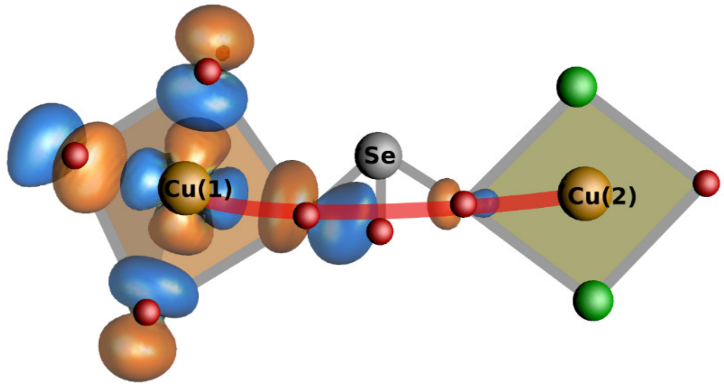

Figure A4: Wannier functions marking the J_1 superexchange path. Cu(1)O_4 (left) and Cu(2)O_2Cl_2 (right) plaquettes are filled. The SeO_3 pyramid is visualized by Se–O bonds (lines). The projection is the same as in Fig. 6.12 (left).

$Cu_2A_2O_7$ (A = P, As, V)

For α-$Cu_2P_2O_7$, the DFT calculations were performed using `fplo8.00-31` [126]. The experimental structure from Ref. 385 was adopted. For the exchange-correlation potential, an LDA [99] as well as a GGA [100] parameterizations were used. Nonmagnetic calculations were performed on a 14×14×8 $\vec{k}$-mesh (429 $\vec{k}$-points in the irreducible wedge). For LSDA+U calculations, three types of supercells were used: (i) a primitive cell with the volume amounting to one-half of the conventional C-centered cell (space group $P1$, 4×4×2 $\vec{k}$-mesh), (ii) a primitive cell doubled along b (space group $P1$, 3×2×2 $\vec{k}$-mesh), and (iii) a primitive cell doubled along c (space group $P1$, 3×3×2 $\vec{k}$-mesh).

For α-$Cu_2As_2O_7$, the structural data from Ref. 386, the code `fplo8.50-32` [126], and the LDA parameterization of Perdew and Wang [99] were used. LDA calculations were done on a 12×12×8 mesh (320 $\vec{k}$-points in the irreducible wedge). LSDA+U calculations were carried out for supercells of the same metrics and $\vec{k}$-meshes, as for α-$Cu_2P_2O_7$ (previous paragraph).

Most of DFT calculations for β-$Cu_2V_2O_7$, including DFT+U supercell calculations, were carried out by A. Tsirlin, while all the relevant details can be found in Ref. 265. WFs for the Cu $3d_{x^2-y^2}$ states were calculated on a 8×8×8 $\vec{k}$-mesh (150 points in the irreducible wedge).

$CdCu_2(BO_3)_2$

Band structure calculations were performed with the code `fplo8.00-31` [126], using the Perdew–Wang parameterization [99] of the exchange-correlation potential. For LDA calculations, a 20×4×8 $\vec{k}$-mesh (246 $\vec{k}$-points in the irreducible wedge) was used. For the supercell DFT+U calculations, two types of supercells were used: a supercell, metrically equivalent to the unit cell (space group $P1$, 4×2×2 $\vec{k}$-mesh) and supercell doubled along c (space group $P1$, 4×1×1 $\vec{k}$-mesh). The DFT+U results for different DCC/U_d values are summarized in Table A4.

Table A4: Cu–Cu distances (d, in Å), transfer integrals (t_i, in meV), antiferromagnetic J_i^{AFM} (in K) contributions, as well as the total exchange integrals J_i (in K) for the leading couplings in $\text{CdCu}_2(\text{BO}_3)_2$. The values of J_i are evaluated within the DFT+U method for two different double-counting correction schemes (AMF and FLL) adopting a value U_d (5.5, 6.5 and 7.5 eV for AMF; 8.5, 9.5 and 10.5 eV for FLL) from the relevant range.

	d	t_i	J_i^{AFM}	J_i											
				LSDA+U						GGA+U					
				AMF			FLL			AMF			FLL		
				5.5 eV	6.5 eV	7.5 eV	8.5 eV	9.5 eV	10.5 eV	5.5 eV	6.5 eV	7.5 eV	8.5 eV	9.5 eV	10.5 eV
J_{d}	2.957	203	425	297	146	70	271	202	146	198	108	49	209	153	111
J_{t1}	5.268	73	55	42	30	19	36	29	23	33	22	14	28	23	17
J_{t2}	6.436	85	75	84	64	49	65	55	45	65	50	39	44	40	32
J_{it}	3.228	47	23	−61	−45	−34	−157	−135	−117	−29	−24	−21	−100	−87	−78
J_{Cd}	6.450	41	17	6	5	3	7	6	5	5	4	3	7	3	2
$J_{\text{t1}} : J_{\text{d}}$ (%)				14	20	27	13	14	16	17	20	29	13	15	15
$J_{\text{it}} : J_{\text{d}}$ (%)				−21	−31	−49	−58	−67	−80	−15	−22	−43	−48	−57	−70
$J_{\text{t1}} : J_{\text{t2}}$ (%)				50	47	39	55	53	51	51	44	36	64	57	53

Dioptase $Cu_6Si_6O_{18}\cdot6H_2O$

For the lattice constants and atomic coordinates, neutron diffraction data were used [276]. Band structure calculations were carried out using `fplo9.00-33` [126] and the LDA parameterization of Perdew and Wang [99]. LDA calculations were done on a 12×12×12 mesh (294 $\vec{k}$-points in the irreducible wedge). For the LSDA+U calculations, $P1$ supercells of the same metrics (4×4×4 $\vec{k}$-points) were used. The U_d-dependence was studied in the relevant ranges: $U_d = 6.5\pm1$ eV within AMF and $U_d = 8.5\pm1$ eV within FLL, keeping $J_d = 1$ eV fixed.

Herbertsmithite $Cu_3Zn(OH)_6Cl_2$

The experimental structural (Table A5) data are based on an XRD study at 100 K [347]. The internal atomic coordiates are taken from Ref. 335. The lattice constants in the rhombohedral setup: $a = 6.12763$ Å, $\alpha = 67.7763°$. The internal coordinates of the H atom were optimized within LDA (Table A5).

atom	experimental			LDA-optimized H		
	x/a	y/a	z/a	x/a	y/a	z/a
Zn	0	0	0			
Cu	1/2	0	0			
O	0.2315	$=x/a$	0.8520			
H	0.276	$=x/a$	0.700	0.27464	$=y/a$	0.66639
Cl	0.3052	$=x/a$	$=x/a$			

Table A5: Experimental and LDA-optimized (the H position, only) crystal structures of herbertsmithite $Cu_3Zn(OH)_6Cl_2$. The coordinates are given in the rhombohedral setup.

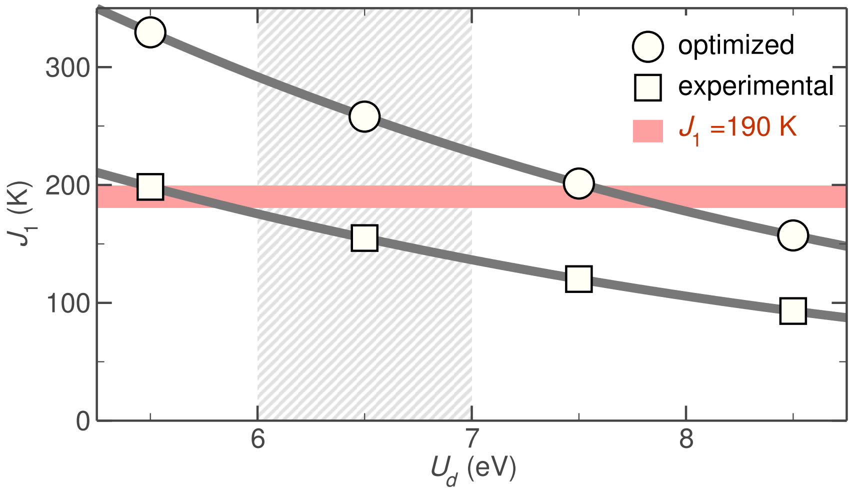

Figure A5: LSDA+U results for the ideal (no Cu–Zn disorder) structure of herbertsmithite $Cu_3Zn(OH)_6Cl_2$. The results for the AMF DCC are presented. The value $J_1 = 190$ K is taken from Ref. 54.

Kapellasite $Cu_3Zn(OH)_6Cl_2$ and haydeeite $Cu_3Mg(OH)_6Cl_2$

Band structure calculations for kapellasite and haydeeite have been performed using the code `fplo6.00-24` [126]. For scalar relativistic calculations, the exchange-correlation potential of PERDEW and WANG [99] has been used. LDA calculations have been performed on a $\vec{k}$-mesh of 10×10×11 points (124 in the irreducible wedge). For the spin-polarized LSDA+U calculations, two different supercells were used. The first cell is metrically equivalent to the crystallographic cell, but contains no symmetry operations except lattice translations (space group $P1$), a 10×10×11 $\vec{k}$-mesh with 1100 points in the irreducible wedge was used. The second cell also lacks rotational symmetry (space group $P1$) and is doubled along a, the $\vec{k}$-mesh for this cell was 3×5×5 with 75 points in the irreducible wedge.

For the structural input, the atomic coordinates from Refs. 329 and 330 were used for kapellasite and haydeeite, respectively. The experimental H position for kapellasite has been relaxed in LDA. By comparing the resulting total energies, the equilibrium position has been evaluated. Since the H position has not been reported for haydeeite, the respective position was adopted from the kapellasite structure, and relaxed in a similar way within LDA. The resulting optimized positions are given in Table A6. The dependence of the total energy on the O–H bond length is depicted in Fig. A6.

Table A6: LDA-optimized H positions for kapellasite $Cu_3Zn(OH)_6Cl_2$ and haydeeite $Cu_3Mg(OH)_6Cl_2$.

compound	H			O–H distance	
	x/a	y/b	z/c	opt. (Å)	exp. (Å)
kapellasite	0.177	$-x/a$	0.172	1.00	0.78
haydeeite	0.203	$-x/a$	0.322	1.00	

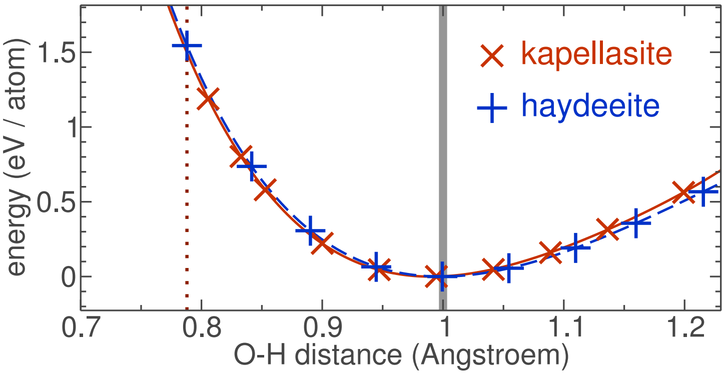

Figure A6: LDA total energy as a function of the O–H distance in kapellasite and haydeeite. The experimental (Ref. 329) H position for kapellasite is marked with a dotted vertical line. The equilibrium position is highlighted by a solid vertical solid line.

Volborthite $Cu_3[V_2O_7](OH)_2 \cdot 2H_2O$

DFT calculations for volborthite have been performed using the code `fplo8.65-32` [126]. For scalar relativistic calculations, the exchange-correlation potentials of PERDEW and WANG [99] and PERDEW, BURKE and Ernzerhof [100] have been used. LDA calculations have been performed on a $\vec{k}$-mesh of 12×12×12 points (476 in the irreducible wedge). For the spin-polarized LSDA+U calculations, three different supercells were adopted. The first cell is equivalent to the primitive crystallographic cell, without rotational symmetry elements (space group $P1$). The calculations were performed on a 4×4×4 $\vec{k}$-mesh with 64 points in the irreducible wedge. The second cell is SC1 doubled along its b axis (space group $P1$) with the respective $3\times 2\times 3$ $\vec{k}$-mesh (18 points in the irreducible wedge). The third cell (SCC) is metrically equivalent to the C-centered crystallographic cell, but belongs to the space group $P1$. A $\vec{k}$-mesh of 24 (2×4×3) points has been used for calculations.

For the initial crystal structure, the model from a combined x-ray and neutron diffraction study [374] was used. The preliminary DFT calculations evidenced sizable forces for this model (up to 0.1 eV/Å). Therefore, a structural optimization was performed, by relaxing atomic positions one by one, and finding a position with minimal forces. The resulting relaxed structure had much smaller forces (up to 0.005 eV/Å), and considerably lower total energy compared to the experimental structure (36 meV/atom in LDA, 26 eV/atom in GGA). The atomic coordinates of the optimized crystal structure are given in Table A7.

atom	x/a	y/b	z/c
Cu	0	0	0
Cu	1/4	1/4	0
V	0.9949	1/2	0.2516
O	0	1/2	1/2
O	0.3428	1/2	0.1115
O	0.0706	0.2635	0.1864
O	0.1622	1/2	0.8541
O	0.3223	1/2	0.4804
H	0.3501	1/2	0.2546
H	0.3536	0.3714	0.5619

Table A7: Optimized crystal structure of volborthite $Cu_3[V_2O_7](OH)_2\cdot 2H_2O$, used in the DFT calculations. Lattice constants are the same as in Ref. 374.

A4 Details of the simulations (Chapters 6 and 7)

$CuSe_2O_5$

QMC simulations have been preformed on $N=1200$ sites finite lattice of $S=1/2$ spins (30 coupled chains of 40 sites each, periodic boundary conditions) using the `loop` [387] algorithm from the `alps-1.3` package [388]. 15 000 and 200 000 sweeps were used for and after thermalization, respectively.

$[NO]Cu(NO_3)_3$

The QMC susceptibility curves were computed using the `loop` [387] and `worm` algorithms, implemented in the `alps` simulation package [388]. The simulations were performed for finite lattices with periodic boundary conditions. The typical lattice size was $N=60$–100 for

1D models and $N = 1500$–2000 for the model of coupled spin chains. Calculations for lattices of different size showed negligible finite-size effects for the temperature range considered.

For the magnetic susceptibility of an anisotropic spin chain, the expression

$$\hat{H} = J \sum_{<ij>} (S_i^x S_j^x + S_i^y S_j^y + (1+\tilde{\Delta}) S_i^z S_j^z) - h_u \sum_i S_i^x - h_s \sum_i (-1)^i S_i^z \tag{A8}$$

from Ref. 389 was used. Here, the first term is the bilinear exchange with the symmetric anisotropy $\tilde{\Delta}$. The effective uniform (h_u) and staggered (h_s) fields depend on the applied external field (H) and on the staggered anisotropy.

$\mathbf{CaCu_2(SeO_3)_2Cl_2}$

Classical energy minimization procedure for collinear spin configurations was carried out using a self-written code. Classical Monte Carlo simulations were performed using the `alps` package [388] for a finite lattice of 48×48×24 spins with periodic boundary conditions. 20 000 sweeps for thermalization and 200 000 sweeps after thermalization were used.

$\mathbf{Cu_2\mathit{A}_2O_7}$

α-$Cu_2P_2O_7$: QMC simulations were performed on $N = 24\times24$ sites finite lattices with periodic boundary conditions using the `looper` [387] and `dirloop` algorithms from the `alps` package [388].

β-$Cu_2V_2O_7$: Spin correlations were computed on $N = 16\times16 = 256$ sites finite lattices using the QMC code `looper` [387] implemented in the `alps` simulation package [388]. For the simulations of the ordered moment, finite lattices up to $N = 2312$ sites were used. For both kinds of simulations, 30 000 sweeps for thermalization and 300 000 sweeps after thermalization were used.

α-$Cu_2As_2O_7$: QMC simulations were performed finite lattices of $N = 2048$ sites (32 coupled chains of 64 spins each) with periodic boundary conditions. A stochastic series expansion algorithm implemented in the code `looper` [387] from the software package `alps` [388] was applied, using 50 000 sweeps for thermalization and 500 000 steps after thermalization.

$\mathbf{CdCu_2(BO_3)_2}$

Magnetic susceptibility was simulated on $N = 16$ sites finite lattices using the full diagonalization code from the package `alps` [388]. Spin correlations and magnetization curve were simulated for $N = 32$ sites lattices, the code `spinpack` [390] was used.

Herbertsmithite $Cu_3Zn(OH)_6Cl_2$

LANCZOS diagonalizations on $N = 26$ sites finite lattices were performed using the sparse diagonalization code from the package `alps` [388].

Kapellasite $Cu_3Zn(OH)_6Cl_2$ and haydeeite $Cu_3Mg(OH)_6Cl_2$

LANCZOS diagonalizations on $N = 36$ sites finite lattices were performed by J. RICHTER at the University of Magdeburg using `spinpack` [390].

Volborthite $Cu_3[V_2O_7](OH)_2{\cdot}2H_2O$

LANCZOS diagonalizations on $N = 36$ sites finite lattices were performed by J. RICHTER at the University of Magdeburg using `spinpack` [390]. The full spectrum was computed by P. SINDZINGRE using an in-house ED code, the respective $N = 24$ sites finite lattices are depicted in Fig. A7.

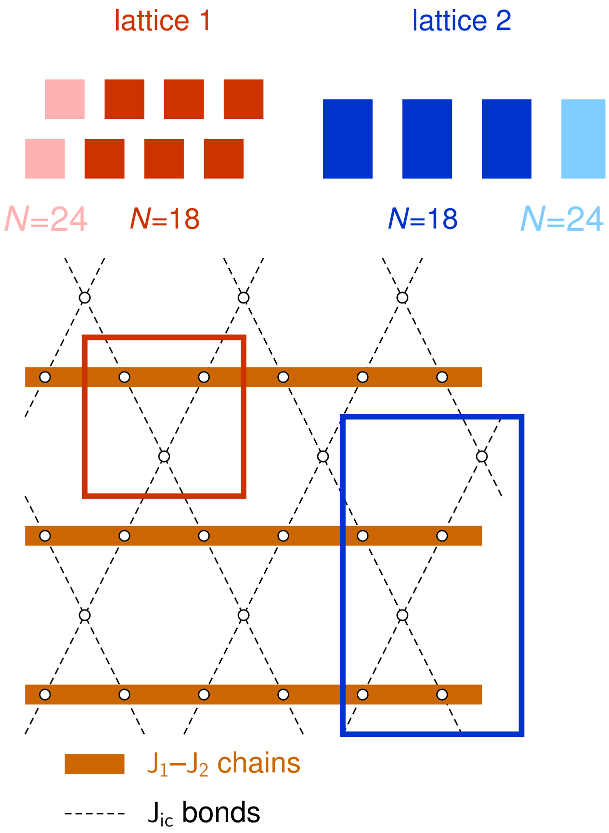

Figure A7: Finite lattices used for the ED studies of volborthite $Cu_3[V_2O_7](OH)_2{\cdot}2H_2O$. Top: $N = 24$ sites lattices used for calculations of $\chi^*(T^*)$. Unit cells are shown as squares and rectangles. Bottom: unit cells used in calculations. Individual spins and $J_1 - J_2$ chains are depicted as empty circles and bold orange lines, respectively.

Bibliography

[1] J. G. Bednorz and K. A. Müller, Possible high Tc superconductivity in the Ba–La–Cu–O system, Z. Phys. B **64**, 189 (1986).

[2] J. Zaanen, A modern, but way too short history of the theory of superconductivity at a high temperature, arXiv:1012.5461.

[3] W. E. Pickett, Electronic structure of the high-temperature oxide superconductors, Rev. Mod. Phys. **61**, 433 (1989).

[4] D. C. Johnston, J. W. Johnson, D. P. Goshorn, and A. J. Jacobson, Magnetic susceptibility of $(VO)_2P_2O_7$: a one-dimensional spin-1/2 Heisenberg antiferromagnet with a ladder spin configuration and a singlet ground state, Phys. Rev. B **35**, 219 (1987).

[5] T. Barnes and J. Riera, Susceptibility and excitation spectrum of $(VO)_2P_2O_7$ in ladder and dimer-chain models, Phys. Rev. B **50**, 6817 (1994), cond-mat/9404060.

[6] A. W. Garrett, S. E. Nagler, D. A. Tennant, B. C. Sales, and T. Barnes, Magnetic excitations in the S=1/2 alternating chain compound $(VO)_2P_2O_7$, Phys. Rev. Lett. **79**, 745 (1997), cond-mat/9704092.

[7] T. Yamauchi, Y. Narumi, J. Kikuchi, Y. Ueda, K. Tatani, T. C. Kobayashi, K. Kindo, and K. Motoya, Two gaps in $(VO)_2P_2O_7$: observation using high-field magnetization and NMR, Phys. Rev. Lett. **83**, 3729 (1999).

[8] T. Masuda, A. Zheludev, A. Bush, M. Markina, and A. Vasiliev, Competition between helimagnetism and commensurate quantum spin correlations in $LiCu_2O_2$, Phys. Rev. Lett. **92**, 177201 (2004), cond-mat/0310126.

[9] S.-L. Drechsler, J. Málek, J. Richter, A. S. Moskvin, A. A. Gippius, and H. Rosner, Comment on “Competition between helimagnetism and commensurate quantum spin correlations in $LiCu_2O_2$”, Phys. Rev. Lett. **94**, 039705 (2005), cond-mat/0411418.

[10] T. Masuda, A. Zheludev, A. Bush, M. Markina, and A. Vasiliev, Reply to “Comment on ‘Competition between helimagnetism and commensurate quantum spin correlations in $LiCu_2O_2$”, Phys. Rev. Lett. **94**, 039706 (2005), cond-mat/0412245.

[11] A. A. Gippius, E. N. Morozova, A. S. Moskvin, A. V. Zalessky, A. A. Bush, M. Baenitz, H. Rosner, and S.-L. Drechsler, NMR and local-density-approximation evidence for spiral magnetic order in the chain cuprate $LiCu_2O_2$, Phys. Rev. B **70**, 020406 (2004), cond-mat/0312706.

[12] T. Masuda, A. Zheludev, B. Roessli, A. Bush, M. Markina, and A. Vasiliev, Spin waves and magnetic interactions in $LiCu_2O_2$, Phys. Rev. B **72**, 014405 (2005), cond-mat/0412625.

[13] H. Kikuchi, Y. Fujii, M. Chiba, S. Mitsudo, T. Idehara, T. Tonegawa, K. Okamoto, T. Sakai, T. Kuwai, and H. Ohta, Experimental observation of the 1/3 magnetization plateau in the diamond-chain compound $Cu_3(CO_3)_2(OH)_2$, Phys. Rev. Lett. **94**, 227201 (2005).

[14] B. Gu and G. Su, Comment on “Experimental observation of the 1/3 magnetization plateau in the diamond-chain compound $Cu_3(CO_3)_2(OH)_2$”, Phys. Rev. Lett. **97**, 089701 (2006).

[15] H. Jeschke, I. Opahle, H. Kandpal, R. Valentí, H. Das, T. Saha-Dasgupta, O. Janson, H. Rosner, A. Brühl, B. Wolf, M. Lang, J. Richter, S. Hu, X. Wang, R. Peters, T. Pruschke, and A. Honecker, Multistep approach to microscopic models for frustrated quantum magnets: the case of the natural mineral azurite, Phys. Rev. Lett. **106**, 217201 (2011), arXiv:1012.1090.

[16] C. Gros, P. Lemmens, K.-Y. Choi, G. Güntherodt, M. Baenitz, and H. H. Otto, Quantum phase transition in the dioptase magnetic lattice, Europhys. Lett. **60**, 276 (2002), cond-mat/0208106.

[17] O. Janson, A. A. Tsirlin, M. Schmitt, and H. Rosner, Large quantum fluctuations in the strongly coupled spin-1/2 chains of green dioptase $Cu_6Si_6O_{18}\cdot 6H_2O$, Phys. Rev. B **82**, 014424 (2010), arXiv:1004.3765.

[18] M. Enderle, C. Mukherjee, B. Fåk, R. K. Kremer, J.-M. Broto, H. Rosner, S.-L. Drechsler, J. Richter, J. Málek, A. Prokofiev, W. Assmus, S. Pujol, J.-L. Raggazzoni, H. Rakoto, M. Rheinstädter, and H. M. Rønnow, Quantum helimagnetism of the frustrated spin-1/2 chain $LiCuVO_4$, Europhys. Lett. **70**, 237 (2005).

[19] M. Enderle, B. Fåk, H.-J. Mikeska, R. K. Kremer, A. Prokofiev, and W. Assmus, Two-spinon and four-spinon continuum in a frustrated ferromagnetic spin-1/2 chain, Phys. Rev. Lett. **104**, 237207 (2010).

[20] J. B. Goodenough, Theory of the role of covalence in the perovskite-type manganites [La, M(II)]MnO_3, Phys. Rev. **100**, 564 (1955).

[21] J. Kanamori, Superexchange interaction and symmetry properties of electron orbitals, J. Phys. Chem. Solids **10**, 87 (1959).

[22] H. A. Jahn and E. Teller, Stability of polyatomic molecules in degenerate electronic states. I. Orbital degeneracy, Proc. R. Soc. London **161**, 220 (1937).

[23] P. W. Anderson, Antiferromagnetism. Theory of superexchange interaction, Phys. Rev. **79**, 350 (1950).

[24] P. W. Anderson, New approach to the theory of superexchange interactions, Phys. Rev. **115**, 2 (1959).

[25] P. Weiss, L'Hypothese du champ moleculaire et de la propriete ferromagnetique, J. de Phys. **6**, 661 (1907).

[26] H. Rosner, H. Eschrig, R. Hayn, S.-L. Drechsler, and J. Málek, Electronic structure and magnetic properties of the linear chain cuprates Sr_2CuO_3 and Ca_2CuO_3, Phys. Rev. B **56**, 3402 (1997), cond-mat/9704210.

[27] M. Braden, G. Wilkendorf, J. Lorenzana, M. Aïn, G. J. McIntyre, M. Behruzi, G. Heger, G. Dhalenne, and A. Revcolevschi, Structural analysis of $CuGeO_3$: relation between nuclear structure and magnetic interaction, Phys. Rev. B **54**, 1105 (1996).

[28] W. E. A. Lorenz, R. O. Kuzian, S.-L. Drechsler, W.-D. Stein, N. Wizent, G. Behr, J. Málek, U. Nitzsche, H. Rosner, A. Hiess, W. Schmidt, R. Klingeler, M. Loewenhaupt, and B. Büchner, Highly dispersive spin excitations in the chain cuprate Li_2CuO_2, Europhys. Lett. **88**, 37002 (2009), arXiv:0909.5687.

[29] Y.-Y. Li, Domain walls in antiferromagnets and the weak ferromagnetism of α-Fe_2O_3, Phys. Rev. **101**, 1450 (1956).

[30] I. Dzyaloshinsky, A thermodynamic theory of "weak" ferromagnetism of antiferromagnetics, J. Phys. Chem. Solids **4**, 241 (1958).

[31] T. Moriya, Anisotropic superexchange interaction and weak ferromagnetism, Phys. Rev. **120**, 91 (1960).

[32] N. D. Mermin and H. Wagner, Absence of ferromagnetism or antiferromagnetism in one- or two-dimensional isotropic Heisenberg models, Phys. Rev. Lett. **17**, 1133 (1966).

[33] K. M. Kojima, Y. Fudamoto, M. Larkin, G. M. Luke, J. Merrin, B. Nachumi, Y. J. Uemura, N. Motoyama, H. Eisaki, S. Uchida, K. Yamada, Y. Endoh, S. Hosoya, B. J. Sternlieb, and G. Shirane, Reduction of ordered moment and Néel temperature of quasi-one-dimensional antiferromagnets Sr_2CuO_3 and Ca_2CuO_3, Phys. Rev. Lett. **78**, 1787 (1997).

[34] F. Sapiña, J. Rodríguez-Carvajal, M. Sanchis, R. Ibáñez, A. Beltrán, and D. Beltrán, Crystal and magnetic structure of Li_2CuO_2, Solid State Commun. **74**, 779 (1990).

[35] T. Thio, T. R. Thurston, N. W. Preyer, P. J. Picone, M. A. Kastner, H. P. Jenssen, D. R. Gabbe, C. Y. Chen, R. J. Birgeneau, and A. Aharony, Antisymmetric exchange and its influence on the magnetic structure and conductivity of La_2CuO_4, Phys. Rev. B **38**, 905 (1988).

[36] F. Mizuno, H. Masuda, I. Hirabayashi, S. Tanaka, M. Hasegawa, and U. Mizutani, Low-temperature ferromagnetism in $La_4Ba_2Cu_2O_{10}$, Nature (London) **345**, 788 (1990).

[37] H. Masuda, F. Mizuno, I. Hirabayashi, and S. Tanaka, Electron-spin resonance and ferromagnetism in a copper oxide: $La_4Ba_2Cu_2O_{10}$, Phys. Rev. B **43**, 7871 (1991).

[38] H. Shiraki, T. Saito, T. Yamada, M. Tsujimoto, M. Azuma, H. Kurata, S. Isoda, M. Takano, and Y. Shimakawa, Ferromagnetic cuprates $CaCu_3Ge_4O_{12}$ and $CaCu_3Sn_4O_{12}$ with *A*-site ordered perovskite structure, Phys. Rev. B **76**, 140403 (2007).

[39] W. Ku, H. Rosner, W. E. Pickett, and R. T. Scalettar, Insulating ferromagnetism in $La_4Ba_2Cu_2O_{10}$: an ab initio Wannier function analysis, Phys. Rev. Lett. **89**, 167204 (2002), cond-mat/0205300.

[40] J.-W. G. Bos, C. V. Colin, and T. T. M. Palstra, Magnetoelectric coupling in the cubic ferrimagnet Cu_2OSeO_3, Phys. Rev. B **78**, 094416 (2008), arXiv:0808.3955.

[41] Y. Yasui, K. Sato, Y. Kobayashi, and M. Sato, Studies of multiferroic system $LiCu_2O_2$: I. sample characterization and relationship between magnetic properties and multiferroic nature, J. Phys. Soc. Jpn. **78**, 084720 (2009), arXiv:0904.4014.

[42] M. Baran, A. Jedrzejczak, H. Szymczak, V. Maltsev, G. Kamieniarz, G. Szukowski, C. Loison, A. Ormeci, S.-L. Drechsler, and H. Rosner, Quasi-one-dimensional $S{=}1/2$ magnet $PbCu(SO_4)(OH)_2$: frustration due to competing in-chain exchange, Phys. Status Solidi C **3**, 220 (2006).

[43] H. Das, T. Saha-Dasgupta, C. Gros, and R. Valentí, Proposed low-energy model Hamiltonian for the spin-gapped system $CuTe_2O_5$, Phys. Rev. B **77**, 224437 (2008), cond-mat/0703675.

[44] M. Schmitt, A. A. Gippius, K. S. Okhotnikov, W. Schnelle, K. Koch, O. Janson, W. Liu, Y.-H. Huang, Y. Skourski, F. Weickert, M. Baenitz, and H. Rosner, Electronic structure and magnetic properties of the spin-gap compound $Cu_2(PO_3)_2CH_2$: Magnetic versus structural dimers, Phys. Rev. B **81**, 104416 (2010).

[45] T. Nikuni, M. Oshikawa, A. Oosawa, and H. Tanaka, Bose–Einstein condensation of dilute magnons in $TlCuCl_3$, Phys. Rev. Lett. **84**, 5868 (2000), cond-mat/9908118.

[46] H. Kageyama, K. Yoshimura, R. Stern, N. V. Mushnikov, K. Onizuka, M. Kato, K. Kosuge, C. P. Slichter, T. Goto, and Y. Ueda, Exact dimer ground state and quantized magnetization plateaus in the two-dimensional spin system $SrCu_2(BO_3)_2$, Phys. Rev. Lett. **82**, 3168 (1999).

[47] R. Darradi, J. Richter, and D. J. J. Farnell, Coupled cluster treatment of the Shastry–Sutherland antiferromagnet, Phys. Rev. B **72**, 104425 (2005), cond-mat/0504283.

[48] A. Koga and N. Kawakami, Quantum phase transitions in the Shastry–Sutherland model for $SrCu_2(BO_3)_2$, Phys. Rev. Lett. **84**, 4461 (2000), cond-mat/0003435.

[49] M. Takigawa, T. Waki, M. Horvatić, and C. Berthier, Novel ordered phases in the orthogonal dimer spin system $SrCu_2(BO_3)_2$, J. Phys. Soc. Jpn. **79**, 011005 (2010).

[50] J. Bobroff, N. Laflorencie, L. K. Alexander, A. V. Mahajan, B. Koteswararao, and P. Mendels, Impurity-induced magnetic order in low-dimensional spin-gapped materials, Phys. Rev. Lett. **103**, 047201 (2009), arXiv:0903.1234.

[51] L. K. Alexander, J. Bobroff, A. V. Mahajan, B. Koteswararao, N. Laflorencie, and F. Alet, Impurity effects in coupled-ladder $BiCu_2PO_6$ studied by NMR and quantum Monte Carlo simulations, Phys. Rev. B **81**, 054438 (2010), arXiv:0912.4353.

[52] Ch. Rüegg, A. Furrer, D. Sheptyakov, T. Strässle, K. W. Krämer, H.-U. Güdel, and L. Mélési, Pressure-induced quantum phase transition in the spin-liquid $TlCuCl_3$, Phys. Rev. Lett. **93**, 257201 (2004).

[53] L. Balents, Spin liquids in frustrated magnets, Nature (London) **464**, 199 (2010).

[54] J. S. Helton, K. Matan, M. P. Shores, E. A. Nytko, B. M. Bartlett, Y. Yoshida, Y. Takano, A. Suslov, Y. Qiu, J.-H. Chung, D. G. Nocera, and Y. S. Lee, Spin dynamics of the spin-1/2 kagome lattice antiferromagnet $ZnCu_3(OH)_6Cl_2$, Phys. Rev. Lett. **98**, 107204 (2007), cond-mat/0610539.

[55] K. I. Kugel' and D. I. Khomskii, The Jahn–Teller effect and magnetism: transition metal compounds, Sov. Phys.–Usp. **25**, 231 (1982).

[56] A. I. Liechtenstein, V. I. Anisimov, and J. Zaanen, Density-functional theory and strong interactions: orbital ordering in Mott–Hubbard insulators, Phys. Rev. B **52**, R5467 (1995).

[57] J. E. Medvedeva, M. A. Korotin, V. I. Anisimov, and A. J. Freeman, Orbital ordering in paramagnetic $LaMnO_3$ and $KCuF_3$, Phys. Rev. B **65**, 172413 (2002), cond-mat/0112423.

[58] E. Pavarini, E. Koch, and A. I. Lichtenstein, Mechanism for orbital ordering in $KCuF_3$, Phys. Rev. Lett. **101**, 266405 (2008), arXiv:0808.3585.

[59] I. Leonov, N. Binggeli, D. Korotin, V. I. Anisimov, N. Stojić, and D. Vollhardt, Structural relaxation due to electronic correlations in the paramagnetic insulator $KCuF_3$, Phys. Rev. Lett. **101**, 096405 (2008), arXiv:0804.1093.

[60] M. Hase, I. Terasaki, and K. Uchinokura, Observation of the spin-Peierls transition in linear Cu^{2+} spin-1/2 chains in an inorganic compound $CuGeO_3$, Phys. Rev. Lett. **70**, 3651 (1993).

[61] A. L. Patterson, Z. Kristallogr. **A90**, 517 (1935).

[62] J. Karle and H. Hauptman, The phases and magnitudes of the structure factors, Acta Crystallogr. **3**, 181 (1950).

[63] H. Hauptman and J. Karle, Structure invariants and seminvariants for noncentrosymmetric space groups, Acta Crystallogr. **9**, 45 (1956).

[64] H. M. Rietveld, A profile refinement method for nuclear and magnetic structures, J. Appl. Crystallogr. **2**, 65 (1969).

[65] T. A. Kodenkandath, J. N. Lalena, W. L. Zhou, E. E. Carpenter, C. Sangregorio, A. U. Falster, W. B. Simmons, C. J. O'Connor, and J. B. Wiley, Assembly of metal–anion arrays within a perovskite host. Low-temperature synthesis of new layered copper–oxyhalides, $(CuX)LaNb_2O_7$, X = Cl, Br, J. Am. Chem. Soc. **121**, 10743 (1999).

[66] A. A. Tsirlin and H. Rosner, Structural distortion and frustrated magnetic interactions in the layered copper oxychloride $(CuCl)LaNb_2O_7$, Phys. Rev. B **79**, 214416 (2009), arXiv:0901.0154.

[67] A. A. Tsirlin, A. M. Abakumov, G. Van Tendeloo, and H. Rosner, Interplay of atomic displacements in the quantum magnet $(CuCl)LaNb_2O_7$, Phys. Rev. B **82**, 054107 (2010), arXiv:1005.4898.

[68] A. A. Tsirlin, R. V. Shpanchenko, E. V. Antipov, C. Bougerol, J. Hadermann, G. van Tendeloo, W. Schnelle, and H. Rosner, Spin ladder compound $Pb_{0.55}Cd_{0.45}V_2O_5$: synthesis and investigation, Phys. Rev. B **76**, 104429 (2007), arXiv:0710.1806.

[69] A. A. Tsirlin, R. Nath, J. Sichelschmidt, Y. Skourski, C. Geibel, and H. Rosner, Frustrated couplings between alternating spin-1/2 chains in $AgVOAsO_4$, Phys. Rev. B **83**, 144412 (2011), arXiv:1101.2546.

[70] R. J. Harrison, Neutron diffraction of magnetic materials, Rev. Mineral. Geochem. **63**, 113 (2006).

[71] T. Ami, M. K. Crawford, R. L. Harlow, Z. R. Wang, D. C. Johnston, Q. Huang, and R. W. Erwin, Magnetic susceptibility and low-temperature structure of the linear chain cuprate Sr_2CuO_3, Phys. Rev. B **51**, 5994 (1995).

[72] G. A. Bain and J. F. Berry, Diamagnetic corrections and Pascal's constants, J. Chem. Educ. **85**, 532 (2008).

[73] J. H. van Vleck, *The Theory of electric and magnetic susceptibilities* (Oxford University Press, London, 1932).

[74] X. Liu, R. Dronskowski, R. K. Kremer, M. Ahrens, C. Lee, and M.-H. Whangbo, Characterization of the magnetic and structural properties of copper carbodiimide, CuNCN, by neutron diffraction and first-principles evaluations of its spin exchange interactions, J. Phys. Chem. C **112**, 11013 (2008).

[75] A. A. Tsirlin and H. Rosner, Uniform spin-chain physics arising from N—C—N bridges in CuNCN, the nitride analog of the copper oxides, Phys. Rev. B **81**, 024424 (2010), arXiv:0910.2056.

[76] S. Eggert, I. Affleck, and M. Takahashi, Susceptibility of the spin-1/2 Heisenberg antiferromagnetic chain, Phys. Rev. Lett. **73**, 332 (1994), cond-mat/9404062.

[77] R. Melzi, P. Carretta, A. Lascialfari, M. Mambrini, M. Troyer, P. Millet, and F. Mila, $Li_2VO(Si,Ge)O_4$, a prototype of a two-dimensional frustrated quantum Heisenberg antiferromagnet, Phys. Rev. Lett. **85**, 1318 (2000), cond-mat/0005273.

[78] S. Kadota, I. Yamada, S. Yoneyama, and K. Hirakawa, Formation of one-dimensional antiferromagnet in $KCuF_3$ with the perovskite structure, J. Phys. Soc. Jpn. **23**, 751 (1967).

[79] R. Nath, D. Kasinathan, H. Rosner, M. Baenitz, and C. Geibel, Electronic and magnetic properties of $K_2CuP_2O_7$: a model $S=1/2$ Heisenberg chain system, Phys. Rev. B **77**, 134451 (2008), arXiv:0804.1262.

[80] S.-L. Drechsler, O. Volkova, A. N. Vasiliev, N. Tristan, J. Richter, M. Schmitt, H. Rosner, J. Málek, R. Klingeler, A. A. Zvyagin, and B. Büchner, Frustrated cuprate route from antiferromagnetic to ferromagnetic spin-1/2 Heisenberg chains: Li_2ZrCuO_4 as a missing link near the quantum critical point, Phys. Rev. Lett. **98**, 077202 (2007), cond-mat/0701741.

[81] L. Néel, Antiferromagnetism and ferrimagnetism, Proc. Phys. Soc., London, Sect. A **65**, 869 (1952).

[82] R. Nath, A. A. Tsirlin, E. E. Kaul, M. Baenitz, N. Büttgen, C. Geibel, and H. Rosner, Strong frustration due to competing ferromagnetic and antiferromagnetic interactions: magnetic properties of $M(VO)_2(PO_4)_2$ (M=Ca and Sr), Phys. Rev. B **78**, 024418 (2008), arXiv:0804.4667.

[83] C. Waldtmann, H.-U. Everts, B. Bernu, C. Lhuillier, P. Sindzingre, P. Lecheminant, and L. Pierre, First excitations of the spin-1/2 Heisenberg antiferromagnet on the kagome lattice, Eur. Phys. J. B **2**, 501 (1998).

[84] T. Lancaster, S. J. Blundell, M. L. Brooks, P. J. Baker, F. L. Pratt, J. L. Manson, M. M. Conner, F. Xiao, C. P. Landee, F. A. Chaves, S. Soriano, M. A. Novak, T. P. Papageorgiou, A. D. Bianchi, T. Herrmannsdörfer, J. Wosnitza, and J. A. Schlueter, Magnetic order in the S=1/2 two-dimensional molecular antiferromagnet copper pyrazine perchlorate $Cu(Pz)_2(ClO_4)_2$, Phys. Rev. B **75**, 094421 (2007), cond-mat/0612317.

[85] E. S. R. Gopal, *Specific Heats at Low Temperatures* (Plenum Press, New York, 1966).

[86] W. Schottky, The rotation of atomic axles in solid bodies. (With magnetic, thermal and chemical connections), Phys. Z. **23**, 448 (1922).

[87] D. C. Johnston, R. K. Kremer, M. Troyer, X. Wang, A. Klümper, S. L. Bud'ko, A. F. Panchula, and P. C. Canfield, Thermodynamics of spin S=1/2 antiferromagnetic uniform and alternating-exchange Heisenberg chains, Phys. Rev. B **61**, 9558 (2000), cond-mat/0003271.

[88] A. Möller, M. Schmitt, W. Schnelle, T. Förster, and H. Rosner, $AgCuVO_4$: a quasi-one-dimensional S=1/2 chain compound, Phys. Rev. B **80**, 125106 (2009), arXiv:0906.3447.

[89] E. Kojima, A. Miyata, Y. Motome, H. Ueda, Y. Ueda, and S. Takeyama, Magnetic orders of highly frustrated spinel, $ZnCr_2O_4$ in magnetic fields up to 400 T, J. Low Temp. Phys. **159**, 3 (2010).

[90] R. Nath, A. A. Tsirlin, H. Rosner, and C. Geibel, Magnetic properties of $BaCdVO(PO_4)_2$: a strongly frustrated spin-1/2 square lattice close to the quantum critical regime, Phys. Rev. B **78**, 064422 (2008), arXiv:0803.3535.

[91] A. A. Tsirlin and H. Rosner, Extension of the spin-1/2 frustrated square lattice model: the case of layered vanadium phosphates, Phys. Rev. B **79**, 214417 (2009), arXiv:0901.4498.

[92] S. Nishimoto, S.-L. Drechsler, R. Kuzian, J. Richter, J. Málek, M. Schmitt, J. van den Brink, and H. Rosner, The strength of frustration and quantum fluctuations in $LiVCuO_4$, arXiv:1105.2810.

[93] S. Miyahara, J.-B. Fouet, S. R. Manmana, R. M. Noack, H. Mayaffre, I. Sheikin, C. Berthier, and F. Mila, Uniform and staggered magnetizations induced by Dzyaloshinskii-Moriya interactions in isolated and coupled spin-1/2 dimers in a magnetic field, Phys. Rev. B **75**, 184402 (2007), cond-mat/0610861.

[94] J. Richter, J. Schulenburg, and A. Honecker, Quantum magnetism in two dimensions: from semi-classical Néel order to magnetic disorder, in *Lecture Notes in Physics*, Vol. 645, edited by U. Schollwöck, J. Richter, D. Farnell, and R. Bishop (Springer Berlin/Heidelberg, 2004) pp. 85–153.

[95] M. Born and R. Oppenheimer, Zur Quantentheorie der Molekeln, Ann. Phys. (Berlin) **389**, 457 (1927).

[96] P. Hohenberg and W. Kohn, Inhomogeneous electron gas, Phys. Rev. **136**, B864 (1964).

[97] W. Kohn and L. J. Sham, Self-consistent equations including exchange and correlation effects, Phys. Rev. **140**, A1133 (1965).

[98] K. Capelle, A bird's-eye view of density-functional theory, Braz. J. Phys. **36**, 1318 (2006), cond-mat/0211443.

[99] J. P. Perdew and Y. Wang, Accurate and simple analytic representation of the electron-gas correlation energy, Phys. Rev. B **45**, 13244 (1992).

[100] J. P. Perdew, K. Burke, and M. Ernzerhof, Generalized gradient approximation made simple, Phys. Rev. Lett. **77**, 3865 (1996).

[101] A. Dal Corso, A. Pasquarello, A. Baldereschi, and R. Car, Generalized-gradient approximations to density-functional theory: a comparative study for atoms and solids, Phys. Rev. B **53**, 1180 (1996).

[102] P. Ziesche, S. Kurth, and J. P. Perdew, Density functionals from LDA to GGA, Comp. Mat. Sci. **11**, 122 (1998).

[103] U. von Barth and L. Hedin, A local exchange-correlation potential for the spin polarized case. I, J. Phys. C **5**, 1629 (1972).

[104] V. I. Anisimov, J. Zaanen, and O. K. Andersen, Band theory and Mott insulators: Hubbard U instead of Stoner I, Phys. Rev. B **44**, 943 (1991).

[105] E. R. Ylvisaker, W. E. Pickett, and K. Koepernik, Anisotropy and magnetism in the LSDA+U method, Phys. Rev. B **79**, 035103 (2009), arXiv:0808.1706.

[106] K. Koch, *Crystal structure, electron density and chemical bonding in inorganic compounds studied by the Electric Field Gradient*, Ph.D. thesis, Techn. Univ. Dresden (2009).

[107] F. de Groot, High-resolution X-ray emission and X-ray absorption spectroscopy, Chem. Rev. **101**, 1779 (2001).

[108] F. M. F. de Groot, J. C. Fuggle, B. T. Thole, and G. A. Sawatzky, $2p$ X-ray absorption of $3d$ transition-metal compounds: an atomic multiplet description including the crystal field, Phys. Rev. B **42**, 5459 (1990).

[109] M. T. Czyżyk and G. A. Sawatzky, Local-density functional and on-site correlations: The electronic structure of La_2CuO_4 and $LaCuO_3$, Phys. Rev. B **49**, 14211 (1994).

[110] A. G. Petukhov, I. I. Mazin, L. Chioncel, and A. I. Lichtenstein, Correlated metals and the LDA+U method, Phys. Rev. B **67**, 153106 (2003), cond-mat/0206548.

[111] A. B. Shick, V. Drchal, and L. Havela, Coulomb-U and magnetic-moment collapse in δ-Pu, Europhys. Lett. **69**, 588 (2005), cond-mat/0502233.

[112] I. I. Mazin, Electronic structure and magnetism in the frustrated antiferromagnet $LiCrO_2$: first-principles calculations, Phys. Rev. B **75**, 094407 (2007), cond-mat/0701520.

[113] H. Lin and D. Truhlar, QM/MM: what have we learned, where are we, and where do we go from here? Theor. Chem. Acc. **117**, 185 (2007).

[114] C. de Graaf, I. de P. R. Moreira, F. Illas, Ò. Iglesias, and A. Labarta, Magnetic structure of Li_2CuO_2: from *ab initio* calculations to macroscopic simulations, Phys. Rev. B **66**, 014448 (2002), cond-mat/0205654.

[115] H.-Y. Huang, N. A. Bogdanov, L. Siurakshina, P. Fulde, J. van den Brink, and L. Hozoi, *Ab initio* calculation of d–d excitations in quasi-one-dimensional Cu d^9 correlated materials, Phys. Rev. B **84**, 235125 (2011), arXiv:1111.2231.

[116] L. Hozoi and M. S. Laad, Quasiparticle bands in cuprates by quantum-chemical methods: towards an *ab initio* description of strong electron correlations, Phys. Rev. Lett. **99**, 256404 (2007), arXiv:0707.4648.

[117] L. Hozoi, L. Siurakshina, P. Fulde, and J. van den Brink, Ab initio determination of Cu 3d orbital energies in layered copper oxides, Sci. Rep. **1**, 65 (2011), arXiv:1012.3603.

[118] A. D. Becke, A new mixing of Hartree–Fock and local density-functional theories, J. Chem. Phys. **98**, 1372 (1993).

[119] P. Rivero, I. de P. R. Moreira, and F. Illas, Electronic structure of single-layered undoped cuprates from hybrid density functional theory, Phys. Rev. B **81**, 205123 (2010).

[120] F. Aryasetiawan, Self-energy of ferromagnetic nickel in the *GW* approximation, Phys. Rev. B **46**, 13051 (1992).

[121] F. Aryasetiawan and O. Gunnarsson, Electronic structure of NiO in the *GW* approximation, Phys. Rev. Lett. **74**, 3221 (1995).

[122] F. Aryasetiawan and O. Gunnarsson, The *GW* method, Rep. Prog. Phys. **61**, 237 (1998), cond-mat/9712013.

[123] A. I. Lichtenstein, M. I. Katsnelson, and G. Kotliar, Finite-temperature magnetism of transition metals: an *ab initio* dynamical mean-field theory, Phys. Rev. Lett. **87**, 067205 (2001), cond-mat/0102297.

[124] J. Kuneš, I. Leonov, M. Kollar, K. Byczuk, V. Anisimov, and D. Vollhardt, Dynamical mean-field approach to materials with strong electronic correlations, Eur. Phys. J. Spec. Top. **180**, 5 (2009), arXiv:1003.3600.

[125] S. Biermann, F. Aryasetiawan, and A. Georges, First-principles approach to the electronic structure of strongly correlated systems: combining the *GW* approximation and dynamical mean-field theory, Phys. Rev. Lett. **90**, 086402 (2003), cond-mat/0207419.

[126] K. Koepernik and H. Eschrig, Full-potential nonorthogonal local-orbital minimum-basis band-structure scheme, Phys. Rev. B **59**, 1743 (1999).

[127] J. P. Perdew and A. Zunger, Self-interaction correction to density-functional approximations for many-electron systems, Phys. Rev. B **23**, 5048 (1981).

[128] H. Eschrig and K. Koepernik, Tight-binding models for the iron-based superconductors, Phys. Rev. B **80**, 104503 (2009), arXiv:0905.4844.

[129] G. Kresse and J. Furthmüller, Efficient iterative schemes for *ab initio* total-energy calculations using a plane-wave basis set, Phys. Rev. B **54**, 11169 (1996).

[130] K. Schwarz, P. Blaha, and G. Madsen, Electronic structure calculations of solids using the WIEN2k package for material sciences, Comp. Phys. Commun. **147**, 71 (2002).

[131] Y. Mokrousov, G. Bihlmayer, and S. Blügel, Full-potential linearized augmented plane-wave method for one-dimensional systems: gold nanowire and iron monowires in a gold tube, Phys. Rev. B **72**, 045402 (2005).

[132] D. D. Koelling and B. N. Harmon, A technique for relativistic spin-polarised calculations, J. Phys. C **10**, 3107 (1977).

[133] O. Janson, `flyswatter`, 2008–2011.

[134] N. Marzari and D. Vanderbilt, Maximally localized generalized Wannier functions for composite energy bands, Phys. Rev. B **56**, 12847 (1997), arXiv:cond-mat/9707145.

[135] J. Hubbard, Electron correlations in narrow energy bands, Proc. R. Soc. Lond. A **276**, 238 (1963).

[136] E. H. Lieb and F. Y. Wu, Absence of Mott transition in an exact solution of the short-range, one-band model in one dimension, Phys. Rev. Lett. **20**, 1445 (1968).

[137] J. Zaanen and G. A. Sawatzky, Systematics in band gaps and optical spectra of 3D transition metal compounds, J. Solid State Chem. **88**, 8 (1990).

[138] J. van den Brink, *The Hubbard model with orbital degeneracy and in polarizable media*, Ph.D. thesis, Rijksuniversiteit Groningen (1997), `http://irs.ub.rug.nl/ppn/161377017`.

[139] B. J. Powell, An introduction to effective low-energy Hamiltonians in condensed matter physics and chemistry, arXiv:0906.1640.

[140] K. A. Chao, J. Spałek, and A. M. Oleś, Kinetic exchange interaction in a narrow S-band, J. Phys. C **10**, L271 (1977).

[141] E. Bousquet and N. Spaldin, J dependence in the LSDA+U treatment of noncollinear magnets, Phys. Rev. B **82**, 220402 (2010), arXiv:1011.0939.

[142] A. R. Machintosh and O. K. Andersen, The electronic structure of transition metals, in *Electrons at the Fermi Surface*, edited by M. Springford (Cambridge Univ. Press, London, 1980) pp. 149–224.

[143] A. I. Liechtenstein, M. I. Katsnelson, V. P. Antropov, and V. A. Gubanov, Local spin density functional approach to the theory of exchange interactions in ferromagnetic metals and alloys, J. Magn. Magn. Mater. **67**, 65 (1987).

[144] V. V. Mazurenko and V. I. Anisimov, Weak ferromagnetism in antiferromagnets: α-Fe_2O_3 and La_2CuO_4, Phys. Rev. B **71**, 184434 (2005), cond-mat/0410767.

[145] V. V. Mazurenko, S. L. Skornyakov, A. V. Kozhevnikov, F. Mila, and V. I. Anisimov, Wannier functions and exchange integrals: the example of $LiCu_2O_2$, Phys. Rev. B **75**, 224408 (2007), cond-mat/0702276.

[146] V. V. Mazurenko, S. L. Skornyakov, V. I. Anisimov, and F. Mila, First-principles investigation of symmetric and antisymmetric exchange interactions of $SrCu_2(BO_3)_2$, Phys. Rev. B **78**, 195110 (2008), arXiv:0804.4771.

[147] A. N. Yaresko, A. Y. Perlov, R. Hayn, and H. Rosner, Exchange integrals of $Sr_2CuO_2Cl_2$ and $Ba_2Cu_3O_4Cl_2$ from LDA+U calculations, Phys. Rev. B **65**, 115111 (2002).

[148] A. Bühler, U. Löw, and G. S. Uhrig, Thermodynamic properties of the dimerized and frustrated S=1/2 chain, Phys. Rev. B **64**, 024428 (2001), cond-mat/0102101.

[149] J. J. Borras-Almenar, E. Coronado, J. Curely, R. Georges, and J. C. Gianduzzo, Alternating chains with ferromagnetic and antiferromagnetic interactions. Theory and magnetic properties, Inorg. Chem. **33**, 5171 (1994).

[150] A. Honecker and A. Läuchli, Frustrated trimer chain model and $Cu_3Cl_6(H_2O)_2{\cdot}2H_8C_4SO_2$ in a magnetic field, Phys. Rev. B **63**, 174407 (2001), cond-mat/0005398.

[151] J. Oitmaa, R. R. P. Singh, and W. Zheng, Quantum spin ladders at T=0 and at high temperatures studied by series expansions, Phys. Rev. B **54**, 1009 (1996), cond-mat/9602055.

[152] H. Rosner, R. R. P. Singh, W. H. Zheng, J. Oitmaa, and W. E. Pickett, High-temperature expansions for the J_1-J_2 Heisenberg models: applications to ab initio calculated models for Li_2VOSiO_4 and Li_2VOGeO_4, Phys. Rev. B **67**, 014416 (2003).

[153] N. Elstner and A. P. Young, Spin-1/2 Heisenberg antiferromagnet on the kagome lattice: high-temperature expansion and exact-diagonalization studies, Phys. Rev. B **50**, 6871 (1994).

[154] Z. Weihong, C. J. Hamer, and J. Oitmaa, Series expansions for a Heisenberg antiferromagnetic model for $SrCu_2(BO_3)_2$, Phys. Rev. B **60**, 6608 (1999), cond-mat/9811030.

[155] G. Misguich and B. Bernu, Specific heat of the S=1/2 Heisenberg model on the kagome lattice: High-temperature series expansion analysis, Phys. Rev. B **71**, 014417 (2005), cond-mat/0407277.

[156] A. A. Tsirlin, R. Nath, A. M. Abakumov, R. V. Shpanchenko, C. Geibel, and H. Rosner, Frustrated square lattice with spatial anisotropy: crystal structure and magnetic properties of $PbZnVO(PO_4)_2$, Phys. Rev. B **81**, 174424 (2010), arXiv:0910.2258.

[157] A. V. Chubukov, S. Sachdev, and J. Ye, Theory of two-dimensional quantum Heisenberg antiferromagnets with a nearly critical ground state, Phys. Rev. B **49**, 11919 (1994), cond-mat/9304046.

[158] J. C. Bonner and M. E. Fisher, Linear magnetic chains with anisotropic coupling, Phys. Rev. **135**, A640 (1964).

[159] G. E. Moore, Cramming more components onto integrated circuits, Proc. IEEE **86**, 82 (1998).

[160] P. Sindzingre, Thermodynamic properties of the spin-1/2 Heisenberg antiferromagnet with anisotropic exchange on the kagome lattice: comparison with volborthite, arXiv:0707.4264.

[161] J. Richter, J. Schulenburg, A. Honecker, and D. Schmalfuß, Absence of magnetic order for the spin-half Heisenberg antiferromagnet on the star lattice, Phys. Rev. B **70**, 174454 (2004), cond-mat/0406103.

[162] A. Lüscher and A. M. Läuchli, Exact diagonalization study of the antiferromagnetic spin-1/2 Heisenberg model on the square lattice in a magnetic field, Phys. Rev. B **79**, 195102 (2009), arXiv:0812.3420.

[163] C. Lanczos, An iteration method for the solution of the eigenvalue problem of linear differential and integral operators, J. Res. Natl. Bur. Stand. **45**, 255 (1950).

[164] N. Laflorencie and D. Poilblanc, Simulations of pure and doped low-dimensional spin-1/2 gapped systems, Lect. Notes Phys. **645**, 227 (2004), cond-mat/0408363.

[165] P. Sindzingre and C. Lhuillier, Low-energy excitations of the kagome antiferromagnet and the spin-gap issue, Europhys. Lett. **88**, 27009 (2009), arXiv:0907.4164.

[166] A. M. Läuchli, Introduction to frustrated magnetism: materials, experiments, theory, in *Introduction to Frustrated Magnetism*, edited by C. Lacroix, P. Mendels, and F. Mila (Springer, 2010) Chap. Numerical Simulations of Frustrated Systems.

[167] N. Shannon, B. Schmidt, K. Penc, and P. Thalmeier, Finite temperature properties and frustrated ferromagnetism in a square lattice Heisenberg model, Eur. Phys. J. B **38**, 599 (2004), cond-mat/0312160.

[168] P. Henelius and A. W. Sandvik, Sign problem in Monte Carlo simulations of frustrated quantum spin systems, Phys. Rev. B **62**, 1102 (2000), cond-mat/0001351.

[169] S. R. White, Density matrix formulation for quantum renormalization groups, Phys. Rev. Lett. **69**, 2863 (1992).

[170] S. R. White, Density-matrix algorithms for quantum renormalization groups, Phys. Rev. B **48**, 10345 (1993).

[171] E. Stoudenmire and S. R. White, Studying two dimensional systems with the density matrix renormalization group, arXiv:1105.1374.

[172] H.-C. Jiang, H. Yao, and L. Balents, Spin liquid ground state of the spin-1/2 square J_1–J_2 Heisenberg model, arXiv:1112.2241.

[173] K. G. Wilson, The renormalization group: critical phenomena and the Kondo problem, Rev. Mod. Phys. **47**, 773 (1975).

[174] R. J. Bursill, T. Xiang, and G. A. Gehring, The density matrix renormalization group for a quantum spin chain at non-zero temperature, J. Phys.: Condens. Matter **8**, L583 (1996), cond-mat/9609001.

[175] X. Wang and T. Xiang, Transfer-matrix density-matrix renormalization-group theory for thermodynamics of one-dimensional quantum systems, Phys. Rev. B **56**, 5061 (1997), cond-mat/9705301.

[176] N. Shibata, Thermodynamics of the anisotropic Heisenberg chain calculated by the density matrix renormalization group method, J. Phys. Soc. Jpn. **66**, 2221 (1997), cond-mat/9706152.

[177] J. Sirker, V. Y. Krivnov, D. V. Dmitriev, A. Herzog, O. Janson, S. Nishimoto, S.-L. Drechsler, and J. Richter, The J_1–J_2 Heisenberg model at and close to its $z=4$ quantum critical point, Phys. Rev. B **84**, 144403 (2011), arXiv:1106.1008.

[178] T. Hikihara, L. Kecke, T. Momoi, and A. Furusaki, Vector chiral and multipolar orders in the spin-1/2 frustrated ferromagnetic chain in magnetic field, Phys. Rev. B **78**, 144404 (2008), arXiv:0807.0858.

[179] O. Kahn, M. Verdaguer, J. J. Girerd, J. Galy, and F. Maury, Orbital interactions in a strongly antiferromagnetically coupled copper(II) linear chain: $CuSe_2O_5$, Solid State Commun. **34**, 971 (1980).

[180] K. Binder, Applications of Monte Carlo methods to statistical physics, Rep. Prog. Phys. **60**, 487 (1997).

[181] A. F. Albuquerque, M. Troyer, and J. Oitmaa, Quantum phase transition in a Heisenberg antiferromagnet on a square lattice with strong plaquette interactions, Phys. Rev. B **78**, 132402 (2008), arXiv:0807.4389.

[182] J. Bobroff, N. Laflorencie, L. K. Alexander, A. V. Mahajan, B. Koteswararao, and P. Mendels, Impurity-induced magnetic order in low-dimensional spin-gapped materials (supplementary information), Phys. Rev. Lett. **103**, 047201 (2009), arXiv:0907.0211.

[183] A. W. Sandvik, Finite-size scaling of the ground-state parameters of the two-dimensional Heisenberg model, Phys. Rev. B **56**, 11678 (1997), cond-mat/9707123.

[184] H. Bethe, Zur Theorie der Metalle, Z. Phys. A **71**, 205 (1931).

[185] A. Luther and I. Peschel, Calculation of critical exponents in two dimensions from quantum field theory in one dimension, Phys. Rev. B **12**, 3908 (1975).

[186] H. Q. Lin and D. K. Campbell, Spin-spin correlations in the one-dimensional spin-1/2, antiferromagnetic Heisenberg chain, J. Appl. Phys. **69**, 5947 (1991).

[187] L. D. Faddeev and L. A. Takhtajan, What is the spin of a spin wave? Phys. Lett. A **85**, 375 (1981).

[188] P. W. Anderson, An approximate quantum theory of the antiferromagnetic ground state, Phys. Rev. **86**, 694 (1952).

[189] R. B. Griffiths, Magnetization curve at zero temperature for the antiferromagnetic Heisenberg linear chain, Phys. Rev. **133**, A768 (1964).

[190] K. Tanaka, M. Konishi, and F. Marumo, Electron-density distribution in crystals of $KCuF_3$ with Jahn–Teller distortion, Acta Crystallogr. **B35**, 1303 (1979).

[191] M. T. Hutchings, E. J. Samuelsen, G. Shirane, and K. Hirakawa, Neutron-diffraction determination of the antiferromagnetic structure of $KCuF_3$, Phys. Rev. **188**, 919 (1969).

[192] S. K. Satija, J. D. Axe, G. Shirane, H. Yoshizawa, and K. Hirakawa, Neutron scattering study of spin waves in one-dimensional antiferromagnet $KCuF_3$, Phys. Rev. B **21**, 2001 (1980).

[193] L. Paolasini, R. Caciuffo, A. Sollier, P. Ghigna, and M. Altarelli, Coupling between spin and orbital degrees of freedom in $KCuF_3$, Phys. Rev. Lett. **88**, 106403 (2002).

[194] R. Caciuffo, L. Paolasini, A. Sollier, P. Ghigna, E. Pavarini, J. van den Brink, and M. Altarelli, Resonant X-ray scattering study of magnetic and orbital order in $KCuF_3$, Phys. Rev. B **65**, 174425 (2002).

[195] M. D. Towler, R. Dovesi, and V. R. Saunders, Magnetic interactions and the cooperative Jahn–Teller effect in $KCuF_3$, Phys. Rev. B **52**, 10150 (1995).

[196] N. Binggeli and M. Altarelli, Orbital ordering, Jahn–Teller distortion, and resonant X-ray scattering in $KCuF_3$, Phys. Rev. B **70**, 085117 (2004), cond-mat/0408568.

[197] S. E. Nagler, D. A. Tennant, R. A. Cowley, T. G. Perring, and S. K. Satija, Spin dynamics in the quantum antiferromagnetic chain compound $KCuF_3$, Phys. Rev. B **44**, 12361 (1991).

[198] D. A. Tennant, T. G. Perring, R. A. Cowley, and S. E. Nagler, Unbound spinons in the $S=1/2$ antiferromagnetic chain $KCuF_3$, Phys. Rev. Lett. **70**, 4003 (1993).

[199] D. A. Tennant, R. A. Cowley, S. E. Nagler, and A. M. Tsvelik, Measurement of the spin-excitation continuum in one-dimensional $KCuF_3$ using neutron scattering, Phys. Rev. B **52**, 13368 (1995).

[200] D. A. Tennant, S. E. Nagler, D. Welz, G. Shirane, and K. Yamada, Effects of coupling between chains on the magnetic excitation spectrum of $KCuF_3$, Phys. Rev. B **52**, 13381 (1995).

[201] B. Lake, D. A. Tennant, and S. E. Nagler, Novel longitudinal mode in the coupled quantum chain compound $KCuF_3$, Phys. Rev. Lett. **85**, 832 (2000), cond-mat/9910459.

[202] I. Yamada, H. Fujii, and M. Hidaka, Experimental evidence of the Dzyaloshinsky–Moriya antisymmetric exchange interaction in the one-dimensional Heisenberg antiferromagnet $KCuF_3$: EPR measurements, J. Phys.: Condens. Matter **1**, 3397 (1989).

[203] M. V. Eremin, D. V. Zakharov, H.-A. Krug von Nidda, R. M. Eremina, A. Shuvaev, A. Pimenov, P. Ghigna, J. Deisenhofer, and A. Loidl, Dynamical Dzyaloshinsky–Moriya interaction in $KCuF_3$, Phys. Rev. Lett. **101**, 147601 (2008), arXiv:0807.3641.

[204] I. Tsukada, Y. Sasago, K. Uchinokura, A. Zheludev, S. Maslov, G. Shirane, K. Kakurai, and E. Ressouche, $BaCu_2Si_2O_7$: a quasi-one-dimensional S=1/2 antiferromagnetic chain system, Phys. Rev. B **60**, 6601 (1999), cond-mat/9902251.

[205] S. Bertaina and R. Hayn, Exchange integrals and magnetization distribution in $BaCu_2X_2O_7$ (X=Ge, Si), Phys. Rev. B **73**, 212409 (2006), cond-mat/0607108.

[206] A. Zheludev, M. Kenzelmann, S. Raymond, E. Ressouche, T. Masuda, K. Kakurai, S. Maslov, I. Tsukada, K. Uchinokura, and A. Wildes, Energy separation of single-particle and continuum states in an S=1/2 weakly coupled chains antiferromagnet, Phys. Rev. Lett. **85**, 4799 (2000), cond-mat/0006426.

[207] A. Zheludev, M. Kenzelmann, S. Raymond, T. Masuda, K. Uchinokura, and S.-H. Lee, Spin dynamics in the quasi-one-dimensional S=1/2 antiferromagnet $BaCu_2Si_2O_7$, Phys. Rev. B **65**, 014402 (2001), cond-mat/0105223.

[208] A. Zheludev, K. Kakurai, T. Masuda, K. Uchinokura, and K. Nakajima, Dominance of the excitation continuum in the longitudinal spectrum of weakly coupled Heisenberg S=1/2 chains, Phys. Rev. Lett. **89**, 197205 (2002), cond-mat/0210568.

[209] A. Zheludev, S. Raymond, L.-P. Regnault, F. H. L. Essler, K. Kakurai, T. Masuda, and K. Uchinokura, Polarization dependence of spin excitations in $BaCu_2Si_2O_7$, Phys. Rev. B **67**, 134406 (2003), cond-mat/0210586.

[210] I. Tsukada, J. Takeya, T. Masuda, and K. Uchinokura, Two-stage spin-flop transitions in the S=1/2 antiferromagnetic spin chain $BaCu_2Si_2O_7$, Phys. Rev. Lett. **87**, 127203 (2001), cond-mat/0107328.

[211] A. Zheludev, E. Ressouche, I. Tsukada, T. Masuda, and K. Uchinokura, Structure of multiple spin-flop states in $BaCu_2Si_2O_7$, Phys. Rev. B **65**, 174416 (2002).

[212] M. Poirier, M. Castonguay, A. Revcolevschi, and G. Dhalenne, Ultrasonic investigation of the magnetic ordering in the quasi-one-dimensional S=1/2 antiferromagnet $BaCu_2Si_2O_7$, Phys. Rev. B **66**, 054402 (2002).

[213] V. N. Glazkov, G. Dhalenne, A. Revcolevschi, and A. Zheludev, Multiple spin-flop phase diagram of $BaCu_2Si_2O_7$, J. Phys.: Condens. Matter **23**, 086003 (2011), arXiv:1012.1702.

[214] A. S. Moskvin, J. Málek, M. Knupfer, R. Neudert, J. Fink, R. Hayn, S.-L. Drechsler, N. Motoyama, H. Eisaki, and S. Uchida, Evidence for two types of low-energy charge transfer excitations in Sr_2CuO_3, Phys. Rev. Lett. **91**, 037001 (2003).

[215] T. Ogasawara, M. Ashida, N. Motoyama, H. Eisaki, S. Uchida, Y. Tokura, H. Ghosh, A. Shukla, S. Mazumdar, and M. Kuwata-Gonokami, Ultrafast optical nonlinearity in the quasi-one-dimensional Mott insulator Sr_2CuO_3, Phys. Rev. Lett. **85**, 2204 (2000), cond-mat/0002286.

[216] J. W. Seo, K. Yang, D. W. Lee, Y. S. Roh, J. H. Kim, H. Eisaki, H. Ishii, I. Jarrige, Y. Q. Cai, D. L. Feng, and C. Kim, Anomalous resonant inelastic x-ray scattering dispersions of Sr_2CuO_3 measured at the Cu $1s \rightarrow 3d$ edge, Phys. Rev. B **73**, 161104 (2006).

[217] D. C. Dender, P. R. Hammar, D. H. Reich, C. Broholm, and G. Aeppli, Direct observation of field-induced incommensurate fluctuations in a one-dimensional S=1/2 antiferromagnet, Phys. Rev. Lett. **79**, 1750 (1997), cond-mat/9704034.

[218] I. Affleck and M. Oshikawa, Field-induced gap in Cu benzoate and other S=1/2 antiferromagnetic chains, Phys. Rev. B **60**, 1038 (1999), cond-mat/9905002.

[219] R. Becker and H. Berger, Reinvestigation of $CuSe_2O_5$, Acta Crystallogr. **E62**, I256 (2006).

[220] I. Živković, K. Prša, O. Zaharko, and H. Berger, Ni_3TeO_6 — a collinear antiferromagnet with ferromagnetic honeycomb planes, J. Phys.: Condens. Matter **22**, 056002 (2010), arXiv:0912.5268.

[221] R. Kubo, The spin-wave theory of antiferromagnetics, Phys. Rev. **87**, 568 (1952).

[222] R. Kubo, The spin-wave theory as a variational method and its application to antiferromagnetism, Rev. Mod. Phys. **25**, 344 (1953).

[223] C. Trapp and J. W. Stout, Magnetic susceptibility of MnF_2, Phys. Rev. Lett. **10**, 157 (1963).

[224] S. Stølen, T. Grande, and N. L. Allan, *Chemical Thermodynamics of Materials* (John Wiley & Sons, Ltd., Chichester, 2004).

[225] G. Meunier and M. Bertaud, Cristallochimie du sélénium(+IV). II. structure cristalline de $ZnSe_2O_5$, Acta Crystallogr. **B30**, 2840 (1974).

[226] S. S. Salunke, M. A. H. Ahsan, R. Nath, A. V. Mahajan, and I. Dasgupta, Electronic structure of spin-1/2 Heisenberg antiferromagnetic systems: $Ba_2Cu(PO_4)_2$ and $Sr_2Cu(PO_4)_2$, Phys. Rev. B **76**, 085104 (2007), arXiv:0709.2228.

[227] H. Rosner, M. Schmitt, D. Kasinathan, A. Ormeci, J. Richter, S.-L. Drechsler, and M. D. Johannes, Comment on "Electronic structure of spin-1/2 Heisenberg antiferromagnetic systems: $Ba_2Cu(PO_4)_2$ and $Sr_2Cu(PO_4)_2$", Phys. Rev. B **79**, 127101 (2009).

[228] S. Salunke, M. A. H. Ahsan, R. Nath, A. V. Mahajan, and I. Dasgupta, Reply to "Comment on 'Electronic structure of spin-1/2 Heisenberg antiferromagnetic systems: $Ba_2Cu(PO_4)_2$ and $Sr_2Cu(PO_4)_2$", Phys. Rev. B **79**, 127102 (2009).

[229] M. D. Johannes, J. Richter, S.-L. Drechsler, and H. Rosner, $Sr_2Cu(PO_4)_2$: a real material realization of the one-dimensional nearest neighbor Heisenberg chain, Phys. Rev. B **74**, 174435 (2006), cond-mat/0609430.

[230] S. Feldkemper, W. Weber, J. Schulenburg, and J. Richter, Ferromagnetic coupling in nonmetallic Cu^{2+} compounds, Phys. Rev. B **52**, 313 (1995).

[231] W. Geertsma and D. Khomskii, Influence of side groups on 90° superexchange: a modification of the Goodenough–Kanamori–Anderson rules, Phys. Rev. B **54**, 3011 (1996).

[232] M. Baran, Y. P. Gaidukov, N. P. Danilova, A. V. Inushkin, A. Jedrzejczak, Y. A. Koksharov, V. N. Nikiforov, A. Revcolevschi, R. Szymczak, and H. Szymczak, Low temperature magnetic ordering in Bi_2CuO_4, J. Magn. Magn. Mater. **196–197**, 532 (1999).

[233] O. Volkova, I. Morozov, V. Shutov, E. Lapsheva, P. Sindzingre, O. Cépas, M. Yehia, V. Kataev, R. Klingeler, B. Büchner, and A. Vasiliev, Realization of the Nersesyan–Tsvelik model in $(NO)Cu(NO_3)_3$, Phys. Rev. B **82**, 054413 (2010), arXiv:1004.0444.

[234] A. A. Nersesyan and A. M. Tsvelik, Spinons in more than one dimension: resonance valence bond state stabilized by frustration, Phys. Rev. B **67**, 024422 (2003), cond-mat/0206483.

[235] O. A. Starykh and L. Balents, Dimerized phase and transitions in a spatially anisotropic square lattice antiferromagnet, Phys. Rev. Lett. **93**, 127202 (2004), cond-mat/0402055.

[236] A. A. Tsirlin and H. Rosner, Microscopic model of (CuCl)$LaNb_2O_7$: coupled spin dimers replace a frustrated square lattice, Phys. Rev. B **82**, 060409 (2010), arXiv:1007.3883.

[237] M. Schmitt, O. Janson, M. Schmidt, S. Hoffmann, W. Schnelle, S.-L. Drechsler, and H. Rosner, Crystal-water-induced switching of magnetically active orbitals in $CuCl_2$, Phys. Rev. B **79**, 245119 (2009), arXiv:0905.4038.

[238] O. A. Starykh, H. Katsura, and L. Balents, Extreme sensitivity of a frustrated quantum magnet: Cs_2CuCl_4, Phys. Rev. B **82**, 014421 (2010), arXiv:1004.5117.

[239] H. Manaka, A. V. Kolomiets, and T. Goto, Disordered states in IPA-$Cu(Cl_xBr_{1-x})_3$ induced by bond randomness, Phys. Rev. Lett. **101**, 077204 (2008).

[240] E. Wulf, S. Mühlbauer, T. Yankova, and A. Zheludev, Disorder instability of the magnon condensate in a frustrated spin ladder, Phys. Rev. B **84**, 174414 (2011), arXiv:1110.0806.

[241] D. J. Scalapino, Y. Imry, and P. Pincus, Generalized Ginzburg–Landau theory of pseudo-one-dimensional systems, Phys. Rev. B **11**, 2042 (1975).

[242] H. J. Schulz, Dynamics of coupled quantum spin chains, Phys. Rev. Lett. **77**, 2790 (1996), cond-mat/9604144.

[243] V. Y. Irkhin and A. A. Katanin, Calculation of Néel temperature for $S{=}1/2$ Heisenberg quasi-one-dimensional antiferromagnets, Phys. Rev. B **61**, 6757 (2000), cond-mat/9909257.

[244] M. Bocquet, Finite-temperature perturbation theory for quasi-one-dimensional spin-1/2 Heisenberg antiferromagnets, Phys. Rev. B **65**, 184415 (2002), cond-mat/0110429.

[245] C. Yasuda, S. Todo, K. Hukushima, F. Alet, M. Keller, M. Troyer, and H. Takayama, Néel temperature of quasi-low-dimensional Heisenberg antiferromagnets, Phys. Rev. Lett. **94**, 217201 (2005), cond-mat/0312392.

[246] S. Todo and A. Shibasaki, Improved chain mean-field theory for quasi-one-dimensional quantum magnets, Phys. Rev. B **78**, 224411 (2008), arXiv:0805.3097.

[247] A. A. Zvyagin, Magnetic phase diagram of a quasi-one-dimensional quantum spin system, Phys. Rev. B **81**, 224407 (2010), arXiv:1007.0919.

[248] A. A. Belik, M. Azuma, and M. Takano, Characterization of quasi-one-dimensional S=1/2 Heisenberg antiferromagnets $Sr_2Cu(PO_4)_2$ and $Ba_2Cu(PO_4)_2$ with magnetic susceptibility, specific heat, and thermal analysis, J. Solid State Chem. **177**, 883 (2004).

[249] A. Möller and J. Jainski, Synthesis and crystal structure of $AgCuVO_4$, Z. Anorg. Allgem. Chem. **634**, 1669 (2008).

[250] O. Janson, A. A. Tsirlin, and H. Rosner, Antiferromagnetic spin-1/2 chains in $(NO)Cu(NO_3)_3$: a microscopic study, Phys. Rev. B **82**, 184410 (2010), arXiv:1007.2798.

[251] R. Coldea, D. A. Tennant, K. Habicht, P. Smeibidl, C. Wolters, and Z. Tylczynski, Direct measurement of the spin Hamiltonian and observation of condensation of magnons in the 2D frustrated quantum magnet Cs_2CuCl_4, Phys. Rev. Lett. **88**, 137203 (2002), cond-mat/0111079.

[252] S. E. Sebastian, N. Harrison, C. D. Batista, L. Balicas, M. Jaime, P. A. Sharma, N. Kawashima, and I. R. Fisher, Dimensional reduction at a quantum critical point, Nature (London) **441**, 617 (2006), cond-mat/0606042.

[253] Ch. Rüegg, D. F. McMorrow, B. Normand, H. M. Rønnow, S. E. Sebastian, I. R. Fisher, C. D. Batista, S. N. Gvasaliya, C. Niedermayer, and J. Stahn, Multiple magnon modes and consequences for the Bose–Einstein condensed phase in $BaCuSi_2O_6$, Phys. Rev. Lett. **98**, 017202 (2007), cond-mat/0607465.

[254] T. Giamarchi, Ch. Rüegg, and O. Tchernyshyov, Bose–Einstein condensation in magnetic insulators, Nature Phys. **4**, 198 (2008), arXiv:0712.2250.

[255] Ch. Rüegg, N. Cavadini, A. Furrer, H.-U. Güdel, K. Krämer, H. Mutka, A. Wildes, K. Habicht, and P. Vorderwisch, Bose–Einstein condensation of the triplet states in the magnetic insulator $TlCuCl_3$, Nature (London) **423**, 62 (2003).

[256] J. Deisenhofer, R. M. Eremina, A. Pimenov, T. Gavrilova, H. Berger, M. Johnsson, P. Lemmens, H.-A. Krug von Nidda, A. Loidl, K.-S. Lee, and M.-H. Whangbo, Structural and magnetic dimers in the spin-gapped system $CuTe_2O_5$, Phys. Rev. B **74**, 174421 (2006), cond-mat/0610458.

[257] A. A. Tsirlin and H. Rosner, Ab initio modeling of Bose–Einstein condensation in $Pb_2V_3O_9$, Phys. Rev. B **83**, 064415 (2011), arXiv:1011.3981.

[258] Z. He and Y. Ueda, Paramagnetic anisotropy and spin-flop transition in single crystals of the quasi-one-dimensional system β-$Cu_2V_2O_7$, Phys. Rev. B **77**, 052402 (2008).

[259] J. Pommer, V. Kataev, K.-Y. Choi, P. Lemmens, A. Ionescu, Y. Pashkevich, A. Freimuth, and G. Güntherodt, Interplay between structure and magnetism in the spin-chain compound $(Cu,Zn)_2V_2O_7$, Phys. Rev. B **67**, 214410 (2003).

[260] M. Yashima and R. O. Suzuki, Electronic structure and magnetic properties of monoclinic β-$Cu_2V_2O_7$:a GGA+U study, Phys. Rev. B **79**, 125201 (2009).

[261] J. A. R. Stiles and C. V. Stager, Magnetic structure of manganese pyrophosphate and copper pyrophosphate, Can. J. Phys. **50**, 3079 (1972).

[262] J. A. R. Stiles and C. V. Stager, Nuclear magnetic resonance in antiferromagnetic $Cu_2P_2O_7$, Can. J. Phys. **51**, 87 (1973).

[263] Y. C. Arango, E. Vavilova, M. Abdel-Hafiez, O. Janson, A. A. Tsirlin, H. Rosner, S.-L. Drechsler, M. Weil, G. Nénert, R. Klingeler, O. Volkova, A. Vasiliev, V. Kataev, and B. Büchner, Magnetic properties of the low-dimensional spin-1/2 magnet α-$Cu_2As_2O_7$, Phys. Rev. B **84**, 134430 (2011), arXiv:1110.0447.

[264] I. S. Camara, R. Gautier, E. Le Fur, J.-C. Trombe, J. Galy, A. M. Ghorayeb, and A. Stepanov, Electron spin resonance in three spin-1/2 dimer systems: $VO(HPO_4)\cdot0.5H_2O$, $KZn(H_2O)(VO)_2(PO_4)_2(H_2PO_4)$, and CsV_2O_5, Phys. Rev. B **81**, 184433 (2010).

[265] A. A. Tsirlin, O. Janson, and H. Rosner, β-$Cu_2V_2O_7$: a spin-1/2 honeycomb lattice system, Phys. Rev. B **82**, 144416 (2010), arXiv:1007.1646.

[266] R. D. Shannon, Revised effective ionic radii and systematic studies of interatomic distances in halides and chalcogenides, Acta Crystallogr. **A32**, 751 (1976).

[267] M. Hase, M. Kohno, H. Kitazawa, O. Suzuki, K. Ozawa, G. Kido, M. Imai, and X. Hu, Coexistence of a nearly spin-singlet state and antiferromagnetic long-range order in quantum spin system $Cu_2CdB_2O_6$, Phys. Rev. B **72**, 172412 (2005), cond-mat/0509094.

[268] M. Hase, M. Kohno, H. Kitazawa, O. Suzuki, K. Ozawa, G. Kido, M. Imai, and X. Hu, Magnetism of $Cu_2CdB_2O_6$: quantum spin system having a nearly singlet state and antiferromagnetic long-range order, J. Appl. Phys. **99**, 08H504 (2006).

[269] M. Hase, A. Dönni, V. Y. Pomjakushin, L. Keller, F. Gozzo, A. Cervellino, and M. Kohno, Magnetic structure of $Cu_2CdB_2O_6$ exhibiting a quantum-mechanical magnetization plateau and classical antiferromagnetic long-range order, Phys. Rev. B **80**, 104405 (2009).

[270] S. Muenchau and K. Bluhm, Synthesis and crystal structure of copper cadmium pyroborate oxide: $Cu_2Cd(B_2O_5)O$, Z. Naturforsch. **B 50**, 1151 (1995).

[271] A. A. Tsirlin, O. Janson, and H. Rosner, Unusual ferromagnetic superexchange in $CdVO_3$: the role of Cd, Phys. Rev. B **84**, 144429 (2011), arXiv:1104.2495.

[272] R. D. Spence and J. H. Muller, Proton resonance in dioptase $(CuSiO_3{\cdot}H_2O)_6$, J. Chem. Phys. **29**, 961 (1958).

[273] R. E. Newnham and R. P. Santoro, Magnetic and optical properties of dioptase, Phys. Status Solidi **19**, K87 (1967).

[274] M. Wintenberger, G. André, and M. Gardette, Magnetic properties of green dioptase $CuSiO_3H_2O$ and of black dioptase $CuSiO_3$, and magnetic structure of black dioptase, Solid State Commun. **87**, 309 (1993).

[275] I. A. Kiseleva, L. P. Ogorodova, L. V. Melchakova, and M. R. Bisengalieva, Thermodynamic properties of copper silicate: dioptase: $Cu_6Si_6O_{18}{\cdot}6H_2O$, J. Chem. Thermodynamics **25**, 621 (1993).

[276] E. L. Belokoneva, Yu. K. Gubina, J. B. Forsyth, and P. J. Brown, The charge-density distribution, its multipole refinement and the antiferromagnetic structure of dioptase, $Cu_6[Si_6O_{18}]{\cdot}6H_2O$, Phys. Chem. Miner. **29**, 430 (2002).

[277] J. M. Law, C. Hoch, M.-H. Whangbo, and R. K. Kremer, Description of anhydrous (black) dioptase as a $S{=}1/2$ uniform antiferromagnetic chain system, Z. Anorg. Allgem. Chem. **636**, 54 (2010).

[278] H.-J. Brandt and H. H. Otto, Synthesis and crystal structure of $Cu_6[Ge_6O_{18}]{\cdot}6H_2O$, a dioptase-type cyclo-germanate, Z. Kristallogr. **212**, 34 (1997).

[279] C. L. Henley, private communication.

[280] L. Onsager, Crystal statistics. I. A two-dimensional model with an order-disorder transition, Phys. Rev. **65**, 117 (1944).

[281] M. Mekata, Kagome: the story of the basketweave lattice, Phys. Today **56** (2), 12 (2003).

[282] I. Syôzi, Statistics of kagome lattice, Prog. Theor. Phys. **6**, 306 (1951).

[283] K. Kanô and S. Naya, Antiferromagnetism. The kagome Ising net, Prog. Theor. Phys. **10**, 158 (1953).

[284] M. Takano, T. Shinjo, and T. Takada, On the spin arrangement in “kagome” lattice of antiferromagnetic $KFe_3(OH)_6(SO_4)_2$, J. Phys. Soc. Jpn. **30**, 1049 (1971).

[285] M. G. Townsend, G. Longworth, and E. Roudaut, Triangular-spin, kagome plane in jarosites, Phys. Rev. B **33**, 4919 (1986).

[286] A. Keren, K. Kojima, L. P. Le, G. M. Luke, W. D. Wu, Y. J. Uemura, M. Takano, H. Dabkowska, and M. J. P. Gingras, Muon-spin-rotation measurements in the kagome lattice systems: Cr-jarosite and Fe-jarosite, Phys. Rev. B **53**, 6451 (1996).

[287] C. Broholm, G. Aeppli, G. P. Espinosa, and A. S. Cooper, Antiferromagnetic fluctuations and short-range order in a kagome lattice, Phys. Rev. Lett. **65**, 3173 (1990).

[288] B. Martínez, A. Labarta, R. Rodríguez-Solá, and X. Obradors, Magnetic transition in highly frustrated $SrCr_8Ga_4O_{19}$: The archetypal kagome system, Phys. Rev. B **50**, 15779 (1994).

[289] P. Schiffer, A. P. Ramirez, K. N. Franklin, and S.-W. Cheong, Interaction-induced spin coplanarity in a kagome magnet: $SrCr_{9p}Ga_{12-9p}O_{19}$, Phys. Rev. Lett. **77**, 2085 (1996).

[290] Y. J. Uemura, A. Keren, K. Kojima, L. P. Le, G. M. Luke, W. D. Wu, Y. Ajiro, T. Asano, Y. Kuriyama, M. Mekata, H. Kikuchi, and K. Kakurai, Spin fluctuations in frustrated kagome lattice system $SrCr_8Ga_4O_{19}$ studied by muon spin relaxation, Phys. Rev. Lett. **73**, 3306 (1994).

[291] A. Keren, P. Mendels, M. Horvatić, F. Ferrer, Y. J. Uemura, M. Mekata, and T. Asano, ^{69,71}Ga NMR in the kagome lattice compound $SrCr_{9-x}Ga_{3+x}O_{19}$, Phys. Rev. B **57**, 10745 (1998).

[292] P. Mendels, A. Keren, L. Limot, M. Mekata, G. Collin, and M. Horvatić, Ga NMR study of the local susceptibility in kagome-based $SrCr_8Ga_4O_{19}$: pseudogap and paramagnetic defects, Phys. Rev. Lett. **85**, 3496 (2000).

[293] J. N. Reimers, A. J. Berlinsky, and A.-C. Shi, Mean-field approach to magnetic ordering in highly frustrated pyrochlores, Phys. Rev. B **43**, 865 (1991).

[294] V. Elser, Nuclear antiferromagnetism in a registered ^{3}He solid, Phys. Rev. Lett. **62**, 2405 (1989).

[295] J. T. Chalker, P. C. W. Holdsworth, and E. F. Shender, Hidden order in a frustrated system: properties of the Heisenberg kagome antiferromagnet, Phys. Rev. Lett. **68**, 855 (1992).

[296] J. N. Reimers and A. J. Berlinsky, Order by disorder in the classical Heisenberg kagome antiferromagnet, Phys. Rev. B **48**, 9539 (1993).

[297] A. Chubukov, Order from disorder in a kagome antiferromagnet, Phys. Rev. Lett. **69**, 832 (1992).

[298] J. Villain, R. Bidaux, J.-P. Carton, and R. Conte, Order as an effect of disorder, J. Phys. (Paris) **41**, 1263 (1980).

[299] S. Sachdev, Kagome- and triangular-lattice Heisenberg antiferromagnets: ordering from quantum fluctuations and quantum-disordered ground states with unconfined bosonic spinons, Phys. Rev. B **45**, 12377 (1992).

[300] A. B. Harris, C. Kallin, and A. J. Berlinsky, Possible Néel orderings of the kagome antiferromagnet, Phys. Rev. B **45**, 2899 (1992).

[301] L. Messio, C. Lhuillier, and G. Misguich, Lattice symmetries and regular magnetic orders in classical frustrated antiferromagnets, Phys. Rev. B **83**, 184401 (2011), arXiv:1101.1212.

[302] R. R. P. Singh and D. A. Huse, Ground state of the spin-1/2 kagome-lattice Heisenberg antiferromagnet, Phys. Rev. B **76**, 180407 (2007), arXiv:0707.0892.

[303] R. R. P. Singh and D. A. Huse, Triplet and singlet excitations in the valence bond crystal phase of the kagome lattice Heisenberg model, Phys. Rev. B **77**, 144415 (2008), arXiv:0801.2735.

[304] G. Evenbly and G. Vidal, Frustrated antiferromagnets with entanglement renormalization: ground state of the spin-1/2 Heisenberg model on a kagome lattice, Phys. Rev. Lett. **104**, 187203 (2010).

[305] M. E. Zhitomirsky and K. Ueda, Valence-bond crystal phase of a frustrated spin-1/2 square-lattice antiferromagnet, Phys. Rev. B **54**, 9007 (1996), cond-mat/9603152.

[306] S. Di Matteo, G. Jackeli, C. Lacroix, and N. B. Perkins, Valence-bond crystal in a pyrochlore antiferromagnet with orbital degeneracy, Phys. Rev. Lett. **93**, 077208 (2004), cond-mat/0404127.

[307] S. V. Isakov, Y. B. Kim, and A. Paramekanti, Spin-liquid phase in a spin-1/2 quantum magnet on the kagome lattice, Phys. Rev. Lett. **97**, 207204 (2006), cond-mat/0607778.

[308] M. Hermele, Y. Ran, P. A. Lee, and X.-G. Wen, Properties of an algebraic spin liquid on the kagome lattice, Phys. Rev. B **77**, 224413 (2008), arXiv:0803.1150.

[309] X. G. Wen, Mean-field theory of spin-liquid states with finite energy gap and topological orders, Phys. Rev. B **44**, 2664 (1991).

[310] M. Hermele, T. Senthil, and M. P. A. Fisher, Algebraic spin liquid as the mother of many competing orders, Phys. Rev. B **72**, 104404 (2005), cond-mat/0502215.

[311] S. Yan, D. A. Huse, and S. R. White, Spin liquid ground state of the S=1/2 kagome Heisenberg antiferromagnet, Science **332**, 1173 (2011), arXiv:1011.6114.

[312] C. Lhuillier, P. Sindzingre, and J. B. Fouet, Exact diagonalization studies of two-dimensional frustrated anti-ferromagnet models, Can. J. Phys. **79**, 1525 (2001), cond-mat/0009336.

[313] S. Dommange, M. Mambrini, B. Normand, and F. Mila, Static impurities in the S=1/2 kagome lattice: dimer freezing and mutual repulsion, Phys. Rev. B **68**, 224416 (2003), cond-mat/0306299.

[314] P. Lecheminant, B. Bernu, C. Lhuillier, L. Pierre, and P. Sindzingre, Order versus disorder in the quantum Heisenberg antiferromagnet on the kagome lattice using exact spectra analysis, Phys. Rev. B **56**, 2521 (1997), cond-mat/9706167.

[315] F. Mila, Low-energy sector of the S=1/2 kagome antiferromagnet, Phys. Rev. Lett. **81**, 2356 (1998).

[316] S. Capponi, A. Läuchli, and M. Mambrini, Numerical contractor renormalization method for quantum spin models, Phys. Rev. B **70**, 104424 (2004), cond-mat/0404712.

[317] K. Hida, Magnetization process of the S=1 and 1/2 uniform and distorted kagome Heisenberg antiferromagnets, J. Phys. Soc. Jpn. **70**, 3673 (2001).

[318] J. Schulenburg, A. Honecker, J. Schnack, J. Richter, and H.-J. Schmidt, Macroscopic magnetization jumps due to independent magnons in frustrated quantum spin lattices, Phys. Rev. Lett. **88**, 167207 (2002), cond-mat/0108498.

[319] A. Honecker, J. Schulenburg, and J. Richter, Magnetization plateaus in frustrated antiferromagnetic quantum spin models, J. Phys.: Condens. Matter **16**, S749 (2004), cond-mat/0309425.

[320] D. C. Cabra, M. D. Grynberg, P. C. W. Holdsworth, A. Honecker, P. Pujol, J. Richter, D. Schmalfuß, and J. Schulenburg, Quantum kagomé antiferromagnet in a magnetic field: low-lying nonmagnetic excitations versus valence-bond crystal order, Phys. Rev. B **71**, 144420 (2005), cond-mat/0404279.

[321] P. Sindzingre, G. Misguich, C. Lhuillier, B. Bernu, L. Pierre, C. Waldtmann, and H.-U. Everts, Magnetothermodynamics of the spin-1/2 kagome antiferromagnet, Phys. Rev. Lett. **84**, 2953 (2000).

[322] G. Misguich and P. Sindzingre, Magnetic susceptibility and specific heat of the spin-1/2 Heisenberg model on the kagome lattice and experimental data on $ZnCu_3(OH)_6Cl_2$, Eur. Phys. J. B **59**, 305 (2007), arXiv:0704.1017.

[323] B. H. Bernhard, B. Canals, and C. Lacroix, Green's function approach to the magnetic properties of the kagome antiferromagnet, Phys. Rev. B **66**, 104424 (2002), cond-mat/0202257.

[324] O. Cépas, C. M. Fong, P. W. Leung, and C. Lhuillier, Quantum phase transition induced by Dzyaloshinskii–Moriya interactions in the kagome antiferromagnet, Phys. Rev. B **78**, 140405 (2008), arXiv:0806.0393.

[325] I. Rousochatzakis, S. R. Manmana, A. M. Läuchli, B. Normand, and F. Mila, Dzyaloshinskii–Moriya anisotropy and nonmagnetic impurities in the $S=1/2$ kagome system $ZnCu_3(OH)_6Cl_2$, Phys. Rev. B **79**, 214415 (2009), arXiv:0903.2884.

[326] Z. Hiroi, M. Hanawa, N. Kobayashi, M. Nohara, H. Takagi, Y. Kato, and M. Takigawa, Spin-1/2 kagome-like lattice in volborthite $Cu_3(OH)_2V_2O_7{\cdot}2H_2O$, J. Phys. Soc. Jpn. **70**, 3377 (2001), cond-mat/0111127.

[327] K. Morita, M. Yano, T. Ono, H. Tanaka, K. Fujii, H. Uekusa, Y. Narumi, and K. Kindo, Singlet ground state and spin gap in $S=1/2$ kagome antiferromagnet $Rb_2Cu_3SnF_{12}$, J. Phys. Soc. Jpn. **77**, 043707 (2008), arXiv:0803.0205.

[328] K. Matan, T. Ono, Y. Fukumoto, T. J. Sato, J. Yamaura, M. Yano, K. Morita, and H. Tanaka, Pinwheel valence-bond solid and triplet excitations in the two-dimensional deformed kagome lattice, Nature Phys. **6**, 865 (2010).

[329] W. Krause, H.-J. Bernhardt, R. S. W. Braithwaite, U. Kolitsch, and R. Pritchard, Kapellasite, $Cu_3Zn(OH)_6Cl_2$, a new mineral from Lavrion, Greece, and its crystal structure, Mineral. Mag. **70**, 329 (2006).

[330] J. Schlüter and T. Malcherek, Haydeeite, $Cu_3Mg(OH)_6Cl_2$, a new mineral from the Haydee mine, Salar Grande, Atacama desert, Chile, Neues Jahrb. Mineral., Abh. **184**, 39 (2007).

[331] E. A. Nytko, J. S. Helton, P. Muller, and D. G. Nocera, A structurally perfect $S=1/2$ metal-organic hybrid kagome antiferromagnet, J. Am. Chem. Soc. **130**, 2922 (2008).

[332] R. H. Colman, A. Sinclair, and A. S. Wills, Magnetic and crystallographic studies of mg-herbertsmithite, γ-$Cu_3Mg(OH)_6Cl_2$ new $S=1/2$ kagome magnet and candidate spin liquid, Chem. Mater. **23**, 1811 (2011).

[333] E. Kermarrec, P. Mendels, F. Bert, R. H. Colman, A. S. Wills, P. Strobel, P. Bonville, A. Hillier, and A. Amato, Spin liquid ground state in the frustrated kagome antiferromagnet $MgCu_3(OH)_6Cl_2$, Phys. Rev. B **84**, 100401 (2011), arXiv:1106.6309.

[334] R. S. W. Braithwaite, K. Mereiter, W. H. Paar, and A. M. Clark, Herbertsmithite, $Cu_3Zn(OH)_6Cl_2$, a new species, and the definition of paratacamite, Mineral. Mag. **68**, 527 (2004).

[335] M. P. Shores, E. A. Nytko, B. M. Bartlett, and D. G. Nocera, A structurally perfect S=1/2 kagome antiferromagnet, J. Am. Chem. Soc. **127**, 13462 (2005).

[336] F. Bert, S. Nakamae, F. Ladieu, D. L'Hôte, P. Bonville, F. Duc, J.-C. Trombe, and P. Mendels, Low temperature magnetization of the S=1/2 kagome antiferromagnet $ZnCu_3(OH)_6Cl_2$, Phys. Rev. B **76**, 132411 (2007), arXiv:0710.0451.

[337] P. Mendels, F. Bert, M. A. de Vries, A. Olariu, A. Harrison, F. Duc, J. C. Trombe, J. S. Lord, A. Amato, and C. Baines, Quantum magnetism in the paratacamite family: towards an ideal kagome lattice, Phys. Rev. Lett. **98**, 077204 (2007), cond-mat/0610565.

[338] A. Olariu, P. Mendels, F. Bert, F. Duc, J. C. Trombe, M. A. de Vries, and A. Harrison, ^{17}O NMR study of the intrinsic magnetic susceptibility and spin dynamics of the quantum kagome antiferromagnet $ZnCu_3(OH)_6Cl_2$, Phys. Rev. Lett. **100**, 087202 (2008), arXiv:0711.2459.

[339] T. Imai, E. A. Nytko, B. M. Bartlett, M. P. Shores, and D. G. Nocera, ^{63}Cu, ^{35}Cl, and ^{1}H NMR in the S=1/2 kagome lattice $ZnCu_3(OH)_6Cl_2$, Phys. Rev. Lett. **100**, 077203 (2008), cond-mat/0703141.

[340] M. Rigol and R. R. P. Singh, Magnetic susceptibility of the kagome antiferromagnet $ZnCu_3(OH)_6Cl_2$, Phys. Rev. Lett. **98**, 207204 (2007), cond-mat/0701087.

[341] M. A. de Vries, K. V. Kamenev, W. A. Kockelmann, J. Sanchez-Benitez, and A. Harrison, Magnetic ground state of an experimental S=1/2 kagome antiferromagnet, Phys. Rev. Lett. **100**, 157205 (2008), arXiv:0705.0654.

[342] A. Zorko, S. Nellutla, J. van Tol, L. C. Brunel, F. Bert, F. Duc, J.-C. Trombe, M. A. de Vries, A. Harrison, and P. Mendels, Dzyaloshinsky–Moriya anisotropy in the spin-1/2 kagome compound $ZnCu_3(OH)_6Cl_2$, Phys. Rev. Lett. **101**, 026405 (2008), arXiv:0804.3107.

[343] S. Chu, P. Müller, D. G. Nocera, and Y. S. Lee, Hydrothermal growth of single crystals of the quantum magnets: clinoatacamite, paratacamite, and herbertsmithite, Appl. Phys. Lett. **98**, 092508 (2011).

[344] D. E. Freedman, T. H. Han, A. Prodi, P. Müller, Q.-Z. Huang, Y.-S. Chen, S. M. Webb, Y. S. Lee, T. M. McQueen, and D. G. Nocera, Site specific X-ray anomalous dispersion of the geometrically frustrated kagomeĄ magnet, herbertsmithite, $ZnCu_3(OH)_6Cl_2$, J. Am. Chem. Soc. **132**, 16185 (2010).

[345] O. Ofer, A. Keren, J. H. Brewer, T. H. Han, and Y. S. Lee, The herbertsmithite Hamiltonian: μSR measurements on single crystals, J. Phys.: Condens. Matter **23**, 164207 (2011), arXiv:1012.3511.

[346] T. Imai, M. Fu, T. H. Han, and Y. S. Lee, Local spin susceptibility of the S=1/2 kagome lattice in $ZnCu_3(OD)_6Cl_2$, Phys. Rev. B **84**, 020411 (2011), arXiv:1103.2457.

[347] T. H. Han, J. S. Helton, S. Chu, A. Prodi, D. K. Singh, C. Mazzoli, P. Müller, D. G. Nocera, and Y. S. Lee, Synthesis and characterization of single crystals of the spin-1/2 kagome-lattice antiferromagnets $Zn_xCu_{4-x}(OH)_6Cl_2$, Phys. Rev. B **83**, 100402 (2011), arXiv:1102.2179.

[348] X. G. Zheng, T. Mori, K. Nishiyama, W. Higemoto, H. Yamada, K. Nishikubo, and C. N. Xu, Antiferromagnetic transitions in polymorphous minerals of the natural cuprates atacamite and botallackite $Cu_2Cl(OH)_3$, Phys. Rev. B **71**, 174404 (2005).

[349] P. W. Leung and V. Elser, Numerical studies of a 36-site kagome antiferromagnet, Phys. Rev. B **47**, 5459 (1993).

[350] O. Janson, J. Richter, and H. Rosner, Modified kagome physics in the natural spin-1/2 kagome lattice systems: kapellasite $Cu_3Zn(OH)_6Cl_2$ and haydeeite $Cu_3Mg(OH)_6Cl_2$, Phys. Rev. Lett. **101**, 106403 (2008), arXiv:0806.1592.

[351] R. H. Colman, C. Ritter, and A. S. Wills, Toward perfection: kapellasite, $Cu_3Zn(OH)_6Cl_2$, a new model S=1/2 kagome antiferromagnet, Chem. Mater. **20**, 6897 (2008), arXiv:0811.4048.

[352] R. H. Colman, A. Sinclair, and A. S. Wills, Comparisons between haydeeite, α-$Cu_3Mg(OD)_6Cl_2$, and kapellasite, α-$Cu_3Zn(OD)_6Cl_2$, isostructural S=1/2 kagome magnets, Chem. Mater. **22**, 5774 (2010).

[353] E. Kermarrec, private communication.

[354] D. A. Huse and A. D. Rutenberg, Classical antiferromagnets on the kagome lattice, Phys. Rev. B **45**, 7536 (1992).

[355] O. A. Starykh, R. R. P. Singh, and G. C. Levine, Spinons in a crossed-chains model of a 2D spin liquid, Phys. Rev. Lett. **88**, 167203 (2002), cond-mat/0106260.

[356] R. Coldea, D. A. Tennant, A. M. Tsvelik, and Z. Tylczynski, Experimental realization of a 2D fractional quantum spin liquid, Phys. Rev. Lett. **86**, 1335 (2001), cond-mat/0007172.

[357] M. Moliner, I. Rousochatzakis, and F. Mila, Emergence of one-dimensional physics from the distorted Shastry–Sutherland lattice, Phys. Rev. B **83**, 140414 (2011), arXiv:1012.5177.

[358] H. Hess, Ueber den Volborthit, ein neues vanadinhaltiges Mineral, Bullet. scient. de l'Academie de Petersb. **44**, 22 (1838).

[359] S. Okubo, H. Ohta, K. Hazuki, T. Sakurai, N. Kobayashi, and Z. Hiroi, High-field ESR study of kagome-like substance $Cu_3V_2O_7(OH)_2{\cdot}2H_2O$, Physica B **294-295**, 75 (2001).

[360] A. Fukaya, Y. Fudamoto, I. M. Gat, T. Ito, M. I. Larkin, A. T. Savici, Y. J. Uemura, P. P. Kyriakou, G. M. Luke, M. T. Rovers, K. M. Kojima, A. Keren, M. Hanawa, and Z. Hiroi, Muon spin relaxation and susceptibility studies of the pure and diluted spin-1/2 kagome-like lattice system $(Cu_xZn_{1-x})_3V_2O_7(OH)_2{\cdot}2H_2O$, Phys. Rev. Lett. **91**, 207603 (2003), cond-mat/0310739.

[361] F. Bert, D. Bono, P. Mendels, F. Ladieu, F. Duc, J.-C. Trombe, and P. Millet, Ground state of the kagome-like $S=1/2$ antiferromagnet volborthite $Cu_3V_2O_7(OH)_2{\cdot}2H_2O$, Phys. Rev. Lett. **95**, 087203 (2005), cond-mat/0507250.

[362] M. Yoshida, M. Takigawa, H. Yoshida, Y. Okamoto, and Z. Hiroi, Phase diagram and spin dynamics in volborthite with a distorted kagome lattice, Phys. Rev. Lett. **103**, 077207 (2009), arXiv:0906.2846.

[363] H. Yoshida, Y. Okamoto, T. Tayama, T. Sakakibara, M. Tokunaga, A. Matsuo, Y. Narumi, K. Kindo, M. Yoshida, M. Takigawa, and Z. Hiroi, Magnetization "steps" on a kagome lattice in volborthite, J. Phys. Soc. Jpn. **78**, 043704 (2009), arXiv:0902.3028.

[364] Z. Hiroi, private communication.

[365] G. J. Nilsen, F. C. Coomer, M. A. de Vries, J. R. Stewart, P. P. Deen, A. Harrison, and H. M. Rønnow, Pair correlations, short-range order, and dispersive excitations in the quasi-kagome quantum magnet volborthite, Phys. Rev. B **84**, 172401 (2011), arXiv:1001.2462.

[366] S. Yamashita, T. Moriura, Y. Nakazawa, H. Yoshida, Y. Okamoto, and Z. Hiroi, Thermodynamic properties of the kagome lattice in volborthite, J. Phys. Soc. Jpn. **79**, 083710 (2010).

[367] F. Wang, A. Vishwanath, and Y. B. Kim, Quantum and classical spins on the spatially distorted kagome lattice: applications to volborthite $Cu_3(OH)_2V_2O_7{\cdot}2H_2O$, Phys. Rev. B **76**, 094421 (2007), arXiv:0704.0933.

[368] T. Yavors'kii, W. Apel, and H.-U. Everts, Heisenberg antiferromagnet with anisotropic exchange on the kagome lattice: description of the magnetic properties of volborthite, Phys. Rev. B **76**, 064430 (2007), arXiv:0704.1441.

[369] E. M. Stoudenmire and L. Balents, Ordered phases of the anisotropic kagome-lattice antiferromagnet in a magnetic field, Phys. Rev. B **77**, 174414 (2008), arXiv:0712.2269.

[370] A. P. Schnyder, O. A. Starykh, and L. Balents, Spatially anisotropic Heisenberg kagome antiferromagnet, Phys. Rev. B **78**, 174420 (2008), arXiv:0807.0285.

[371] A. A. Kashaev and V. V. Bakakin, Crystal structure of volborthite $Cu_3(OH)_2V_2O_7{\cdot}2H_2O$, Dokl. Akad. Nauk SSSR **181**, 967 (1968).

[372] R. Basso, A. Palenzona, and L. Zefiro, Crystal structure refinement of volborthite from Scrava Mine (Eastern Liguria, Italy), N. Jb. Miner. Mh. **9**, 385 (1988).

[373] A. Kashaev, I. Rozhdestvenskaya, I. Bannova, A. Sapozhnikov, and O. Glebova, Balance, uniformity, and asymmetry of the structure of volborthite $Cu_3(OH)_2V_2O_7{\cdot}2H_2O$, J. Struct. Chem. **49**, 708 (2008).

[374] M. A. Lafontaine, A. Le Bail, and G. Férey, Copper-containing minerals — I. $Cu_3(OH)_2V_2O_7{\cdot}2H_2O$: the synthetic homolog of volborthite; crystal structure determination from X-ray and neutron data; structural correlations, J. Solid State Chem. **85**, 220 (1990).

[375] M. Kato, A. Hatazaki, K. Yoshimura, and K. Kosuge, One-dimensional magnetic behavior of $CuSb_2O_6$, Physica B **281–282**, 663 (2000).

[376] D. Kasinathan, K. Koepernik, and H. Rosner, Quasi-one-dimensional magnetism driven by unusual orbital ordering in $CuSb_2O_6$, Phys. Rev. Lett. **100**, 237202 (2008), arXiv:0805.4080.

[377] D. Manthey, Orbital viewer, `http://www.orbitals.com/orb`.

[378] O. A. Starykh, private communication.

[379] O. Janson, J. Richter, P. Sindzingre, and H. Rosner, Coupled frustrated quantum spin-1/2 chains with orbital order in volborthite $Cu_3V_2O_7(OH)_2{\cdot}2H_2O$, Phys. Rev. B **82**, 104434 (2010), arXiv:1004.2185.

[380] G. Meunier, C. Svenssen, and A. Carpy, Cristallochimie du sélénium(+IV). III. Structure cristalline de $CuSe_2O_5$, Acta Crystallogr. **B32**, 2664 (1976).

[381] J. Bandyopadhyay and K. Gupta, Low temperature lattice parameters of Al and Al-Zn alloys and Grüneisen parameter of Al, Cryogenics **18**, 54 (1978).

[382] E. R. Jette and F. Foote, Precision determination of lattice constants, J. Chem. Phys. **3**, 605 (1935).

[383] M. E. Straumanis and A. Jevins, Die Gitterkonstanten des NaCl und des Steinsalzes, Z. Phys. **102**, 353 (1936).

[384] K. O. Znamenkov, I. V. Morozov, and S. I. Troyanov, Synthesis and crystal structure of copper(II) nitrato complexes $NO[Cu(NO_3)_3]$, $Na_2[Cu(NO_3)_4]$, and $Ag_2[Cu(NO_3)_4]$, Russ. J. Inorg. Chem. **49**, 172 (2004).

[385] K. Pogorzelec-Glaser, A. Pietraszko, B. Hilczer, and M. PoÅĆomska, Structure and phase transitions in $Cu_2P_2O_7$. Phase Transit. **79**, 535 (2006).

[386] M. Weil, C. Lengauer, E. Füglein, and E. J. Baran, The reversible $\alpha \rightarrow \beta$ phase transition of $Cu_2As_2O_7$, Cryst. Growth Des. **4**, 1229 (2004).

[387] S. Todo and K. Kato, Cluster algorithms for general-S quantum spin systems, Phys. Rev. Lett. **87**, 047203 (2001), cond-mat/9911047.

[388] A. Albuquerque, F. Alet, P. Corboz, P. Dayal, A. Feiguin, S. Fuchs, L. Gamper, E. Gull, S. Gürtler, A. Honecker, R. Igarashi, M. Körner, A. Kozhevnikov, A. Läuchli, S. R. Manmana, M. Matsumoto, I. P. McCulloch, F. Michel, R. M. Noack, G. Pawlowski, L. Pollet, T. Pruschke, U. Schollwöck, S. Todo, S. Trebst, M. Troyer, P. Werner, and S. Wessel, The ALPS project release 1.3: open-source software for strongly correlated systems, J. Magn. Magn. Mater. **310**, 1187 (2007), arXiv:0801.1765.

[389] M. Oshikawa and I. Affleck, Field-induced gap in S=1/2 antiferromagnetic chains, Phys. Rev. Lett. **79**, 2883 (1997), cond-mat/9706085.

[390] J. Schulenburg, `http://www-e.uni-magdeburg.de/jschulen/spin`.

List of publications

[1] H. Rosner, M. Johannes, S.-L. Drechsler, M. Schmitt, O. Janson, W. Schnelle, W. Liu, Y.-X. Huang, and R. Kniep, Cu^{II} materials — from crystal chemistry to magnetic model compounds, Sci. Tech. Adv. Mater. **8**, 352 (2007).

[2] O. Janson and H. Rosner, Electronic structure and magnetic properties of Bi_2CuO_4, Physica B **460–462**, 458 (2007).

[3] O. Janson, R. O. Kuzian, S.-L. Drechsler, and H. Rosner, Electronic structure and magnetic properties of the spin-1/2 Heisenberg magnet Bi_2CuO_4, Phys. Rev. B **76**, 115119 (2007).

[4] O. Janson, J. Richter, and H. Rosner, Modified kagome physics in the natural spin-1/2 kagome lattice systems: kapellasite $Cu_3Zn(OH)_6Cl_2$ and haydeeite $Cu_3Mg(OH)_6Cl_2$, Phys. Rev. Lett. **101**, 106403 (2008), arXiv:0806.1592.

[5] M. Schmitt, O. Janson, M. Schmidt, S. Hoffmann, W. Schnelle, S.-L. Drechsler, and H. Rosner, Crystal-water-induced switching of magnetically active orbitals in $CuCl_2$, Phys. Rev. B **79**, 245119 (2009), arXiv:0905.4038.

[6] O. Janson, W. Schnelle, M. Schmidt, Y. Prots, S.-L. Drechsler, S. K. Filatov, and H. Rosner, Electronic structure and magnetic properties of the spin-1/2 Heisenberg system $CuSe_2O_5$, New J. Phys. **11**, 113034 (2009), arXiv:0907.4874.

[7] O. Janson, J. Richter, and H. Rosner, Intrinsic peculiarities of real material realizations of a spin-1/2 kagome lattice, J. Phys.: Conf. Ser. **145**, 012008 (2009), arXiv:0807.2005.

[8] O. Janson, A. A. Tsirlin, and H. Rosner, Antiferromagnetic spin-1/2 chains in $(NO)Cu(NO_3)_3$: a microscopic study, Phys. Rev. B **82**, 184410 (2010), arXiv:1007.2798.

[9] A. A. Tsirlin, O. Janson, and H. Rosner, β-$Cu_2V_2O_7$: a spin-1/2 honeycomb lattice system, Phys. Rev. B **82**, 144416 (2010), arXiv:1007.1646.

[10] A. A. Tsirlin, I. Rousochatzakis, D. Kasinathan, O. Janson, R. Nath, F. Weickert, C. Geibel, A. M. Läuchli, and H. Rosner, Bridging frustrated-spin-chain and spin-ladder physics: quasi-one-dimensional magnetism of $BiCu_2PO_6$, Phys. Rev. B **82**, 144426 (2010), arXiv:1008.1771.

[11] O. Janson, J. Richter, P. Sindzingre, and H. Rosner, Coupled frustrated quantum spin-1/2 chains with orbital order in volborthite $Cu_3V_2O_7(OH)_2 \cdot 2H_2O$, Phys. Rev. B **82**, 104434 (2010), arXiv:1004.2185.

[12] M. Schmitt, A. A. Gippius, K. S. Okhotnikov, W. Schnelle, K. Koch, O. Janson, W. Liu, Y.-H. Huang, Y. Skourski, F. Weickert, M. Baenitz, and H. Rosner, Electronic structure and magnetic properties of the spin-gap compound $Cu_2(PO_3)_2CH_2$: Magnetic versus structural dimers, Phys. Rev. B **81**, 104416 (2010).

[13] O. Janson, A. A. Tsirlin, M. Schmitt, and H. Rosner, Large quantum fluctuations in the strongly coupled spin-1/2 chains of green dioptase $Cu_6Si_6O_{18} \cdot 6H_2O$, Phys. Rev. B **82**, 014424 (2010), arXiv:1004.3765.

[14] O. Janson, A. A. Tsirlin, E. S. Osipova, P. S. Berdonosov, A. V. Olenev, V. A. Dolgikh, and H. Rosner, $CaCu_2(SeO_3)_2Cl_2$: Spin-1/2 Heisenberg chain compound with complex frustrated interchain couplings, Phys. Rev. B **83**, 144423 (2011), arXiv:1011.5827.

[15] J. Sirker, V. Y. Krivnov, D. V. Dmitriev, A. Herzog, O. Janson, S. Nishimoto, S.-L. Drechsler, and J. Richter, The J_1–J_2 Heisenberg model at and close to its $z = 4$ quantum critical point, Phys. Rev. B **84**, 144403 (2011), arXiv:1106.1008.

[16] O. Janson, A. A. Tsirlin, J. Sichelschmidt, Y. Skourski, F. Weickert, and H. Rosner, Long-range superexchange in $Cu_2A_2O_7$ (A=P, As, V) as a key element of the microscopic magnetic model, Phys. Rev. B **83**, 094435 (2011), arXiv:1011.5393.

[17] S. Lebernegg, A. A. Tsirlin, O. Janson, R. Nath, J. Sichelschmidt, Y. Skourski, G. Amthauer, and H. Rosner, Magnetic model for $A_2CuP_2O_7$ (A=Na, Li): one-dimensional versus two-dimensional behavior, Phys. Rev. B **84**, 174436 (2011), arXiv:1107.0250.

[18] Y. C. Arango, E. Vavilova, M. Abdel-Hafiez, O. Janson, A. A. Tsirlin, H. Rosner, S.-L. Drechsler, M. Weil, G. Nénert, R. Klingeler, O. Volkova, A. Vasiliev, V. Kataev, and B. Büchner, Magnetic properties of the low-dimensional spin-1/2 magnet α-$Cu_2As_2O_7$, Phys. Rev. B **84**, 134430 (2011), arXiv:1110.0447.

[19] H. Jeschke, I. Opahle, H. Kandpal, R. Valentí, H. Das, T. Saha-Dasgupta, O. Janson, H. Rosner, A. Brühl, B. Wolf, M. Lang, J. Richter, S. Hu, X. Wang, R. Peters, T. Pruschke, and A. Honecker, Multistep approach to microscopic models for frustrated quantum magnets: the case of the natural mineral azurite, Phys. Rev. Lett. **106**, 217201 (2011), arXiv:1012.1090.

[20] A. A. Tsirlin, O. Janson, and H. Rosner, Unusual ferromagnetic superexchange in $CdVO_3$: the role of Cd, Phys. Rev. B **84**, 144429 (2011), arXiv:1104.2495.

[21] O. Janson, I. Rousochatzakis, A. A. Tsirlin, J. Richter, Y. Skourski, and H. Rosner, Decorated Shastry–Sutherland lattice in the spin-1/2 magnet $CdCu_2(BO_3)_2$, Phys. Rev. B **85**, 064404 (2012), arXiv:1112.5323.

[22] A. A. Tsirlin, A. M. Abakumov, C. Ritter, P. F. Henry, O. Janson, and H. Rosner, Short-range order of br and three-dimensional magnetism in $(CuBr)LaNb_2O_7$, Phys. Rev. B **85**, 214427 (2012), arXiv:1204.2293.

Acknowledgments

It is my greatest pleasure to thank people that supported me during the years of working on this thesis. It is, however, my greatest concern that some of these people would be mistakenly absent in this list. Therefore, I would like to apologize for my absent-mindedness beforehand, and thank all people whom I forgot to mention explicitly.

I would like to start this part of the thesis by acknowledging my supervisor Dr. Helge Rosner. Claiming that this work would have been possible without his guidance, is not only a commonplace, it is an evident understatement. On our first acquaintance, I could hardly decipher "DFT" and likely had a vague idea what the spin is. A hopeless case. I'm very grateful to you, Helge, that instead of waving me goodbye, you found time for laborious discussions (probably, interminable for you, but truly enlightening for me) and patiently waited for the perceptible outcomes. My understanding of quantum magnetism gradually improved. However, I'm still puzzled how to acquire a scientific intuition like that of yours. Well, life is not only science. You belong to the endangered type of leaders that care not only about the results, but the people as well. It was a real pleasure to work with you. And I'm happy that I still enjoy it.

Prof. Dr. Helmut Eschrig is acknowledged for guiding this work and valuable comments on the results. It was a pleasure to enjoy the wonderful working conditions at the Chemical metal science department of MPI CPfS, which is led by Prof. J. Grin. I highly appreciate his assistance in the arrangement of my short-term visits to the institute that preceded this work, and fruitful discussions. I would also like to acknowledge particularly the opportunity to attend a number of scientific events and meet the leading scientists in person. A substantial part of the results presented in this thesis was engendered by the discussions that would have never been possible otherwise. *Deutsche Forschungsgemeinschaft* (DFG) is kindly acknowledged for financial support.

I certainly owe a debt of gratitude to all present and past members of our wonderful and coherent group. Ms. Miriam Schmitt, Drs. Deepa Kasinathan, Vivien Petzold, Katrin Rose, Monika Gamża, Alexander A. Tsirlin, and Luis Craco—you were always ready to lend a hand and maintained an inspirational working atmosphere! I'm especially grateful to you, Sasha, for your ability to perform a painstaking analysis of the experimental data and scrutinize the scientific literature (even the papers anyone else would find mundane), and especially, for numerous discussions that impacted this thesis. *Spasibo*!

My sincere thanks to Prof. Dr. Johannes Richter, without whom we could have hardly forced our way to better understanding of the kagome compounds. Johannes, your scientific intuition, your grasp of the essential physics in murky models and your brisk working style are really admirable. It was an honor and pleasure to work with you!

Dr. Martin Rotter is acknowledged for critical reading of this thesis. Martin, I really admire your painstaking attention to the very details of a text! Thank you for your valuable comments and suggestions.

Although the thesis is focused on the computational results, comparison to the related experiments is an integral part of the developed approach. In certain cases, the comparison was impeded by the quality of the published data, or no experimental information was available. For me, it was a piece of luck to have the relevant experts sitting next door. I'm very grateful to Drs. Walter Schnelle, Marcus Schmidt, Alexander A. Tsirlin, Shuang Chen, Stefan Hoffmann, Jörg Sichelschmidt, and Yurii Prots for their effort to synthesize and to measure.

A nice thing about doing solid state research in Dresden is that the relevant institutions are within walking distance from each other. Thus not surprising, the collaborations between the institutes are flourishing, and this work is no exception. First, I would like to thanks the colleagues from the IFW-based team of FPLO developers, and particularly, Dr. Klaus Koepernik. Many thanks for fruitful discussions and collaborations to Drs. Stefan-Ludwig Drechsler, Roman O. Kuzian, Yulieth C. Arango, and Vladislav Kataev. Drs. Yurii Skourski (HLD) and Franziska D. Weickert are acknowledged for high-field magnetization measurements. Many thanks to the former employees of MPI PKS, Dr. Ioannis Rousochatzakis and Prof. Dr. Andreas M. Läuchli, for enlightening discussions and fruitful collaboration. Ioannis, recalling how we first met on a conference dinner in Lyon only because I was terribly late for it, and people (of whom I knew no one) at the "Lausanne" table were so kind to bunch up and arrange a free seat next to you, makes me quite confident that most of advances, discoveries, breakthroughs, and simply good things are often made by chance or even mistake.

A substantial part of this work was stimulated or inspired by discussions (some of them developed into successful collaborations) with the experts in theoretical physics and numerical simulations: Dr. Philippe Sindzingre, Dr. Olivier Cépas, Prof. Dr. Claire Lhuillier, Prof. Dr. Roser Valentí, Prof. Dr. Harald O. Jeschke, Dr. Ingo Opahle, Dr. Laura Messio, Prof. Dr. Oleg Starykh, Dr. Andreas Honecker, Dr. Nicolas Laflorencie, Prof. Dr. Christopher L. Henley, Prof. Dr. Frédéric Mila, Dr. Salvatore R. Manmana, Dr. Kai P. Schmidt, Dr. Vladimir V. Mazurenko, Prof. Dr. Nic Shannon, and Prof. Dr. Claudine Lacroix. Certainly, not least were discussions with the experimental colleagues, Prof. Dr. Young S. Lee, Mr. Tianheng H. Han, Prof. Dr. Philippe Mendels, Dr. Fabrice Bert, Mr. Edwin Kermarrec, Dr. Reinhard K. Kremer, Dr. Joseph M. Law, Prof. Andrew S. Wills, Prof. Z. Hiroi, Dr. Gøran Nilsen, Dr. Mladen Horvatić, and Dr. Peter S. Berdonosov are kindly acknowledged.

Starting from my first visit to MPI CPfS, I continuously admire the hospitality and

excellent organization of the institute. This *genius loci* is maintained by the professional and keen people that keep the institute running. For the visitor, the institute starts at the guest service. Thank you, Mrs. Katarina Klein, Mrs. Claudia Strohbach, Mrs. Katrin Demian, and Mrs. Tatjana Vogel, for your kind assistance and willingness to help. Many thanks to the administration of the institute, particularly, Mrs. Margot Pester, Mrs. Susanne Zücker, Mrs. Monika Lintz, and Mrs. Rita Krause.

Performing numerical calculations naturally implies continuous maintenance of the hardware, and solving software-related problems as well. Dr. Burkhard Schmidt, Dr. Frank R. Wagner, Mr. Johannes Steinmetz, and the entire IT-service team largely alleviated the usage of the computational facilities, and are gratefully acknowledged therefor. Sincere thanks to my room mates Alexander and Enkhe, is was a pleasure to share the office with you!

On behalf of my family, I would like to thank all our friends who brightened up our life in Dresden. Besides the people I have mentioned on the other occasions, many thanks to Lena, Nicolay, Misha, Igor, Roman, Konrad, Sandra, and Victor! In addition, we really enjoyed hosting the courageous people who took a trip to Dresden and stayed over at our place. Our own trips to the motherland would have never been so pleasant without the people who took great care over and ensured the smooth running of our visit, especially our relatives and our dear friends. Vlad and Alina, wherever and whenever we met, it made our day!

Personally, I largely enjoyed visiting the department of crystallography at the University of St. Petersburg, and meeting the open-hearted people who are probably inherent to this place. It was always nice to meet you and talk to you.

I'm deeply indebted to the supervisor of my Bachelor and Master theses, the man who brought me into science, Prof. Dr. Stanislav K. Filatov. During my university years, I was lucky enough to have a mentor, other students could only dream of. I dare say, making Prof. Filatov acquaintance shaped my life. Thank you, dear *Uchitel'*!

Finally, it is my pleasure to acknowledge the people to whom I'm most deeply indebted, my family. Dear parents, although you live far from Dresden, your backing was crucial for me. Your moral support is that kind of support only parents can give. Your contribution to the work should not be undervalued. Thank you.

P. S. In spring, the cherry and magnolia trees started to bloom. I would wake up early on a Saturday morning to take a family walk and admire the wonderful scenery. Then, we would probably drop at some nice café nearby. Over a cup of coffee, absorbed in reverie, we would concur that it's so nice to be here. Julia and Stasia, these years were wonderful, because we were together. I wish only I could have spent a bit more time with you. Thank you for everything, especially for your understanding. Thank you for being my home and my family. I'm proud of you. I feel confident that little Emily parked herself in the right place.

Versicherung

Hiermit versichere ich, dass ich die vorliegende Arbeit ohne unzulässige Hilfe Dritter und ohne Benutzung anderer als der angegebenen Hilfsmittel angefertigt habe; die aus fremden Quellen direkt oder indirekt übernommenen Gedanken sind als solche kenntlich gemacht. Die Arbeit wurde bisher weder im Inland noch im Ausland in gleicher oder ähnlicher Form einer anderen Prüfungsbehörde vorgelegt.

Die vorliegende Dissertation wurde unter der Betreuung von Prof. Dr. Helmut Eschrig und Dr. Helge Rosner in der Kompetenzgruppe Theoretische Physik im Max-Planck-Institut für chemische Physik fester Stoffe angefertigt.

Janson Oleg

Dresden, den 09.01.2012 Oleg Janson